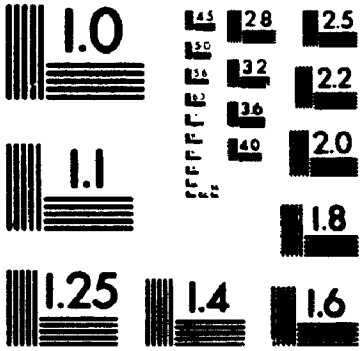

The Aerodynamics of Turbine Blades With Tip Damage

by

Stefano F. De Cecco
B. Eng. (Aerospace Engineering)

A thesis submitted to
the Faculty of Graduate Studies and Research
in partial fulfilment of the requirements
for the degree of

Master of Engineering
in
Aerospace Engineering

Ottawa-Carleton Institute for Mechanical
and Aerospace Engineering

Department of Mechanical and Aerospace Engineering
Carleton University
Ottawa, Ontario
April, 1995

ISBN 0-612-03019-9

Name STEFANO DE CECCO

Dissertation Abstracts International is arranged by broad, general subject categories. Please select the one subject which most nearly describes the content of your dissertation. Enter the corresponding four-digit code in the spaces provided.

AEROSPACE ENGINEERING — SUBJECT TERM

0538 — SUBJECT CODE

U·M·I

Subject Categories

THE HUMANITIES AND SOCIAL SCIENCES

COMMUNICATIONS AND THE ARTS
Architecture 0729
Art History 0377
Cinema 0900
Dance 0378
Fine Arts 0357
Information Science 0723
Journalism 0391
Library Science 0399
Mass Communications 0708
Music 0413
Speech Communication 0459
Theater 0465

EDUCATION
General 0515
Administration 0514
Adult and Continuing 0516
Agricultural 0517
Art 0273
Bilingual and Multicultural 0282
Business 0688
Community College 0275
Curriculum and Instruction 0727
Early Childhood 0518
Elementary 0524
Finance 0277
Guidance and Counseling 0519
Health 0680
Higher 0745
History of 0520
Home Economics 0278
Industrial 0521
Language and Literature 0279
Mathematics 0280
Music 0522
Philosophy of 0998
Physical 0523
Psychology 0525
Reading 0535
Religious 0527
Sciences 0714
Secondary 0533
Social Sciences 0534
Sociology of 0340
Special 0529
Teacher Training 0530
Technology 0710
Tests and Measurements 0288
Vocational 0747

LANGUAGE, LITERATURE AND LINGUISTICS
Language
- General 0679
- Ancient 0289
- Linguistics 0290
- Modern 0291

Literature
- General 0401
- Classical 0294
- Comparative 0295
- Medieval 0297
- Modern 0298
- African 0316
- American 0591
- Asian 0305
- Canadian (English) 0352
- Canadian (French) 0355
- English 0593
- Germanic 0311
- Latin American 0312
- Middle Eastern 0315
- Romance 0313
- Slavic and East European 0314

PHILOSOPHY, RELIGION AND THEOLOGY
Philosophy 0422
Religion
- General 0318
- Biblical Studies 0321
- Clergy 0319
- History of 0320
- Philosophy of 0322

Theology 0469

SOCIAL SCIENCES
American Studies 0323
Anthropology
- Archaeology 0324
- Cultural 0326
- Physical 0327

Business Administration
- General 0310
- Accounting 0272
- Banking 0770
- Management 0454
- Marketing 0338

Canadian Studies 0385
Economics
- General 0501
- Agricultural 0503
- Commerce Business 0505
- Finance 0508
- History 0509
- Labor 0510
- Theory 0511

Folklore 0358
Geography 0366
Gerontology 0351
History
- General 0578
- Ancient 0579
- Medieval 0581
- Modern 0582
- Black 0328
- African 0331
- Asia, Australia and Oceania 0332
- Canadian 0334
- European 0335
- Latin American 0336
- Middle Eastern 0333
- United States 0337

History of Science 0585
Law 0398
Political Science
- General 0615
- International Law and Relations 0616
- Public Administration 0617

Recreation 0814
Social Work 0452
Sociology
- General 0626
- Criminology and Penology 0627
- Demography 0938
- Ethnic and Racial Studies 0631
- Individual and Family Studies 0628
- Industrial and Labor Relations 0629
- Public and Social Welfare 0630
- Social Structure and Development 0700
- Theory and Methods 0344

Transportation 0709
Urban and Regional Planning 0999
Women's Studies 0453

THE SCIENCES AND ENGINEERING

BIOLOGICAL SCIENCES
Agriculture
- General 0473
- Agronomy 0285
- Animal Culture and Nutrition 0475
- Animal Pathology 0476
- Food Science and Technology 0359
- Forestry and Wildlife 0478
- Plant Culture 0479
- Plant Pathology 0480
- Plant Physiology 0817
- Range Management 0777
- Wood Technology 0746

Biology
- General 0306
- Anatomy 0287
- Biostatistics 0308
- Botany 0309
- Cell 0379
- Ecology 0329
- Entomology 0353
- Genetics 0369
- Limnology 0793
- Microbiology 0410
- Molecular 0307
- Neuroscience 0317
- Oceanography 0416
- Physiology 0433
- Radiation 0821
- Veterinary Science 0778
- Zoology 0472

Biophysics
- General 0786
- Medical 0760

EARTH SCIENCES
Biogeochemistry 0425
Geochemistry 0996
Geodesy 0370
Geology 0372
Geophysics 0373
Hydrology 0388
Mineralogy 0411
Paleobotany 0345
Paleoecology 0426
Paleontology 0418
Paleozoology 0985
Palynology 0427
Physical Geography 0368
Physical Oceanography 0415

HEALTH AND ENVIRONMENTAL SCIENCES
Environmental Sciences 0768
Health Sciences
- General 0566
- Audiology 0300
- Chemotherapy 0992
- Dentistry 0567
- Education 0350
- Hospital Management 0769
- Human Development 0758
- Immunology 0982
- Medicine and Surgery 0564
- Mental Health 0347
- Nursing 0569
- Nutrition 0570
- Obstetrics and Gynecology 0380
- Occupational Health and Therapy 0354
- Ophthalmology 0381
- Pathology 0571
- Pharmacology 0419
- Pharmacy 0572
- Physical Therapy 0382
- Public Health 0573
- Radiology 0574
- Recreation 0575
- Speech Pathology 0460
- Toxicology 0383

Home Economics 0386

PHYSICAL SCIENCES

Pure Sciences

Chemistry
- General 0485
- Agricultural 0749
- Analytical 0486
- Biochemistry 0487
- Inorganic 0488
- Nuclear 0738
- Organic 0490
- Pharmaceutical 0491
- Physical 0494
- Polymer 0495
- Radiation 0754

Mathematics 0405
Physics
- General 0605
- Acoustics 0986
- Astronomy and Astrophysics 0606
- Atmospheric Science 0608
- Atomic 0748
- Electronics and Electricity 0607
- Elementary Particles and High Energy 0798
- Fluid and Plasma 0759
- Molecular 0609
- Nuclear 0610
- Optics 0752
- Radiation 0756
- Solid State 0611

Statistics 0463

Applied Sciences

Applied Mechanics 0346
Computer Science 0984
Engineering
- General 0537
- Aerospace 0538
- Agricultural 0539
- Automotive 0540
- Biomedical 0541
- Chemical 0542
- Civil 0543
- Electronics and Electrical 0544
- Heat and Thermodynamics 0348
- Hydraulic 0545
- Industrial 0546
- Marine 0547
- Materials Science 0794
- Mechanical 0548
- Metallurgy 0743
- Mining 0551
- Nuclear 0552
- Packaging 0549
- Petroleum 0765
- Sanitary and Municipal 0554
- System Science 0790

Geotechnology 0428
Operations Research 0796
Plastics Technology 0795
Textile Technology 0994

PSYCHOLOGY
General 0621
Behavioral 0384
Clinical 0622
Developmental 0620
Experimental 0623
Industrial 0624
Personality 0625
Physiological 0989
Psychobiology 0349
Psychometrics 0632
Social 0451

The undersigned hereby recommend to the
Faculty of Graduate Studies and Research
acceptance of the thesis

The Aerodynamics of Turbine Blades with Tip Damage

submitted by

Stefano F. De Cecco, B. Eng.

in partial fulfilment of the requirements for
the degree of Master of Engineering

Thesis Co-Supervisor

Thesis Co-Supervisor

Chairman, Department of Mechanical and Aerospace Engineering

Carleton University

April, 1995

to my family

Abstract

The effect of tip damage on the aerodynamics of turbine blades is examined experimentally and computationally. The work is part of a study investigating the aerodynamics of turbines which have experienced in-service damage and is related to Engine Health Monitoring.

Measurements have been made for tip clearances up to 15% of chord in a turbine cascade which has been used previously to study tip-leakage flow at smaller clearances. Detailed flow field measurements have been made upstream and downstream of the cascade using a combination of pitot, three-hole, and seven-hole probes. In addition, static pressure distributions have been measured at the endwall, blade midspan, and near the blade tip. The most unexpected result was that the end losses (that is, the sum of the secondary and tip-leakage losses) reached a maximum for clearances of about 6 or 7% of chord. At the largest clearance (15% of chord), the measured end losses were significantly reduced and were in fact comparable to the secondary losses measured at zero clearance. The physics of the flow and the reasons for the observed reduction in losses are discussed in some detail. In particular, the attenuation of the driving pressure differences across the gap, and the resulting reduced mass flow rate per unit area in the gap, were found to account for a large part of the observed reduction in losses. The measurements are also compared with the predictions of some existing tip-leakage loss models.

In addition to the experimental study, a computational investigation was conducted using a three-dimensional Navier-Stokes solver developed by Dawes (1986a). The results of the investigation, which was conducted primarily to evaluate the code's ability to predict the flow field around blades with large clearances, are compared with the measurements and are found to be encouraging.

Acknowledgements

I wish to express my profound gratitude to my thesis supervisors, Dr. Steen A. Sjolander and Dr. Metin I. Yaras, for their invaluable guidance and advice throughout the course of this research.

Financial support for this study provided by GasTOPS Ltd., Ottawa, Ontario, Canada, the Government of Ontario (under the University Research Incentives Fund), and the Natural Sciences and Engineering Research Council of Canada (through the Postgraduate Scholarship Program) is gratefully acknowledged.

I would also like to extend my sincere thanks to my colleagues Michael W. Benner and Peter J. Serjak for their valuable suggestions and constant interest in my work. In addition, I would like to thank my close friend George Khoury for his assistance on all electrical matters.

Finally, I would like to express my gratitude to the laboratory technicians, Fred Barrett and Terry Goodwin, the technicians of ETC Mechanical, Stephen J. Szick in particular, and the staff of the Department of Mechanical & Aerospace Engineering office.

Table of Contents

List of Figures

List of Tables

Nomenclature

English Symbols

A	area
c	blade chord
c_x	blade axial chord length
C	velocity (Sect. 6.1.1.4 and Appendix J)
C_D	tip gap discharge coefficient
C_L	blade lift coefficient $= \dfrac{L}{\frac{1}{2}\rho V_m^2 c}$
C_P	static-pressure coefficient $= \dfrac{P-P_{CL}}{\frac{1}{2}\rho V_{CL}^2}$
C_{P_o}	total-pressure coefficient $= \dfrac{P_o - P_{o_{CL}}}{\frac{1}{2}\rho V_{CL}^2}$
C_{P_o}'	pitchwise mass-averaged total-pressure loss coefficient (Eqn. 6.3)
C_{P_o}''	total-pressure loss coefficient averaged over reference mass flow rate (Eqn. 6.1)
C_{P_P}	static-pressure coefficient at gap inlet (pressure side)
C_{P_S}	static-pressure coefficient at gap outlet (suction side)
d	leading-edge diameter
E	total internal energy
h	span; enthalpy (Sect. 6.1.2.1)
H	total enthalpy

H_x	boundary-layer shape factor $= \frac{\delta_x^*}{\theta_{xx}}$
$\hat{i}_r, \hat{i}_\theta, \hat{i}_x$	unit vectors in r, θ, x directions
i_{des}	design incidence
I	rothalpy (Sect. 5.1.1)
I, J, K	indices for computational grid
k_s	fraction of zero-clearance secondary loss still present with clearance
K_E, K_G	constants dependent on blade loading distribution (Sects. 2.4 and 6.1.5)
L	lift force
M	Mach number
$\dot{m}_g$	tip gap mass flow rate
$\dot{m}_{ref}$	reference passage mass flow rate at the inlet
P	static pressure
P_o	total pressure
q	dynamic pressure $= \frac{1}{2} \rho V^2$
$\bar{q}$	relative velocity (Sect. 5.1.1)
r	radial co-ordinate
r, θ, x	cylindrical co-ordinates
Re	Reynolds number based on blade chord $= \frac{\rho V_{CL} c}{\mu}$
s	streamwise co-ordinate; specific entropy (Sect. 6.1.2.1)
S	blade spacing
t_{max}	blade maximum thickness
T	absolute temperature
u, v, w	components of velocity in x, y, z directions
u'	root-mean-square velocity fluctuation in x-direction
V	velocity; volume (Sect. 5.1.1)

We	leading-edge wedge angle
x, y, z	co-ordinates in axial, pitchwise and spanwise directions
x'	co-ordinate in chordwise direction
y', z'	local pitchwise and spanwise co-ordinates
Y	total-pressure loss coefficient $= \dfrac{P_{o_1} - P_{o_2}}{\frac{1}{2}\rho V_2^2}$

Greek Symbols

α	flow angle, measured from axial direction
β	blade metal angle, measured from axial direction
γ	blade stagger angle; specific heat ratio (Sect. 5.1.1)
Γ	circulation
Γ'	non-dimensional circulation $= \left(\dfrac{\Gamma}{V_{CL}\, c}\right)$
δ	boundary-layer thickness
δ_x^*	boundary-layer displacement thickness $= \displaystyle\int_0^\delta \left(\frac{V_{x_e}}{V_e} - \frac{V_x}{V_e}\right) dz$
κ	clearance-to-span ratio (Appendix J)
μ	dynamic viscosity
θ_{xx}	boundary-layer momentum thickness $= \displaystyle\int_0^\delta \left(\frac{V_{x_e}}{V_e} - \frac{V_x}{V_e}\right)\frac{V_x}{V_e}\, dz$

ρ	density
τ	height of tip gap
$\bar{\bar{\tau}}$	stress tensor (Sect. 5.1.1)
ω	vorticity
ω'	non-dimensional vorticity $= \left(\frac{\omega c}{V_{CL}}\right)$
Ω	rotational speed

Subscripts

a	component in axial direction (Sect. 6.1.1.4 and Appendix J)
B	bound
CL	centerline value at inlet
e	boundary-layer edge value
g	gap
m	mean value through blade row
o	stagnation (total) conditions
p	passage; profile (Sect. 2.4)
PS	pressure surface
r, θ, x	components in radial, tangential and axial directions
ref	reference
rel	relative
SS	suction surface
TV	tip vortex
x, y, z, s	components in axial, pitchwise, spanwise, and streamwise directions
$1, 2$	cascade inlet and outlet

Superscripts

$'$	pitchwise-averaged value
$''$	mass-averaged over reference mass flow rate

Abbreviations

AVR	axial velocity ratio
CFD	computational fluid dynamics
CFL	Courant-Friedrichs-Lewy number
EHM	engine health monitoring
GCI	grid convergence index
PS	pressure surface
SS	suction surface

Chapter 1
INTRODUCTION

Engine Health Monitoring (EHM) systems are routinely used by most civilian and military operators of gas turbine engines to detect gradual or abrupt deterioration of engine performance (e.g., Cue & Muir (1991)). The deterioration is usually the result of in-service damage which can take a number of forms. These include: blade surface roughening due to fouling, erosion or corrosion; damage to blade tips due to rubs or cooling problems; and leading- and trailing-edge damage due to foreign-object ingestion, severe vibration, or lack of sufficient blade cooling. Current EHM systems can identify the presence of damage, and sometimes even the general area in the engine where the problem exists, but they cannot distinguish its specific nature. As a result, a significant portion of the maintenance time is spent determining the source of the problem. The goal of future EHM systems will be to distinguish among the different types of damage, minimizing the required diagnostic time.

Developing such future EHM systems will require a knowledge of the aerothermodynamic effects specific to each of the different modes of damage. Although such knowledge could be gained statistically by correlating data from engines which have experienced known types of damage, this would likely prove to be difficult and costly. An alternative approach, used in the present study, is to determine the effects of the specific faults at the blade level first. From the changed loss and flow-turning characteristics of the blade, the changes in both the stage performance, and ultimately the overall engine performance, can be predicted. This approach has been applied to surface damage (e.g., Abbott (1993)) and trailing-edge damage (e.g., Sjolander *et al.* (1993)). The objective of the present research was to investigate the effects of tip damage.

In practice, tip damage can include rounding of the blade tip in the chordwise and tangential directions (i.e., rounding of the pressure- and suction-surface corners). However, for the present study the damage was taken to consist simply of opening the clearance gap to unusually large values. Thus, this study is largely an extension of earlier measurements made using the low-speed tip-leakage test section at smaller, healthy-engine clearances. These earlier measurements have examined numerous aspects of the clearance flow, including its effect on blade loading (e.g., Sjolander & Amrud (1987)) and on losses (e.g., Yaras & Sjolander (1989)). The effect of relative wall motion has also been investigated using a moving-belt endwall (e.g., Yaras & Sjolander (1992b) and Yaras *et al.* (1992)). Most recently, Chan *et al.* (1994) examined the interaction of the tip-leakage and endwall flows for varying inlet boundary-layer thicknesses. All previous studies examined clearances from 0 to 5.5% of the blade chord; the present measurements extend this range to 15% clearance.

In addition to the experimental measurements, a computational investigation was conducted using a three-dimensional Navier-Stokes solver developed by Dawes (1986a). The calculations were obtained using a two-dimensional cascade geometry identical to that used in the measurements. Solutions were calculated for numerous clearances ranging from 0 to 15% of the blade chord. Since the primary objective of the investigation was to assess the Dawes code's ability to predict the aerodynamics of damaged turbine blades, the flow conditions were kept subsonic to allow comparison with the experimental results.

A summary of the more recent tip-leakage literature is presented in Chapter 2 along with a review of some existing tip-leakage loss models. Details of the experimental setup are presented in Chapter 3.

As was the case for the earlier measurements, the present results were obtained under somewhat idealized conditions. Although the measurements are made at a realistic Reynolds number, the freestream turbulence intensity and Mach number were less than

the engine values. Chapter 4 describes in detail the tunnel operating point and the preliminary flow quality measurements made.

A summary of the Dawes code and a discussion of some of its more prominent features are presented in Chapter 5. In addition, this chapter presents the grid refinement study used to determine the appropriate mesh geometry for gathering near grid-independent results.

The experimental results, presented in Chapter 6, provide insights into the physics of the flow, including the mechanisms of loss production, which are not as easily obtained at the smaller, healthy-engine clearances where the tip-leakage and endwall flows interact more strongly. The later portion of Chapter 6 presents the computational results and compares them with the measurements. Lastly, conclusions and recommendations for future work are presented in Chapter 7.

Chapter 2
LITERATURE REVIEW

The purpose of this chapter is to review previous research on tip clearance flows. The chapter begins with a discussion of the loss terminology and loss breakdown used for turbomachinery flows. Following this, a brief description of the flow in rotor blade passages is presented. The chapter concludes with a review of some existing tip-leakage loss models, with attention directed mainly towards the models of Denton (1993) and Yaras & Sjolander (1992a) which are compared with the measurements in Chapter 6. Although both models were developed for normal clearances, they later proved useful in understanding the loss trends at larger clearances in the present work.

2.1 Introduction

It is widely recognized that the necessary running clearance between the blade tips and the casing in an unshrouded turbine results in significant losses. At normal running clearances (typically 1 to 2% of the blade chord) the losses resulting from the leakage flow account for as much as one third of the total loss through the stage (Denton, 1993). However, as a result of in-service damage to the rotor blade tips, substantially larger clearances can occur. A review of available literature has shown that there is no published data on the loss and flow turning characteristics of blades with tip damage. Since the flows at extended clearances are expected to be largely similar to those observed at smaller clearances, the remainder of the literature review focuses attention towards existing measurements of the tip-leakage flow at these "healthy" engine clearances. An extensive, critical review of the tip-leakage literature was completed by

Yaras & Sjolander (1991). The following is essentially a summary of that earlier work with emphasis focused primarily on the more recent literature.

2.2 Loss Terminology and Breakdown

Losses occur when useful mechanical energy is degraded to internal energy through irreversible processes such as the viscous effects in boundary layers and mixing processes. Since most turbomachines are nearly adiabatic, entropy production is a direct measure of these irreversibilities, and consequently, a measure of loss (Denton, 1993). However, since entropy is a rather abstract quantity that cannot be measured directly, it is rarely used.

The total-pressure loss coefficient is a more convenient loss parameter which gives an indirect measure of the entropy production for stationary blade rows. This parameter is perhaps the most commonly used since it is easily obtained from cascade measurements. The coefficient is defined as the loss in total pressure through the passage normalized with the outlet dynamic pressure:

$$Y = \frac{P_{o_1} - P_{o_2}}{P_{o_2} - P_2} \tag{2.1}$$

Historically, losses have been divided into components which are assumed to act independently, and therefore can be linearly superimposed. Although it is now clearly recognized that the loss mechanisms are seldom truly independent (e.g., Chan *et al.* (1994) and Denton (1993)), the traditional loss breakdown continues to be widely used. The basic loss components are as follows:

Profile loss: loss generated in the blade boundary layers away from the endwalls where the flow is two-dimensional; loss arising at the blade trailing edge is usually included;

Secondary loss: loss arising from the endwall boundary layer flows at zero clearance;

Tip-leakage loss: loss generated by the leakage flow.

Numerous correlations exist in the literature for the prediction of each of the loss components. Since the present research is primarily interested in the flow characteristics of blades with large clearances, attention is focused on the tip-leakage loss component. A review of some of the recent tip-leakage loss models is presented in Section 2.4.

2.3 General Description of Flow in Rotor Blade Passages

This section describes briefly the flow structures generally observed in turbomachinery rotor blade passages. Prior to discussing the effects of tip-leakage flows and their interaction with other flow structures, the flow field at zero clearance is first presented.

2.3.1 Secondary Flows in Axial Turbomachinery

Figure 2.1 shows the structures typically associated with the endwall boundary-layer flow in a blade passage (Sharma & Butler, 1987). As shown in the figure, the endwall boundary layer is redirected by the blade-to-blade pressure gradient and rolls up into a passage vortex. This vortex migrates across the blade passage along the endwall towards the blade suction surface, and eventually along the blade suction surface away from the endwall. The secondary velocities created by the passage vortex cause

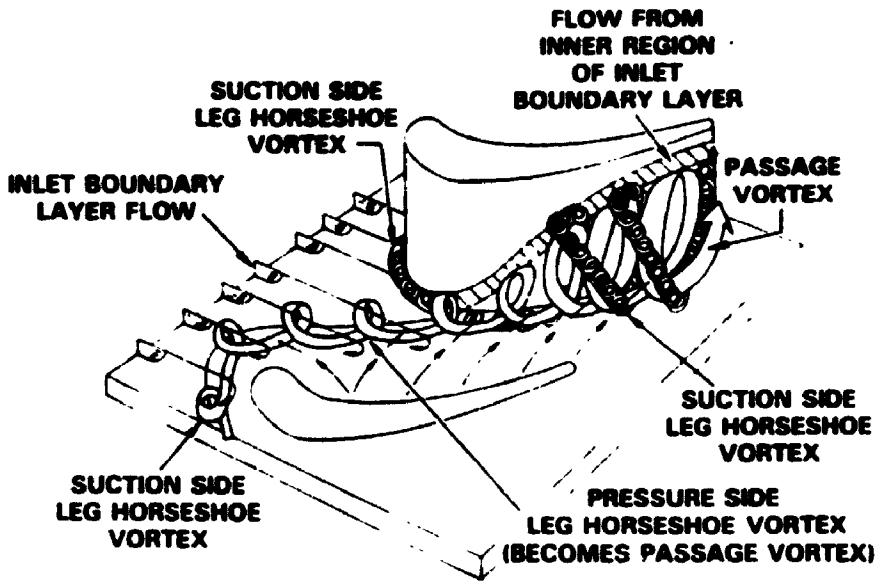

Figure 2.1 Endwall flow structures, reproduced from Sharma & Butler (1987).

significant flow angle variations at the exit of the blade passage, resulting in flow overturning at the endwall and flow underturning away from the endwall.

In addition to the passage vortex, Figure 2.1 shows that a horseshoe vortex[1] is also formed at the leading edge of the blade where the inlet endwall boundary layer separates and rolls up. The pressure-side leg of the horseshoe vortex, which has the same sense of rotation as the passage vortex, merges and becomes part of the passage vortex. The suction-side leg, however, has the opposite sense of rotation and remains distinct. The flow visualization studies of Sieverding & Van den Bosche (1983) and the ethylene flow-trajectory studies of Moore (1983) show that this vortex wraps itself around the larger passage vortex, as illustrated in Figure 2.1.

Another vortical structure (not illustrated in Figure 2.1) often observed behind high-turning blade rows is called the corner vortex. This relatively small vortex is invariably located in the endwall/suction-surface corner. It rotates in the opposite sense to the passage vortex and has the effect of reducing the overturning near the endwall (e.g., Gregory-Smith *et al.* (1988) and Harrison (1989)). Harrison (1989) attributes the corner vortex to the new laminar boundary layer, developing downstream of the passage vortex separation line, which is rolled up into a small vortex by the passage crossflow.

In the absence of clearance, the flow field discussed above holds for both the hubwall and tipwall flows. When the tip gap is opened, the tipwall flow becomes more complicated. This is discussed in more detail in the following section.

---

[1] The term "horseshoe vortex" likely stems from the vortex shape which is observed to wrap around the blade leading edge with one "leg" positioned on either side of the blade.

2.3.2 Tip Clearance Flows

Figure 2.2 shows a schematic diagram of the passage flows observed at clearance. The hubwall flow structures are basically the same as the endwall flows described in Section 2.3.1 for a stationary blade row. Near the tipwall, however, the flow is dominated by the tip-leakage and passage vortices. The leakage flow is driven by the pressure difference between the pressure and suction surfaces of the blade. The interaction of the mainstream fluid with the tip-leakage flow causes the formation of a vortex sheet which rolls up into a concentrated vortex. As indicated in the figure, this tip-leakage vortex displaces the passage vortex away from the endwall/suction-surface corner.

The horseshoe vortex is shown to be absent near the tipwall in Figure 2.2. The work of Sjolander & Amrud (1987) found that the classic horseshoe vortex separation was present in their cascade, in a diminished form, only for clearances below 1% of chord. Even then, the pressure-side leg of the vortex was swept over the blade tip to become part of the leakage vortex. Similar results were noted in the smoke flow visualization studies of Bindon (1987b), who also observed the horseshoe vortex to be absent for clearances larger than 1% of chord.

Figure 2.3 shows the description of the tip-leakage flow structure proposed by Sjolander & Amrud (1987). The figure indicates that in addition to the endwall boundary-layer, fluid is also swept radially up the pressure surface of the blade and into the gap. A separation bubble is formed at the pressure-side corner of the blade tip as the fluid is forced to turn sharply through 90 degrees. The smoke flow visualization studies of Bindon (1987b), however, indicated that the leading edge of the separation bubble was actually inboard of the pressure corner. Bindon went on to speculate that this would force the leakage flow at the gap entrance to have a small radius of curvature which would give rise to low pressures, high surface velocities, and large heat transfer rates. More recently,

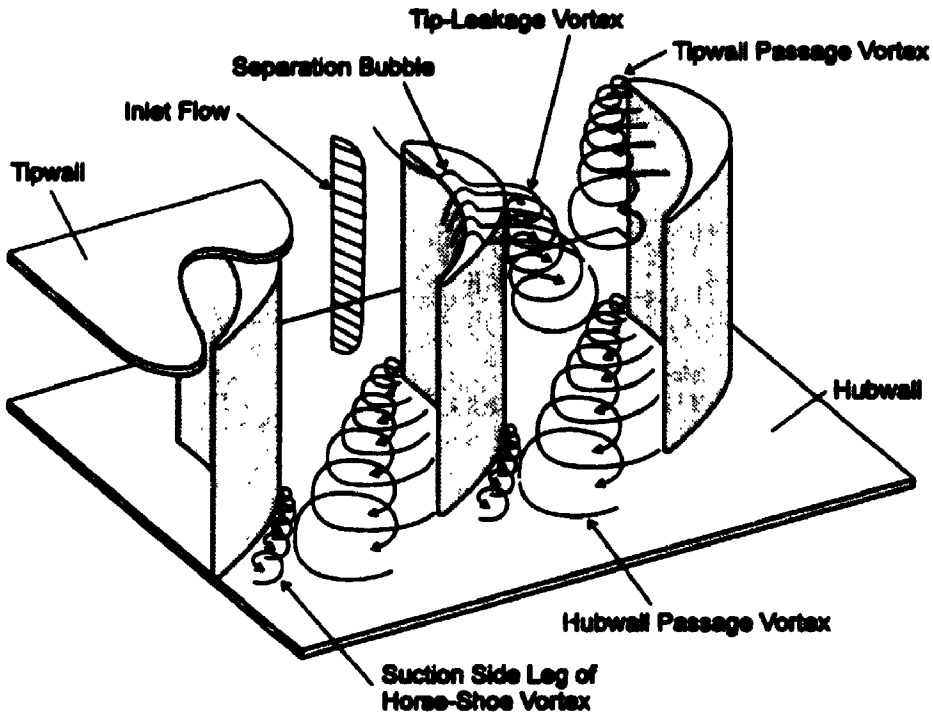

Figure 2.2 Flows in a turbine blade passage with clearance.

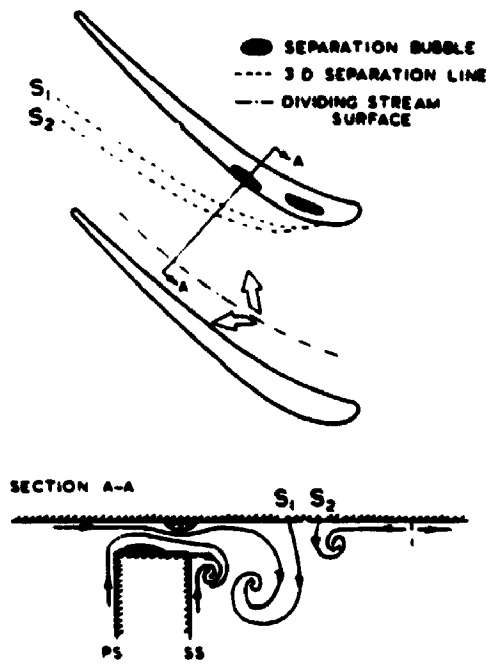

Figure 2.3 Interpretation of the tip-gap flow structures, reproduced from Sjolander & Amrud (1987).

detailed measurements by Sjolander & Cao (1994), in an idealized turbine tip gap, indicated that the separation bubble does originate at the pressure-side corner of the blade tip. However, their results also show that the separation bubble is in fact comprised of two counter-rotating vortices, as illustrated in Figure 2.4. The net effect of these two vortices appears to be the formation of a separation line (marked S in Figure 2.4) within the bubble. This multiple vortex structure gives rise to a region of attached flow near the pressure corner. The authors suggest that the high wall shear stress present in this region may help account for the "burnout" which sometimes occurs near the pressure corner of turbine blades.

Another aspect of the separation bubble, first noted in the smoke flow visualization studies of Bindon (1987b), is that the flow within the separation bubble appears to have a substantial chordwise component of velocity due to a fairly strong pressure gradient in the chordwise direction. Bindon (1989) proposed that the separation bubble was ejected from the tip gap as the pressure gradient fell away towards the rear of the blade (see Figure 2.5). This observation was later confirmed by Yaras *et al.* (1989) and Kang & Hirsch (1993a, 1993b) who both concluded that the separation bubble was in fact a separation vortex which aligned with the blade tip for a certain chordwise distance before separating.

The discussion of the previous paragraphs assumed that the separated flow reattaches to the blade tip prior to exiting the tip gap. Investigations by Storer & Barton (1991), however, showed that this is not always the case. By varying the clearance in their compressor cascade, Storer & Barton (1991) were able to determine that reattachment was unlikely to occur for thickness-to-clearance ratios less than 1.5. The authors concluded that the reattachment length of the separated flow was generally insensitive to the Reynolds number and that it was dictated primarily by the pressure gradients and inertia forces. These results agree with the more recent findings of Hétu (1993), who studied the behaviour of separation bubbles in two-dimensional sharp-edged gaps, and are consistent with the measurements of Yaras *et al.* (1989) who reported

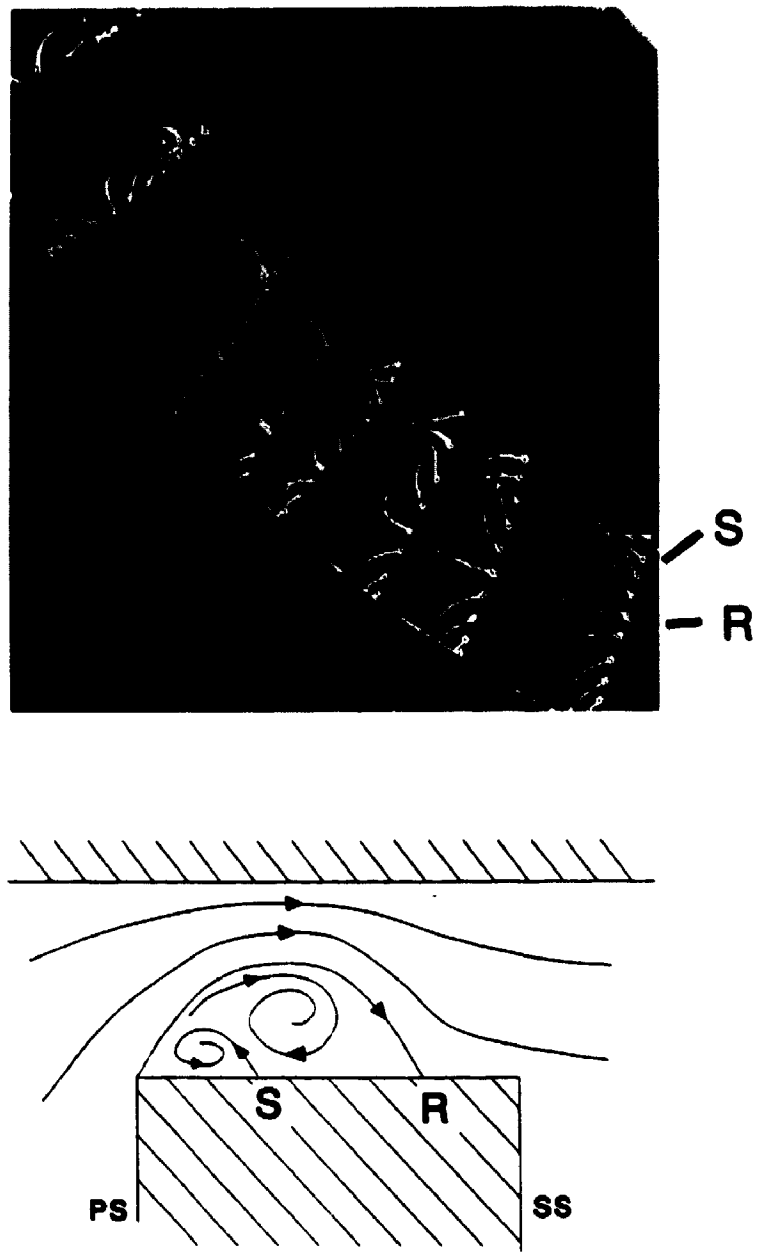

Figure 2.4 Interpretation of the separation bubble flow structure, reproduced from Sjolander & Cao (1994).

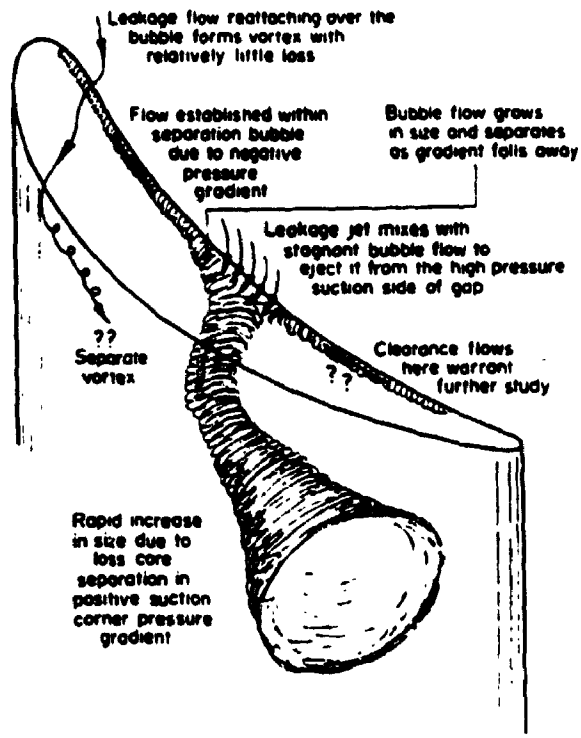

Figure 2.5 Development of the clearance gap separation bubble, reproduced from Bindon (1989).

that reattachment occurred on their blade tip for clearances varying from 1.5 to 5% of chord (t/τ = 1.79 to 6.56).

Outside of the separation bubble/vortex and before the vena contracta, the flow is essentially inviscid. This observation was first noted by Rains (1954) and later confirmed by Booth *et al.* (1982) and Yaras *et al.* (1989). The measurements of Yaras *et al.* (1989) showed the bulk of the leakage flow to be free-stream fluid which had essentially completed its acceleration prior to entering the gap. Their measurements also showed that the majority of the inlet boundary layer passed over the tip very close to the leading edge (within the first 10% of chord) and had little influence over the gap flow as a whole.

Downstream of the vena contracta significant mixing occurs. Figure 2.6 shows two recent simplified models which have been proposed for the gap flow. The first, presented by Moore & Tilton (1988), assumes that the flow undergoes a sudden expansion beyond the vena contracta and mixes out to uniform conditions at the exit of the gap. In contrast, Heyes *et al.* (1992) assume that the mixing of the flow is incomplete by the gap exit and that the core of the gap flow is occupied by loss-free fluid, which the authors refer to as an *isentropic jet*. Similar assumptions are made in the gap-flow model of Yaras *et al.* (1989), discussed in more detail in Section 2.4. The recent measurements of Sjolander & Cao (1994) show that the mixing was not complete by the gap exit and appear to support the models of Heyes *et al.* (1992) and Yaras *et al.* (1989).

Both of the previous models assume that the gap can be treated as an orifice. That is to say, the static pressure is assumed to be uniform across the gap. This was confirmed by the measurements of Yaras *et al.* (1989), who found that there was no significant attenuation of the driving pressure difference across the gap for clearances less than 5.5% of chord (t/τ = 1.79). However, recent measurements by Sjolander & Cao (1994) showed that at the largest clearance studied (t/τ = 1.5) significant attenuation of the endwall pressure had occurred.

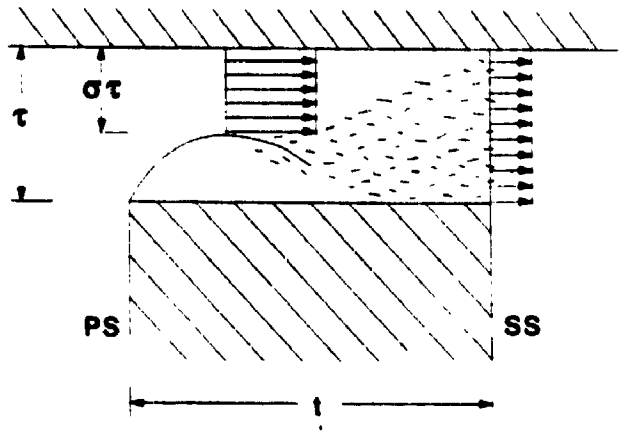

(a) Moore and Tilton (1988)

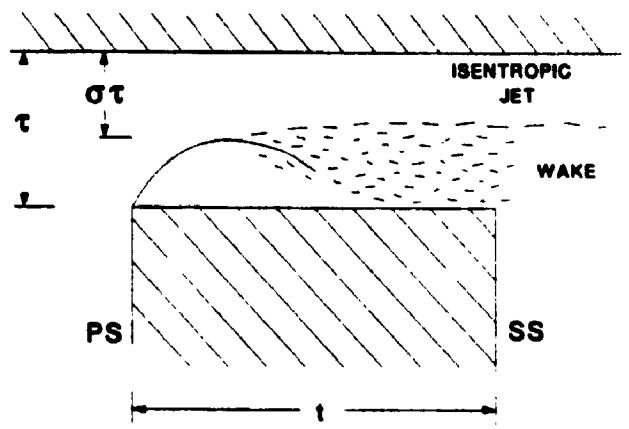

(b) Heyes et al. (1992)

Figure 2.6 Simple models for the turbine gap flow, reproduced from Sjolander & Cao (1994).

Upon emerging from the gap, the leakage jet quickly interacts with the mainstream flow and wraps into a vortex with a sense of rotation opposite to that of the tipwall passage vortex. The results of Yaras & Sjolander (1989) show that the gap outlet does not act as a simple sudden expansion since much of the gap kinetic energy appears to be recovered by the blade trailing edge. The authors suggest that the orderly roll up of the tip-leakage vortex allows for a temporary recovery of a portion of the gap kinetic energy. This recovery is considered temporary since the energy is eventually lost as the passage and tip-leakage vortices mix with the surrounding fluid downstream of the cascade. In general, Yaras & Sjolander (1989) found the "mixing loss" to increase with larger clearances.

2.3.3 Effects of Relative Blade Motion

The results discussed in the previous sections were, for the most part, obtained using linear cascades. While simplifying the study of the flow, stationary cascades neglect the effect of relative blade motion found in actual turbomachinery. Recent studies by Yaras & Sjolander (1992b) and Yaras *et al.* (1992) simulated rotation in a linear turbine cascade by using a moving-belt tip wall. Their studies indicated that the strength of the tip-leakage vortex was reduced considerably with the introduction of wall motion, while the passage vortex appeared to be strengthened by the scraping effect of the blades. In addition, both the tip-leakage and passage vortices were dragged towards the suction side of the passage where they partially blocked the gap outflow. This blockage apparently led to a reduction of the driving pressure difference across the gap, and hence a reduced leakage flow rate.

2.4 Tip-Leakage Loss Models

As reviewed by Yaras & Sjolander (1991), tip-leakage loss models can be divided into two broad categories: those that arrive at the tip-leakage loss indirectly as a result of a momentum balance, and those that are based directly on energy considerations.

The models based on momentum considerations treat the blade section as a finite wing and use inviscid flow theory to predict the induced drag on the blade due to the trailing edge vortex structure. By assuming that the loss is distributed uniformly over the passage mass flow[2], the momentum equations can be used to convert the resulting momentum deficiency into a total pressure loss.

Ainley & Mathieson (1951) developed a method based on this approach that became well known and widely used. Their tip-leakage model, which was adapted from the earlier secondary flow theory of Carter (1948), is given below:

$$Y_{tip} = 0.5 \frac{1}{S/c} \left(\frac{\tau}{S}\right) \frac{\cos^2(\alpha_2)}{\cos^3(\alpha_m)} \frac{C_L^2}{h/c} \tag{2.2}$$

where τ is the tip gap height, C_L is the lift coefficient of the blade, and α_m is the mean flow angle through the cascade. Dunham & Came (1970) modified Ainley and Mathieson's model to reflect more recent turbine designs:

$$Y_{tip} = 0.47 \frac{1}{(S/c)^2} \left(\frac{\tau}{c}\right)^{0.78} \frac{\cos^2(\alpha_2)}{\cos^3(\alpha_m)} \frac{C_L^2}{h/c} \tag{2.3}$$

---

[2] This assumption essentially implies that the models based on momentum considerations predict the fully mixed-out value of the loss.

The results of Yaras & Sjolander (1992a) and Kacker & Okapuu (1982) both show that the losses are over-estimated by the Dunham and Came model.

The second general classification of models are those which are based on energy considerations. Within this group of models, it is assumed that the kinetic energy of the gap flow normal to the blade chord is ultimately lost. This idea was first proposed by Rains (1954), who developed an involved analysis for the resulting efficiency drop in the stage. The Rains model was later simplified by Vavra (1960).

Yaras *et al.* (1989) showed that the leakage flow passed through the gap with little change in the chordwise momentum. This indicated that the driving pressure difference experienced by the fluid went entirely to accelerating the flow normal to the chord line. The measurements of Yaras *et al.* indicated that the bulk of the leakage flow, which occurred near the endwall, experienced no loss as it passed through the gap. Furthermore, the authors found that the pressure difference experienced by this flow was essentially the *undistorted* blade pressure difference: the pressure difference that would occur on the blade tip profile in the absence of clearance. Yaras *et al.* (1989) went on to propose a simple gap flow model which gave good predictions of the leakage-flow kinetic energy. The nomenclature for the model is shown in Figure 2.7.

The model of Yaras *et al.* (1989) assumes that the normal component of velocity can be obtained using Bernoulli's equation, such that

$$V_N = \left(\frac{2\,(P_{PS} - P_{SS})}{\rho} \right)^{1/2}$$

and, therefore, the resulting mass flow rate through the gap is then given by:

$$\dot{m} = C_D \int \rho V_N \, dA$$

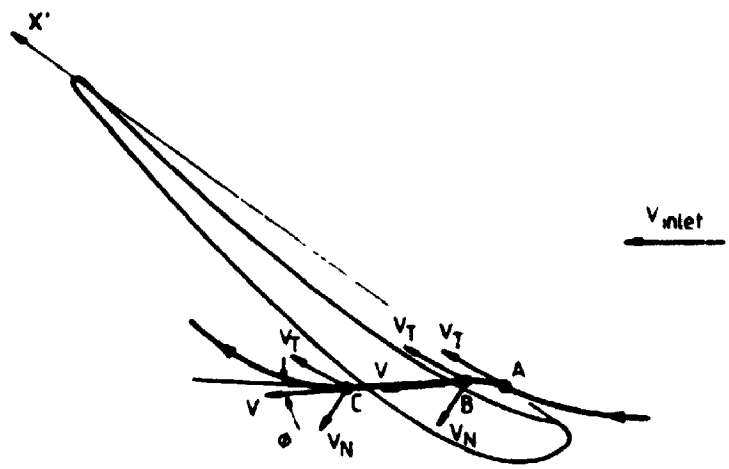

Figure 2.7 Gap flow model, reproduced from Yaras *et al.* (1989).

where C_D is the discharge coefficient. The driving static pressure difference is generally taken to be the blade pressure difference at the chordwise position being considered. This differs from the iterative model of Booth *et al.* (1982) which suggested that the static pressure difference that determines V_N should be taken along the trajectory of the streamline in question. However, the experimental results of Yaras *et al.* showed that the leakage flow had essentially completed its acceleration prior to entering the gap, justifying the simplification.

Using the model developed by Vavra as a starting point, Yaras & Sjolander (1992a) were able to incorporate the gap flow model of Yaras *et al.* (1989) in an improved tip-leakage loss model. The resulting equation for the losses generated during the mixing of the tip-leakage flow with the mainstream is given below:

$$Y_{tip} = 2\, K_E\, C_D \left(\frac{\tau}{S}\right) \frac{\cos^2(\alpha_2)}{\cos^3(\alpha_m)} \frac{C_L^{1.5}}{h/c} \tag{2.4}$$

where K_E is a constant related to the blade loading distribution: $K_E = 0.566$ for a front- or aft-loaded blade; $K_E = 0.5$ for a mid-loaded blade. Yaras & Sjolander (1992a) also developed an expression for the losses generated in the tip gap:

$$Y_{gap} = C\, K_G \left(\frac{1}{S/c}\right) \frac{C_D}{\cos \alpha_m} \frac{C_L^{0.5}}{h/c} \tag{2.5}$$

where $C = 0.007$ and K_G is another constant related to the blade loading distribution: $K_G = 0.943$ for a front- or aft-loaded blade; $K_G = 1.0$ for a mid-loaded blade.

Recently, Denton (1993) derived a simple model based on first principles, which uses a control-volume analysis to predict the loss that results from the mixing of the leakage flow and the passage flow. The gap is treated as a simple orifice and the leakage

mass flow rate is determined by the blade pressure difference, similar to the model of Yaras & Sjolander (1992a). The resulting expression is given below:

$$Y_{tip} = \frac{2 C_D \tau c}{h S \cos \alpha_2} \int_0^1 \left(\frac{V_{SS}}{V_2}\right)^3 \left(1 - \frac{V_{PS}}{V_{SS}}\right) \sqrt{1 - \left(\frac{V_{PS}}{V_{SS}}\right)^2} \, d\left(\frac{x'}{c}\right) \tag{2.6}$$

where V_{PS} is the velocity at the gap inlet (blade pressure surface) and V_{SS} is the velocity at the gap outlet (blade suction surface).

The experimental studies of Yamamoto (1988), Yaras & Sjolander (1989), and Chan *et al.* (1994) all showed that the secondary losses generally decreased with clearance. This clearly indicates that the conventional loss breakdown, discussed in Section 2.2, does not accurately reflect the actual physics of the flow. Yaras & Sjolander (1992a) proposed a different loss breakdown for use with their tip-leakage loss model, that is,

$$Y_{total} = Y_p + (Y_{sec})_{HUB} + (Y_{end})_{TIP}$$

where

$$(Y_{end})_{TIP} = Y_{gap} + k_s Y_{sec,0} + Y_{tip}$$

and $Y_{sec,0}$ is the secondary loss coefficient at the tip for zero clearance. The factor k_s is the fraction of the secondary loss that remains identifiably associated with the secondary flow structure at clearance. The results of Chan *et al.* (1994) found that the value of k_s was generally on the order of 0.4 - 0.6 for clearances below 5.5% of chord. The dependence of k_s on other factors, such as relative endwall motion, still remains to be investigated.

Chapter 3
TEST APPARATUS

One can conclude from the previous chapter that there is little information available in literature on the performance of damaged turbine blades. Existing tip-leakage loss models predict an ever increasing loss with larger clearances and do not account for the apparent reduction in the tipgap driving pressure difference at extended clearances. Since there appears to be a lack of full understanding of the flow dynamics at large blade clearances, it was decided to pursue the subject experimentally.

This chapter describes the experimental setup used for the current study. Detailed descriptions of the wind tunnel, test section, pressure probes, traverse gear, and data acquisition system are included.

3.1 Wind Tunnel

The open-circuit wind tunnel employed in the experiments is shown schematically in Figure 3.1. The wind tunnel uses a centrifugal fan, driven by a variable speed 40 HP DC motor, as the wind source. The centrifugal fan is capable of delivering a maximum flow rate of 4 *kg/sec* at a total pressure rise of 480 *mm* of water. Prior to entering the settling chamber, the fan delivery air is diffused through a straight conical diffuser with an area ratio of 2.72 and an equivalent cone angle of 14°. Hexagonal honeycomb with 9.5-*mm*-wide and 76-*mm*-deep cells is used to remove any swirl at the diffuser exit. The settling chamber contains three stainless steel screens (7.9 *mesh/cm* and an open area ratio of 0.58) which are used to reduce the mean flow non-uniformities and large scale turbulence. The first screen, situated approximately 125 *mm* from the diffuser outlet, is

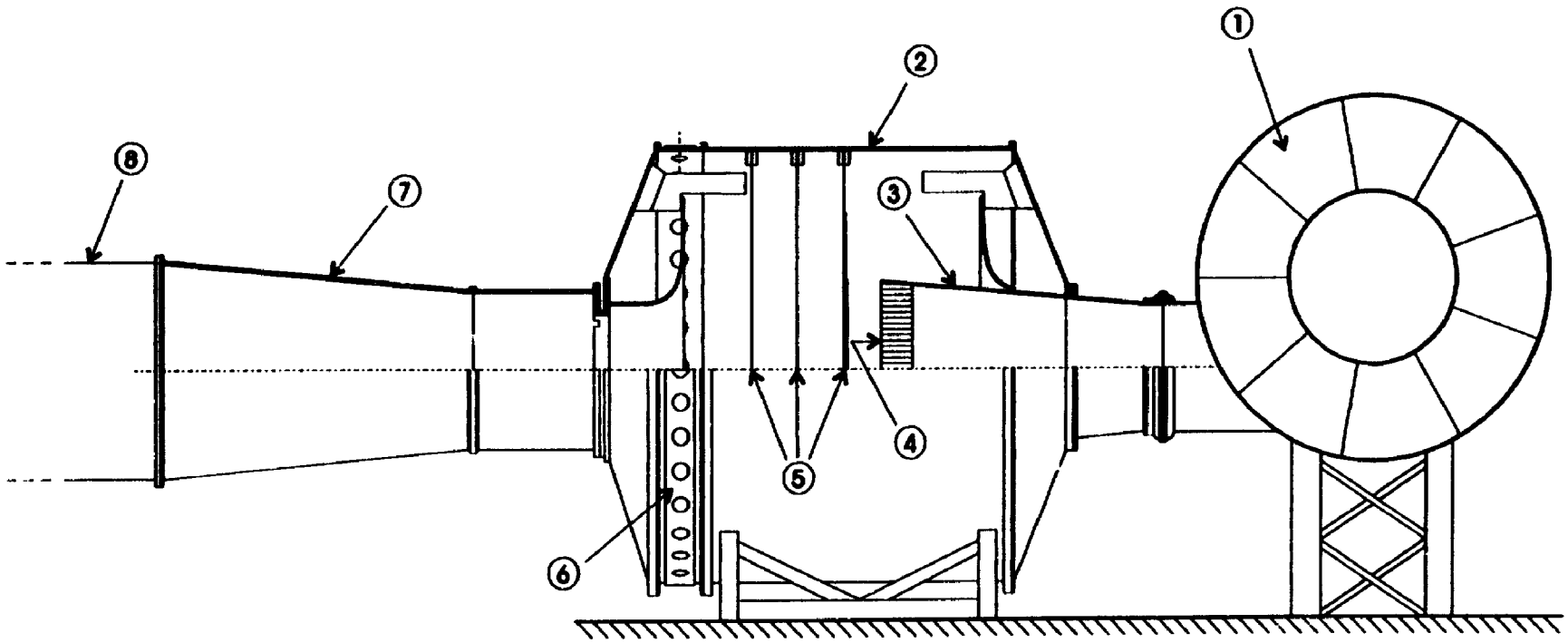

1	Centrifugal Fan	4	Honeycomb	7	Transition Section
2	Settling Chamber	5	Screens	8	Test Cascade
3	Diffuser	6	Bleed Ring		

Figure 3.1 Wind tunnel schematic, adapted from Tremblay (1989).

layered to help spread the flow uniformly inside the settling chamber. The other two screens are single-layered and evenly spaced 140 *mm* apart.

A bleed ring, consisting of thirty-six 51-*mm*-diameter holes is located at the downstream end of the settling chamber. A sliding stainless steel band allows the bleed holes to be blocked by any desired amount. All data for the present experiment was obtained with the bleed ring entirely closed.

The flow leaves the settling chamber through a contraction prior to entering a circular-to-rectangular transition section. The transition section has an exit-to-inlet area ratio of 1.2 which diffuses the flow somewhat prior to entering the test section.

3.2 Test Section and Cascade Geometry

The test section, shown in Figure 3.2, consists of a linear cascade designed by Amrud (1985) to study the effects of tip leakage flows. The cascade has been used in numerous earlier studies including: Sjolander & Amrud (1987), Yaras *et al.* (1989), Yaras & Sjolander (1990), and Chan *et al.* (1994).

The inside dimensions of the test section are 675 *mm* wide and 203 *mm* deep. It accommodates a row of five turbine blades mounted on a 7.9-*mm*-thick steel backplate which forms the mainstay of the structure. All other walls are made of 12.7-*mm*-thick plexiglass to facilitate flow visualization. The blades are scaled versions of the tip section of a power turbine blade of relatively recent design by Pratt and Whitney, Canada. A summary of the main geometric specifications of the blade are presented in Figure 3.3.

The current configuration being tested has a slightly different stagger and solidity than the actual turbine, resulting in somewhat more forward-loaded blades. In addition,

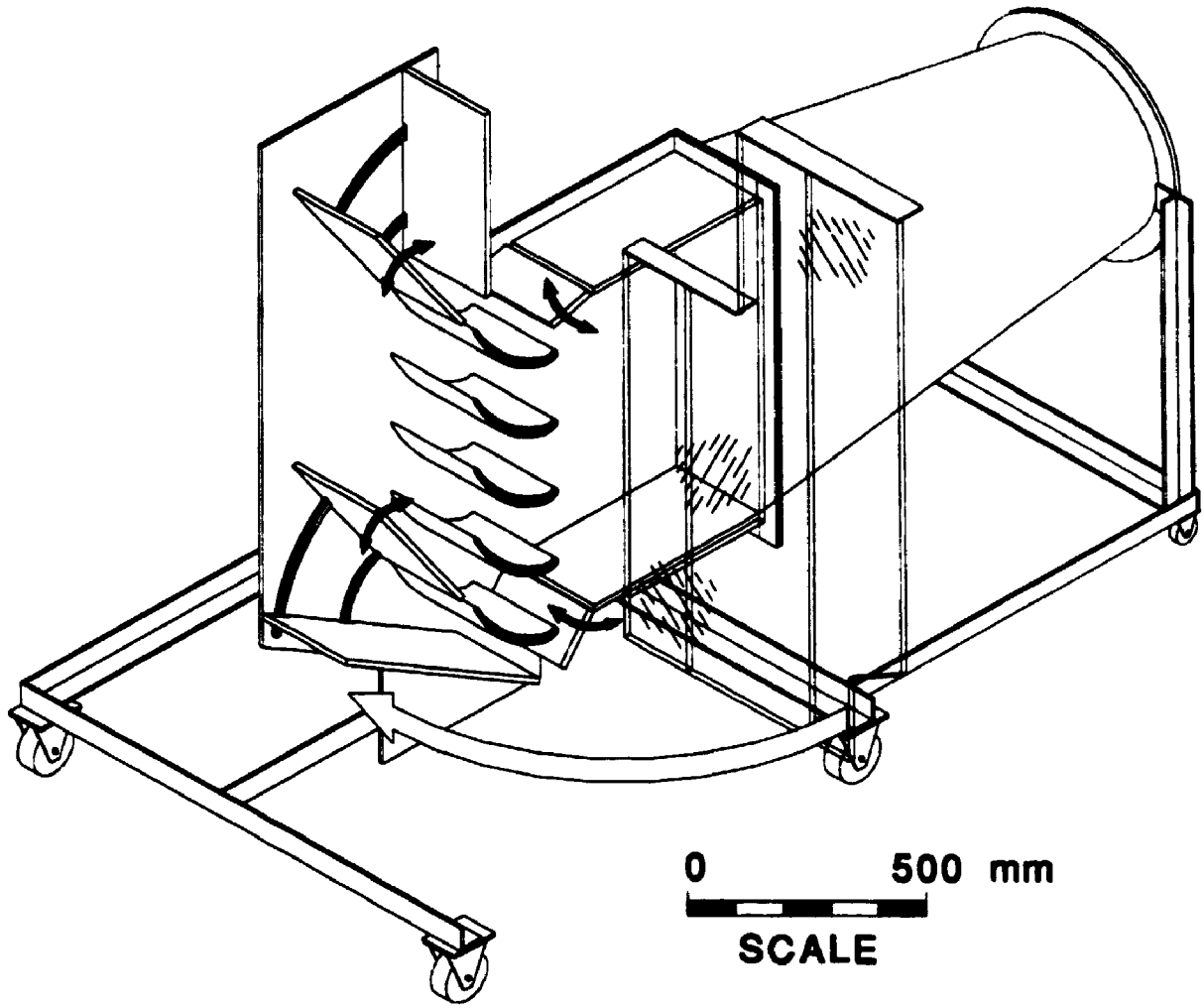

Figure 3.2 Schematic of the cascade test section.

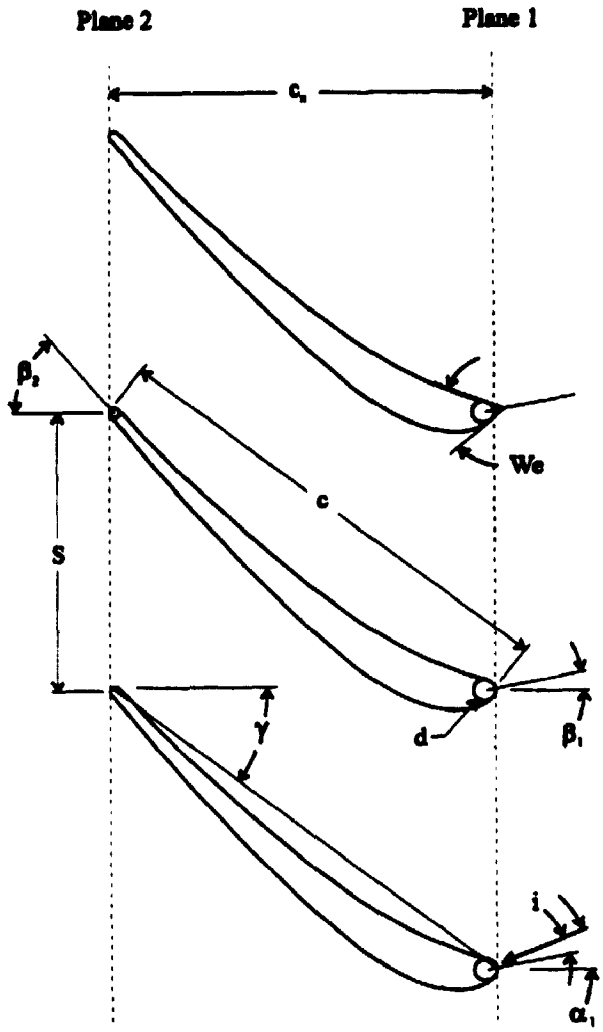

Inlet flow angle, α_1	0.0°	Chord length, c	250 mm
Inlet metal angle, β_1	11.1°	Axial chord length, c_x	199 mm
Outlet metal angle, β_2	49.6°	Blade spacing, S	150 mm
Design incidence, i_{des}	-11.1°	Blade span, h	203 mm
Stagger, γ	37.2°	Leading-edge diameter, d	10.2 mm
Leading-edge wedge angle, We	54.0°	Maximum blade thickness, t_{max}	24.6 mm

Figure 3.3 Summary of the cascade geometry.

the blades have rather low turning for a turbine and, as a result, the secondary flows are expected to be weaker.

Each of the blades was milled from plexiglass with the exception of the instrumented middle blade which was milled from aluminum. The tipwall window is hinged upstream of the blade row allowing easy access to the cascade. The tip gap is varied by inserting shims between the sidewalls and the plexiglass tipwall window. A gradual increase in the passage depth is achieved by using wedge-shaped spacers upstream of the window, beginning about two chord lengths ahead of the blade leading edge plane.

Clearances of 0, 10, and 15% of the blade chord were examined in the present study. These clearances correspond to physical gap heights of 0.0, 25.0, and 37.5 *mm*. It is estimated that the clearances can be set with an accuracy of ±1 *mm* for all five blades.

Inlet flow uniformity and outlet flow periodicity is obtained by adjusting movable control surfaces. These control surfaces include sideflaps and tailboards located upstream and downstream of the blade row, respectively. The side flaps are used to regulate the amount of flow being blown off laterally while the tailboards guide the outflow from the blade row and prevent uncontrolled expansion of the flow. Appendix B tabulates the control surface settings used for each clearance.

For a more detailed description of the cascade and wind tunnel, see the previous work of Amrud (1985).

3.3 Tipwall and Blade Instrumentation

The plexiglass tipwall window is instrumented with an array of 223 closely-spaced static pressure taps of 0.51 *mm* diameter (see Figure 3.4). The grid, which extends over one blade pitch, is located at the tip of the second blade from the test section bottom. A constant axial spacing of 15 *mm* (0.075 c_x) is used between static-tap columns. A similar pitchwise spacing is used except near the blade tip where the spacing is halved. Repeatability tests suggest an accuracy of ±0.02 for the measured static-pressure coefficients.

The centre blade in the cascade is instrumented with 14 rows of 0.51-*mm*-diameter static pressure taps. Each row consists of 37 taps on the pressure side and 36 on the suction side. For the present study only the midspan row and the row nearest the blade tip were used. Appendix C lists the blade surface static tap locations. Again, the uncertainty in the measured blade static-pressure coefficients is estimated at ±0.02.

3.4 Pressure Probes

Apart from the blade and tipwall static pressure measurements, all flowfield measurements were obtained using pressure probes. Sections 3.4.1 through 3.4.3 describe the pitot-, three-, and seven-hole probes used in the present experiment. Section 3.4.4 discusses some sources of error typically associated with the seven-hole probe measurements.

3.4.1 Pitot Probe

A pitot probe with a 0.7 *mm* tip diameter was manufactured to measure the boundary layers both at the inlet traverse station, located 1.83 axial-chord-lengths (c_x)

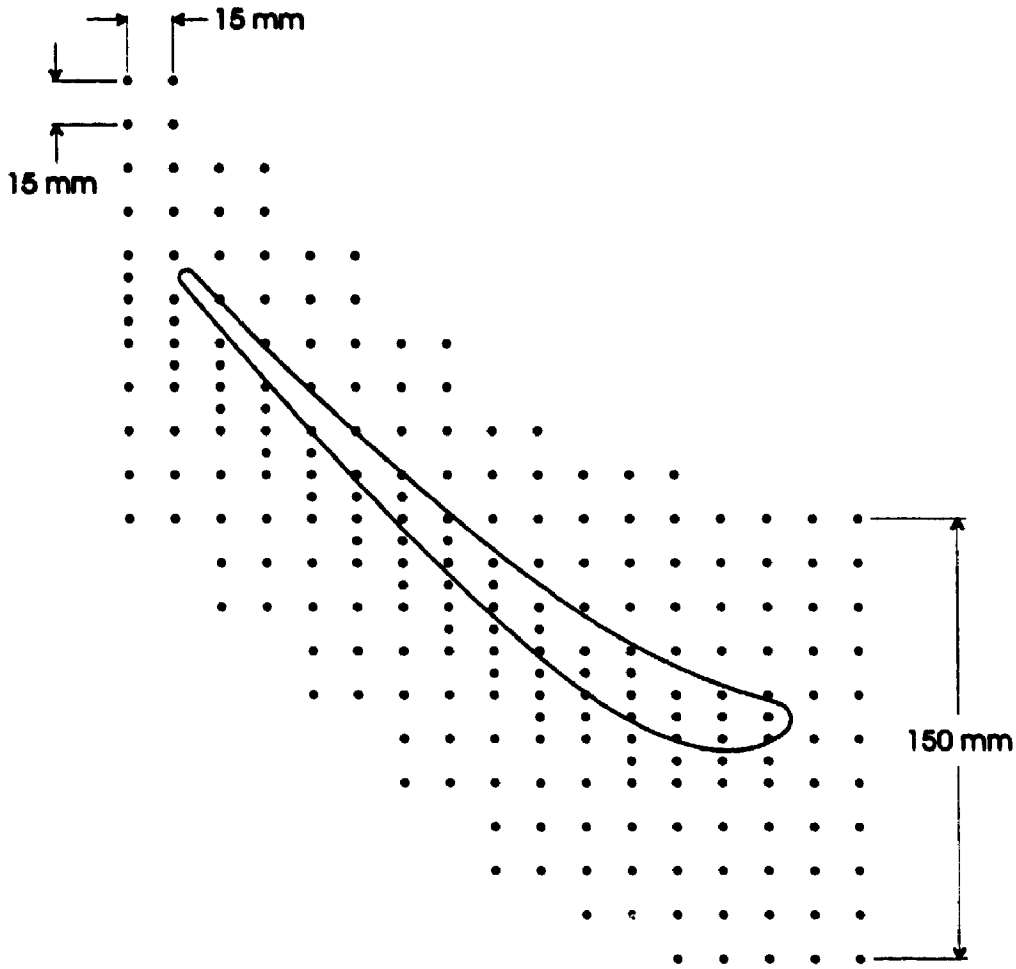

Figure 3.4 Tipwall static-pressure tap locations.

upstream of the blade leading edge, and at the reference station, located 1.10 c_x ahead of the blade leading edge. The pitot probe's small size allowed for good resolution of the thin boundary layers upstream of the blade row which typically had displacement thicknesses greater than 4 *mm*.

3.4.2 Three-Hole Probe

Figure 3.5 gives the geometry of the three-hole probe used in the present research. The probe, designed by Yaras (1990), was used in the non-nulling mode to monitor the inlet flow uniformity and the exit flow periodicity. It was also used to obtain the blade profile losses at the downstream measurement plane.

The probe was calibrated over a range of ±10° at a 0.5° interval. A description of the calibration procedure, adapted from Lewis (1966), and the resultant calibration curves are given in Appendix D. The uncertainty is estimated as ±0.5° for the measured yaw angles and ±2% of the local dynamic pressure for measured pressures.

3.4.3 Seven-Hole Probe

A seven-hole probe, employed in the non-nulling mode, was used to measure the complex three-dimensional flow field downstream of the blades. The seven-hole probe was preferred over the more commonly used five-hole probe because of its sensitivity to larger flow angle misalignments.[1]

The probe, designed by Amrud (1985), has been used successfully by numerous researchers including: Danias (1987), Yaras (1990), Cao (1993), and Hétu (1993). The

[1] Even with the probe axis aligned with the outlet metal angle, misalignment angles as large 50° were observed within the leakage jet at the downstream measurement plane. These angles are well in excess of the ±25° range for which five-hole probes are typically calibrated.

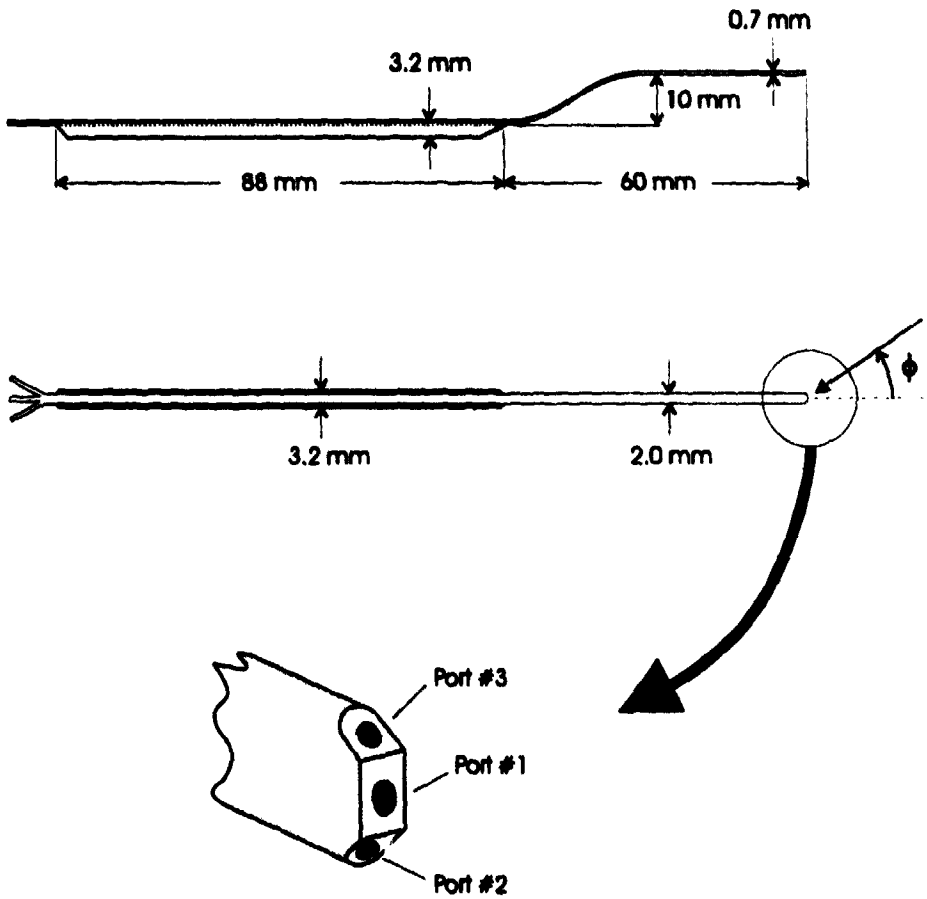

Figure 3.5 Three-hole pressure probe geometry.

probe is constructed from seven stainless steel hypodermic tubes each with an outer diameter of 0.64 *mm* and an inner diameter of 0.33 *mm*. The tubes are arranged in an axisymmetric bundle with one at the centre and the remaining six surrounding it. This bundle is contained within a 2.4-*mm*-outer-diameter brass tube. With the space between the individual tubes filled with solder, the probe head is machined to a conical tip with an apex angle of 60°. The overall probe dimensions are given in Figure 3.6.

The probe was calibrated in 5° steps for all combinations of the pitch angle and yaw angle for up to 50° of flow misalignment with the probe axis. A description of the calibration procedure, adapted from Gerner and Maurer (1981), and selected calibration curves are presented in Appendix E. The uncertainty associated with the seven-hole probe is estimated at ±1° for the measured angles, and ±3% of the local dynamic pressure for the measured total and static pressures.

The values of uncertainty stated above are slightly different from the uncertainties quoted in earlier works (e.g., ±1.5° for measured flow angles, and ±4% of the local dynamic pressure for pressure measurements, Yaras (1990)). This disparity is attributable to the difference in the data reduction methods used. Previously, higher-order polynomials (typically 4th order) were fitted to the data, resulting in spurious oscillations in regions where the calibration data varied rapidly. The current data reduction routine uses a bi-linear interpolation scheme which was found to be more accurate.

3.4.4 Sources of Measurement Error for the Seven-Hole Probe

Even though great care was taken when gathering the calibration data for the seven-hole probe, a certain degree of scatter is observed in the resultant calibration curves (see Appendix E). The uncertainty quoted in the previous section is due primarily to the errors introduced into the bi-linear interpolation scheme (used in the seven-hole probe

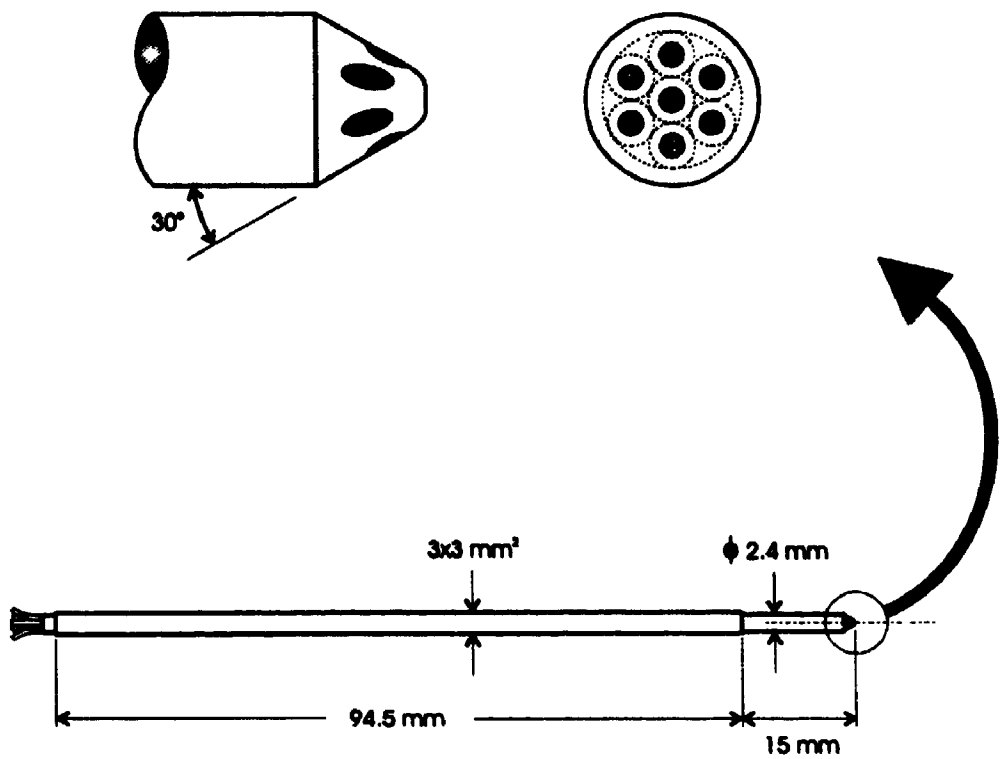

Figure 3.6 Seven-hole pressure probe geometry.

reduction procedure) as a result of this scatter. The following paragraphs briefly outline other common sources of error encountered with multi-hole probe measurements.

Turbulence Effects:

Both the three- and seven-hole probes used in the present study were calibrated in flows with low turbulence intensities. Probe measurements in flows with higher turbulence intensities are therefore likely to be slightly erroneous. Sitaram *et al.* (1981) did extensive measurements with a five-hole probe and suggested that the errors measured in the mean velocity were on the order of 0.33% of the actual mean velocity for turbulence intensities of less than 10%.

Reynolds Number Effects:

Dominy & Hodson (1993) examined the effect of Reynolds number on the calibration of various five-hole probes. They observed that the flow which separates from the probe head appeared to be sensitive to the Reynolds number. The nature of the resulting separation bubble, which was noted to extend over the downwind port, was observed to change with Reynolds number with some apparent pressure recovery taking place at lower values. However, as discussed in Appendix E, the seven-hole probe reduction scheme does not make use of the leeward pressure port readings when at relatively large angles of attack. Exclusion of these readings significantly reduces the Reynolds number sensitivity of the seven-hole probe. This was confirmed by Yaras (1990) who noted that the current probe had negligible Reynolds number sensitivity.

Wall Proximity Effects:

When a probe is near a solid surface, flow acceleration may occur between the probe and the solid surface. Studies by Sitaram *et al.* (1981) with a five-hole probe show that the probe tends to read higher than the actual velocity. The resulting error caused by this effect is negligible if the probe is located more than 3 to 4 probe diameters away from the solid surface. With their five-hole probe in contact with a solid wall, Sitaram

et al. observed errors of 2% in the measured total pressure and 4% in the measured velocities.

Pressure- and Velocity-Gradient Effects:

Multi-hole probe measurements taken within cascades are often exposed to complex flow fields containing steep pressure and velocity gradients. Spatial resolution errors result when any intrusive pressure probe is inserted into such a flow since each of the pressure ports is actually measuring at a slightly different physical location in space. Furthermore, when a probe is placed within a velocity gradient, streamwise deflection occurs towards regions of lower velocity causing errors in probe measurements. A review by Yaras (1990) showed that correction methods for these error sources were not available in published literature.

3.5 Probe Traverse Gears

The spanwise and pitchwise positions of the probes are controlled using a traverse gear. The traverse gear has two translational degrees of freedom and is mounted behind the backplate of the test section. Access to the test section is provided by six 20-*mm*-wide and 3.2-*mm*-deep vertical grooves located at various axial locations in the backplate. Within each groove is a 7.9-*mm*-wide slot milled through the thickness of the backplate. Aluminum sliders, which move with the probe stem, are inserted into the vertical grooves to provide a step-free transition on the hubwall.

The traverse mechanism uses two 4-phase stepping motors, each driving a ¼-20 threaded rod, to provide the translational motion. The accuracy of the positioning provided by the traversing mechanism is estimated at ±0.25 *mm*. The motors are driven by controllers manufactured by Rapidsyn Precision Industries Inc.. Communication between the motor controllers and the computer is provided by TTL signals from the

computer's parallel port. The reader is referred to Yaras (1990) for a more detailed description of the traverse gear.

3.6 Data Acquisition System

The data acquisition system consisted of the following components:

- two Baratron capacitive-type differential pressure transducers (Model 220CD);
- a Sciemetric Instruments Model 81 Electronic Measurement System (M81);
- a Sciemetric Instruments Model 901 CPU and Serial Interface (M901);
- and a PC-AT desktop computer.

The Baratron pressure transducers (temperature regulated at 45°C to minimize the effects of zero-drift) were used to convert the pressure signals measured in the cascade into analog signals. The transducers have an input range of ±1.0 *psid* and a full scale output range of ±10.0 *V* DC with an repeatability of ±0.5 *mV*. Both pressure transducers were calibrated using a micro-manometer and exhibited good linearity characteristics with negligible hysteresis. The resultant calibration curves are presented in Appendix F.

The analog output signals from the pressure transducers are digitized by the M81 unit which acts as a 12-bit-plus-sign, dual slope, integrating analog-to-digital (A/D) converter. The integration serves as a form of active filtering, eliminating high frequency noise.

The M81 unit has four gain settings adjustable through software, corresponding to input ranges of: ±5 *V*, ±0.5 *V*, ±0.05 *V*, and ±0.001 *V*. The 12-bit-plus-sign A/D conversion has a resolution of 0.012% of the selected range: 1.22 *mV* at the lowest gain (1) and 2.4 μV at the highest gain (500). All but the lowest gain setting provide better resolutions than the transducer accuracy. Therefore, all measurements for the

present research were obtained at the lowest gain setting obviating the need for gain time sampling and selection.

The M901 serial interface unit provides the link between the computer and the M81 module. All data acquired during one sampling period is stored in the 24 Kbyte random access memory (RAM) of the M901 unit. This enables acquisition of approximately five samples per second from each of the two transducers. Once the sampling period is completed, the data is transferred to the computer for further processing. Communication is through a RS232 serial port at a rate of 2400 *bps*.

Schematic diagrams of the data acquisition setup are included in Figures 3.7 and 3.8 for probe-pressure and static-pressure measurements, respectively.

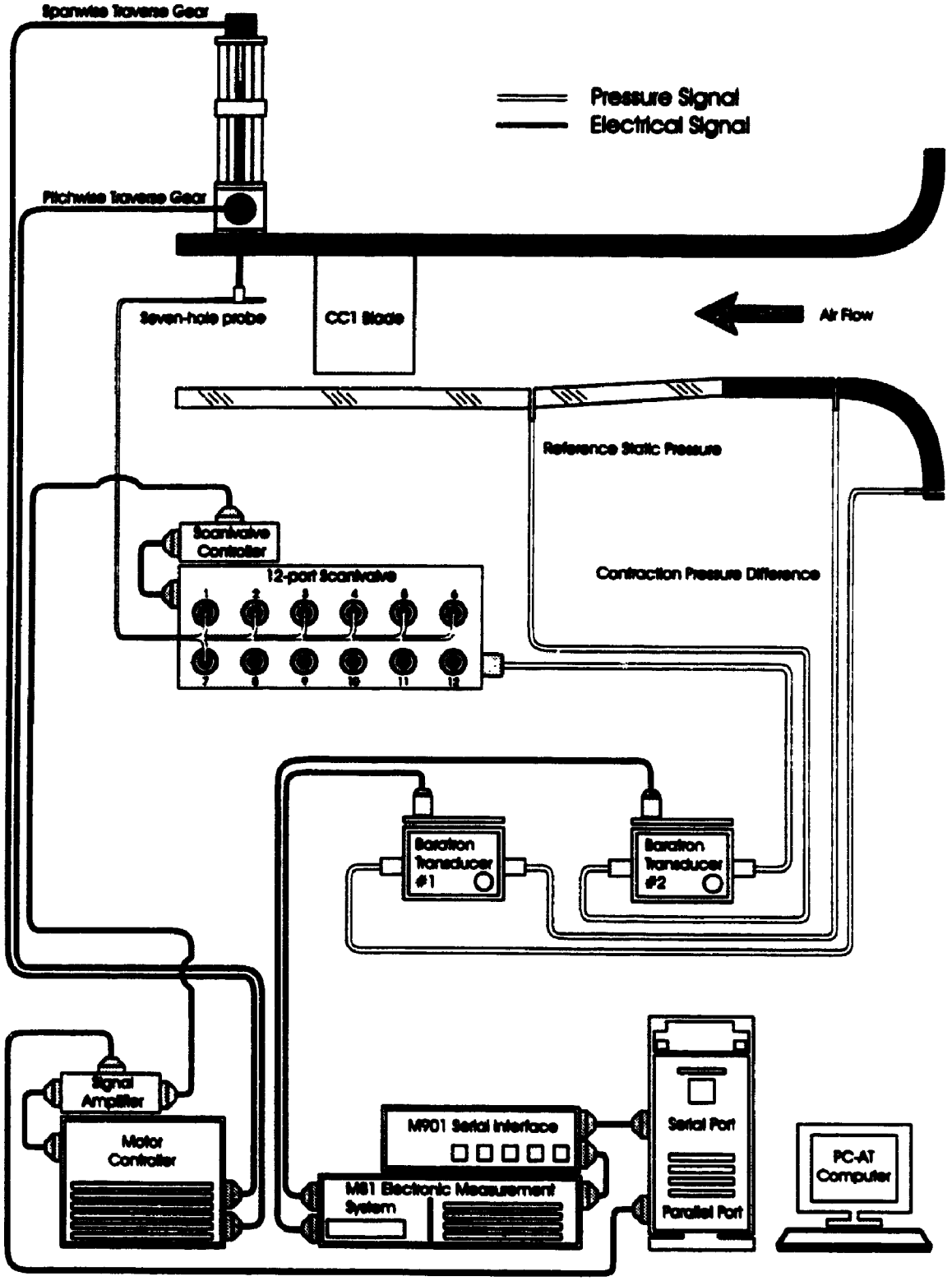

Figure 3.7 Data acquisition setup for probe-pressure measurements.

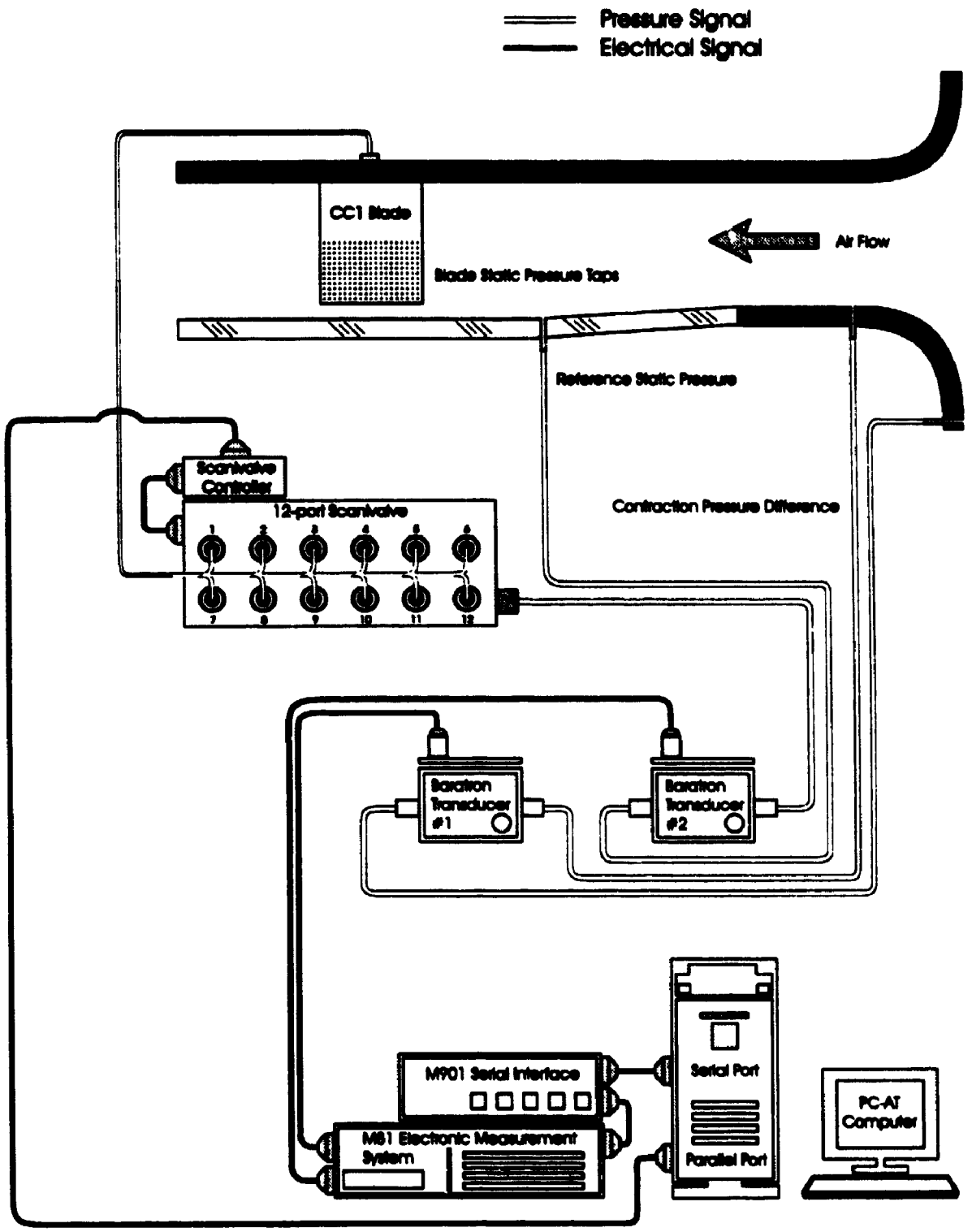

Figure 3.8 Data acquisition setup for static-pressure measurements.

Chapter 4
EXPERIMENTAL TECHNIQUE

All measurements for the flow field involved the averaging of a number of samples in order to obtain representative mean values. This chapter describes the data acquisition technique and the sampling procedure used. Preliminary flow quality measurements, including inlet flow uniformity and outlet flow periodicity, are also presented. A brief description of the cascade operating point is given first.

4.1 Tunnel Operating Point

All experiments were performed at a nominal Reynolds number of 4.3×10^5. This value is based on the blade chord length and the cascade inlet centreline velocity. The latter was obtained from the wind-tunnel contraction pressure difference, which had been calibrated against the centreline dynamic pressure. During the experiments, the temperature of the delivery air varied by as much as $20°F$. In order to maintain the operating Reynolds number, the inlet centreline velocity was adjusted to compensate for any variations in the air density and viscosity of the delivery air. Thus, by monitoring the contraction pressure difference and making the necessary adjustments to the fan rotational speed when required, the reference Reynolds number was held constant to within $\pm0.1\times10^5$.

At large clearances there is a significant redistribution of the mass flow rate across the span of the cascade (see Section 6.1.1.4). The tip gap becomes the preferential flow path with more mass flow participating in the leakage streamtube. A corresponding decrease in the mass flow rate over the blade span is observed. This implies that the

effective Reynolds number seen by the blade varies with clearance even though the nominal Reynolds number at the upstream reference station is held constant. The results of section 6.1.1.4 suggest that the Reynolds number experienced by the blade may have varied by as much as 20% of the reference value. However, this change in the blade Reynolds number does not appear to have significantly affected the blade boundary layers as the measured profile loss was nearly the same for all three clearances.

The inlet free-stream turbulence intensity was measured by Yaras (1990) using a hot-wire anemometer. The root-mean-square of the fluctuation in the longitudinal direction, u′, was found to be about 1.5% of the centreline velocity.

Although the measurements are made at realistic Reynolds numbers, the low turbulence intensity, the essentially incompressible flow conditions, and the lack of relative tipwall motion make them somewhat idealized. However, there has been a long-standing and successful history of using low-speed cascade data for gaining useful insights into the physics of turbomachinery flows.

4.2 Data Acquisition Technique

When sampling either static pressures or probe pressures with a scanivalve, it is necessary that the data acquisition system wait long enough for the pressure transients in the system to dissipate prior to commencing. Likewise, it is important for the data acquisition system to sample long enough, in order to obtain a sufficient number of samples, for an accurate evaluation of the long-term averaged value. The following sections discuss the selection of *wait* and *sampling* times employed and the sampling procedure used.

4.2.1 Data Sampling Times

Whenever the scanivalve switches ports, a pressure transient is set up in the system as a result of the step change in the measurement pressure. Prior to sampling, the data acquisition system must wait for the pressures measured by the transducers to become asymptotic and for any transients in the pressure lines to dissipate. The amount of *wait* time required generally depends on both the type of flow in which the measurement is taken and the geometry of the measurement equipment.

A simplified treatment of the unsteady response of pneumatic systems has been described in many papers and textbooks (e.g., Benedict (1960), Kinsler & Frey (1962)). The analysis generally proceeds by making the analogy of a single-degree-of-freedom mechanical system with velocity damping: the air in the pressure lines is treated as a rigid body, the friction in the tubing is treated as a damper, and the transducer, treated as a finite volume reservoir, serves as the spring (see Figure 4.1). The analysis shows that the resultant time constant of the system is found to be inversely proportional to d_1^4 (where d_1 is the smallest diameter tubing in the system), and proportional to the effective length of the tubing and the volume of the system.

It is generally desirable from an experimental standpoint to minimize the time constant of the data acquisition setup and hence the *wait* time necessary. The analysis discussed above shows that the tubing diameter is the predominant controlling factor. However, the smallest diameter will normally occur at the static tap or at the probe, locations where the experimentalist has little control. This leaves only the length of tubing and the volume of the system as variables which can be manipulated.

Prior to beginning the present research, all static pressure lines were shortened by bringing the pressure transducers as close as possible to the cascade test section. The effective volume of the system was reduced by scaling the pressure lines down to 3/32"

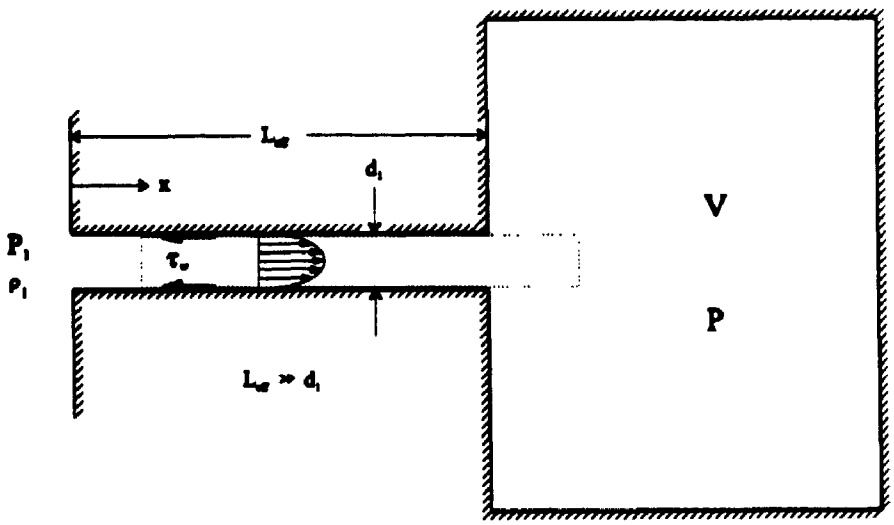

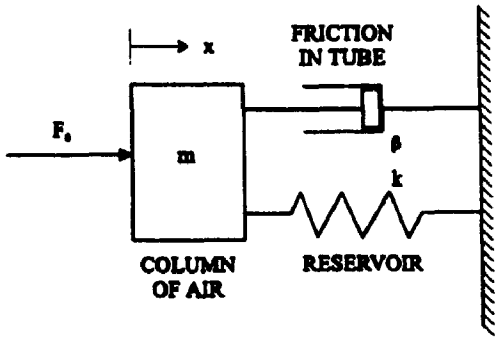

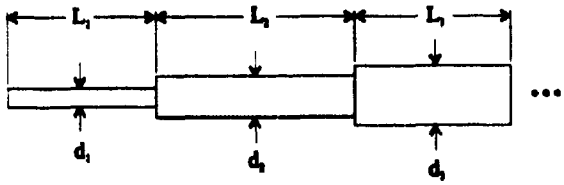

$$L_{eq} = L_1 + L_2 (d_1/d_2)^4 + L_3 (d_1/d_3)^4 + \ldots$$

Figure 4.1 Analogy of the unsteady response of pneumatic systems.

flexible Tygon tubing wherever possible. In addition, brass inserts were designed (see Appendix G) to reduce the volume of the Baratron transducers.

Figure 4.2 shows a typical plot of the transducer output voltage against time when the transducer is subjected to a step in the pressure signal (i.e., scanivalve steps between probe ports). It is evident from the figure that the selected 25 second *wait* time for downstream measurements is very conservative.

In order to establish the *sampling* time required, the cumulative average of the transducer output voltages was calculated. Figure 4.3 shows a typical plot of the cumulative average against sampling time. Also included in the figure, centered about the long-term averaged value, is a band which is representative of the data acquisition system resolution with a gain setting of 1.0. Again, it is evident from the figure that a *sampling* time of 20 seconds, the value chosen for downstream seven-hole probe measurements, is conservative. Table 4.1 lists both the *wait* and *sampling* times used for each type of pressure measurement taken.

Measurement Location	Wait Time (sec)	Sampling Time (sec)
downstream multi-hole probe	25	20
upstream pitot-probe	10	25
blade static	40	30
endwall static	30	30

Table 4.1 Experimental *wait* and *sampling* times used for data collection.

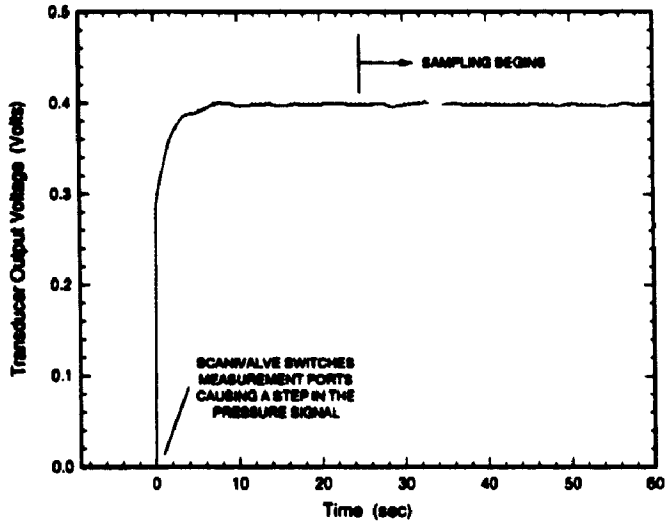

Figure 4.2 Transducer output voltage versus time.

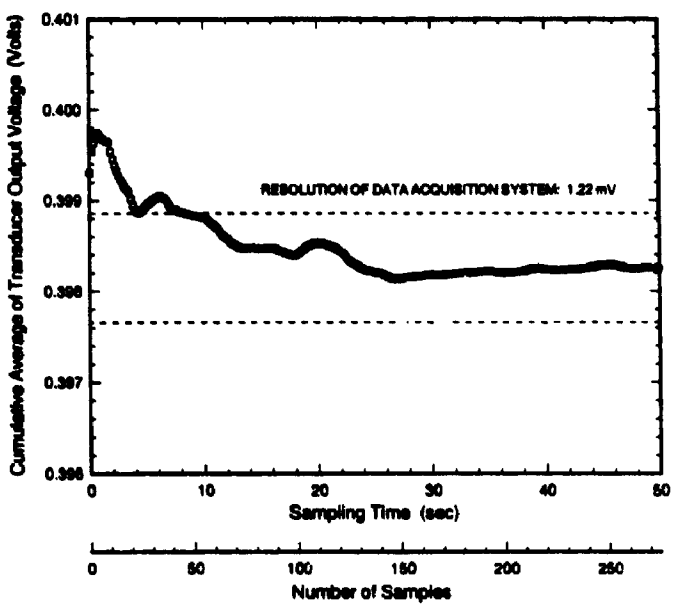

Figure 4.3 Cumulative average of the transducer output voltage versus time.

4.2.2 Data Sampling Procedure

All test section pressures are non-dimensionalized by the reference inlet centreline dynamic pressure to form pressure coefficients. As previously mentioned, the reference inlet centreline dynamic pressure is inferred from the contraction pressure difference through calibration. This implies that both the contraction pressure and the test section pressure must be monitored simultaneously using two separate transducers.

Because the data acquisition system can only sample one quantity at any given time, the test section and contraction pressures are sampled sequentially. All data accumulated during the sampling period is stored in the random access memory (RAM) of the M901 unit. At the end of the sampling period, the data are transmitted from the M901 RAM to the computer prior to beginning the next sampling sequence. These data are then grouped to form measurement cycles consisting of *reference pressure - test section pressure - reference pressure;* each test section pressure is then non-dimensionalized by the average of the contraction pressure differences acquired in the same measurement cycle. An average of the individual non-dimensional values is then taken to apply for the given sampling period. For example, during the 20 *sec* sampling period used for downstream measurements, roughly 110 samples are taken from each of the two transducers (corresponding to slightly more than 5 *samples/sec* from each transducer). These samples are then non-dimensionalized to form roughly 110 non-dimensional pressures coefficients which are then averaged to give one representative value for the sampling period. Yaras (1990) showed that the sampling procedure outlined above provides improved repeatability of the data.

4.3 Flow Quality

Prior to doing any detailed measurements of the three-dimensional flowfield downstream of the blade row, the status of the inlet and outlet flows was documented. The following sections outline the preliminary measurements made upstream and downstream of the blade row.

4.3.1 Inlet Flow Uniformity

The uniformity of the cascade inlet flow was determined using spanwise pitot-tube traverses. These traverses were made at seven discrete pitchwise locations 1.83 axial-chord-lengths upstream of the blade leading edge (see Figure 4.4). Each traverse extended across approximately 95% of the blade span beginning at the tipwall window.

The position datum for these traverses was determined aerodynamically. This was done by bringing the head of the pitot probe increasingly closer to the tipwall, with the wind on. From the point where the probe first makes contact with the wall, the total pressure measured by the probe remains constant while the probe bends slightly as it is further pulled towards the tipwall. The position datum was taken to be the one where the total pressure first starts to level off.

The results of the spanwise pitot-tube traverses for 0, 10 and 15% clearance are presented in Figures 4.5 through 4.7. The non-dimensional velocities observed in Figures 4.6 and 4.7 are slightly higher than those seen at zero clearance. This is as a result of the diffusion which occurs between the inlet traverse station and the downstream reference station when the wedge-shaped spacers are inserted for clearance. It is evident from the figures that the inlet tipwall boundary layers are essentially uniform over the region of interest.

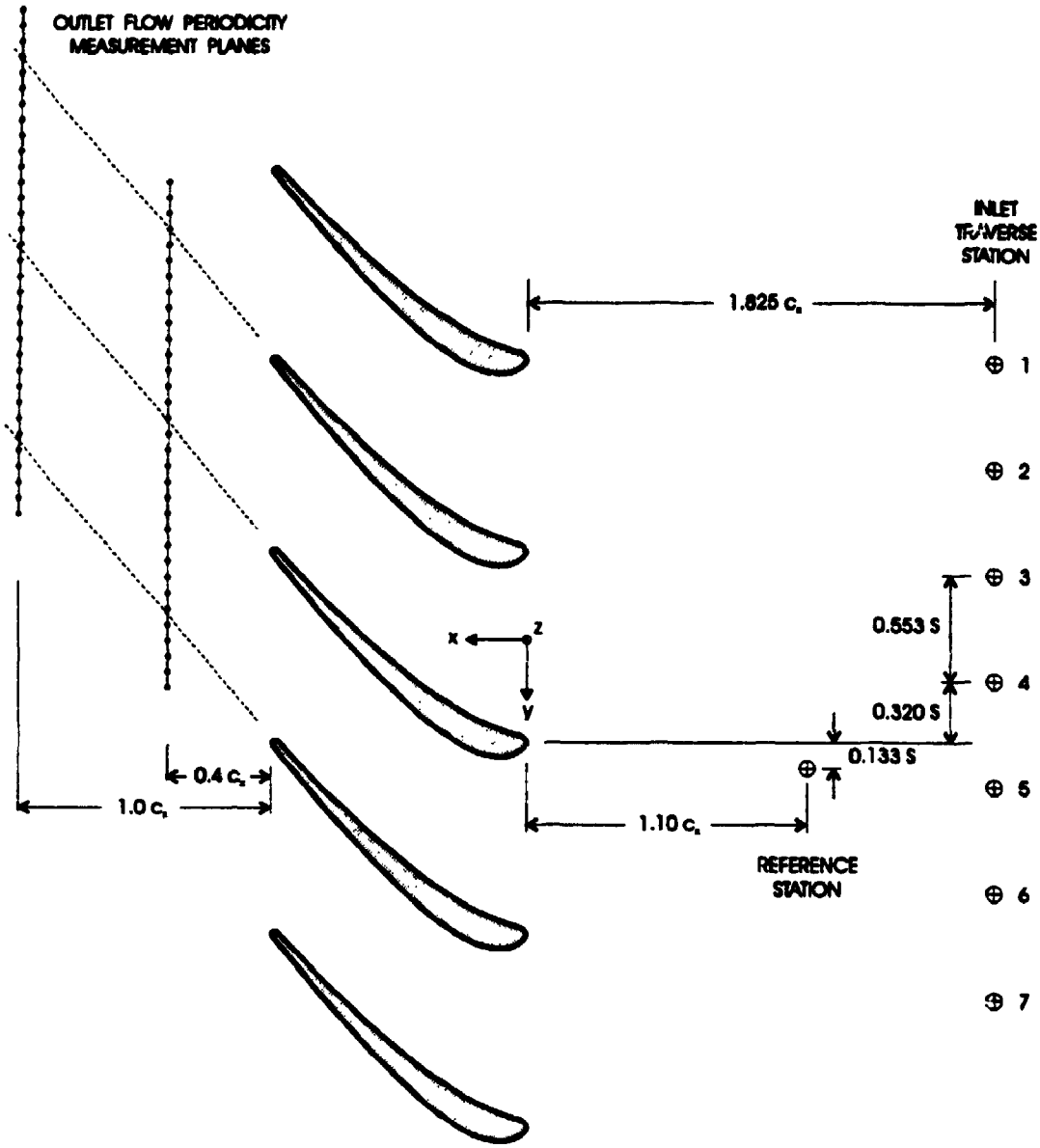

Figure 4.4 Inlet and outlet flow quality measurement locations.

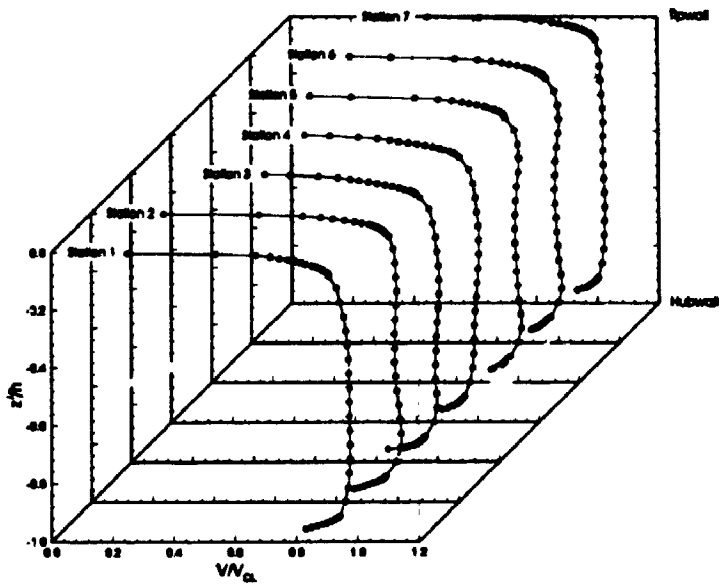

Figure 4.5 Inlet flow uniformity for $\tau/c = 0.00$.

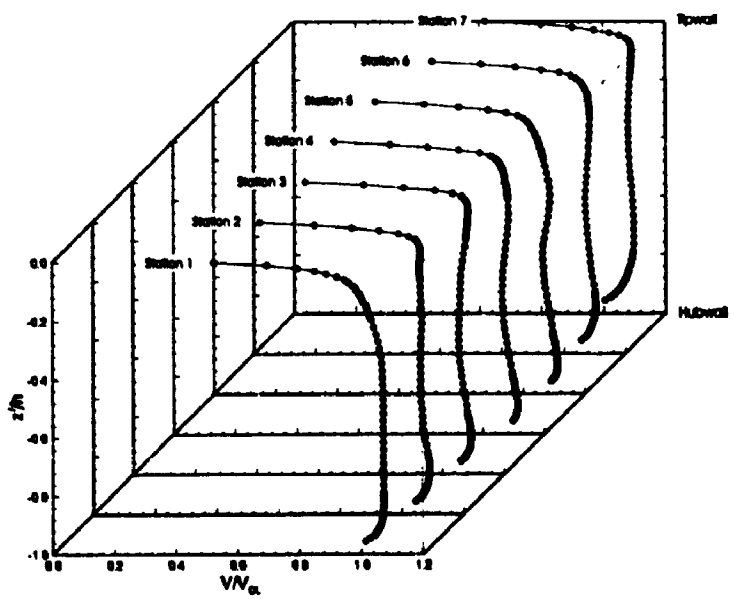

Figure 4.6 Inlet flow uniformity for $\tau/c = 0.10$.

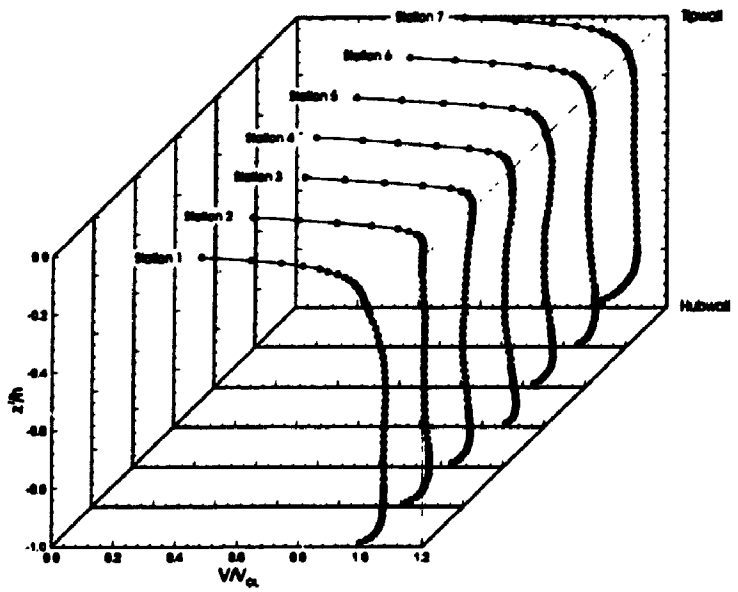

Figure 4.7 Inlet flow uniformity for $\tau/c = 0.15$.

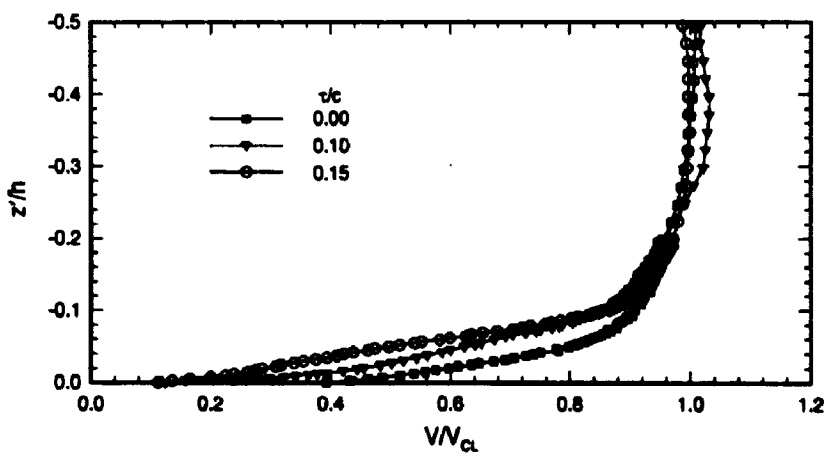

Figure 4.8 Inlet tipwall boundary layers.

To document the inlet flow and calculate the inlet losses, detailed measurements of the boundary layer were also made at the reference station, located 1.1 c_x upstream of the blade leading edge plane. The results for each of the three clearances are shown in Figure 4.8. Table 4.2 lists the integral boundary-layer parameters for each clearance.

Inlet Boundary Layer Parameters	Clearance Size (τ/c)		
	0.00	0.10	0.15
δ^*_x [mm]	3.6	5.7	7.5
θ_{xx} [mm]	3.0	3.7	5.0
H_x	1.2	1.6	1.5

Table 4.2 Inlet tipwall integral boundary layer parameters.

4.3.2 Outlet Flow Periodicity

To establish a periodic outlet flow, such as would be present at the outlet of an actual turbomachine, a linear turbine cascade would in theory require an infinite number of blades. In practice, however, due to physical limitations, cascades consist of a finite number of blades and incorporate additional control surfaces to *trim* the outlet flow in order to establish periodicity. The present cascade makes use of only 5 blades in conjunction with 4 control surfaces (see Section 3.2) to establish a reasonably periodic outlet flow.

Flow periodicity measurements were made using the three-hole probe at blade midspan. Figure 4.9 shows the total pressure and flow angle distributions through blade wakes measured one axial chord length downstream of the blade row for 0% clearance. Significant diffusion of the wake structures has occurred by this plane. Because of this,

the outlet flow measurement plane was moved closer to the blade row (approximately 0.4 c_x downstream of the blade trailing edge plane) for the subsequent measurements at 10 and 15% clearance, shown in Figures 4.10 and 4.11, respectively.

The midspan exit flow angles are observed to be within ±2° across the entire cascade outlet. Although this deviation is higher than the ±0.5° used by others for two-dimensional profile loss measurements (e.g., Tremblay (1989), Whitehouse (1992), Rodger (1992), and Abbott (1993)), it was considered to be acceptable for the current three-dimensional measurements, in which the flow is governed by more local effects such as the blade driving pressure difference.

4.3.3 Effects of Screen Fouling

Figure 4.12 presents the inlet flow angle and total pressure distributions for both clean and fouled screens. The fouling of the settling chamber screens is seen to have serious detrimental effects on the inlet flow uniformity. A spanwise variation in the measured total pressure is observed when the screens are fouled, particularly near the tipwall, where the losses are observed to become significant. This, in turn, makes the interpretation of the downstream losses ambiguous since the reference total pressure level in the passage is not constant. Similarly, the inlet flow angle is observed to become very non-uniform. This non-uniformity could lead to spanwise changes in the blade loading which would affect the blade boundary layers.

During the experiments, great care was taken to ensure that the screens remained clean. The screens were cleaned prior to beginning any measurements at each new clearance. This ensured that the "wind-on" time was kept below 100 *hrs* between each cleaning.

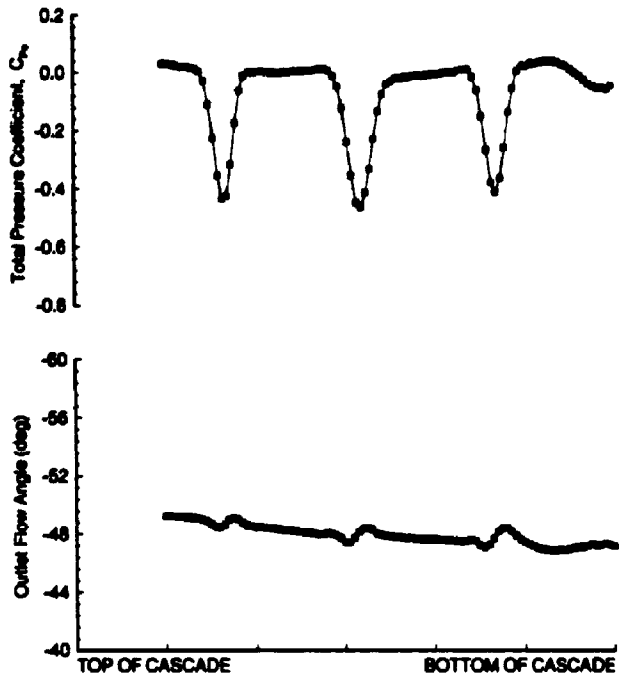

Figure 4.9 Outlet flow periodicity for 0% clearance, located $1.0c_x$ downstream of the blade row.

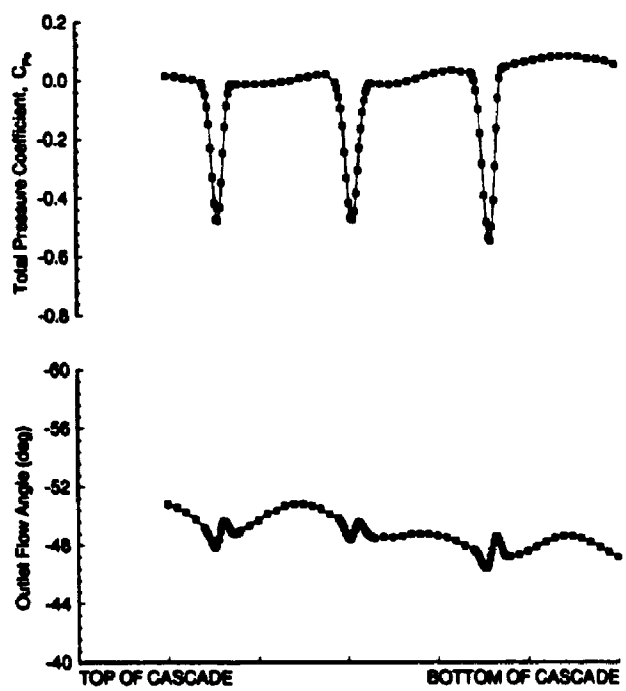

Figure 4.10 Outlet flow periodicity for 10% clearance, located $0.4c_x$ downstream of the blade row.

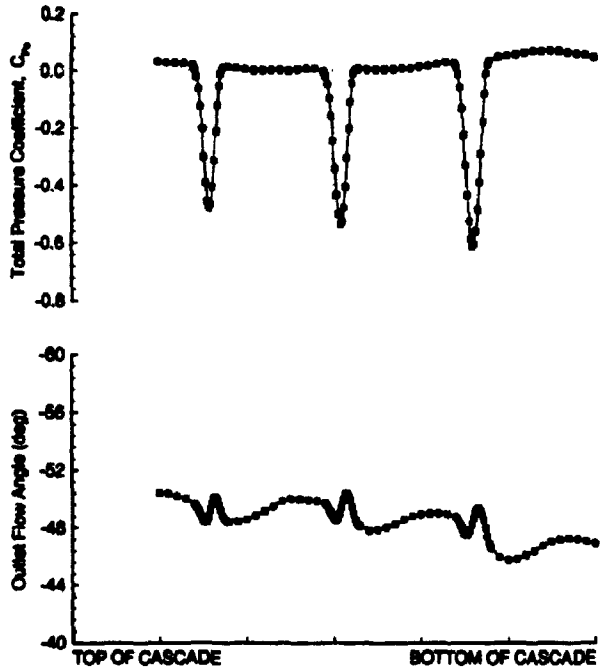

Figure 4.11 Outlet flow periodicity for 15% clearance, located $0.4c_x$ downstream of the blade row.

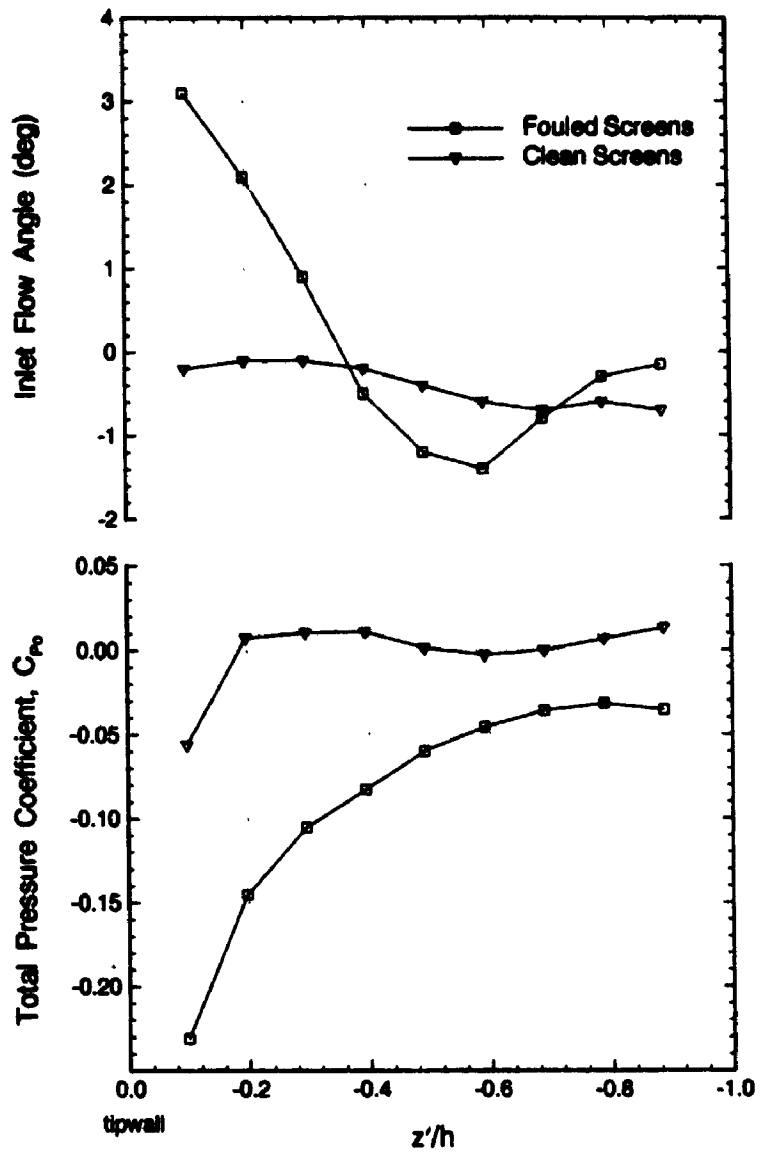

Figure 4.12 Effects of screen fouling on the flow angle and total pressure distributions at the reference plane.

Chapter 5
COMPUTATIONAL MODEL

A computational analysis of the tip-leakage flow at large clearances was conducted using a three-dimensional Navier-Stokes solver (BTOB3D) developed by Dawes (1986b). A brief summary of the code and a discussion of some of its more prominent features is presented. The chapter concludes with a presentation of the grid refinement study used to determine the appropriate mesh geometry required for obtaining near-grid-independent results.

5.1 The Dawes Code

The BTOB3D code developed by Dawes has been shown to be a useful design and analysis tool for many turbomachinery applications. The generality and robustness of the code has been demonstrated through extensive testing over a wide range of turbomachinery cases including: transonic flow through a compressor rotor (e.g., Dawes (1987)), secondary flow in a radial-inflow turbine (e.g., Dawes (1988)), flow through an axial compressor with tip clearance (e.g., Storer & Cumpsty (1991)), and the flow through a turbine cascade with trailing edge damage (e.g., Sjolander *et al.* (1993)).

The present computations were intended to test the code's ability to predict correctly the flow physics at very large clearances. Providing that this was successful, the Dawes code was viewed as an useful vehicle for testing numerous cases to complement the experimental results. The resulting computational trends are compared with the experimental results and presented in Chapter 6.

5.1.1 Governing Equations

The three-dimensional, compressible, Reynolds-averaged Navier-Stokes equations can be expressed in strong conservation form and cast in the blade-relative frame of reference using cylindrical coordinates (r, θ, x) as follows:

$$\frac{\partial}{\partial t} \oint_V \overline{U}\, dV = \oint \overline{H} \cdot d\overline{A} + \oint \rho \overline{S}\, dV \tag{5.1}$$

where

$$\overline{U} = \begin{bmatrix} \rho \\ \rho V_x \\ r\rho V_\theta \\ \rho V_r \\ \rho E \end{bmatrix} \qquad \overline{H} = \begin{bmatrix} \rho \overline{q} \\ \rho V_x \overline{q} + \overline{\overline{\tau}}\, \hat{i}_x \\ r\rho V_\theta \overline{q} + \overline{\overline{\tau}}\, \hat{i}_\theta \\ \rho V_r \overline{q} + \overline{\overline{\tau}}\, \hat{i}_r \\ \rho I \overline{q} \end{bmatrix} \qquad \overline{S} = \begin{bmatrix} 0 \\ 0 \\ -2\Omega r V_r \\ \dfrac{V_\theta^2}{r} + r\Omega^2 + 2\Omega V_\theta \\ 0 \end{bmatrix}$$

with

relative velocity:	$\overline{q} = V_x \hat{i}_x + V_r \hat{i}_r + V_\theta \hat{i}_\theta$
rotational speed:	Ω
rothalpy:	$I = h_{0_{rel}} - \frac{1}{2}(\Omega r)^2$
and stress tensor:	$\overline{\overline{\tau}} = \begin{vmatrix} -p + \tau_{xx} & \tau_{rx} & \tau_{\theta x} \\ \tau_{xr} & -p + \tau_{rr} & \tau_{\theta r} \\ \tau_{x\theta} & \tau_{r\theta} & -p + \tau_{\theta\theta} \end{vmatrix}$.

The system of equations summarized above represent, in order, conservation of mass, x-momentum, θ-momentum, r-momentum, and rothalpy. Closure is obtained using the

equation of state, which can be expressed in terms of the total internal energy, E, as follows:

$$p = \rho(\gamma - 1)\left(E - \frac{1}{2}\left[\bar{q}\cdot\bar{q} - (\Omega r)^2\right]\right) \tag{5.2}$$

and the Baldwin & Lomax (1978) two-layer mixing length turbulence model. The conservation of rothalpy, expressed in Equation 5.1, is essentially a statement of energy conservation with viscous stresses and heat conduction terms neglected; this simplification is reasonable for high speed flows with no external heat addition.

5.1.2 Computational Mesh

The Dawes code uses a structured H-mesh, chosen for its simplicity and flexibility. The mesh is formed from the intersection of three families of surfaces: streamwise (x, θ), quasi-orthogonal (r, θ), and meridional (x, r), shown in Figure 5.1. The streamwise surfaces are taken to be surfaces of revolution, the first coinciding with the hub and the last with the casing. Likewise, the first and last meridional surfaces coincide with the blade suction and pressure surfaces, respectively. The spacing between the mesh lines is user specified and need not be uniform. However, Dawes (1986b) recommends that the relative spacing between adjacent grid cells be kept below ±30% for acceptable accuracy. The resulting grid consists of a three-dimensional network of hexahedral cells; the geometry is defined by the cell nodes (or corners), and the flow variables are associated with the cell centers (see Figure 5.2).

5.1.3 Discretization Scheme and Solution Algorithm

The governing equations are discretized using a finite-volume formulation. The integral of the various flux terms, $\overline{H}$, in Equation 5.1 can be replaced by a discrete summation over the faces of the hexahedral cells as follows:

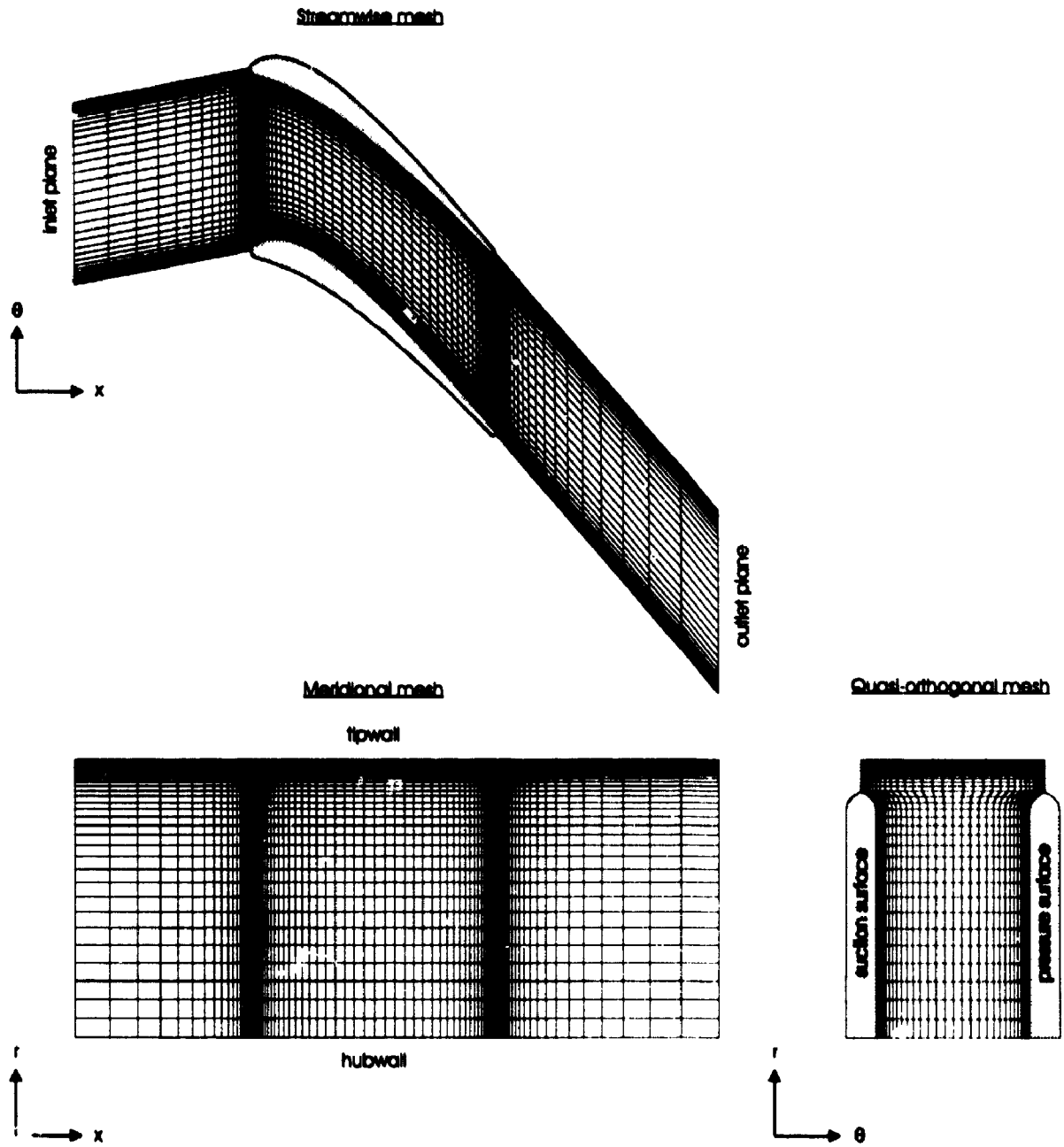

Figure 5.1 Structured H-mesh used by the Dawes code.

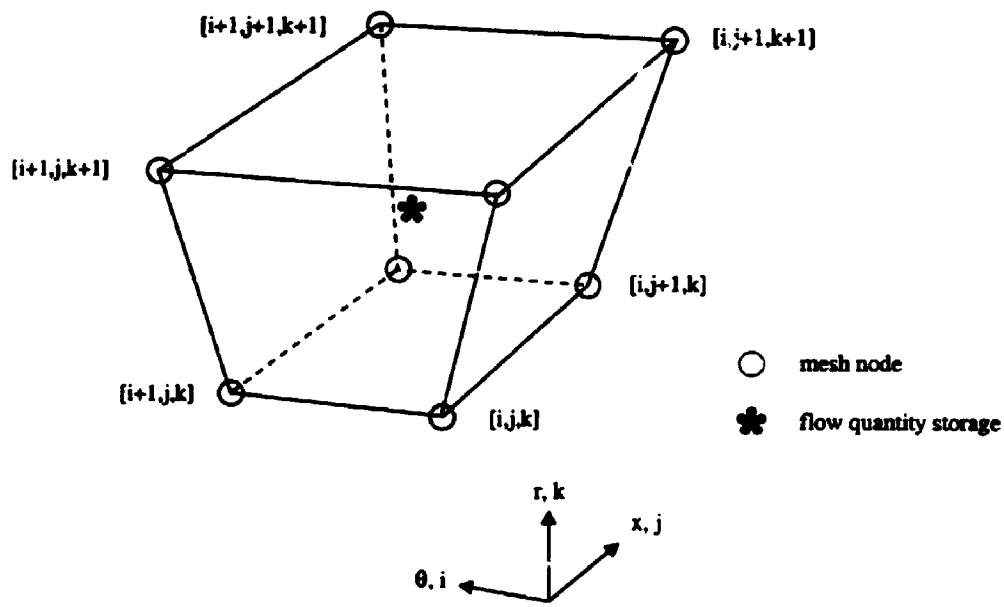

Figure 5.2 Typical finite volume cell.

$$\frac{\Delta \overline{U_{ijk}}}{\Delta t} \Delta V_{ijk} = \sum_{Cell\ ijk} \overline{H} \cdot \overline{\Delta A} + \rho \overline{S_{ijk}} \Delta V_{ijk} + \overline{D_{ijk}} \tag{5.3}$$

where the flux through any given face is interpreted as being formed from the linear average of the flow variables between the two cell centers to either side of the face. This method ensures global conservation and allows for second-order spatial accuracy as long as the relative spacing between adjacent grid cells is kept below the recommended ±30%. The additional term $\overline{D_{ijk}}$ is an adaptive artificial diffusion, discussed in more detail in the following section.

The solution algorithm used by the Dawes code time marches the finite-volume form of the Navier-Stokes equations to a steady state solution using a two-step explicit/one-step implicit method. The method is similar to the Beam & Warming (1978) implicit scheme but makes use of a preprocessing matrix in order to ensure diagonal dominance; this allows for an efficient inversion of the resulting tridiagonal matrices. Although, in principle, the algorithm can be made stable for any time step (Dawes, 1986a), extensive testing by Dawes has shown that optimum convergence is achieved for Courant-Friedrichs-Lewy (CFL) values in the range of 1-3.

5.1.4 Artificial Viscosity

The artificial viscosity scheme adopted by the Dawes code is based on the method developed by Jameson & Baker (1984). Artificial diffusion, $\overline{D_{ijk}}$, is added to the discretized finite-volume equations (Equation 5.3) in order to prevent odd-even point solution decoupling and to suppress oscillations in regions with strong pressure gradients (e.g., at shock waves). A shock-sensing pressure parameter is used to switch from a low-level fourth-difference background smoothing to a more rigorous second-difference smoothing in the immediate vicinity of the shock. The current formulation of the artificial viscosity algorithm incorporates three constants; all testing for the present

research made use of the values recommended by Dawes (1986a). Lastly, it should be noted that for cells adjacent to solid boundaries, the artificial viscosity is set to zero in directions normal to surface to avoid masking the physical viscosity.

5.1.5 Multigrid Acceleration

The version of the Dawes code used here employs one level of multigrid, based on the Brandt Full Approximation Scheme (FAS). By allowing the overall flow pattern information to propagate rapidly over a coarse grid, while resolving details on a fine grid, the multigrid procedure is capable of roughly halving the required computational time (Dawes, 1986a). The code generates the coarse grid simply by eliminating every second surface (streamwise, meridional, and quasi-orthogonal) in each coordinate direction. The multigrid process involves sweeps that transfer the residuals from the fine grid to the coarse grid and then subsequently interpolate corrections from the coarse grid back to the fine grid. In order to save computational time, viscous stresses are evaluated only on the fine grid and frozen on the coarse grid.

5.1.6 Baldwin-Lomax Turbulence Model

As previously mentioned, closure of the Reynolds-averaged Navier-Stokes equations is obtained via the Baldwin & Lomax (1978) turbulence model. This two-layer model, based on the Prandtl mixing-length concept, has gained wide acceptance in the turbomachinery community. Although the model cannot capture the effects of upstream history, as the higher order models can, its simplicity and computational efficiency make it attractive.

Dawes (1990) found that the loss predicted using a mixing-length model was of similar accuracy to that of a higher-order turbulent kinetic energy transport model. The results of the study indicated that the majority of the losses (for the transonic compressor

tested) were generated deep within the boundary layer where both of the models were tuned to reproduce the log-law portion of the "universal" law-of-the-wall. Cleak & Gregory-Smith (1992) performed a similar study where they compared a mixing length, a one-equation model, and a k-ϵ/mixing-length hybrid model using the Moore (1985) code. Again, it was found that all three models gave comparable results, with the mixing length model giving the best mean flow predictions while the k-ϵ/mixing-length hybrid model gave the best predictions for the turbulent kinetic energy and turbulent shear stresses.

5.1.7 Boundary Conditions

Several boundary conditions and initial conditions must be specified at the inflow and outflow boundaries in order to initialize the computations. At the subsonic inflow boundary, the inlet total temperature, total pressure, and flow angle are entered for all streamwise surfaces and held fixed throughout the calculations. The inlet flow angle consists of two components: a pitch component and a swirl component. Typically, the pitch angle is set to zero (denoting zero radial component of velocity) while the swirl angle is adjusted to set the incidence of the inlet flow. At the outflow, the hub static pressure is specified and held fixed while the radial variation in the static pressure is determined from the radial equilibrium equation. Extensive testing by Dawes (1986b) showed that both the inflow and outflow boundaries should be located at least half an axial chord upstream and downstream of the blades, respectively.

All cell faces within the computational domain which align with the solid walls (hub, casing, and blades) are subject to the no slip and no flux (mass, momentum, and energy) conditions. Likewise, cells adjacent to periodic boundaries are treated as if they were interior cells and the fluxes across the periodic boundaries are calculated by linear interpolation between cells at either side of the boundary.

5.2 Grid Refinement Studies

Factors such as the grid density, number of time steps used and the cascade inlet Mach number all have significant effects on the accuracy of the results predicted by the Dawes code. Since all these factors are interrelated, the grid refinement study was conducted in an iterative manner. However, in order to keep the presentation simple, these effects are discussed separately below.

5.2.1 Effects of Grid Density

The effects of grid density were examined for the zero clearance case; subsequent modification of the grid to accommodate tip clearance will be discussed in Section 5.2.4. In Section 5.1.2, it was noted that the grid spacing had to be varied smoothly and that the relative spacing between mesh lines had to be kept below ±30% for accurate predictions. Even when these conditions are satisfied, additional modifications to the grid will likely be necessary to ensure acceptable accuracy. For example, grid refinement will likely be necessary near the blade leading- and trailing-edges where large axial gradients are present[1], and also near the blade pressure- and suction-surfaces where viscous effects are important. For the zero clearance case, accurate prediction of the passage vortex development requires a sufficient number of cells in the tipwall and/or hubwall regions.

Due to computer memory constraints, it was impossible to refine the meridional mesh sufficiently to achieve, simultaneously, a detailed evaluation of both the tipwall and the hubwall flow structures. Therefore, it was decided to use only one-sided clustering in the radial direction with the grid refined only near the tipwall (see Figure 5.1). This compromise allowed for a sufficient number of cells to accurately model the tipwall

[1] The blade leading edge and trailing edge have always been problematic areas for conventional H-mesh solvers because of the resulting grid skewness and slope discontinuities in these regions (e.g., Chung & Back (1992) and Turner *et al.* (1993)).

passage vortex (and the tip-leakage vortex at clearance, which is the primary flow structure of interest in the current study) but was too coarse to model the hubwall flow structure and tended to promote excessive mixing in this region due to the limited number of cells present. Consequently, all mass-averaged results presented in the following sections and in Chapter 6 are calculated using only the 60% of span nearest the tipwall (see Section 6.1.1.1).

Tests were run using three difference grids of varying mesh density with $I_{max} \times J_{max} \times K_{max}$ dimensions of 17×53×17, 27×81×27, and 35×107×35. The finest grid represents roughly a doubling of the coarsest grid in each coordinate direction. This was found to be the largest grid size which could fit into the computer memory without making excessive use of the machine's virtual memory/swap-space. Figure 5.3 presents the blade-to-blade mesh and the predicted Mach number contours for each of the three grids. It is evident from the figure that the smoothness of the solution is greatly improved by using a denser grid. However, the overall solutions appear to be qualitatively similar, even between the coarsest and finest grids.

Closer examination of the Mach number contours in Figure 5.3 shows that there are oscillations near the blade leading- and trailing-edges where the largest axial gradients are present. In order to improve the flow resolution in these regions, further adjustment of the axial grid clustering was required. Figure 5.4 shows the leading- and trailing edge nodes for the 27×81×27 grid before and after the reclustering. While the number of axial nodes is kept constant for both cases and the inflow and outflow boundaries are kept at the same axial positions, the relative spacing parameter has been increased for the newer grid. The new reclustered grid is observed to have more nodes on the blade leading- and trailing-edge diameters allowing for better definition of the blade profile in these regions.

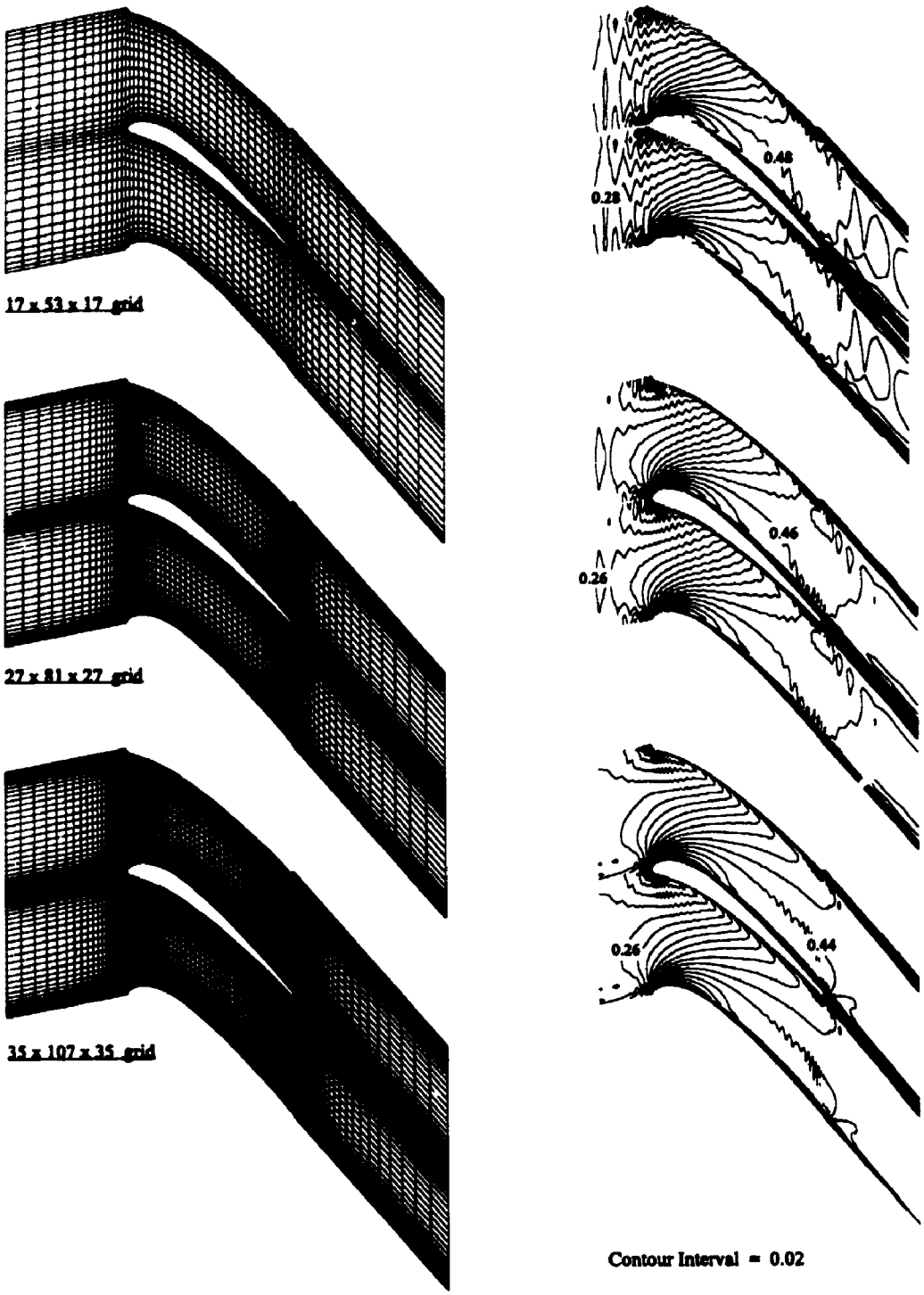

Figure 5.3 Comparison of three different meshes and the predicted mid-span Mach number distributions [M_{IN} = 0.26, 5000 timesteps, τ/c = 0.00].

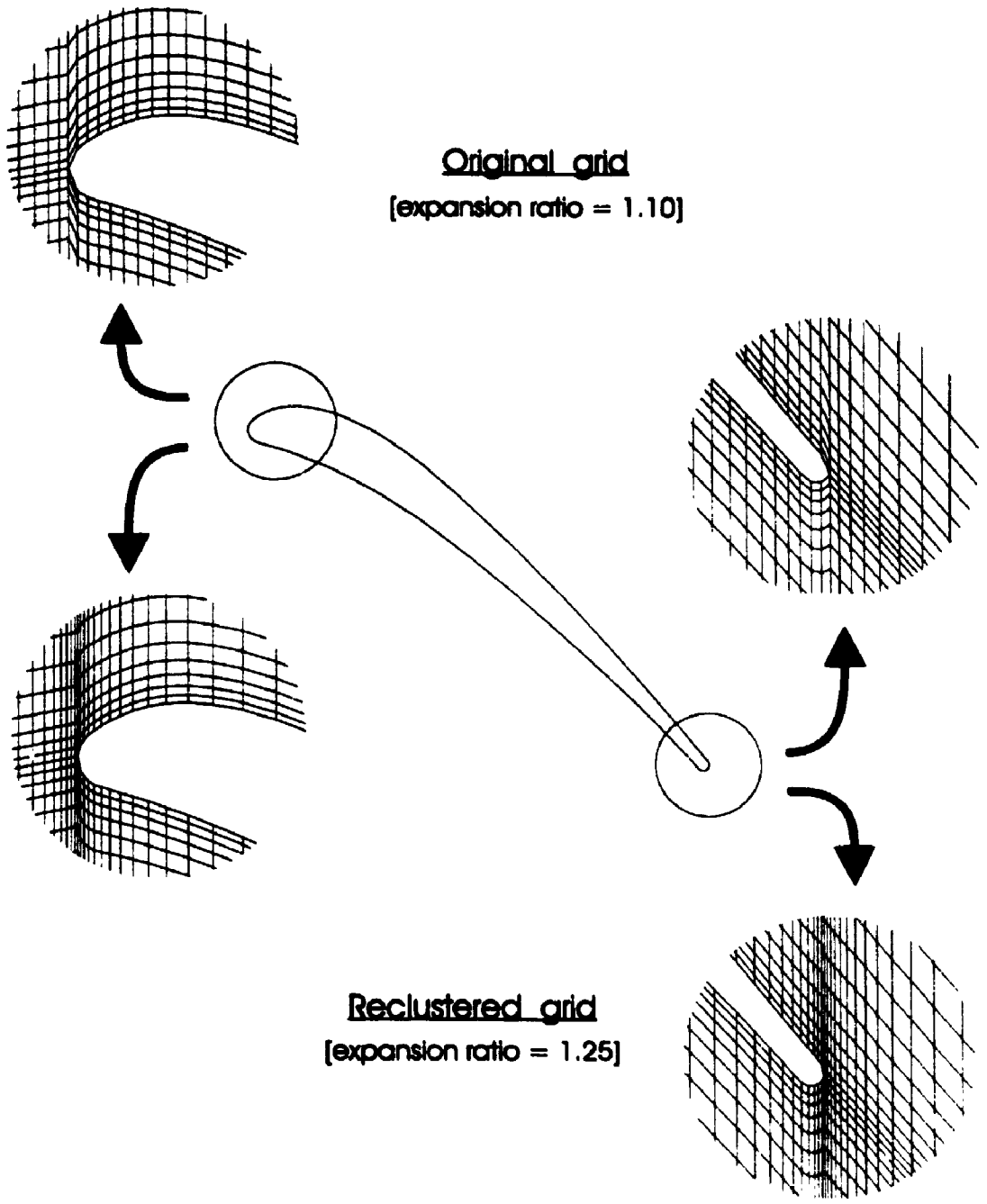

Figure 5.4 Effects of axial grid reclustering on the leading- and trailing-edge nodes for the 27×81×27 grid.

Figure 5.5 shows the new reclustered meshes for all three grid densities and the predicted Mach number contours. The velocity field around the blades is observed to be much smoother for all three modified grids.

Although the Mach number contours present a quick method for evaluating the smoothness of a predicted solution, the total pressure coefficient is the parameter of interest in the current study[2]. Figure 5.6 presents the pitchwise mass-averaged total pressure coefficient at a plane 0.5 c_x downstream of the blade trailing edge. The results of the 27×81×27 and the 35×107×35 grids are found to be quite similar. The inset shows the variation of the mass-averaged total-pressure coefficient (net loss) with the number of grid nodes. As discussed in earlier, the mass-averaging was performed using the 60% of span nearest the tipwall. The trend clearly indicates that the solution predicted by the 35×107×35 grid is asymptotically approaching the grid-independent result. Henceforth, all discussion will pertain to this grid.

Roache (1994) recently addressed the issue of quantifying uncertainty in grid refinement studies. He found that there was a lack of uniformity in the presentation of the predicted uncertainties and proposed a method of *a posteriori* error estimation. The method is based on the Richardson Extrapolation technique and relates the error estimation obtained for an arbitrary grid refinement to one which would be expected from a grid refinement study of the same problem but using a grid doubling and a second-order spatially accurate scheme. That is to say, the error estimate obtained from an arbitrary grid refinement is normalized to give an *equivalent* error estimate, which Roache refers to as the Grid Convergence Index (GCI), that is based on a grid doubling using a second-order spatially accurate scheme.

---

[2] Dawes (1988) claims that the loss coefficient is the last parameter to converge in numerical simulations.

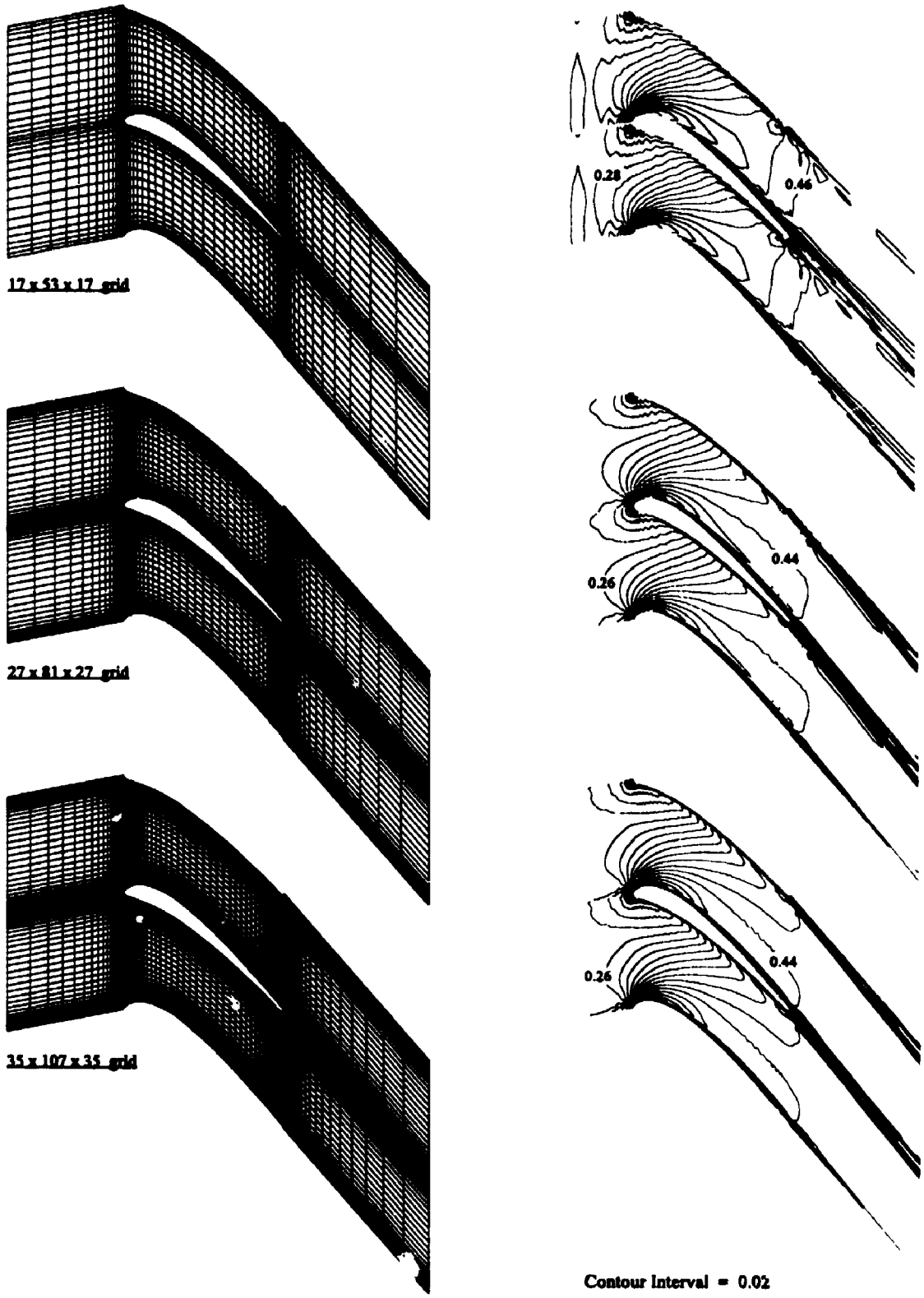

Figure 5.5 Comparison of the mid-span Mach number distributions for the reclustered grids [M_{IN} = 0.26, 5000 timesteps, τ/c = 0.00].

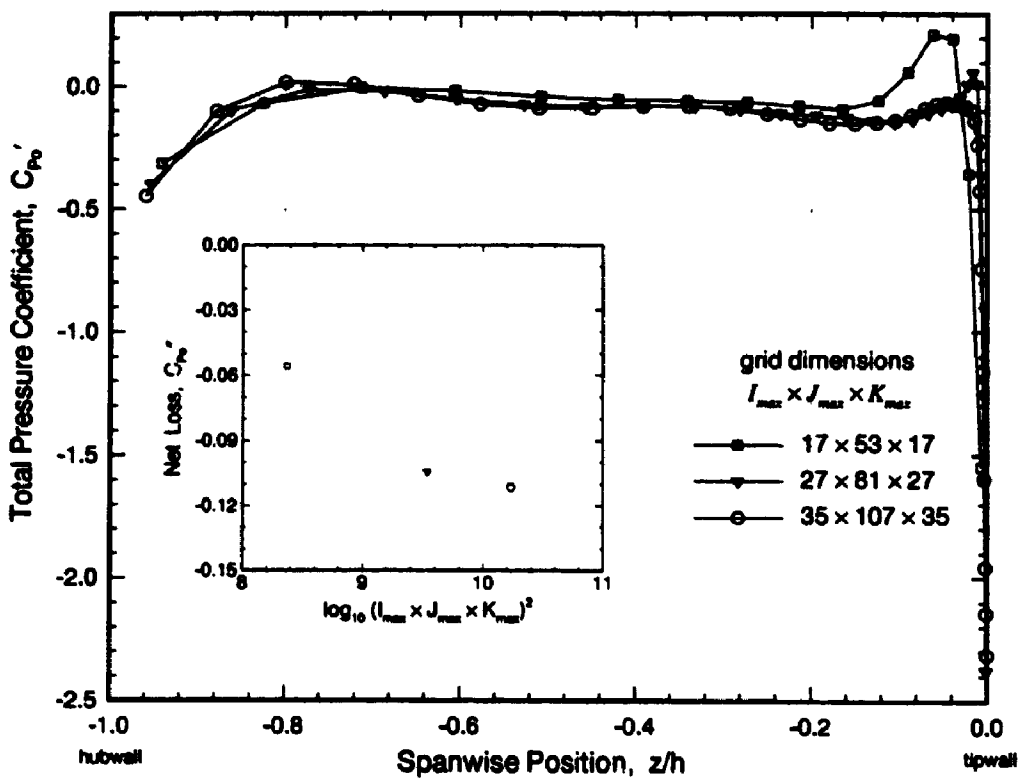

Figure 5.6 Predicted distributions of the total-pressure coefficient for each of the three reclustered grids.

For a prediction scheme with spatial accuracy p (e.g., p = 1 for a first-order method, p = 2 for a second-order method, etc.) and for a grid refinement r (e.g., r = 1.5 for a grid density increase of 50% in each coordinate direction, r = 2.0 for a grid doubling in each coordinate direction, etc.), Roache states that the Grid Convergence Index gives a conservative estimate of the error, with GCI given as:

$$GCI\ [fine\ grid] = \frac{3\,|\epsilon|}{r^p - 1}$$

with

$$\epsilon = (f_2 - f_1)/f_1$$

where ϵ is the relative error between the fine grid solution, f_1, and the coarse grid solution, f_2. The method not only applies to the point-by-point solution values but also to the solution functionals (e.g., the mass-averaged loss coefficient).

Table 5.1 presents the mass-averaged total pressure coefficients at 0.5 c_x. One can observe from the table that the net loss predicted for the 27×81×27 grid is within 6.5% of the fine grid (35×107×35) value. This relative error is often the error estimator quoted in papers. However, Roache (1994) noted that this value is a function of the amount of grid refinement done and the spatial accuracy of the solver. In fact, the value can be misleading if the grid refinement is made sufficiently small. The grid refinement between the 27×81×27 and the 35×107×35 grids represents a 30% increase in the number of nodes in each coordinate direction (r = 1.3), and so the GCI of 28.3% is a more conservative estimate of the error.

GRID DIMENSIONS $I_{max} \times J_{max} \times K_{max}$	Mass-Averaged Total Pressure Coefficient C_{P_o}''	ε [%]	GCI [%]
17×53×17	-0.0557	---	---
27×81×27	-0.1042	6.5	28.3
35×107×35	-0.1114		

Table 5.1 Mass-averaged total-pressure coefficients for each of the grids.

5.2.2 Number of Time Steps for Convergence

All of the grid refinement studies were performed using 5000 timesteps and a CFL number of 0.5. Although the number of time steps is undoubtedly coupled with the fineness of the spatial grid, through the CFL number, experience showed that this was a sufficient number of time steps to represent a fully converged solution. However, with typical run times of approximately 78 *hrs* using a Sun Sparc Station 2 (i.e., convergence rate of 4.3×10^{-4} *secs/node/timestep*) one should not waste computational time by using an excessive number of timesteps. The following section examines the effect of the number of time steps on the convergence of the 35×107×35 solution.

The Dawes codes provides two output files which detail the convergence history of the solution and provide a measure of the residual; the residual being indicative of the average imbalance of mass, momentum, and energy over the entire computational grid. Other parameters monitored by these output files include the peak suction pressure over the blade and the maximum error in the mass flux through the computational domain.

Figure 5.7 presents the convergence history for the present grid. A rapid decrease in the residual is observed up to about 3000 timesteps whereupon the residual starts to

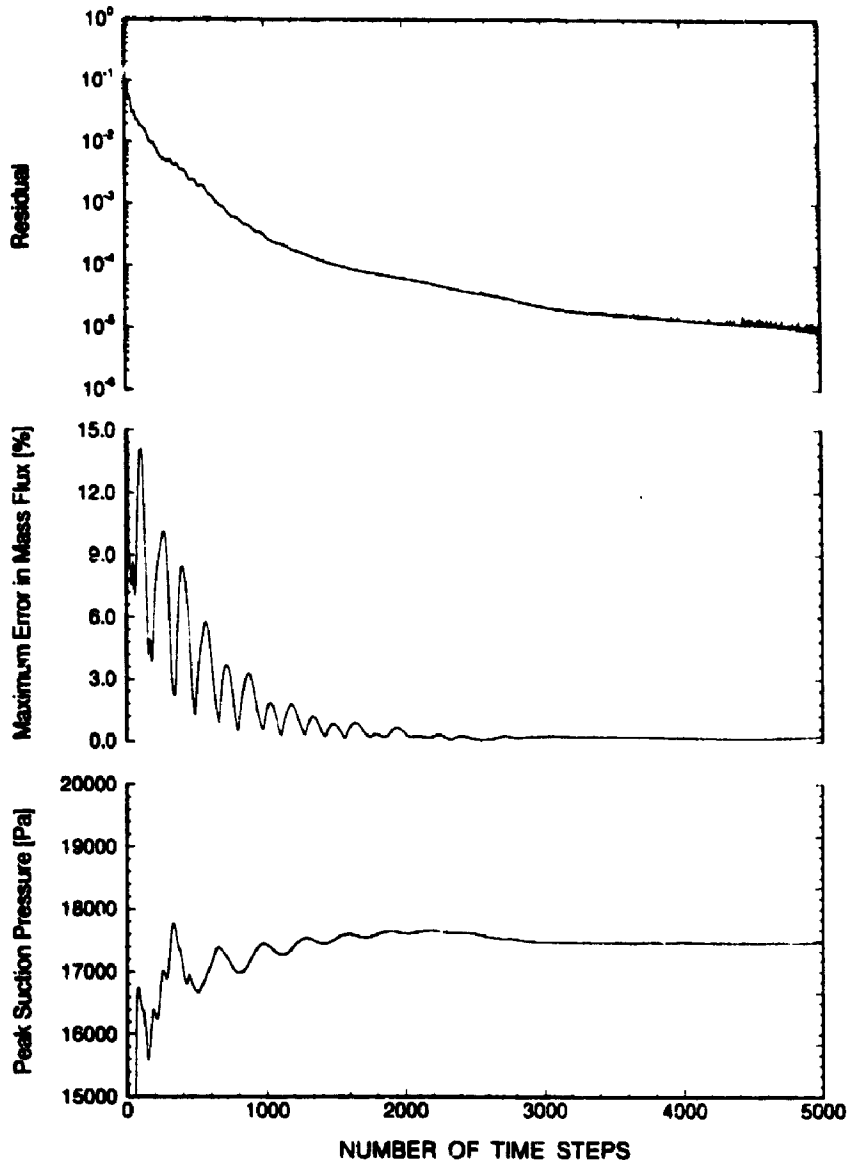

Figure 5.7 Grid convergence history.

2

PM-1 3½"x4" PHOTOGRAPHIC MICROCOPY TARGET
NBS 1010a ANSI/ISO #2 EQUIVALENT

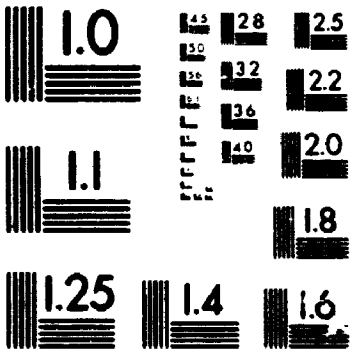

PRECISION℠ RESOLUTION TARGETS

level off. Likewise, the peak suction pressure and the maximum error in mass flux are initially quite oscillatory, but appear to have converged after 3000 timesteps. Although these three parameters provide a strong indication of convergence, it is worthwhile to examine the trend in the total pressure coefficient, the primary quantity of interest in the present research. Figure 5.8 plots the trend in the pitchwise mass-averaged total pressure coefficient at 1000, 2000, 3000, 4000, and 5000 timesteps. The results, extracted from a plane 0.5 c_x downstream of the blade trailing edge, show that there is little change in the predicted solution beyond 3000 timesteps. Figures 5.7 and 5.8 both indicate that the solution has converged at 3000 timesteps. All subsequent testing, including the results presented in Chapter 6, are based on this number of timesteps.

It should be kept in mind that the previous analysis was performed with one level of multigrid enabled. Without the multigrid, convergence would likely have taken twice as long (Dawes, 1986a).

5.2.3 Effects of the Cascade Inlet Mach Number

As discussed in Section 5.1, the Dawes code solves the compressible Navier-Stokes equations. At low Mach numbers, the convergence rate of the code is severely reduced and divergence may occur. Walker & Dawes (1990) state that:

> Conventional time-marching flow solvers perform poorly when integrating compressible flow equations at low Mach number levels. This is shown to be due to unfavourable interaction between long-wavelength errors and the inflow and outflow boundaries.

Walker & Dawes (1990) modified the Dawes code to include Chorin's method of artificial compressibility as a means of extending the range of applicability down to zero Mach-number conditions. Unfortunately, the version of the code at Carleton University does not include this feature.

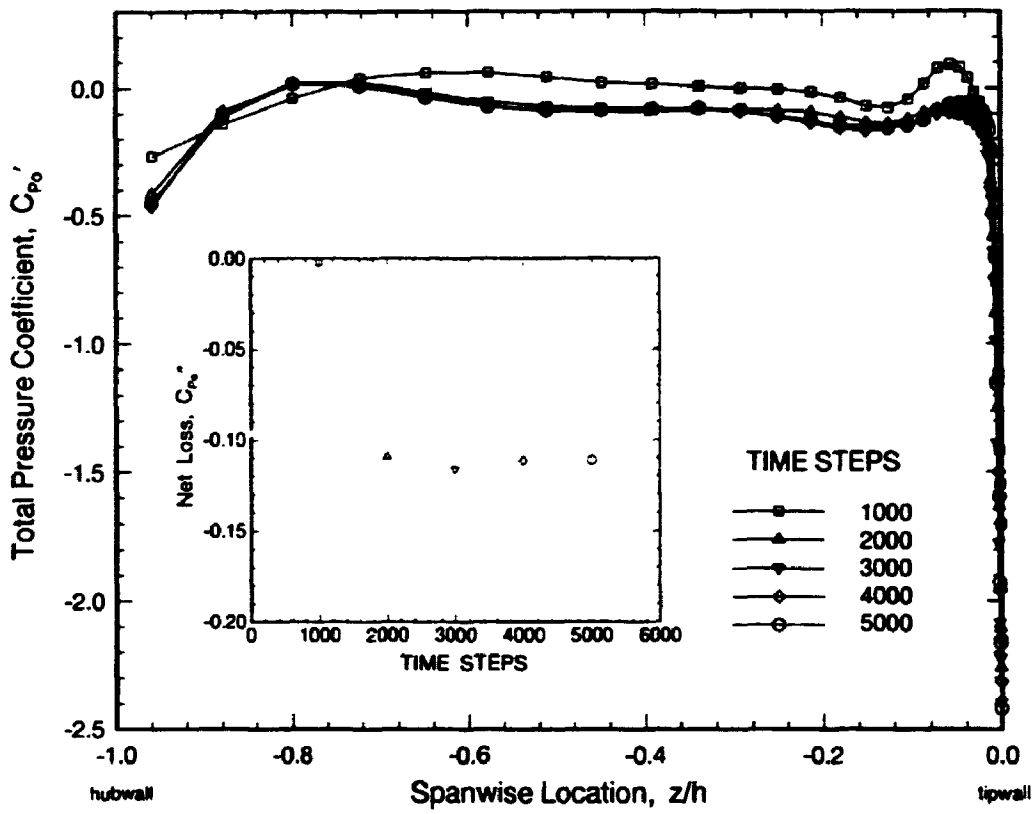

Figure 5.8 Predicted variation of the total-pressure coefficient for various time steps.

All of the experimental results were obtained at incompressible flow conditions, with an inlet velocity of roughly 30 m/s corresponding to an inlet Mach number of 0.09. Although it would be desirable to run the solver at this Mach number, the Dawes code was found to become divergent. Testing was required to determine the minimum Mach number at which the code could be run with an acceptable rate of convergence.

The previous studies on the appropriate spatial mesh sizing and the minimum number of timesteps required for convergence, discussed above in Sections 5.2.1 and 5.2.2, were both performed for an inlet Mach number of 0.26. Testing showed that this was the minimum Mach number that could be used with the present 35×107×35 grid without causing numerical instability. The deterioration of the convergence rate with decreasing inlet Mach number level is illustrated in Figure 5.9. With an inlet Mach number of 0.16, the residual is observed to decrease only over the first few hundred timesteps before becoming oscillatory. Unless otherwise noted, all subsequent results were obtained using inlet and outlet Mach numbers of 0.26 and 0.42, respectively.

5.2.4 Grid Modifications Required for Non-Zero Tip Clearances

The ultimate goal of the present computational research is to determine if the Dawes code can properly predict the flow physics at extended clearances. This section discusses the grid modifications necessary to incorporate blade clearance.

The current version of the Dawes code is incapable of handling sharp cornered blade tips. If tip clearance is to be modelled, the blade tip must be tapered from a finite thickness to zero at the blade tip in a smooth but rapid manner. Figure 5.10 shows the blade tip region for a typical quasi-orthogonal mesh. As it stands, the code does not attempt to resolve the flow in the clearance space but simply models the gap flow using a single grid line and periodic conditions.

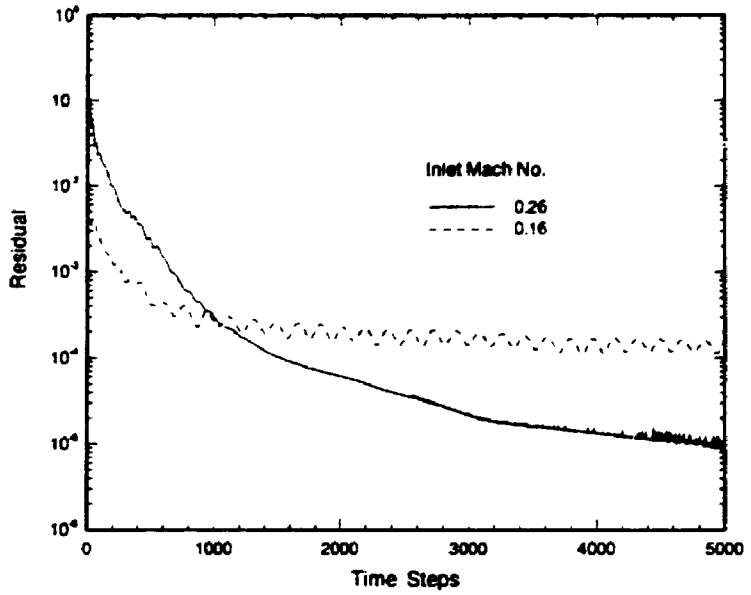

Figure 5.9 Effect of inlet Mach number on the solution convergence.

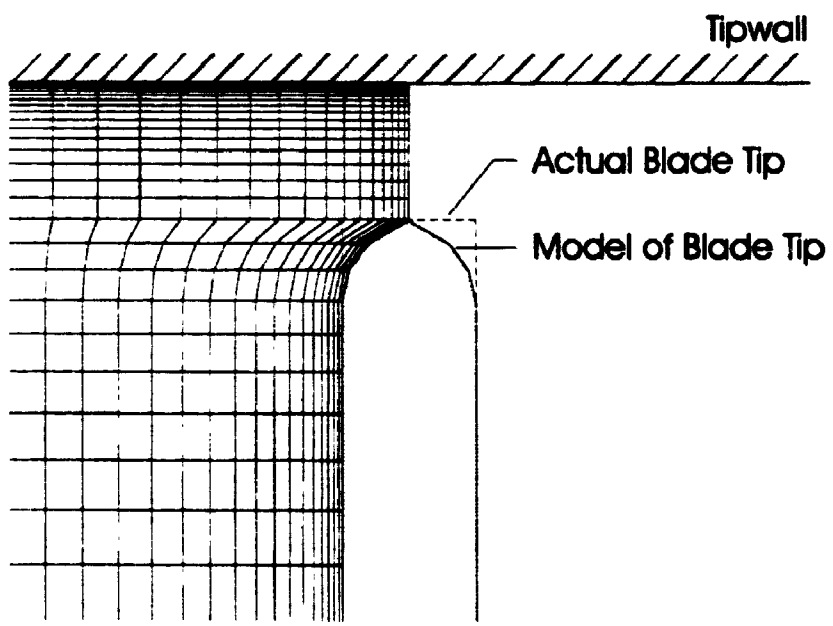

Figure 5.10 Quasi-orthogonal mesh at blade tip.

The rather crude method of modelling the blade tip is unlikely to correctly predict the tipgap mass flowrate. Typically, the clearance flow separates at the pressure side corner as it enters the gap. The resulting separation bubble introduces additional blockage in the tip gap reducing the gap flowrate. This effect is not modelled using a tapered blade tip and so the tipgap flowrate is expected to be over-predicted. However, at large clearances this result is mitigated somewhat since the blockage presented by the bubble becomes an ever decreasing fraction of the gap height.

5.3 Pre- and Post-Processors

All Dawes code input files were created using the CASTLE pre-processor developed by Isaacs (1994). This *command-line* driven program, which is written in FORTRAN, facilitates the grid generation process by allowing the blade geometry, boundary conditions, and initial conditions to be specified with ease. The grid clustering in each of the streamwise, meridional, and quasi-orthogonal directions is calculated using a trigonometric algorithm (refer to Isaacs (1994) for more details) which ensures a smooth variation of the local grid spacing. Appendix I details all modifications made to CASTLE in the course of the present research.

As discussed in Section 5.1.2, the Dawes code stores all flow variables (e.g., axial velocity, radial velocity, tangential velocity, relative Mach number, static pressure, density, and viscosity) at the cell centers while storing the grid geometry at the cell nodes. CENTREPOINT is a post-processor, written by Isaacs (1994), which calculates the coordinates of each cell centre throughout the computational domain. This is done by subdiving each cell into a number of planes. The centroid and area of each plane is then calculated assuming that each forms a two-dimensional trapezoid. The coordinates of the centroids are then averaged, weighted by their respective areas, to get the coordinates of the centre of the each finite volume cell.

The program, which is implemented in FORTRAN, allows the user to extract flow values from any streamwise, meridional, or quasi-orthogonal plane. Data extracted from the quasi-orthogonal surfaces can be mass-averaged over the entire axial plane, or simply mass-averaged in the pitchwise direction. A specified number of endwall cells can be excluded from the mass-averaging calculation if desired (see Section 5.2.1). All modifications made to CENTREPOINT in the course of the present research are detailed in Appendix I.

Chapter 6
PRESENTATION AND DISCUSSION OF RESULTS

This chapter presents both the computational and experimental results. In Section 6.1, the experimental results obtained from a linear turbine cascade at large clearances will be discussed. In light of these new data, the accuracy of some existing tip-leakage models will be evaluated at extended clearances. Section 6.2 presents the results of a complementary computational investigation conducted using a three-dimensional Navier-Stokes solver (BTOB3D) developed by Dawes (1986a).

6.1 Experimental Results

Typically, unshrouded turbines are designed with tipgap heights on the order of 1 to 2% of the blade chord; however, as a result of in-service damage, considerably larger clearances may occur. The present work, which is motivated by Engine Health Monitoring (EHM), examines turbine blades with tip clearances of up to 15% of chord, in a cascade which has previously been used to study tip-leakage flow at smaller clearances. Although tip damage can include rounding of the blade tip in both the chordwise and tangential directions, these effects were not considered in the study, making it somewhat idealized. For the purposes of the following experiments, the tip damage was taken to consist simply of a clearance gap opened to unusually large values.

6.1.1 Total-Pressure Loss and Flow Angle Distributions

6.1.1.1 Averaging Procedures and Experimental Uncertainty

To interpret the flow physics and obtain results that can be compared at various axial planes, total pressure losses and other flow quantities of interest need to be expressed in mass-averaged form. This mass-averaging should be performed over the same mass flow rate, ideally over the same streamtube, at each measurement plane. Typically, the measurement plane extends one blade spacing in the pitchwise direction and over a spanwise extent large enough to contain the flow structure of interest. Moore & Adhye (1985), who investigated secondary flows downstream of a turbine, mass averaged over one blade pitch and ½ span. Bindon (1989), on the other hand, found that mass averaging over an area of one blade pitch by ¼ chord in the spanwise direction was sufficient to include the entire extent of the tip-leakage fluid that he was studying.

In the present study, the flow quantities are averaged over a reference mass flow rate, $\dot{m}_{ref}$, which corresponds to inlet free stream fluid passing through an area one pitch high and 60% of span wide. This area was found to correspond to a streamtube large enough to contain the flow structures of interest, namely, the tip-leakage vortex and tipwall passage vortex. Similar reference mass flow rates were used by Yaras & Sjolander (1989) and Chan *et al.* (1994) when examining tip-leakage flows at smaller clearances in the current cascade. The resulting expression for the mass-averaged total pressure coefficient then takes the form:

$$C_{P_o}'' = \frac{\iint C_{P_o} \rho V_x dy' dz}{\dot{m}_{ref}} \tag{6.1}$$

while the mass-averaged outlet flow angle is given by:

$$\alpha'' = \tan^{-1}\left(\frac{\iint \rho V_x V_y dy' dz}{\iint \rho V_x^2 dy' dz}\right) \tag{6.2}$$

The mass flow rates measured in the downstream plane were found to be from 2 to 12% less than the reference mass flow rate, for 15 and 10% clearance, respectively. This implies that the full extent of the inlet streamtube was not captured at the downstream measurement plane. The deficit in mass flow rate can be attributed to the blockage effect of the tip-leakage and secondary flow structures which induces a spanwise displacement of fluid away from the tipwall. This displaced flow can reasonably be assumed to be made up predominantly of free stream fluid. When mass-averaging at the downstream plane, it was required to *top up* the measured mass flow with loss free fluid until the reference mass flow rate was reached. Therefore, an appropriate amount of loss-free mass flow is added to the numerator in Equation 6.1 so that the integration is effectively over the reference mass flow at each clearance.

It is often convenient to do a local pitchwise mass-averaging in order to evaluate the spanwise distributions of the flow quantities. The pitchwise mass-averaged total-pressure coefficient and flow angle are defined below:

$$C_{P_o}' = \frac{\int_0^1 C_{P_o} \rho V_x d\left(\frac{y'}{S}\right)}{\int_0^1 \rho V_x d\left(\frac{y'}{S}\right)}$$

$$\alpha' = \tan^{-1}\left(\frac{\int_0^1 \rho V_x V_y d\left(\frac{y'}{S}\right)}{\int_0^1 \rho V_x^2 d\left(\frac{y'}{S}\right)}\right) \tag{6.3}$$

It is difficult to quantify the uncertainty associated with the mass-averaged quantities. This uncertainty results from probe measurement errors (discussed in Section 3.4.4), flow resolution error due to the finite number of sampled points, the averaging technique, and fouling of the screens in the settling chamber. Based on repeatability tests, the mass-averaged total pressure coefficients at the inlet plane are estimated to be accurate within ±0.01. Because of the larger shear effects downstream of the blade row and the increased uncertainty associated with the seven-hole probe, the mass-averaged total pressure quantities at this plane are conservatively estimated at ±0.02.

6.1.1.2 Inlet and Profile Losses

As discussed in Section 4.3.1, the inlet boundary-layer profiles were determined from pitot-probe traverses made 1.1 axial-chord-lengths upstream of the blade leading-edge. At this plane, the only total-pressure deficit present in the outer half of the cascade is that in the tipwall boundary layer. Because of the uniformity of the inlet flow, the mass-averaged total-pressure deficit for the plane was inferred from a single spanwise traverse.

Location	Mass-Averaged Flow Property	Clearance Size τ/c		
		0.00	0.10	0.15
Inlet	C_{Po}'' *(inlet)*	-0.044	-0.051	-0.080
Midspan	α' (deg)	-47.4	-47.4	-49.2
	C_{Po}' *(profile)*	-0.042	-0.049	-0.045
Mixed-out	C_{Po}' *(profile)*	-0.044	-0.050	-0.047

Table 6.1 Calculated inlet and profile losses.

The results quoted in Table 6.1 show an increase in the inlet mass-averaged loss coefficient with increasing clearance. This trend can be explained by the successive thickening of the tipwall boundary-layer, which results from the adverse pressure gradient induced as the ramp slope is increased to accommodate the larger clearances (see Section 3.2).

The blade profile losses were determined using three-hole probe traverses made at a plane 0.475 axial-chord-lengths downstream of the blade trailing edge, henceforth referred to as Plane A. The losses were then calculated using a local pitchwise mass-averaging of the total-pressure deficit (Equation 6.3) through the wakes at midspan. Table 6.1 cites both the fully mixed-out profile losses (see Section 6.1.1.5 for a discussion on the mixing calculations) and the values measured at Plane A. It is evident that there is little loss associated with the mixing of the wake. This is in agreement with the results of Goobie (1989) who found the diffusion losses of the wake to be small.

6.1.1.3 Downstream Losses

All downstream measurements were obtained at Plane A using the seven-hole probe (described in Section 3.4.3). The probe was traversed on the staggered grid shown schematically in Figure 6.1. This measurement grid extended from the tipwall to roughly 60% of span, and covered 1.33 blade spacings in the pitchwise direction.

Figures 6.2 to 6.4 present contours of the total pressure coefficient measured at Plane A for clearances of 0, 10 and 15% of the blade chord. The extent of the secondary flow present at Plane A, in the absence of clearance, is clearly illustrated in Figure 6.2. The figure indicates that although the passage vortex is reasonably large it is quite weak. This is likely due to the relatively low flow turning (approx. 50°) of the present cascade.

Figures 6.3 and 6.4 show that the flow field near the endwall region is considerably changed with clearance. In both figures a large, roughly-axisymmetric

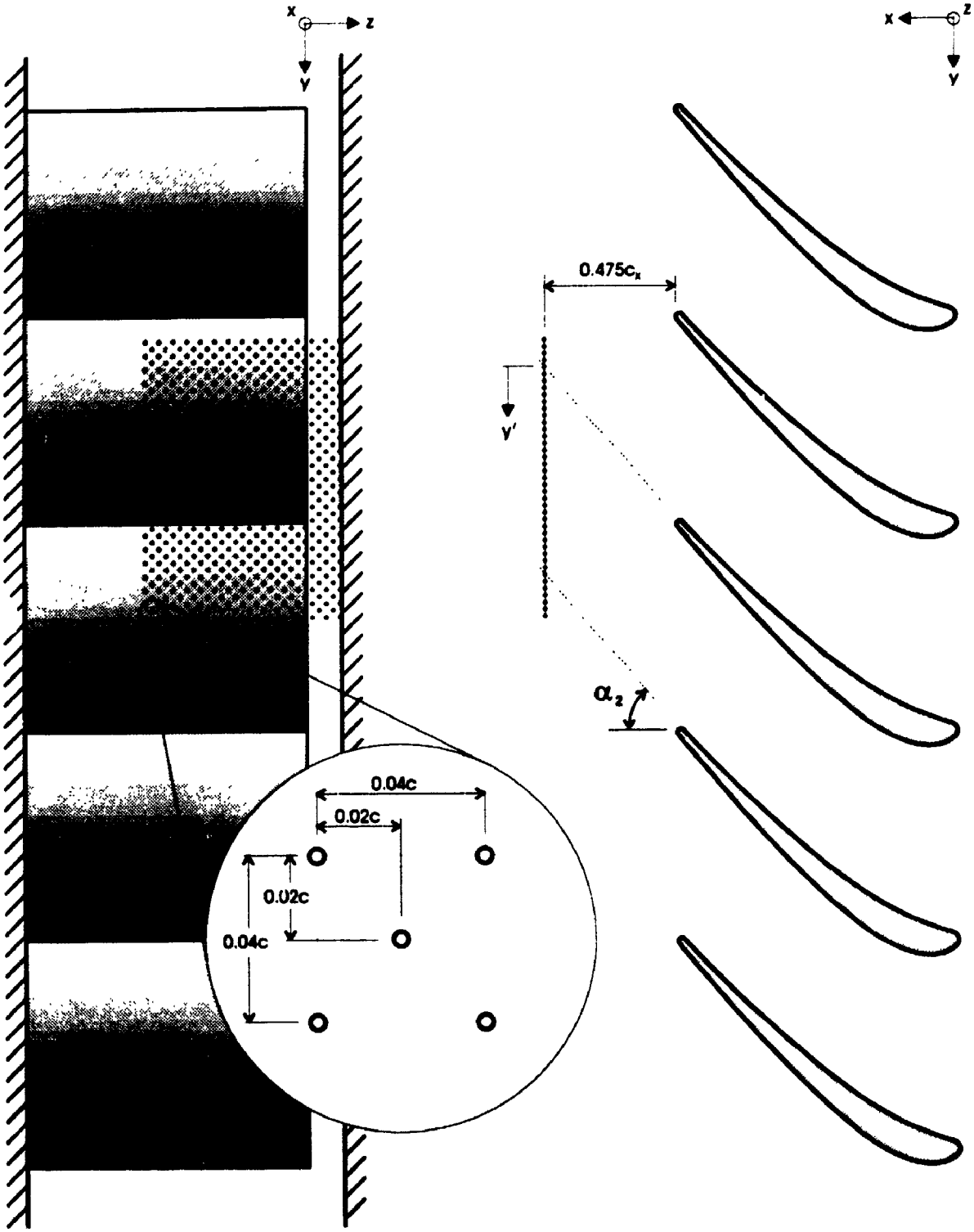

Figure 6.1 Schematic of the downstream measurement grid.

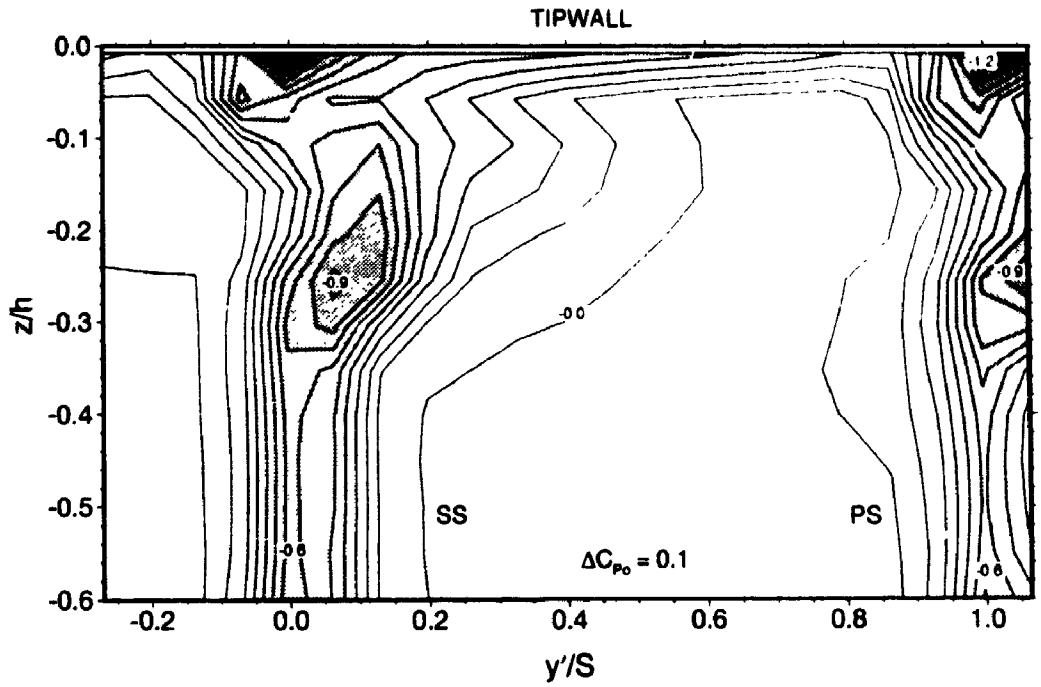

Figure 6.2 Contours of the total-pressure coefficient measured at Plane A for $\tau/c = 0.00$.

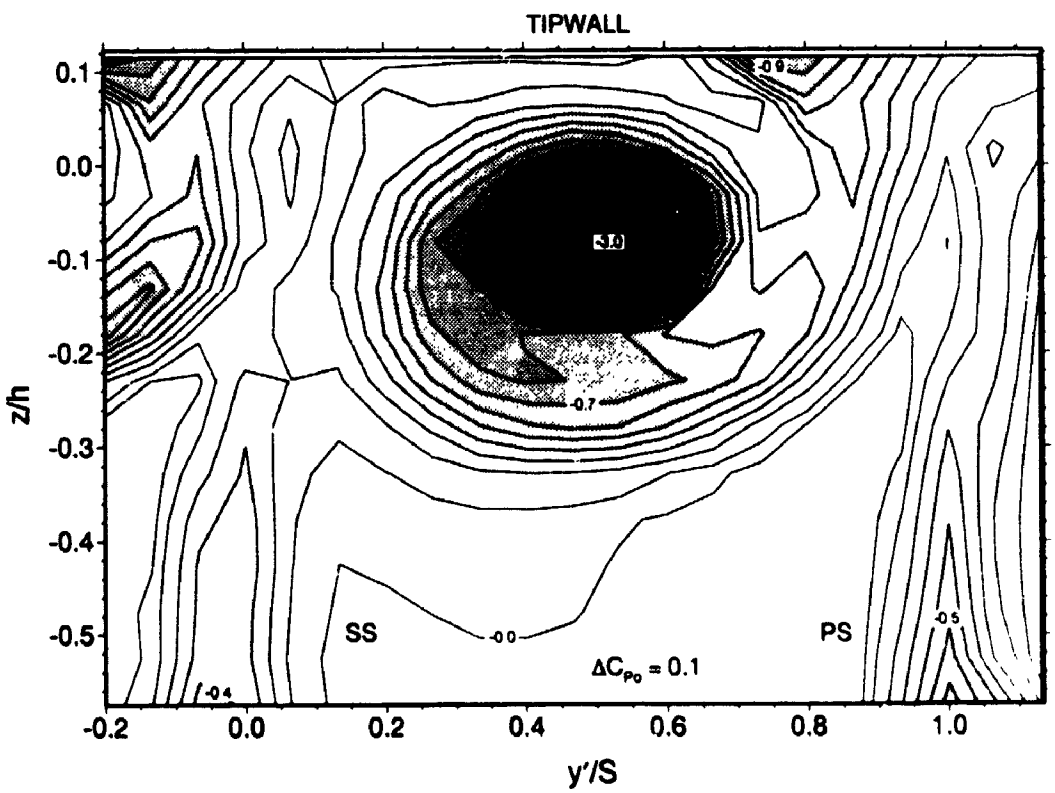

Figure 6.3 Contours of the total-pressure coefficient measured at Plane A for $\tau/c = 0.10$.

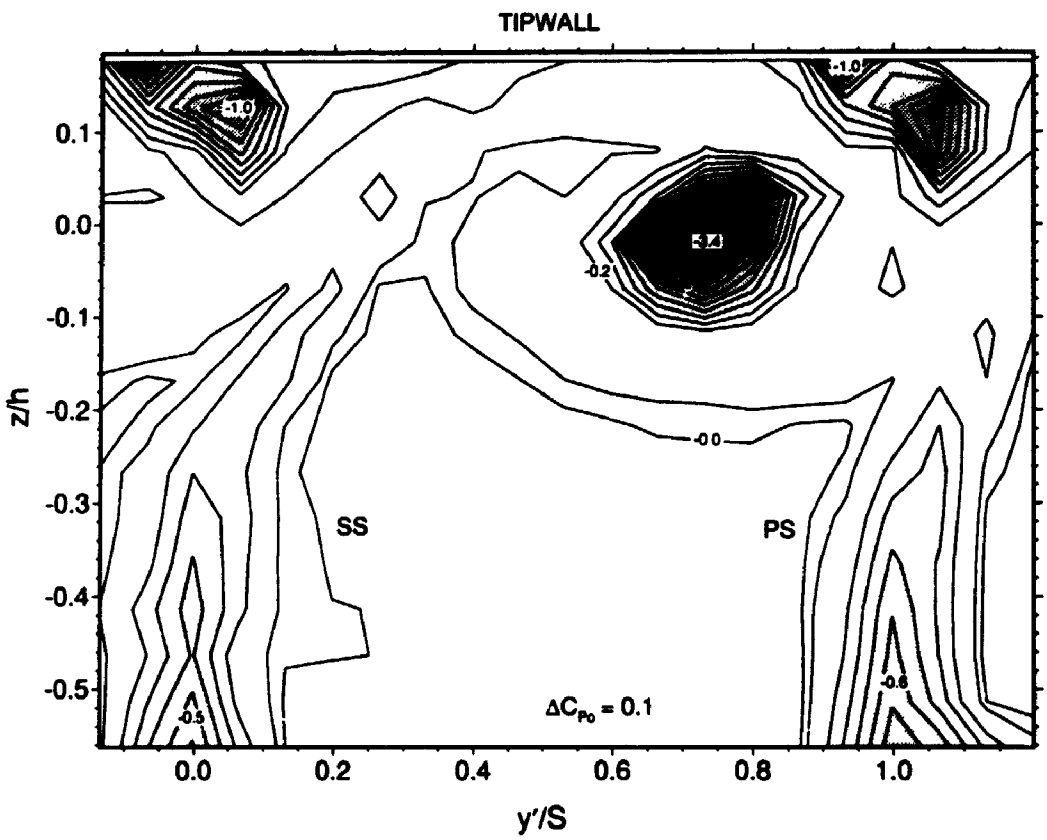

Figure 6.4 Contours of the total-pressure coefficient measured at Plane A for $\tau/c = 0.15$.

region of high loss is observed. Typically, this region has been identified as the tip-leakage vortex. At 10% clearance, the loss structure is observed to extend from blade wake to blade wake and its spanwise growth appears to have displaced the loss core inwards of the blade tip. On the endwall, above the core of tip-leakage vortex, the remnants of the passage vortex are just discernible. At 15% clearance, the size of the tip-leakage vortex has diminished. However, the flow structure on the endwall (discussed in more detail in Section 6.1.2.2) appears to have been strengthened.

Comparing Figures 6.3 and 6.4, one observes that the tip-leakage vortex core has moved closer to the pressure surface at 15% clearance, implying that the pitch angle of the vortex centreline has decreased relative to the midspan flow angle as the gap size was increased from 10 to 15% clearance. Yaras (1990) observed a similar trend at smaller clearances. He concluded that the increased mass flow rate associated with larger clearances resulted in a larger momentum normal to the blade chord, which, in turn, drives the tip vortex farther away from the blade suction surface. However, this conclusion appears to be inconsistent with the current results at large clearances. It will be shown in Section 6.1.5 that the momentum normal to the chord decreased as the gap was opened to extended clearances. The results, therefore, appear to indicate that the tip-leakage vortex experienced a reduced blade-to-blade pressure gradient near the blade tip at 15% clearance.

Figure 6.5 shows the spanwise variation of the pitchwise-mass-averaged total-pressure deficit for each of the three clearances. It is evident from the plot that the spanwise region of influence of the tip-leakage vortex is significantly smaller at 15% clearance. In fact, at this clearance the losses appear to be substantially reduced and are comparable to the zero clearance measurements. A discussion of the possible mechanisms which result in this unexpected and intriguing reduction in losses at large clearances is deferred until the blade-surface and endwall static pressures have been presented.

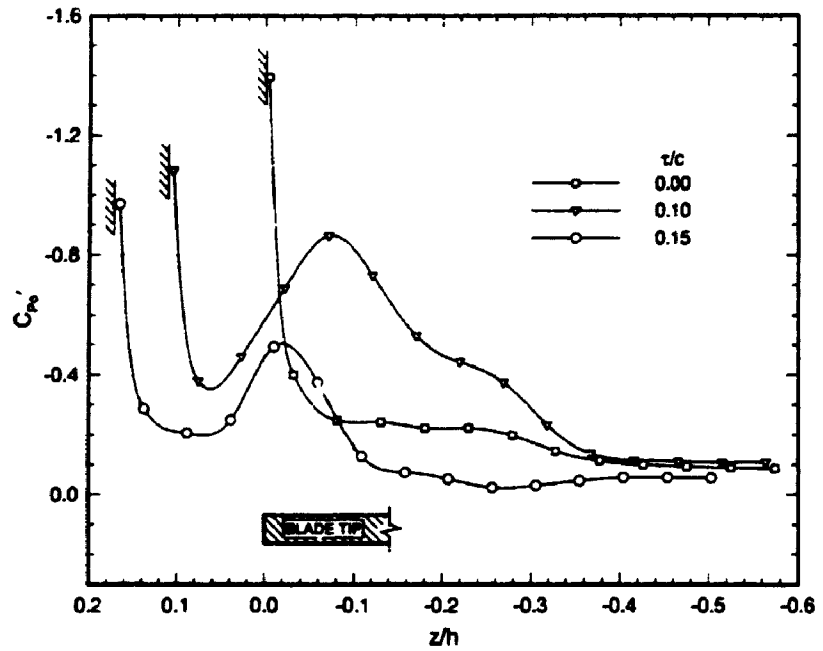

Figure 6.5 Spanwise distribution of the total-pressure deficit at Plane A.

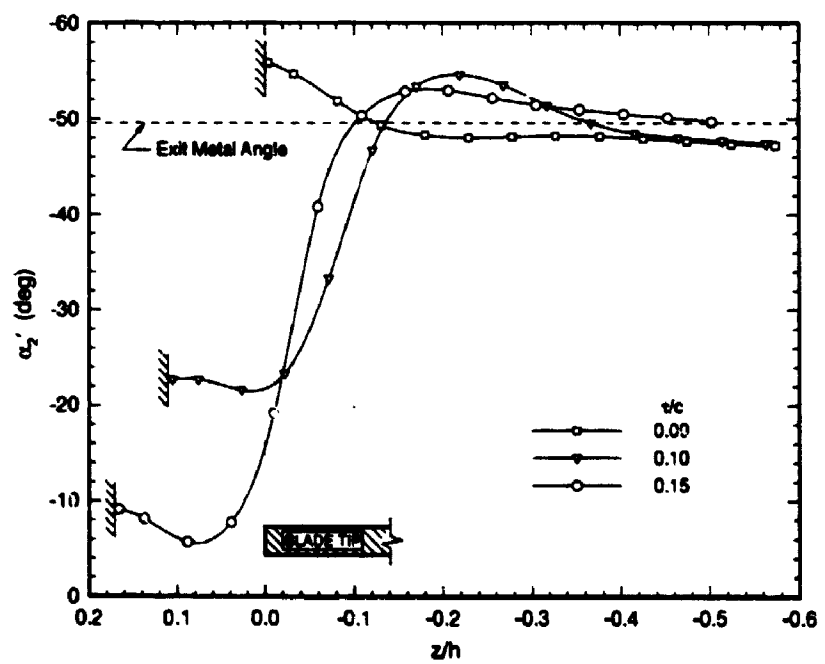

Figure 6.6 Spanwise distribution of the outlet flow angle at Plane A.

6.1.1.4 Main-Flow Underturning and Redistribution of Mass Flow

The behaviour of a blade row with tip damage will be determined not only by the changes in the observed losses but also by the changes in the flow-turning characteristics of the blade. Figure 6.6 shows the spanwise distribution of the pitchwise mass-averaged outlet flow angle for 0, 10 and 15% clearance. At zero clearance, there is a noticeable overturning of the flow near the endwall that is characteristic of the passage vortex. Some researchers, i.e., Gregory-Smith *et al.* (1988), have observed behind their high-turning cascades an attenuation of this overturning close to the endwall which they attribute to the corner vortex. The lack of this attenuation in the present measurements would seem to indicate that for the present cascade the corner vortex must be weak. When the clearance is opened, a large region of flow underturning is observed near the endwall. At 10% clearance, the leakage flow is turned only about half as much as the main flow, while at 15% clearance most of the gap fluid experiences little turning (approx. 8°) and passes through the cascade as a jet flow. Well away from the endwall region, the flow turning is essentially unchanged.

The static pressure at the outlet of the blade row is determined essentially by the turning of the main flow. Since the leakage jet experiences less turning, its axial velocity must increase to match the static pressure drop experienced by the main flow as it is accelerated through the turbine blade row. This implies that the mass flow must be redistributed across the passage span from its essentially uniform distribution well upstream of the blades. The redistributed mass flow is shown in Figure 6.7, which presents the spanwise variation in the outlet axial velocity normalized by the mass-averaged value for each distribution. The effect is observed to be quite substantial, particularly at the largest clearance where the axial velocity of the gap flow is approximately 30% greater than the mean value, while away from the tip the axial velocity is reduced by about 20%. It should be noted that this effect is a function of the clearance-to-span ratio. Therefore, the trend with clearance observed in Figure 6.7 for the relatively low aspect ratio of the current cascade row should not be generalized.

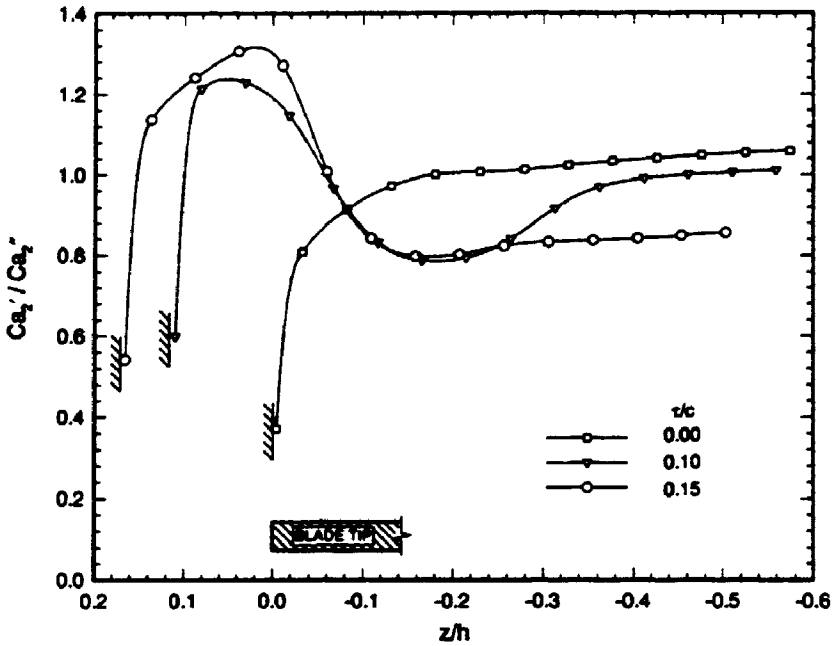

Figure 6.7 Spanwise distribution of the axial velocity at Plane A.

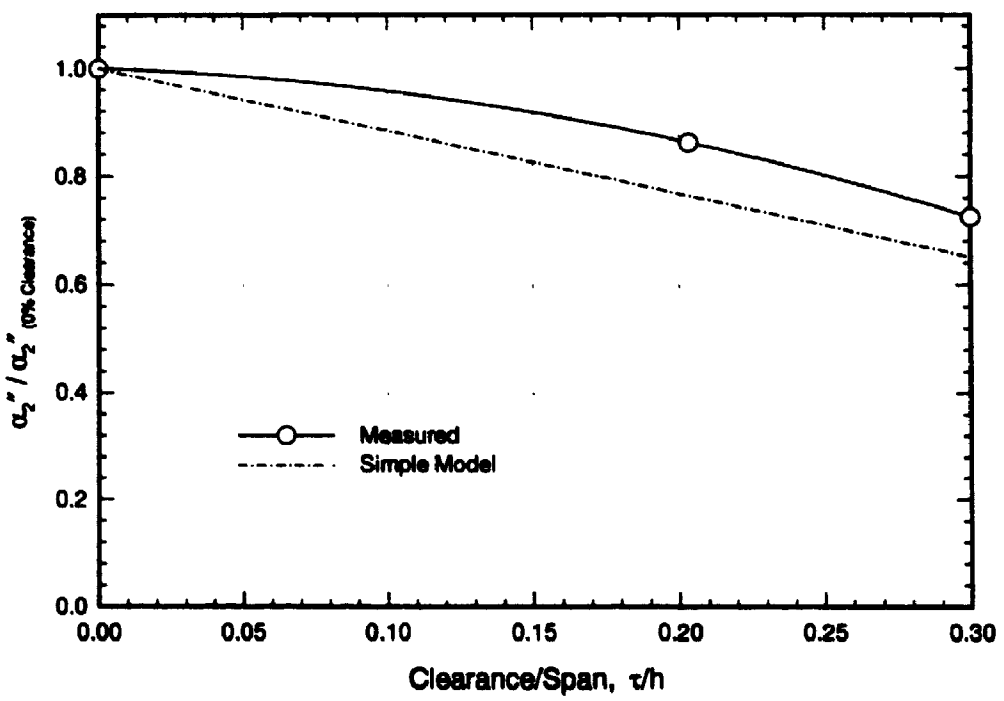

Figure 6.8 Variation of the mass-averaged outlet flow angle with clearance (Plane A).

Figure 6.8 plots the variation of the fully mass-averaged outlet flow angle (normalized by the zero-clearance value) with the clearance-to-span ratio. As noted earlier, all mass-averaged quantities are based on the mass flow over 60% of span. Therefore, this was the effective *span* used to normalize the clearance in the τ/h term, rather than the physical span of the blade. It can be seen that the overall reduction in the blade flow-turning can become quite large at extended clearances.

Appendix J details the derivation of a simple model for predicting the underturning at large clearances. The model, which assumes that all the fluid passing through the gap experiences no tangential force, uses a simple control volume formulation to calculate the mass-averaged outlet flow angle. Knowing the inlet velocity, C_1, inlet flow angle, α_1, the nominal (zero clearance) outlet flow angle, α_2, and the clearance-to-span ratio, κ, it is possible to express the mass-averaged outlet flow angle at extended clearances as:

$$\alpha_2'' = \tan^{-1}\left(\left(\frac{1}{1-\kappa}\right)\left[1-\kappa\left(\frac{Ca_{2g}}{Ca_1}\right)\right]^2 \tan\alpha_2 - \kappa\left(\frac{Ca_{2g}}{Ca_1}\right)\tan\alpha_1\right) \tag{6.4}$$

with

$$\frac{Ca_{2g}}{Ca_1} = \frac{-b \pm \sqrt{b^2 - 4ac}}{2a}$$

where

$$a = 1 - \frac{\kappa^2}{\cos^2\alpha_2}\left(\frac{1}{1-\kappa}\right)^2$$

$$b = \frac{2\kappa}{\cos^2\alpha_2}\left(\frac{1}{1-\kappa}\right)^2$$

$$c = \frac{1}{\cos^2\alpha_1} - 1 - \frac{1}{\cos^2\alpha_2}\left(\frac{1}{1-\kappa}\right)^2$$

The variation of the predicted outlet flow angle, for the present cascade, is also included in Figure 6.8. Agreement with the experimental results is acceptable, especially

at the largest clearance where the assumption that the gap flow experiences no tangential force is found to be most valid.

6.1.1.5 Mixing Calculations

By applying the continuity and momentum equations between the measurement plane (Plane A) and a downstream plane where the flow is assumed to be fully mixed-out, it is possible to calculate the additional mixing losses. This diffusion is assumed to occur at constant area, under incompressible conditions, until uniform static pressure and streamwise velocity are achieved. The choice of a control volume which extends over the entire blade pitch provides periodic side boundaries. The resultant expressions for mixed-out velocity, static pressure coefficient and total pressure loss coefficient, derived by Yaras (1990), are given below:

$$\frac{V_{mixed}}{V_{CL}} = \frac{1}{A_{mixed}} \int_{A_{mixed}} \left(\frac{V_{Plane\,A}}{V_{CL}} \right) dA$$

$$C_{P_{mixed}} = \frac{1}{A_{mixed}} \left\{ \int_{A_{mixed}} C_P \, dA - 2 \left(\frac{V_{mixed}}{V_{CL}} \right)^2 A_{mixed} + 2 \int_{A_{mixed}} \left(\frac{V_{Plane\,A}}{V_{CL}} \right)^2 dA \right\} \tag{6.5}$$

$$C_{P_{o\,mixed}} = C_{P_{mixed}} + \left(\frac{V_{mixed}}{V_{CL}} \right)^2 - 1$$

with

$$dA = dy\, dz \cos\alpha''$$

where A_{mixed} is the area of the control volume exit plane measured perpendicular to the streamwise direction and α'' is the mass-averaged outlet flow angle.

Although the control volume in the previous analysis extends to the endwall, the force due to the wall shear stress was not included in the momentum balance. Yaras &

Sjolander (1989) found that this term was significant near the trailing edge of their blade row at smaller clearances. They concluded that the tip-leakage vortex amplified the velocity gradients on the endwall and hence increased the entropy production in the endwall boundary layer. However, recalling Figure 6.5, no increase in the endwall loss is noted with clearance; in fact, a decrease is observed. This would seem to indicate that the wall shear stress term is small by Plane A and can likely be neglected in the mixing calculations without incurring serious error.

As a final note, it should be mentioned that the mixed-out losses, tabulated in the following section, are used solely as a convenience for presenting and comparing cascade results. A completely uniform mixed-out flow is not representative of what happens in a real turbomachine, where variations in the flow will certainly remain at the entry to the next blade row.

6.1.1.6 Conventional Loss Breakdown

Having identified all the different loss sources upstream and downstream of the cascade, it is now possible to do a comparison of the relative magnitudes of each. Conventionally, the inlet losses are subtracted from the downstream loss measurements to give the net loss across the blade row. The implicit assumption that the inlet losses convect through the passage without causing additional losses is supported by data compiled by Sharma & Butler (1987), and more recently by Chan *et al.* (1994). The profile loss, which is assumed constant over the entire blade span at the midspan value, is then subtracted from the zero clearance net loss to give the secondary loss. Finally, at non-zero clearances, the tip-leakage loss is calculated by subtracting both the profile loss and the zero clearance secondary loss from the resultant net loss at clearance.

The subdivision of losses outlined above is undoubtedly open to criticism. Yamamoto (1988), Yaras & Sjolander (1992a), and Chan *et al.* (1994) all found that the secondary losses measured downstream of their blade rows varied with clearance. These

results evidence a strong interaction between the tip-leakage vortex and the passage vortex not accounted for by the conventional breakdown. Likewise, the effect of tip leakage on the loading near the blade tip, studied by Sjolander & Amrud (1987) and Storer & Cumpsty (1991), will alter the profile losses associated with the boundary layers in this region. Recognizing these shortcomings, Table 6.2 presents the results for the current measurements.

Location	Mass-Averaged Flow Property	Clearance Size τ/c		
		0.00	0.10	0.15
Inlet	C_{Po}'' *(inlet)*	-0.044	-0.051	-0.080
Plane A	α'' (deg)	-48.7	-42.0	-35.3
	q_2''/q_1''	2.17	1.56	1.78
	C_{Po}' *(profile)*	-0.042	-0.049	-0.045
	C_{Po}'' *(secondary)*	-0.085	-0.085	-0.085
	C_{Po}'' *(tip-leakage)*	-----	-0.176	0.024
	C_{Po}'' *(endloss)*	-0.085	-0.261	-0.061
	C_{Po}'' *(total)*	-0.172	-0.361	-0.186
Mixed-out	C_{Po}' *(profile)*	-0.044	-0.050	-0.047
	C_{Po}'' *(secondary)*	-0.109	-0.109	-0.109
	C_{Po}'' *(tip-leakage)*	-----	-0.291	-0.045
	C_{Po}'' *(endloss)*	-0.109	-0.400	-0.154
	C_{Po}'' *(total)*	-0.198	-0.501	-0.282

Table 6.2 Total-pressure coefficients obtained using the conventional loss-breakdown method.

The endloss[1] (secondary loss + tip-leakage loss) for various clearances is plotted in Figure 6.9. The earlier results of Yaras & Sjolander (1990) and Chan *et al.* (1994), who studied clearances of up to 5.5% of chord, are also included in the plot. The results of Chan *et al.* (1994) were also obtained at Plane A, and so, are directly comparable. To allow comparison with the results of Yaras & Sjolander (1989), which were obtained at a different traverse plane, the fully mixed-out losses are also presented. Where the three studies overlap, the results are seen to be consistent with each other.

Figure 6.9 highlights the physical inconsistency of the conventional loss breakdown. As the clearance is first opened, the endloss is observed to increase up to about 7% clearance; beyond this clearance, the endloss is found to decrease. At 15% clearance, the combined secondary and tip-leakage losses are essentially the same as the secondary losses measured at zero clearance. It is clear that physically implausible results are obtained if the secondary and tip-leakage loss components are decomposed in the usual way; in fact, this would lead to negligible or even negative tip-leakage losses at extended clearances. An alternate loss breakdown method based on the streamwise vorticity field will be presented in Section 6.1.2.3.

[1] The endloss term, which is representative of the mass-averaged loss generated in the tip region due to three-dimensional flow effects, avoids the uncertainty associated with the conventional subdivision of losses.

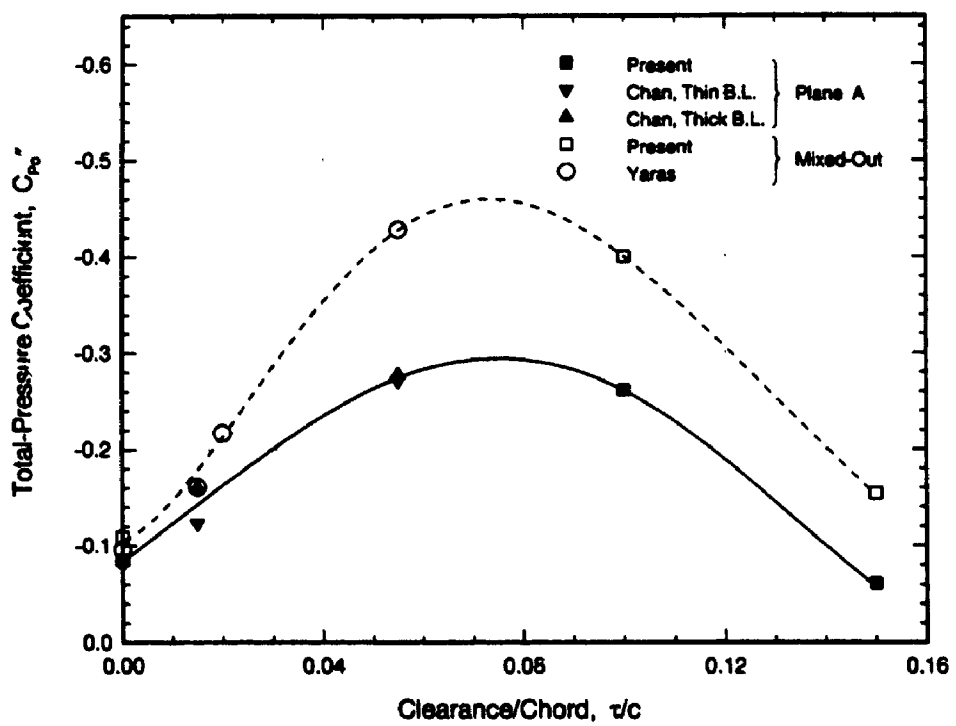

Figure 6.9 Variation of the endloss with clearance.

6.1.2 Streamwise Vorticity Field

Vorticity has been used by many researchers (e.g., Inoue & Kuroumaru (1989), Gregory-Smith *et al.* (1988), Harrison (1989), Walsh & Gregory-Smith (1990), Yaras & Sjolander (1990,1992b), Kang & Hirsch (1993b), and Chan *et al.* (1994)) to study the three-dimensional flow structures downstream of the blade row. It is especially effective in studying vortical structures with opposite senses of rotation which would appear merged if viewed in terms of more conventional parameters such as total pressure. To this author's knowledge, Harrison (1989) was the first to quantitatively isolate loss components using the streamwise vorticity field measured downstream of a high-turning cascade. The following section defines vorticity and outlines the equations used to experimentally calculate its components downstream of the blade row.

6.1.2.1 Calculation of Streamwise Vorticity

The vorticity vector $\boldsymbol{\omega}$ is defined as the curl of the velocity vector $\mathbf{V}$

$$\boldsymbol{\omega} = \nabla \times \mathbf{V} \tag{6.6}$$

For a Cartesian coordinate system, as shown in Figure 6.1, having x, y, z in the axial, pitchwise, and spanwise directions, respectively, the components of vorticity are:

$$\begin{aligned} \omega_x &= \frac{\partial w}{\partial y} - \frac{\partial v}{\partial z} \\ \omega_y &= \frac{\partial u}{\partial z} - \frac{\partial w}{\partial x} \\ \omega_z &= \frac{\partial v}{\partial x} - \frac{\partial u}{\partial y} \end{aligned} \tag{6.7}$$

It is evident from Equation 6.7 that the x-component of vorticity can be evaluated directly from the measurements within Plane A. However, the calculation of the axial velocity

gradients $\partial w/\partial x$ and $\partial v/\partial x$ incorporated in the y- and z-components of vorticity would require measurements in at least two closely spaced y-z planes. An alternative is to use Crocco's equation which provides the relationship between vorticity and entropy:

$$\frac{\partial \mathbf{V}}{\partial t} - \mathbf{V} \times \boldsymbol{\omega} = T\nabla s - \nabla H \tag{6.8}$$

where $H = h + \frac{1}{2}V^2$. For steady, adiabatic flows the above equation reduces to:

$$\mathbf{V} \times \boldsymbol{\omega} = \frac{1}{\rho}\nabla P_o$$

From the resultant pitchwise component

$$w\,\omega_x - u\,\omega_z = \frac{1}{\rho}\frac{\partial P_o}{\partial y}$$

and spanwise component

$$u\,\omega_y - v\,\omega_x = \frac{1}{\rho}\frac{\partial P_o}{\partial z}$$

it is possible to isolate ω_y and ω_z to obtain

$$\begin{aligned} \omega_y &= \frac{1}{u}\left(v\,\omega_x + \frac{1}{\rho}\frac{\partial P_o}{\partial z}\right) \\ \omega_z &= \frac{1}{u}\left(w\,\omega_x - \frac{1}{\rho}\frac{\partial P_o}{\partial y}\right) \end{aligned} \tag{6.9}$$

with ω_x given by Equation 6.7.

Yaras (1990) verified the applicability of the above equations to the downstream flow. He observed that the vorticity obtained using two closely spaced measurement planes (employing Equation 6.7) was in excellent agreement with the vorticity calculated

using Equation 6.9. The largest differences were found to occur near the edge of the tip-leakage vortex core where the velocity gradient was changing most rapidly and the viscous effects were most important. However, even there, the maximum observed deviation was found to be less than 10% of the vortex centreline streamwise vorticity.

The non-dimensional vorticity components can be expressed as follows:

$$\omega_x' = \frac{\partial(w/V_{CL})}{\partial(y/c)} - \frac{\partial(v/V_{CL})}{\partial(z/c)}$$

$$\omega_y' = \frac{1}{(u/V_{CL})}\left[\frac{v}{V_{CL}}\omega_x' + \frac{1}{2}\frac{\partial C_{P_o}}{\partial(z/c)}\right] \tag{6.10}$$

$$\omega_z' = \frac{1}{(u/V_{CL})}\left[\frac{w}{V_{CL}}\omega_x' - \frac{1}{2}\frac{\partial C_{P_o}}{\partial(y/c)}\right]$$

with length scales non-dimensionalized by the blade chord, velocities by the cascade inlet centreline velocity, and the total pressure by the inlet centreline dynamic pressure. The differential terms in these equations were evaluated using central differencing, except at the boundaries of the measurement plane where one-sided differencing was used.

Having defined the x- and y-components of vorticity, the streamwise vorticity can be evaluated using the following expression:

$$\omega_s' = \omega_x' \cos\alpha'' + \omega_y' \sin\alpha'' \tag{6.11}$$

where α'' is the mass-averaged outlet flow angle given by Equation 6.2.

6.1.2.2 Downstream Vorticity Field

Figures 6.10 to 6.12 show contours of the positive and negative streamwise vorticity flooded over the total-pressure coefficient contours for 0, 10 and 15% clearance.

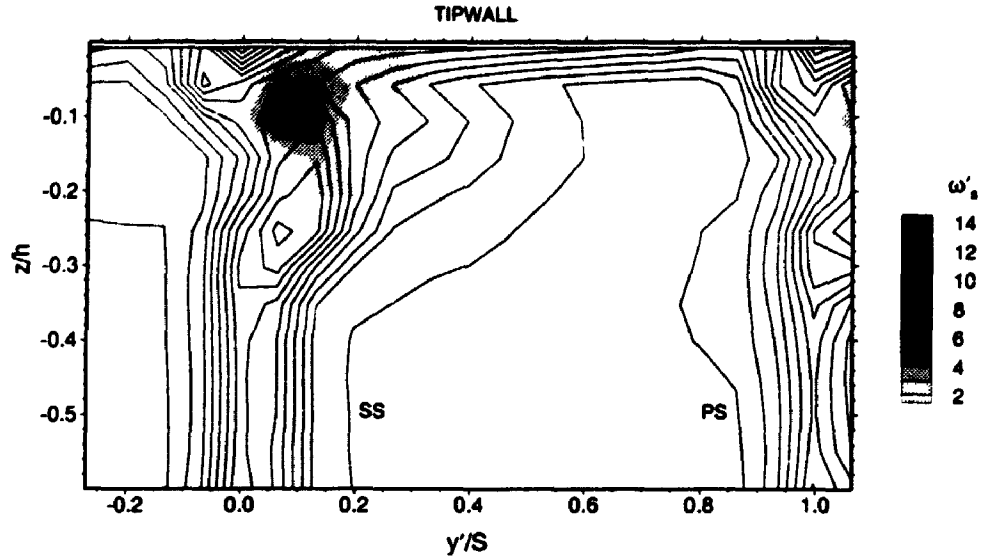

a) Positive streamwise vorticity.

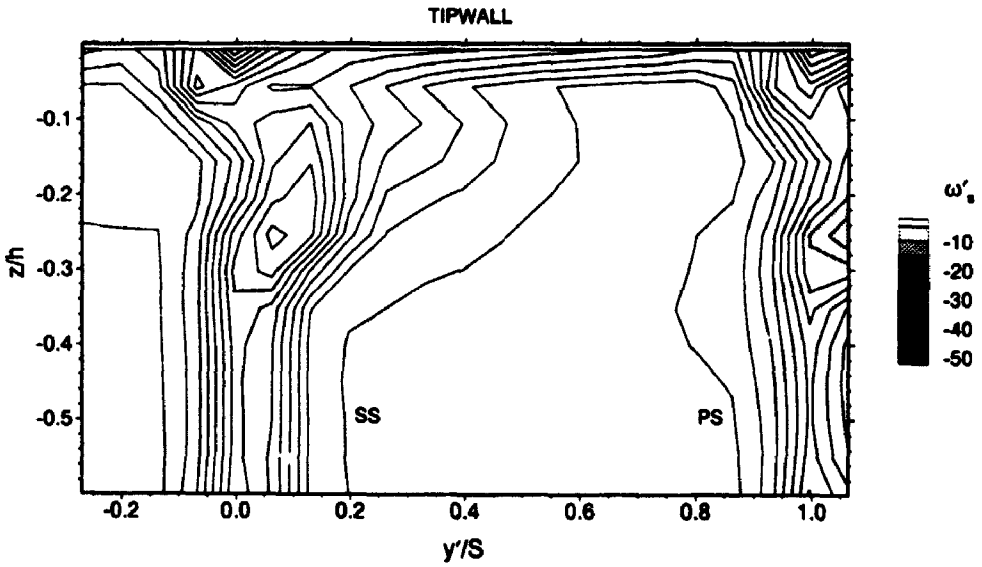

b) Negative streamwise vorticity.

Figure 6.10 Flooded regions of positive and negative streamwise vorticity for $\tau/c = 0.00$. [Superimposed on contours of the total-pressure coefficient at Plane A].

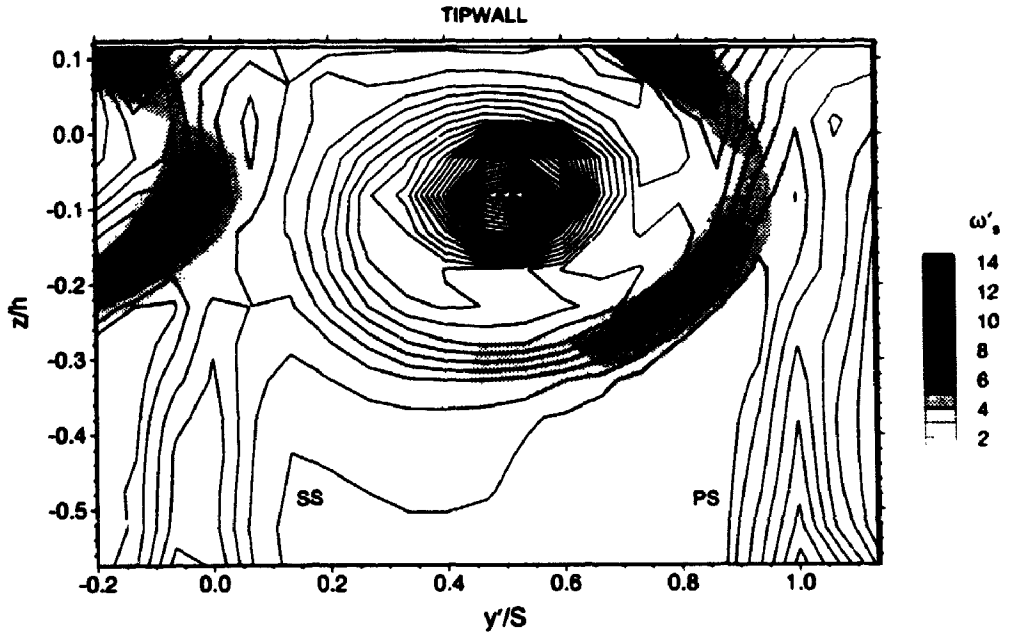

a) Positive streamwise vorticity.

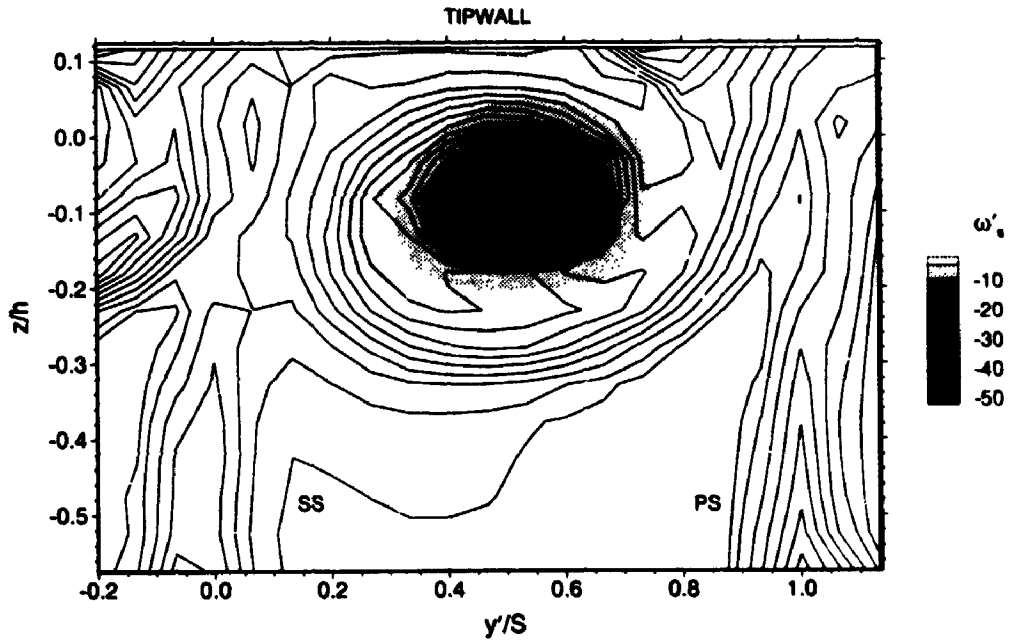

b) Negative streamwise vorticity.

Figure 6.11 Flooded regions of positive and negative streamwise vorticity for $\tau/c = 0.10$. [Superimposed on contours of the total-pressure coefficient at Plane A].

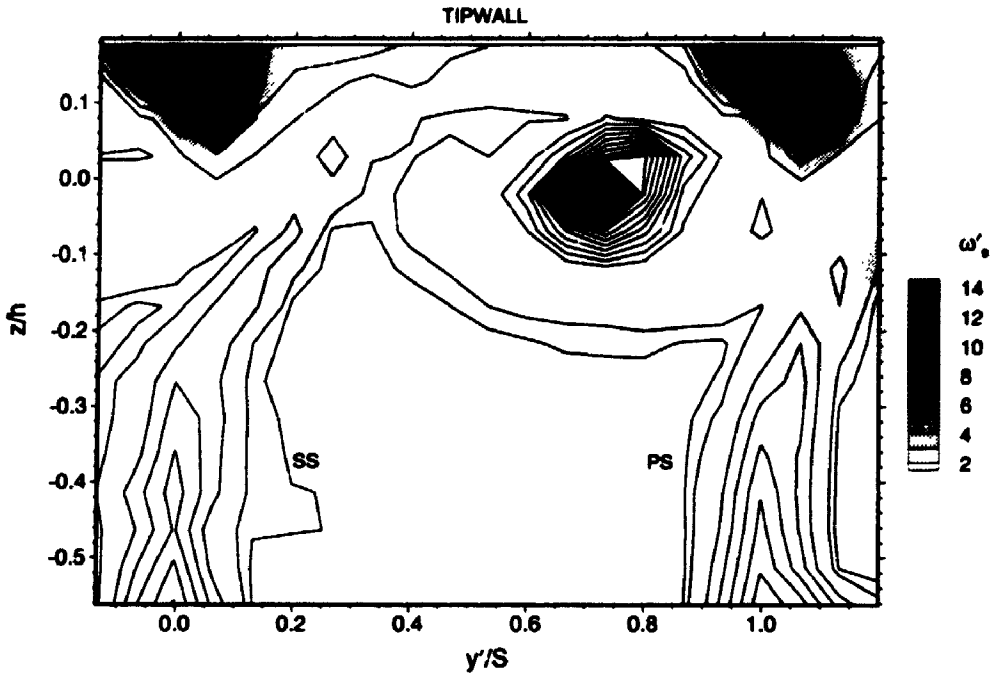

a) Positive streamwise vorticity.

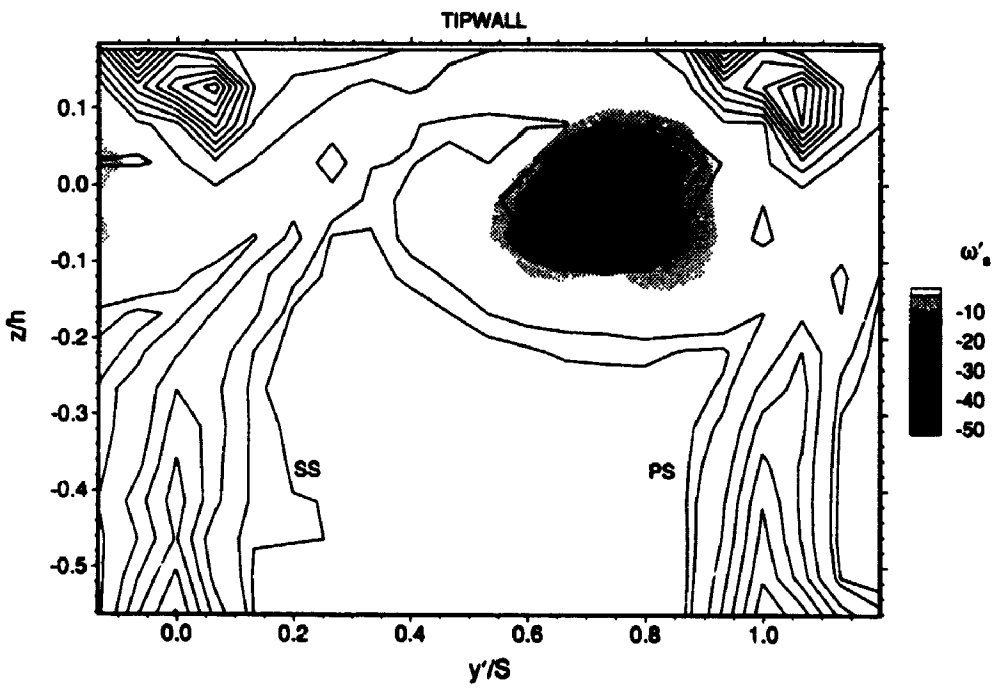

b) Negative streamwise vorticity.

Figure 6.12 Flooded regions of positive and negative streamwise vorticity for $\tau/c = 0.15$. [Superimposed on contours of the total-pressure coefficient at Plane A].

The same contour interval is used in all three plots to allow quick comparison between each figure.

At zero clearance (Figure 6.10), the passage vortex is identified by a region of relatively high positive vorticity observed to lie near the endwall/suction side corner. At the base of the blade wake, on the endwall, a small corner vortex is noticeable.

The large region of negative vorticity fluid associated with the tip-leakage vortex dominates the outer half of the passage at 10% clearance (Figure 6.11). The passage vortex, identified by its sign of positive vorticity, is displaced from its zero clearance (endwall/suction-side corner) position and now lies much closer to the pressure-surface corner. A band of positive vorticity fluid, entrained from both the endwall boundary layer and passage vortex, appears to wrap itself about the leakage vortex. In fact, this figure illustrates that much of the loss that has typically been associated with the tip-vortex structure is actually composed of this positive vorticity fluid which has been entrained from the endwall. The mixing of these two flows with opposite signs of vorticity is likely a significant source of loss production.

At 15% clearance (Figure 6.12), the interaction between the tip-leakage vortex and the endwall boundary layer appears to be negligible; the two flows are now separated by a region of low-loss fluid. As a consequence, the tip-leakage vortex is observed to be much smaller and composed exclusively of negative vorticity fluid. Data to be presented in Section 6.1.3.2 will show that the driving pressure difference across the tipgap decreased at the largest clearance, reducing the mass flow per unit area in the gap. In Section 6.1.5, it is demonstrated that this reduced driving pressure difference is the main reason for the observed reduction of the endloss at 15% clearance.

The flow on the endwall is clearly seen to be composed of positive vorticity fluid. Measurements show that the total-pressure deficit carried by this flow is only slightly larger than that measured in the inlet boundary layer. With the reduced blade-to-blade

pressure gradient experienced by the gap flow at large clearances, it is unlikely that much of this positive vorticity endwall fluid is attributable to the weakened passage vortex. Yaras & Sjolander (1989) found that for the clearances they examined (1.5 to 5.5% of blade chord) the inlet endwall boundary layer was largely mixed-out and inseparable from the secondary and tip-leakage fluid downstream of their cascade. This appears to be consistent with the present measurements at 10% clearance. However, at 15% clearance, the entrainment of endwall boundary layer fluid by the smaller tip-leakage vortex appears to be negligible, and apparently, the endwall flow structures are regions where the inlet endwall boundary layer fluid has accumulated.

6.1.2.3 Loss Component Breakdown Using the Streamwise Vorticity Field

As was noted earlier, the tip-leakage vortex and passage vortex contain vorticity of opposite signs. This feature of the streamwise vorticity field makes it useful for decomposing the downstream end losses. Chan *et al.* (1994) were the first investigators to separate the tip-leakage and secondary loss components measured downstream of their turbine cascade using the vorticity field.

Prior to decomposing the tip-leakage and secondary losses based on their signs of streamwise vorticity, the profile losses were removed from the downstream measurements. This was done by excluding grid cells visibly associated with the blade wakes from the downstream loss integration. The subsequent mass averaging of the total pressure deficit over the negative vorticity field provided the tip-leakage loss component along with the inlet deficit carried by that streamtube. Subtraction of this loss from the gross loss measured at Plane A (excluding the loss associated with the wake structures) resulted in the secondary loss component, together with the inlet loss convected by that streamtube. The removal of the inlet loss from the tip-leakage and secondary components was the final step in the process. As discussed in Section 6.1.2.2, the inlet loss was largely mixed-out between the tip-leakage and secondary loss structures at 10% clearance. However, it was concluded that at 15% clearance, most of the inlet loss was associated

with the positive vorticity flow on the endwall. Because of these different inlet loss distributions, two separate methods were used to remove the inlet total pressure deficit from the downstream components. The first, referred to as Method A, splits the mass-averaged inlet total pressure deficit between the secondary and tip-leakage flows in proportion to the mass flow associated with each. On the other hand, Method B assigns all of the inlet loss to only the positive vorticity fluid.

With the method outlined above, the mechanism of the loss breakdown will now be described. All downstream data obtained at Plane A were obtained using a staggered grid (recall Figure 6.1). This staggered grid results in grid cells consisting of five nodes: four corner nodes and a centre node. The mass-averaged total pressure deficit carried by each cell was distributed between the secondary and tip-leakage losses depending on the sign of vorticity of these individual nodes. Each of the corner nodes carried a weighting factor of 1/6 while the central node had a weighting factor of 1/3. For example, if a given corner node were to have a negative sign of vorticity, one sixth of the total pressure deficit carried by that cell would be allocated to the tip-leakage loss component.

The uncertainty involved with this loss breakdown is estimated at ±0.02 for the mass-averaged total-pressure coefficients. This estimate was obtained by comparing the loss coefficients determined using the staggered grid, which has 5 nodes per grid cell, with those obtained using the two constituent, rectangular grids, which each have 4 nodes per grid cell.

Table 6.3 tabulates the results for 0, 10 and 15% clearance; the loss components obtained using the conventional method are also included for comparison.

Clearance Size (τ/t)	Mass-Averaged Total Pressure Loss	Loss Breakdown Method		
		Conventional	Vorticity (Method A)	Vorticity (Method B)
0.00	C_{Po}'' *(inlet)*	-0.044	-----	-----
	C_{Po}' *(profile)*	-0.042	-----	-----
	C_{Po}'' *(secondary)*	-0.085	-----	-----
	C_{Po}'' *(tip-leakage)*	-----	-----	-----
	C_{Po}'' *(endloss)*	-0.085	-----	-----
	C_{Po}'' *(total)*	-0.172	-----	-----
0.10	C_{Po}'' *(inlet)*	-0.051	-0.051	-0.051
	C_{Po}' *(profile)*	-0.049	-0.039	-0.039
	C_{Po}'' *(secondary)*	-0.085	-0.094	-0.075
	C_{Po}'' *(tip-leakage)*	-0.176	-0.178	-0.196
	C_{Po}'' *(endloss)*	-0.261	-0.271	-0.271
	C_{Po}'' *(total)*	-0.361	-0.361	-0.361
0.15	C_{Po}'' *(inlet)*	-0.080	-0.080	-0.080
	C_{Po}' *(profile)*	-0.045	-0.022	-0.022
	C_{Po}'' *(secondary)*	-0.085	-0.017	0.024
	C_{Po}'' *(tip-leakage)*	0.024	-0.067	-0.108
	C_{Po}'' *(endloss)*	-0.061	-0.084	-0.084
	C_{Po}'' *(total)*	-0.186	-0.186	-0.186

Table 6.3 Comparison of the total-pressure coefficients for Plane A obtained using the conventional and vorticity methods.

6.1.3 Static Pressure Measurements

As noted in Chapter 2, most gap flow models (e.g., Moore & Tilton (1988), and Heyes & Hodson (1993)) and tip-leakage loss prediction schemes (e.g., Yaras & Sjolander (1992a), and Denton (1993)) treat the gap as an orifice with a uniform static pressure difference across the span at any chordwise position along the blade. In other words, the pressure difference (which is usually obtained from the blade loading near the tip) is assumed to apply across the gap, from the blade tip to the endwall, without any attenuation.

The following section presents the static pressure measurements which have been made at midspan, near the blade tip (1.98% span), and at the endwall for the present experiment. In light of these new data, the validity of treating the gap as an orifice is examined at large clearances.

6.1.3.1 Blade Loading

The blade static-pressure measurements at midspan are presented in Figure 6.13. The plot clearly shows an unloading of the blade with increasing clearance. Sjolander & Amrud (1987) observed a similar trend in their measurements at smaller clearances (0.0 to 2.86% of blade chord) and attributed the midspan unloading to the lower incidence experienced by the blade in an effect analogous to the downwash experienced by wings of finite span. Although this interpretation appears consistent with the observed trend, it is unlikely that this effect alone is responsible for such a large decrease in blade loading. Instead, it is believed that the unloading can be explained almost entirely by the redistributed axial velocity plotted in Figure 6.7. The reduction in the outlet axial velocity also appears to explain why the blade turning at midspan is nearly identical for all clearances despite the large reduction in lift implied by Figure 6.13.

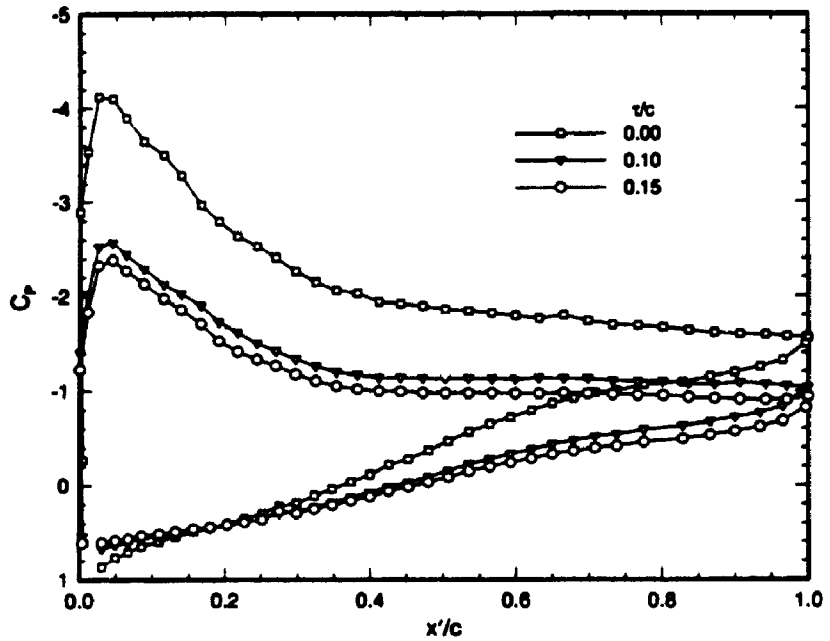

Figure 6.13 Variation of the midspan pressure distribution with clearance.

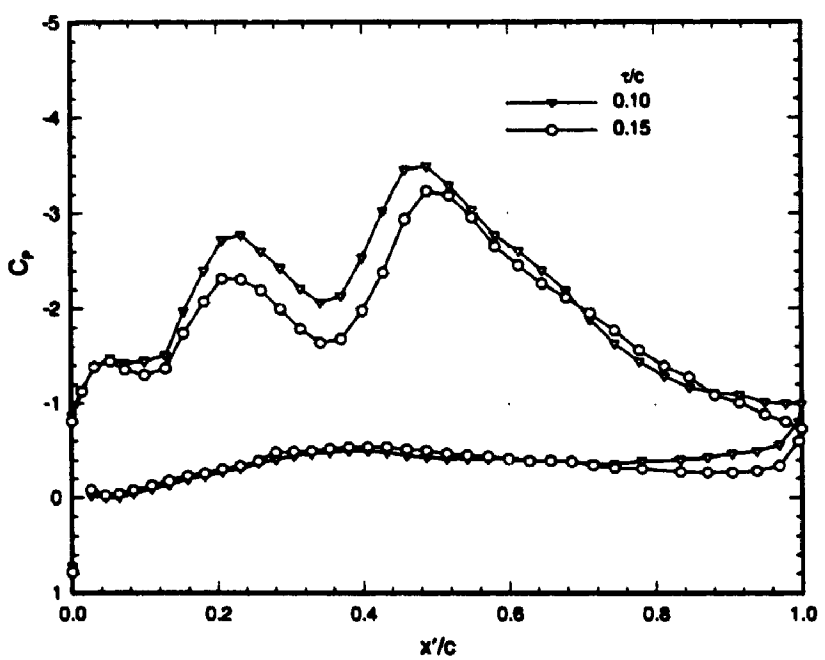

Figure 6.14 Variation of the static pressure distribution near the blade tip (1.98% span) with clearance.

Figure 6.14 shows the pressure distribution near the blade tip for 10% and 15% clearance. Both distributions clearly show signs of multiple tip-leakage vortices. This phenomenon has also been observed by others including Sjolander & Amrud (1987), Bindon (1989) and Kang & Hirsch (1993a,1993b).

Although Figure 6.14 shows that the local blade pressure field is highly distorted, it has been found experimentally (i.e., Yaras & Sjolander (1990)) that, at least for normal clearances, the *undisturbed* tip loading can be applied without attenuation to the gap flow. For the present experiment, this *undisturbed* loading is represented by the midspan measurements.

6.1.3.2 Endwall Static-Pressure Measurements and Tipgap Driving Pressure Field

In addition to the blade-surface static-pressure measurements, the static-pressure distributions on the endwall were also examined. The endwall static-pressure contours for both 10% and 15% clearance are plotted in Figure 6.15. At 10% clearance, the minimum pressure observed on the endwall is only slightly less than the minimum pressure observed on the blade suction surface, while at 15% clearance, the minimum pressure on the endwall is noticeably reduced.

It is apparent that there is an attenuation of the pressure gradients near the endwall as the clearance size is increased. This effect is not entirely surprising since one would expect the pressure variations on the endwall to tend to zero as the clearance tends to infinity. However, the measurements of Bindon (1987a) and Yaras *et al.* (1989) show no noticeable attenuation of the driving pressure difference for clearances of less than 5% of chord. The results of Sjolander & Cao (1994), who took detailed flow measurements in an idealized turbine tipgap, also show no attenuation of the driving pressure difference for the smaller clearances studied by the authors. However, at their largest clearance ($\tau/t = 0.667$), they too observed a significant attenuation of the endwall pressure gradients.

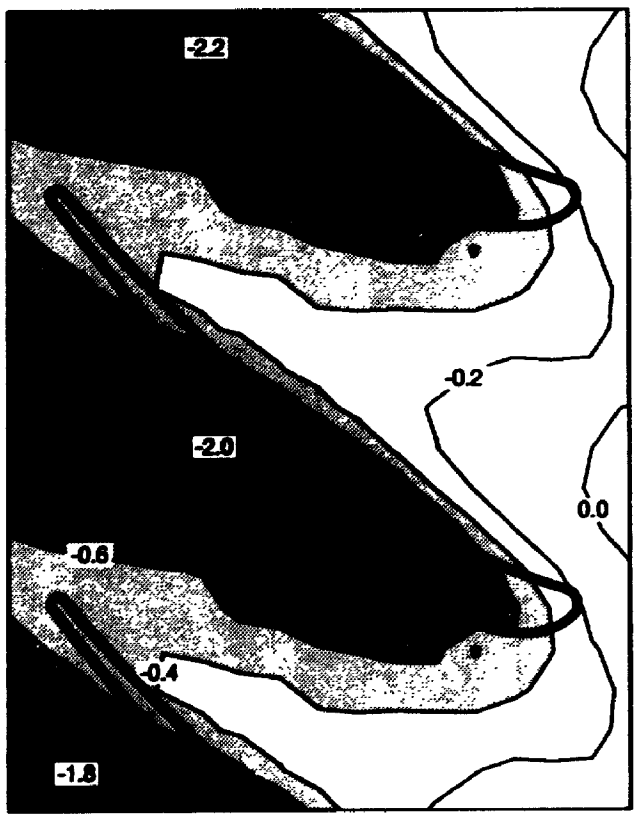

(a) $\tau/c = 0.10$

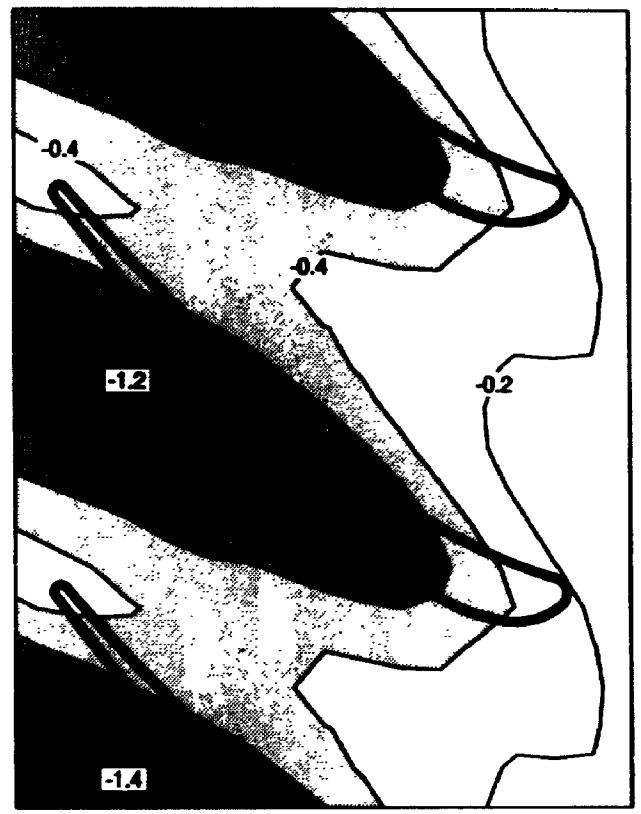

(b) $\tau/c = 0.15$

Figure 6.15 Tipwall static pressure contours.

To quantify the driving pressure differences[2], the endwall pressure variations normal to the blade chord were examined. The maximum static pressure difference along this direction was extracted from Figure 6.15 at various chordwise planes and plotted with the measured midspan pressure difference in Figure 6.16. The results measured by Yaras (1990) at smaller clearances are reproduced in Figure 6.17 for comparison. The earlier measurements show a much closer agreement between the blade and endwall driving pressure differences. At large clearances, it is evident that using the blade pressure difference as an approximation of the driving pressure difference is not satisfactory. The decreasing endwall driving pressure difference, observed in Figure 6.16 between 10 and 15% clearance, suggests that the gap no longer behaves as a simple orifice but that there is in fact a pressure gradient over the height of the gap.

6.1.4 Comparison of the Bound and Tip-Vortex Circulations

The effect of clearance size on the tip-vortex strength has been examined by a number of authors (e.g., Lakshminarayana & Horlock (1962), Lewis & Yeung (1977), Inoue *et al.* (1986), and Yaras & Sjolander (1990)). In each case it was found that the circulation of the tip-leakage vortex was significantly less than the bound circulation of the blade. Lakshminarayana & Horlock (1962) offered an explanation for this phenomenon in terms of a modified lifting-line model whereby not all of the bound circulation of the blade is shed downstream in the tip vortex. Instead, it was postulated that a fraction of the vorticity spans the gap between the blade tip and the endwall as a vortex sheet. This *retained lift* concept, as it became known, has been widely accepted amongst tip-clearance researchers.

More recently, however, Yaras *et al.* (1992) and Kind *et al.* (1994) have outlined some serious theoretical difficulties associated with the retained lift model and have

[2] The term "driving pressure difference" refers to the pressure difference which determines the component of velocity normal to the tip gap near the endwall, where most of the leakage occurs.

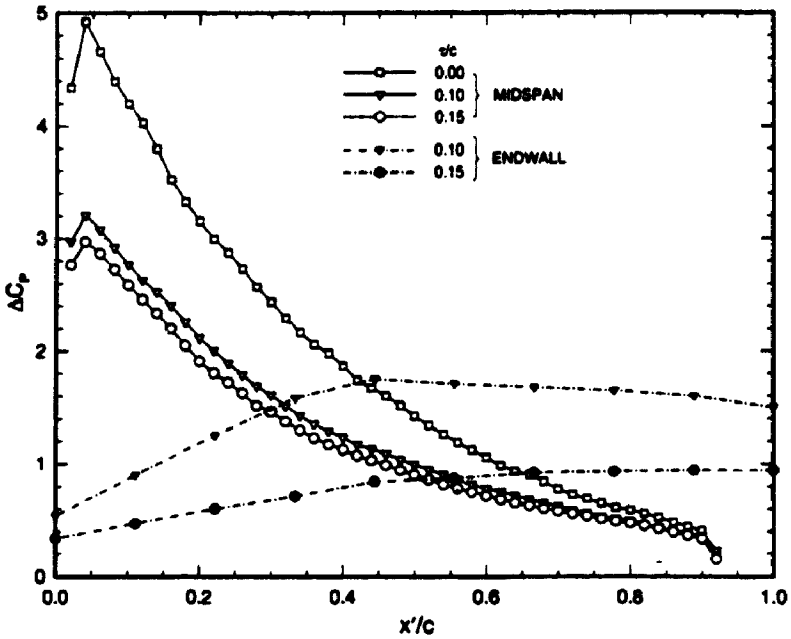

Figure 6.16 Variation of the blade pressure differences and the endwall driving pressure differences with clearance.

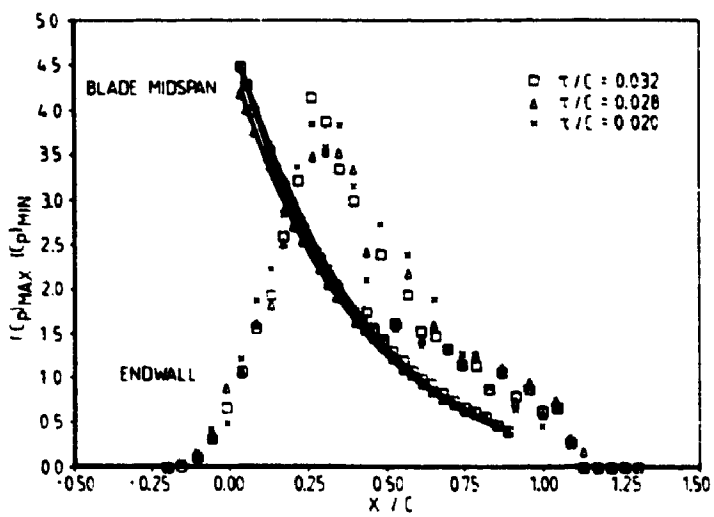

Figure 6.17 Comparison between midspan pressure differences and driving pressure differences at endwall, reproduced from Yaras (1990).

suggested an alternate explanation which appears to be more consistent with the observed flow physics. Based on recent cascade experiments which have shown the gap flow to be essentially inviscid and irrotational (e.g., Yaras & Sjolander (1989), Storer & Cumpsty (1991), Heyes & Hodson (1993)), they argue that no plausible mechanism exists which would allow vorticity to span the gap. Instead, they attribute the reduced tip-vortex circulation to the endwall fluid entrained into the tip-leakage vortex. As seen in Figure 6.18, this endwall boundary layer fluid must have an opposite sign of vorticity to that generated on the blade tip by vi.aue of the no slip condition. The mixing of these two flows with opposite signs of vorticity would result in an overall reduction of the tip vortex circulation.

6.1.4.1 Calculation of the Bound and Tip-Vortex Circulations

Circulation is defined as the line integral of the velocity around any closed curve C and is given by:

$$\Gamma = \oint_C \vec{V} \cdot d\vec{s}$$

where $\vec{V} \cdot d\vec{s}$ is the scalar product of the velocity vector and the differential vector along the path of integration. In the absence of total-pressure losses, the non-dimensional value of the bound circulation is given by

$$\Gamma'_B = \frac{\Gamma_B}{V_{CL}\, c} = \frac{1}{V_{CL}\, c} \oint_C \vec{V} \cdot d\vec{s} = \oint_C \sqrt{1 - C_P}\; d\left(\frac{s}{c}\right) \tag{6.12}$$

where V_{CL} is the reference centreline velocity, c is the blade chord length, and C_P is the blade static pressure measured at midspan.

Using Stokes' theorem, the circulation around any portion of the downstream flow field can be determined using:

$$\Gamma = \int_A \omega_n \, dA \tag{6.13}$$

where ω_n is the vorticity component normal to the area A. Since the Plane A measurements were parallel to the y-z plane, the easiest approach for calculating the tip vortex circulation was simply to integrate the x-wise component of vorticity over the area visibly associated with the vortex.

6.1.4.2 Measured Circulations at Large Clearances

Figure 6.19 presents the variation of the bound circulation and tip-vortex circulation at Plane A with increasing clearance; also included in the figure are selected results at lower clearances from Yaras (1990). At the smaller clearances, the circulation measured in the tip-vortex was found to be noticeably less than the bound circulation. However, at 15% clearance the blade is observed to behave as a wing, with all of the bound circulation appearing in the tip vortex. This result implies that there is negligible interaction between the vorticity being shed from the blade tip and that being generated on the endwall.

The lack of interaction between the endwall boundary layer and the tip-leakage vortex is also significant from the point of view of losses. As discussed in Section 6.1.2.2, much of the fluid around the periphery of the tip-leakage vortex at 10% clearance was observed to be composed of positive vorticity fluid which had been entrained from the passage vortex and the endwall boundary layer and convected towards midspan. The mixing of this positive vorticity fluid with the negative vorticity fluid of the tip-vortex is expected to be an important source of loss production. The near equality of the bound- and tip-vortex circulations at 15% clearance indicates that no such mixing occurred at the larger clearance. This lack of mixing between the tip-leakage vortex and

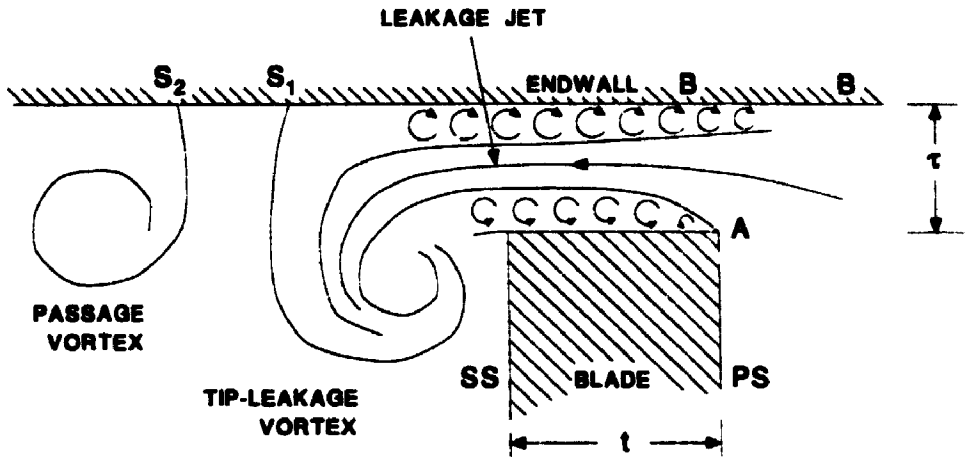

Figure 6.18 Interaction between the vorticity at the blade tip and the vorticity layer on the endwall, reproduced from Kind *et al.* (1994).

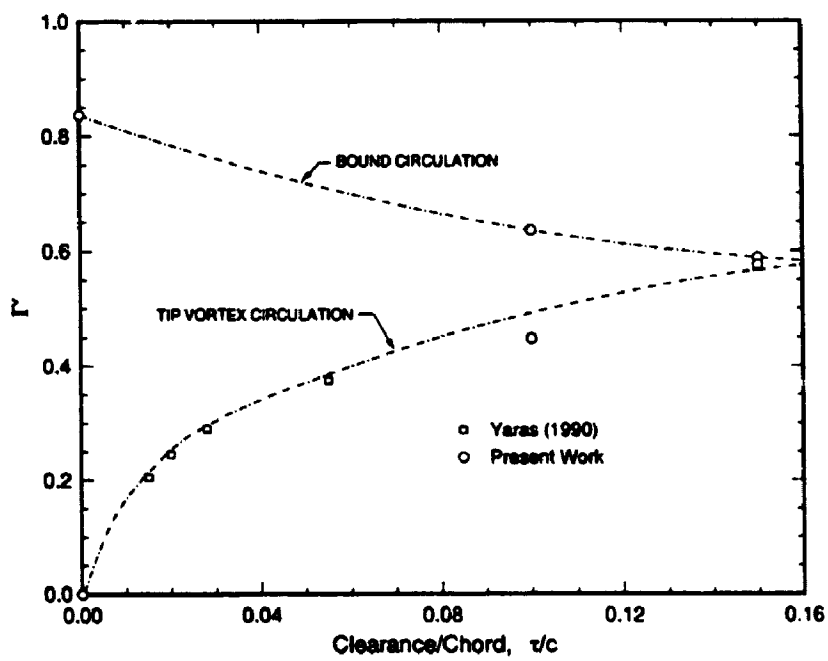

Figure 6.19 Variation of the bound and tip-vortex circulations with clearance.

the endwall flow is suspected of having contributed to the reduced losses observed at Plane A for 15% clearance. However, it will be shown in the next section that the majority of the observed loss reduction can be attributed to the reduced driving pressure difference across the gap.

6.1.5 Loss Model Evaluation at Large Clearances

Numerous models have been proposed for estimating the tip-leakage losses. The brief review presented in Chapter 2 showed that some of these models were simple empirical correlations while others attempted to model the physics of the flow. In this section, two of these models will be reviewed briefly and compared with the present experimental results.

Rains (1954) was the first to suggest that the kinetic energy of the gap flow normal to the blade chord was eventually lost and that this accounted for the whole of the tip-leakage loss. The accurate prediction of the mass flow rate through the gap, or more precisely, the magnitude of the velocity component normal to the gap, was critical to the application of this idea. Rains himself developed a somewhat involved analysis for the resulting efficiency drop in the stage. The model was subsequently modified by Vavra (1960) who incorporated several simplifying assumptions. However, the results of Yaras *et al.* (1989) showed that Vavra's model inaccurately predicted the gap kinetic energy and, as a result, gave poor predictions of the tip-leakage loss. Believing the underlying idea to be physically sound, Yaras & Sjolander (1992a) proposed an improved version of Vavra's model which incorporated a more accurate estimate of the gap kinetic energy.

Recently, Denton (1993) developed a simple tip-leakage loss model from first principles. Using a control volume analysis, the loss associated with the mixing of the leakage flow with the surrounding passage flow could be calculated. Although several

simplifying assumptions are incorporated into the analysis (e.g., mixing occurs at constant pressure, endwall shear stress is neglected), the method is believed to be quite sound.

The present results will be compared with the models of Denton (1993) and Yaras & Sjolander (1992a). The goal of the comparison is not to verify the models quantitatively, since both are not directly applicable to large clearance flows without modifications, but to examine whether the observed changes in the tip-leakage losses can be captured by the models since both are believed to embody valid flow physics.

The losses predicted by both models are strongly dependent on the mass flow rate through the gap. In both cases, the gap is treated as an orifice. By applying Bernoulli's equation, the leakage mass flow over a length dx' along the chord can be expressed as:

$$d\dot{m}_g = C_D \tau \sqrt{2\,\Delta P\,\rho}\; dx'$$

where C_D is the discharge coefficient, τ is gap height and ΔP is the blade pressure difference. However, as noted in Section 6.1.3.2, the present results indicate that the gap no longer behaves as an orifice at large clearances but that there is an attenuation of the pressure difference near the endwall. Therefore, if these models are to be used at larger clearances, they need to be supplemented by a correlation for the attenuation of the driving pressure difference with clearance.

The tip-leakage loss coefficient predicted by the Denton (1993) model can be written as:

$$Y_{tip} = \frac{2\tau C_D c}{hS}\frac{q_1}{q_2}\int_0^1 \left(\sqrt{1 - C_{P_s}}\right)^3 \left(1 - \sqrt{\frac{1 - C_{P_p}}{1 - C_{P_s}}}\right)\sqrt{1 - \left(\frac{1 - C_{P_p}}{1 - C_{P_s}}\right)}\, d\left(\frac{x'}{c}\right) \qquad (6.14)$$

where h is the passage height used to define the reference mass flow rate, C_{P_p} and C_{P_s} are the blade static-pressure coefficients at the inlet and outlet of the gap, and q_1/q_2 is the mass-averaged dynamic pressure ratio across the blade row, based on the reference mass flow rate.

Similarly, the tip-leakage loss coefficient for the Yaras & Sjolander (1992a) model can be expressed as:

$$Y_{tip} = \frac{2K_E \tau C_D c}{hS} \frac{\cos^2\alpha_2}{\cos^3\alpha_m} C_L^{1.5} \tag{6.15}$$

where C_L is the blade lift coefficient obtained by integrating the blade pressure distribution. The term K_E is a constant which depends on the blade loading distribution:

$K_E = 0.566$ for a front- or aft loaded blade,

$K_E = 0.5$ for a mid-loaded blade.

It is evident from Equations 6.14 and 6.15 that both models use the blade pressure difference to approximate the driving pressure difference. In order to demonstrate the effect of the attenuated driving pressures, the calculations were made with three different distributions: the blade pressure differences, the pressure differences obtained from the endwall, and lastly, the average of the previous two. In terms of the Yaras & Sjolander (1992a) model, this involved the calculation of an *effective* lift coefficient, obtained by integrating the appropriate distribution.

The predicted loss coefficients for each of the three pressure differences are presented in Table 6.4. Since both models predict the final mixed-out tip-leakage loss, the mixed-out endloss is included for comparison. At large clearances, the blockage effect presented by the separation on the blade tip is expected to become smaller, and so, to keep the analysis simple, the empirical discharge coefficient incorporated by both models was simply set to 1.0. Finally, both models estimate the losses produced

downstream of the gap and do not incorporate the gap flow loss. Although expressions do exist for predicting this loss component (e.g., Yaras & Sjolander (1992a) and Heyes & Hodson (1993)) it is generally found that the gap loss is small compared with the downstream loss and so, again for simplicity, it was neglected in the present analysis.

Table 6.4 shows that both models predict higher losses than those measured. At 10% clearance, the losses predicted using the blade, endwall and average pressure distributions are all found to be quite similar; this is a good indication that the tip gap is still behaving like an orifice at this clearance. However, at 15% clearance, both models indicate that the predicted loss depends on the pressure distribution used. Since much of the leakage occurs near the endwall, it can be argued that use of endwall pressure distribution would seem to be the most appropriate. Using this distribution, Table 6.4 indicates that both models predict a halving of the predicted losses as the clearance is opened from 10 to 15% clearance. This is somewhat smaller than the decrease observed experimentally. Regardless, the calculations indicate that the attenuation of the driving pressure difference was the *main* reason for the observed reduction in end losses.

Source	Mixed-out Loss Coefficient	Pressure Distribution	Clearance Size τ/c	
			0.10	0.15
Measured	Y *(endloss)*	-----	0.256	0.086
Denton Model	Y *(tip-leakage)*	Blade	0.464	0.523
		Endwall	0.461	0.216
		Average	0.416	0.319
Yaras & Sjolander Model	Y *(tip-leakage)*	Blade	0.345	0.395
		Endwall	0.389	0.192
		Average	0.343	0.267

Table 6.4 Comparison of the measured and predicted total-pressure loss coefficients.

6.2 Computational Results

The objective of the present computational investigation was to evaluate the ability of the Dawes code to predict the flow field around blades with large clearances. All of the results presented in this chapter were obtained using a two-dimensional cascade geometry identical to that used in the measurements. As discussed in Chapter 5, all computations were run using a 35×107×35 grid[3]. The number of nodes within the tip gap varied from 5 at the smallest clearance ($\tau/c = 0.025$) to 17 at the largest clearance ($\tau/c = 0.150$). The calculations were marched for 3000 timesteps using a fine grid CFL number of 0.5 and an outlet Mach number of 0.42. Where possible, the experimental results are presented for comparison with the predicted solution.

6.2.1 Total-Pressure Distribution Downstream of the Blade Row

Figures 6.20 to 6.22 present the contours of the predicted total-pressure coefficient at a plane 0.475 c_x downstream of the blade trailing edge (referred to as Plane A) for 0, 10 and 15% clearance. Included below each figure are the corresponding measurements. In Figure 6.20, it can be seen that the extent and shape of the secondary flows at zero clearance are predicted fairly accurately by the Dawes code. Examining the blade wakes, however, one notes that the peak loss in the predicted wake is larger than that measured while the width of the wake is smaller than that seen experimentally. These results appear to indicate that less diffusion of the wakes has occurred in the predicted solution than observed experimentally. Similar results were observed by Dawes (1990) and at the 1994 ASME-IGTI Turbo Expo (Sjolander, 1994). The problem is generally attributed to the Baldwin-Lomax model which has difficulty predicting the wake development with downstream distance.

---

[3] The grid size quoted is representative of the number of nodes ($I_{max} \times J_{max} \times K_{max}$) used in the pitchwise, axial, and spanwise directions, respectively.

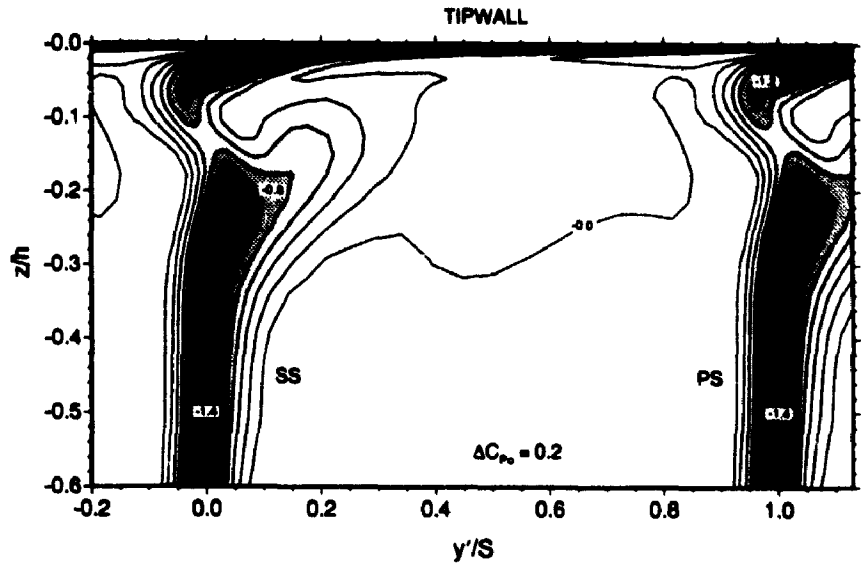

a) Predicted

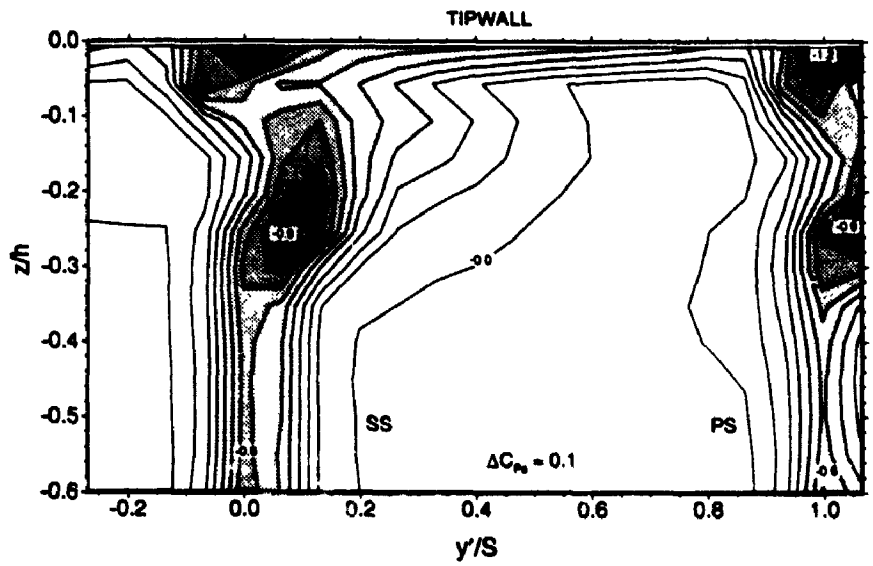

b) Measured

Figure 6.20 Comparison of the measured and predicted total-pressure coefficient contours at Plane A for $\tau/c = 0.00$.

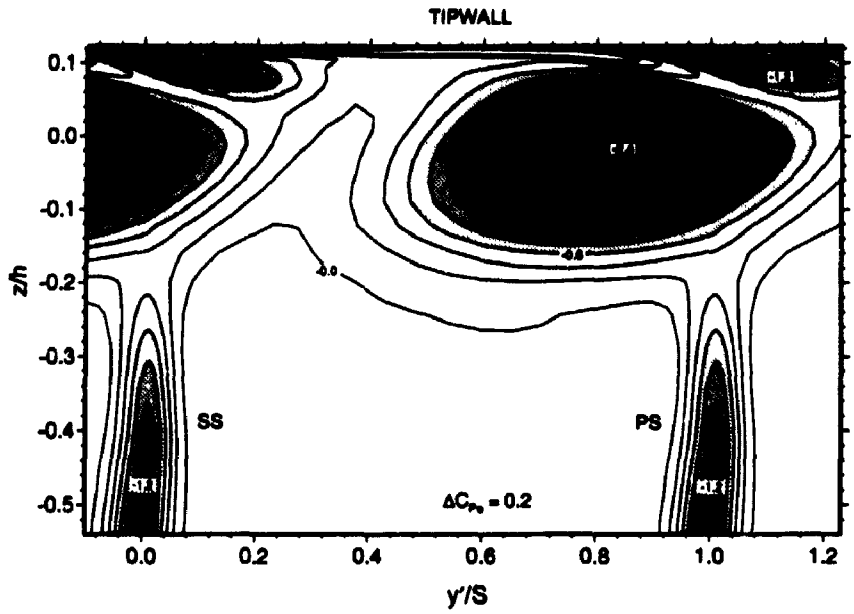

a) Predicted

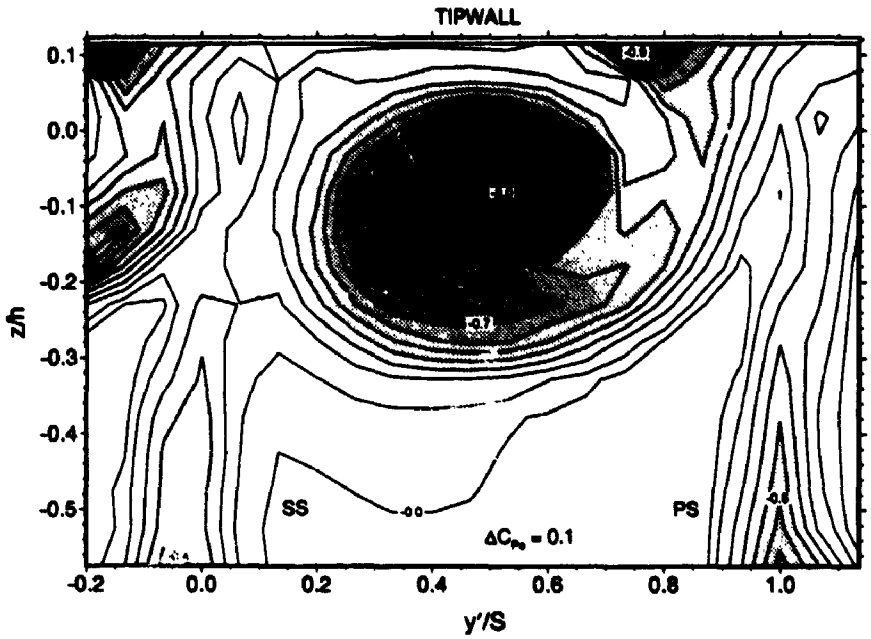

b) Measured

Figure 6.21 Comparison of the measured and predicted total-pressure coefficient contours at Plane A for $\tau/c = 0.10$.

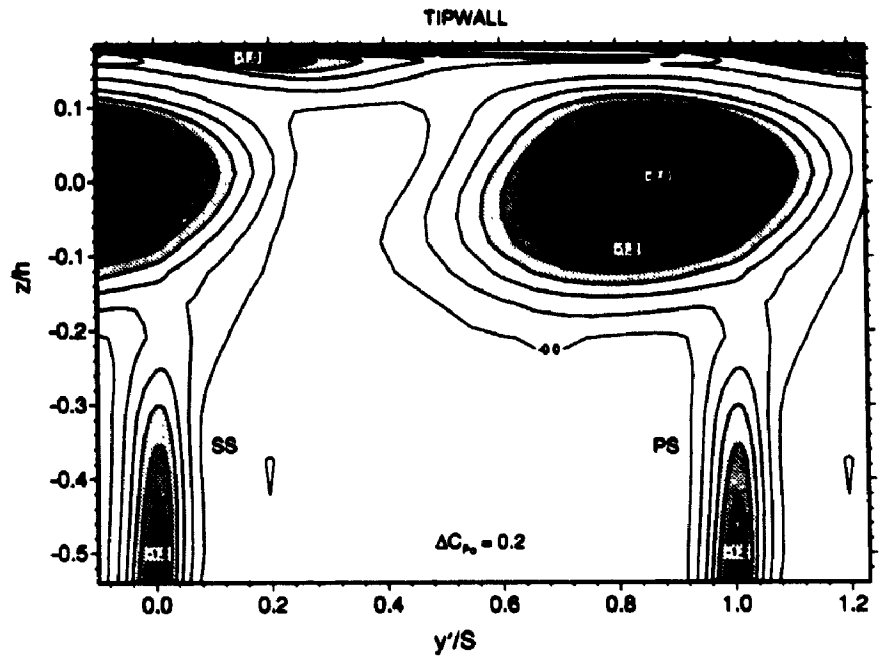

a) Predicted

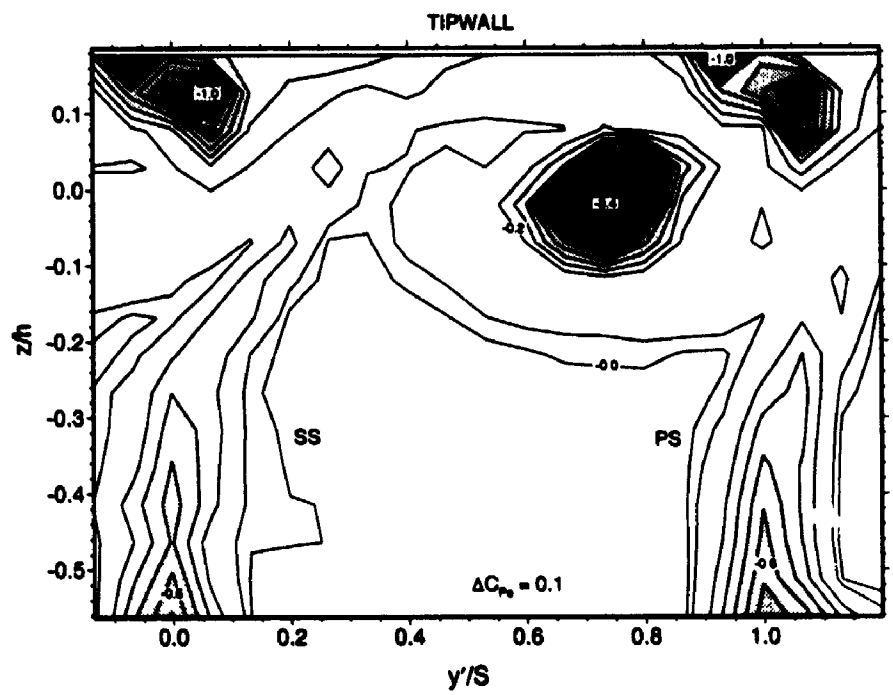

b) Measured

Figure 6.22 Comparison of the measured and predicted total-pressure coefficient contours at Plane A for $\tau/c = 0.15$.

Figure 6.21 shows the presence of a large tip-leakage vortex dominating the endwall region at 10% clearance. The peak loss of the vortex is observed to be lower than that measured and the spanwise extent of the vortex appears to be less than that observed experimentally. As discussed in Section 6.1.2.2, much of the fluid around the periphery of the tip-leakage vortex was found to be composed of positive vorticity fluid which had been entrained from the endwall. The reduction in the spanwise extent of the predicted tip-leakage vortex might be partly attributable to a reduced entrainment of endwall and secondary flow fluid in the predictions.

At 15% clearance (Figure 6.22), the predicted solution shows the tip vortex to be somewhat smaller than the one observed for 10% clearance, in Figure 6.21. Again, the peak loss of the vortex is significantly less than that measured and, in general, the vortex appears to be more diffused than that observed experimentally.

6.2.2 Mass-Averaged Total-Pressure Losses and Flow Angles

Figure 6.23 presents the distributions of the predicted pitchwise-averaged total-pressure deficits for various clearances. The plot clearly shows a reduction in the peak mass-averaged loss with increasing clearance. The predicted distributions for 0, 10 and 15% clearance are replotted in Figure 6.24 to allow easier comparison with the measured results, plotted in Figure 6.25. Good agreement between the computational and measured results are observed at zero clearance. However, at clearance the loss generally tends to be over-predicted by the Dawes code. This is likely due in part to the blade tip rounding (see Section 5.2.4) necessary to keep the code stable. With a rounded blade tip, the separation bubble on the tip is not resolved and the tipgap mass flow will tend to be high. This, in turn, will lead to larger tip-leakage losses.

Figure 6.26 presents the predicted variation of the mass-averaged endloss (tip-leakage loss + secondary loss) at Plane A with clearance. As discussed in Chapter 5, all

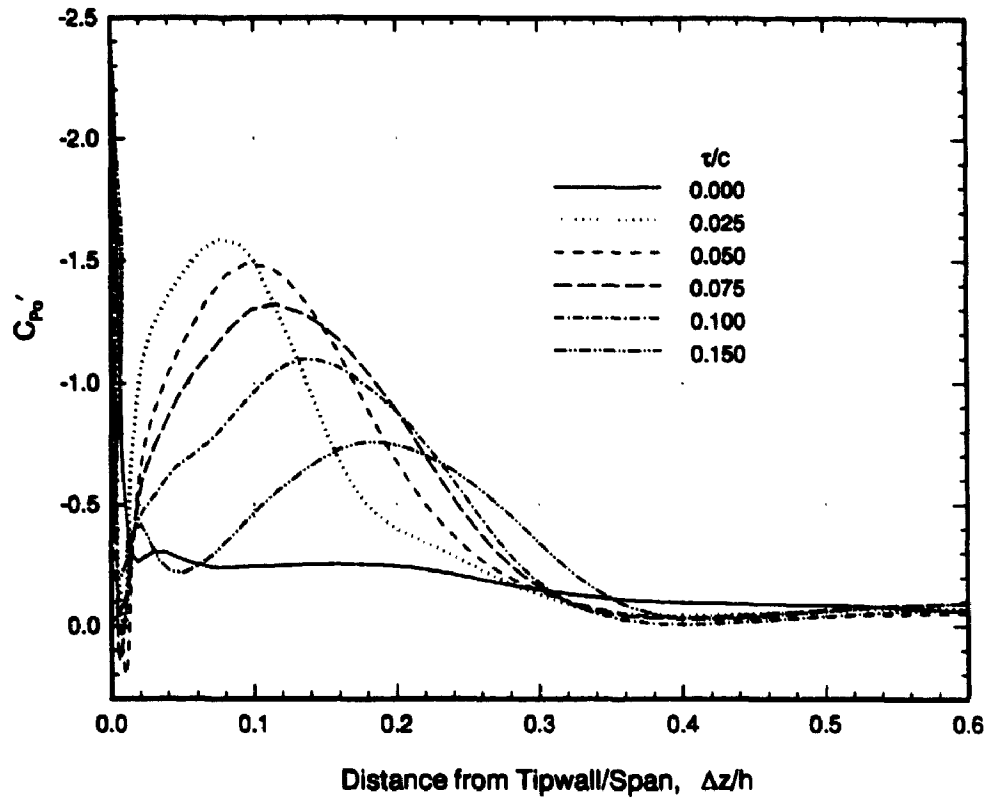

Figure 6.23 Spanwise distributions of the predicted total-pressure deficit at Plane A.

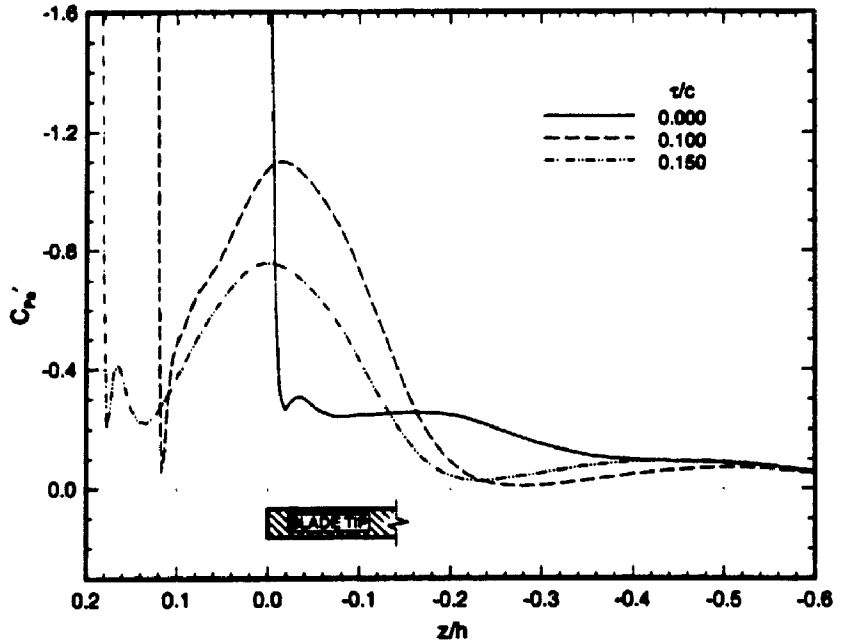

Figure 6.24 Spanwise variation of the predicted total-pressure deficit for 0, 10 and 15% clearance at Plane A.

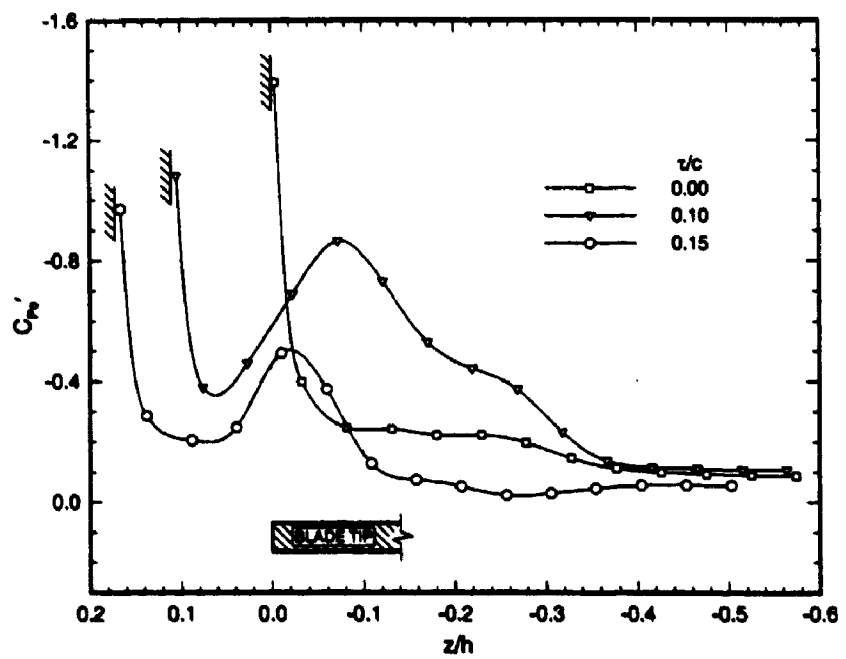

Figure 6.25 Spanwise distribution of the total-pressure deficit at Plane A [reproduced from Section 6.1.1.3].

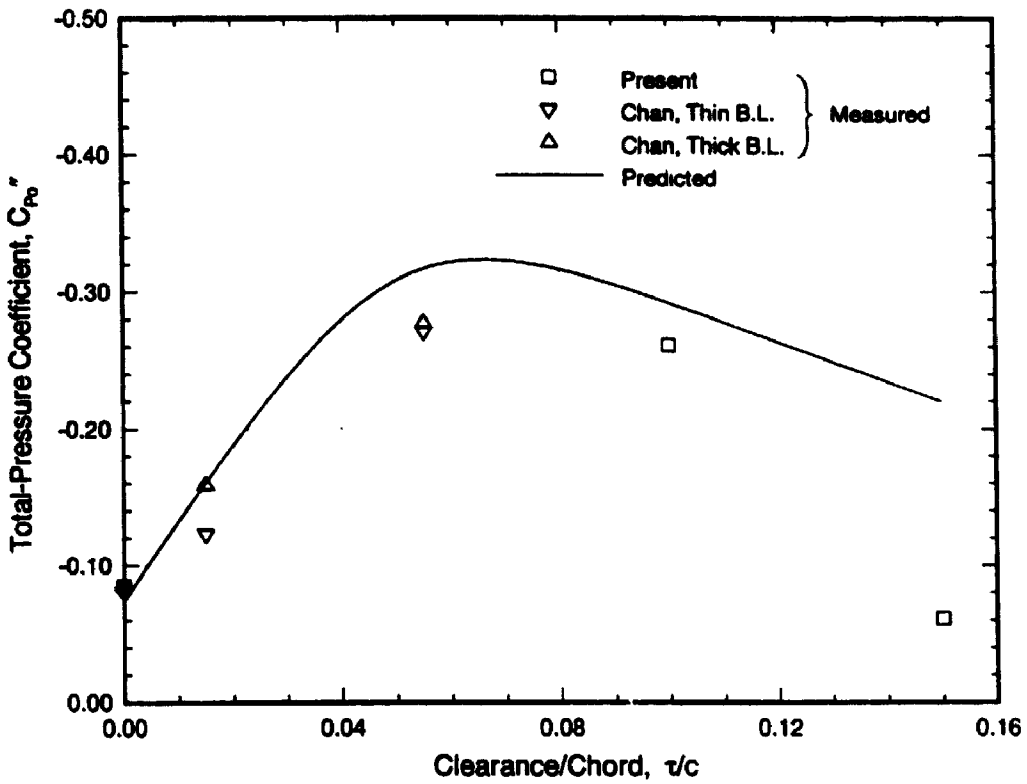

Figure 6.26 Predicted variation of the endloss at Plane A.

mass-averaged results were obtained using the 60% of span nearest the tipwall. The Dawes code is observed to predict the trend reasonably well despite the rather crude modelling of the blade tip region. The predicted endloss is observed to peak at a clearance of about 7%, which is similar to the trend observed experimentally. At the largest clearances, the predicted endloss is noted to be significantly larger than the measured value.

As noted, all endloss data presented in Figure 6.26 are as obtained at Plane A. Although it would have been desirable to compare the predicted and measured mixed-out end losses, this could not be done since time did not allow for the modification of the post-processor to calculate the predicted mixed-out losses.

Figure 6.27 presents the predicted variation of the outlet flow angle at Plane A for various clearances. The underturning in the endwall region is observed to become progressively larger as the clearance increases. The predicted results for 0, 10 and 15% clearance are replotted in Figure 6.28 to allow easier comparison with the measured results, plotted in Figure 6.29. The predicted outlet flow angle distributions are seen to be reasonably accurate at 0 and 15% clearance. However, at 10% clearance the Dawes code appears to overpredict the underturning of the flow in the tipgap region. Again, this likely results from the inability of the Dawes code to capture the blockage effect presented by the separation bubble. This blockage would decease the gap mass flow rate, and hence momentum normal to the chord, reducing the mass-averaged underturning. Lastly, Figure 6.30 presents the variation of the mass-averaged outlet flow angle predicted by the Dawes code; the measured results are again included for comparison. The predicted mass-averaged underturning is found to agree reasonably well with the measurements.

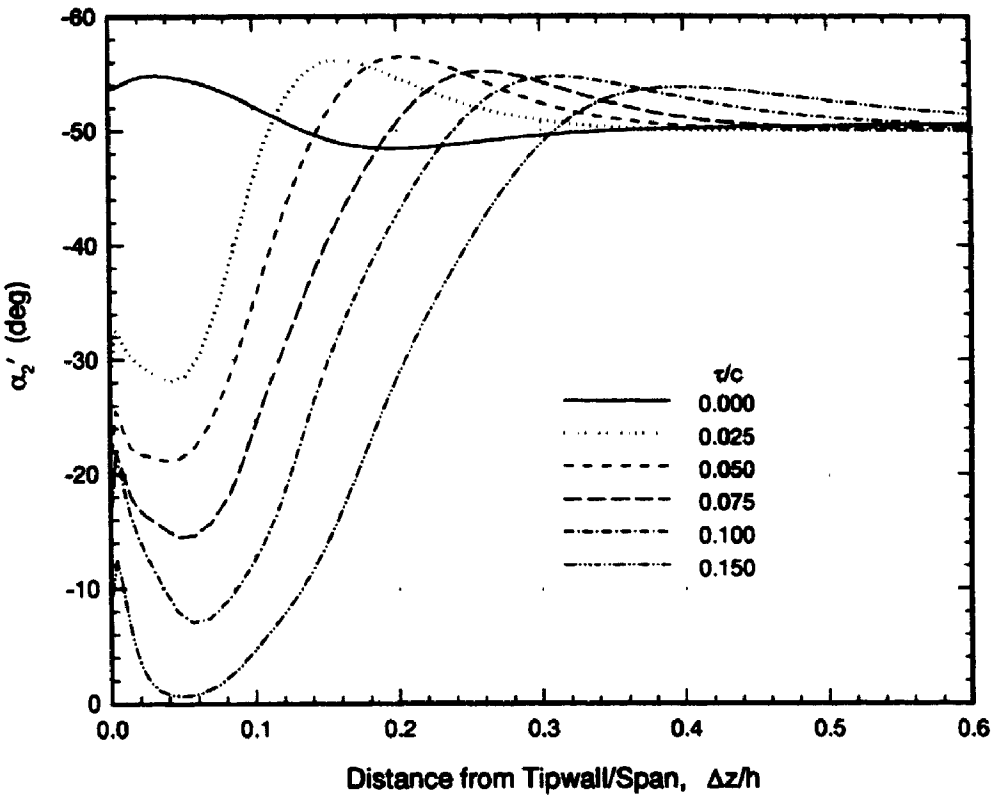

Figure 6.27 Spanwise distributions of the predicted outlet flow angle at Plane A.

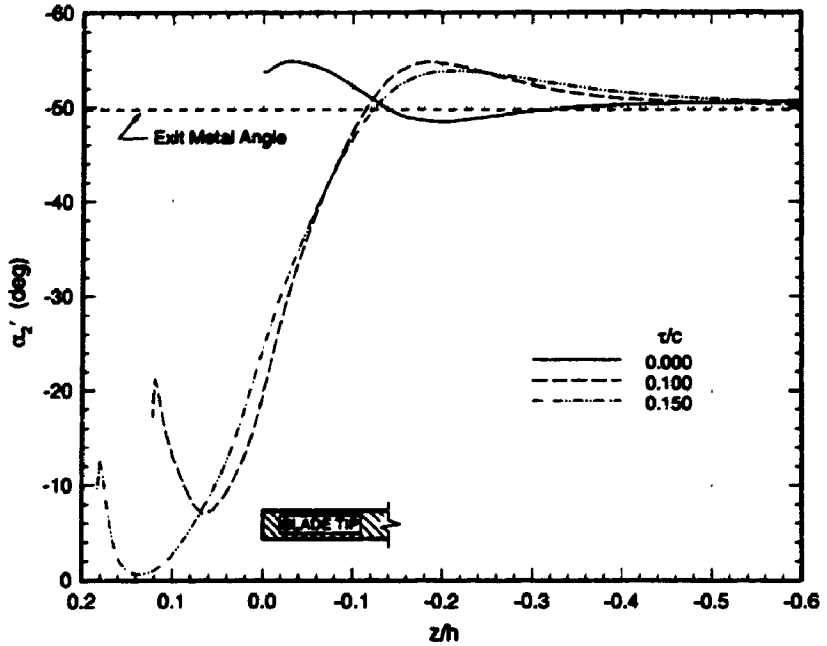

Figure 6.28 Spanwise variation of the predicted outlet flow angle for 0, 10 and 15% clearance at Plane A.

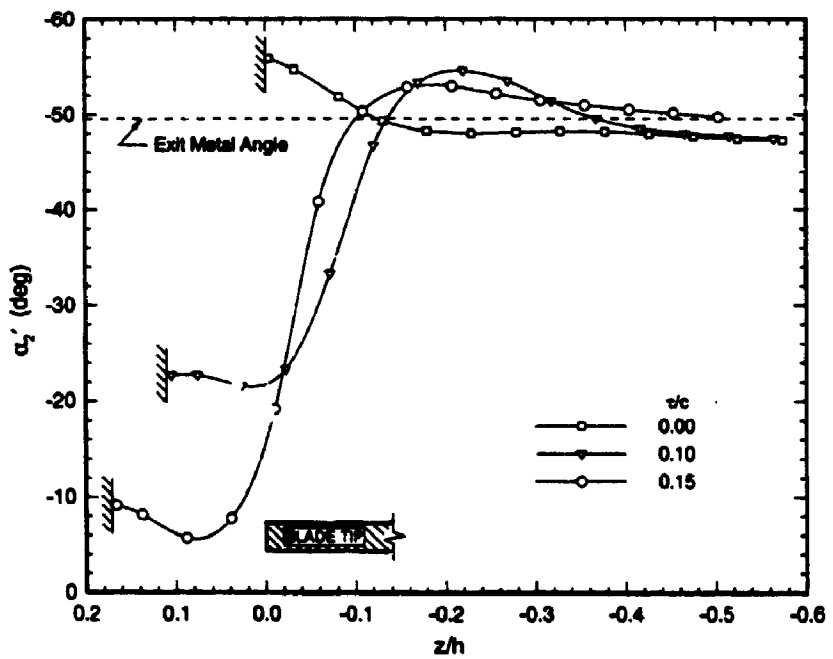

Figure 6.29 Spanwise distribution of the outlet flow angle at Plane A [reproduced from Section 6.1.1.4].

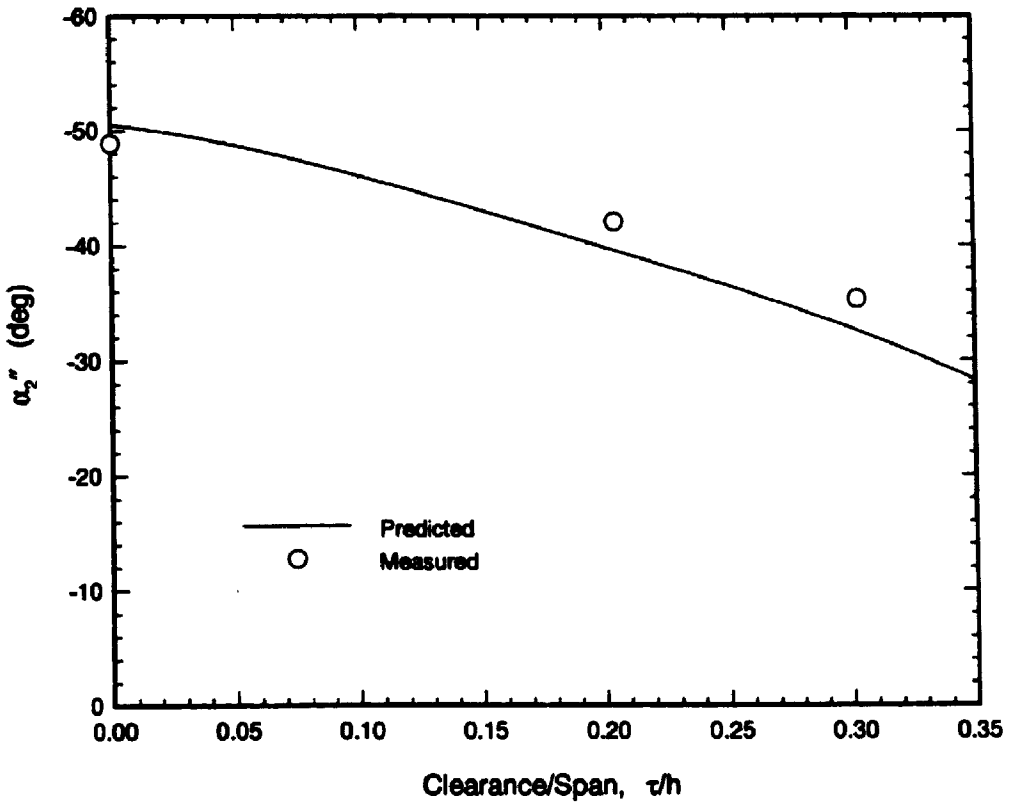

Figure 6.30 Predicted variation of the mass-averaged outlet flow angle at Plane A.

6.2.3 Static-Pressure Distributions

The predicted static-pressure distributions at midspan are presented in Figure 6.31. The distributions are seen to be quite similar to those measured (see Section 6.1.3.1). However, the predicted reduction of the blade loading at midspan with clearance is less than that observed experimentally. This is surprising since the flow underturning at clearance was generally over-predicted by the Dawes code. One would have expected this to lead to a more pronounced redistribution of the mass flow across the passage span with a more significant reduction of the loading at midspan. The discrepancy might be partly attributable to the different Mach numbers at which the computational and experimental results were obtained. Although both results were obtained at similar Reynolds numbers, the computational data was obtained using an outlet Mach number of 0.42 while the experimental data was obtained under essentially incompressible flow conditions (outlet Mach number of 0.12).

Finally, Figure 6.32 presents the predicted endwall static-pressure contours for various clearances. The endwall pressure gradients are observed to decrease with increasing clearance. Although the peak pressures measured on the endwall were larger than those measured experimentally at 10 and 15% clearances (see Section 6.1.3.2), the endwall driving pressure differences were observed to be quite similar.

6.2.4 Conclusions

The Dawes code has predicted many of the measured results: the reduction in the midspan loading, the spanwise redistribution of the mass flow, and the attenuation of the endwall driving pressure difference have all been duplicated to some extent by the solver. The majority of the discrepancies observed can likely be attributed to the inability of the Dawes code to correctly resolve the tip gap flow, in particular, the blockage presented by the separation bubble. Overall, the Navier-Stokes code predictions should be regarded

as encouraging. The next logical step would be to use the Dawes code to examine the effects of other parameters (e.g., blade loading, blade geometry, and Mach number) in order to expand and extrapolate from the somewhat limited number of cases examined experimentally.

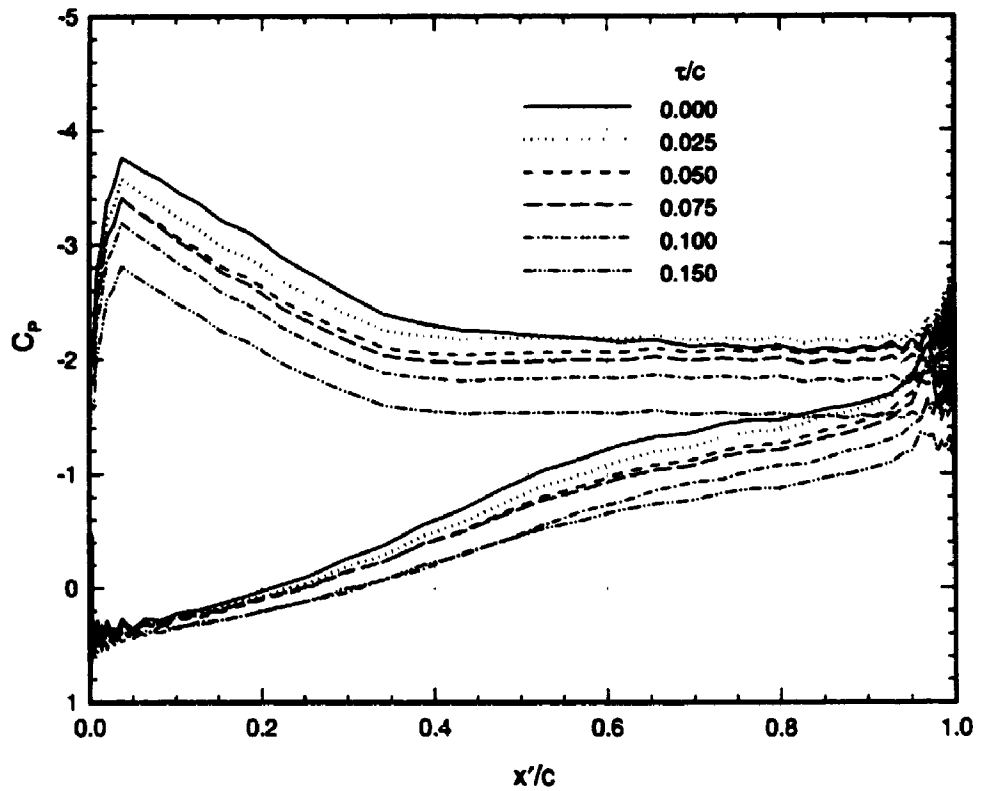

Figure 6.31 Predicted midspan static-pressure distributions.

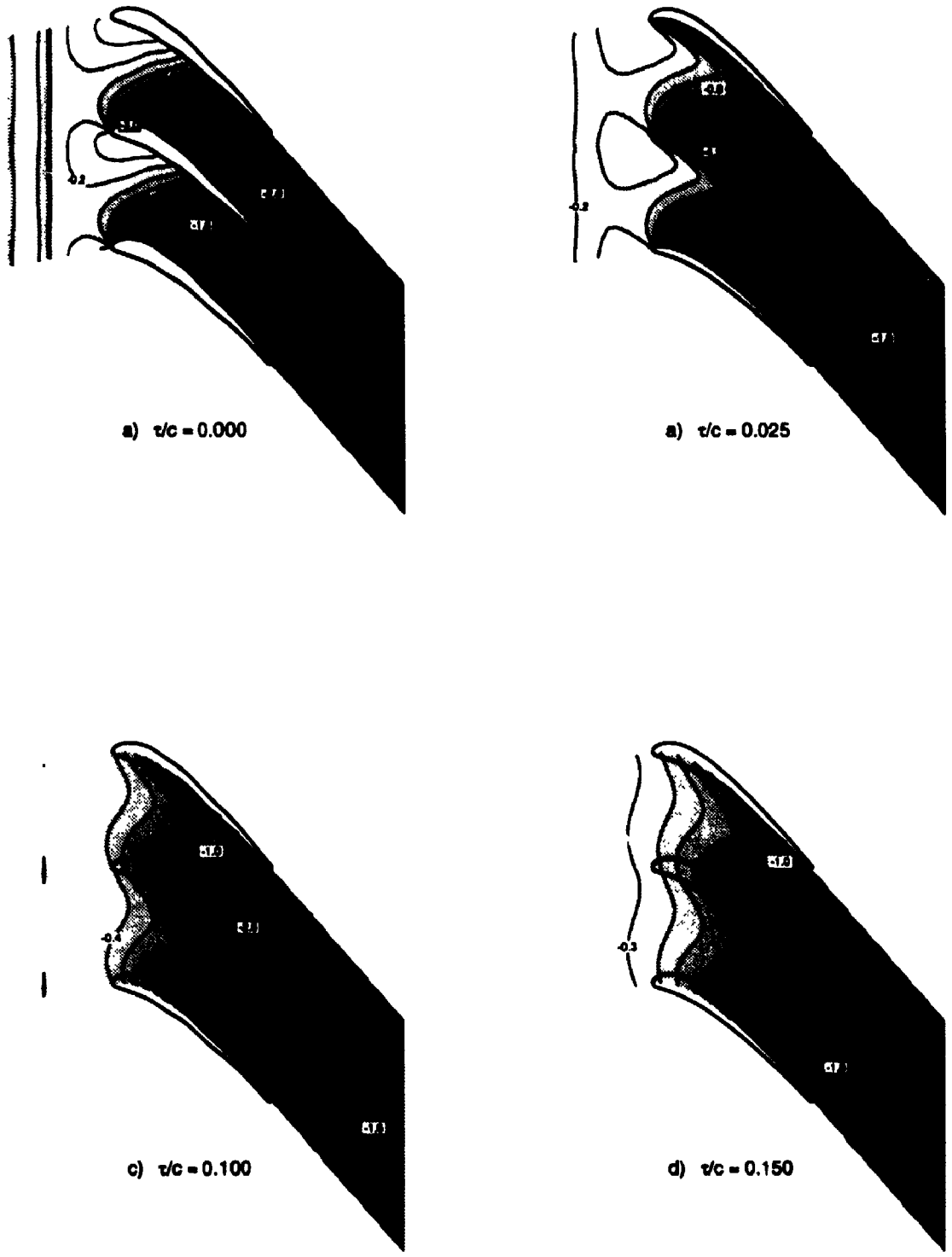

Figure 6.32 Predicted contours of the static-pressure coefficient for various clearances.

Chapter 7
CONCLUSIONS AND RECOMMENDATIONS

7.1 Conclusions

Measurements were made in a linear turbine cascade with very large clearances in order to determine the aerodynamic effect of in-service damage to the blade tip region.

The losses measured in the blade-end region were observed to reach a maximum at a clearance of about 6 or 7% of the blade chord; beyond this clearance, the measured losses were substantially reduced. At 15% clearance, the endloss was comparable to the secondary losses measured at zero clearance. The reduction in losses appears to be due primarily to the attenuated gap driving pressure differences observed near the endwall at enlarged clearances.

A strong interaction between the tip-leakage and endwall flows was observed at 10% clearance where a substantial amount of positive vorticity fluid was entrained from the endwall boundary layer, by the tip vortex, and convected towards midspan. At the largest clearance, the interaction of the tip-leakage and endwall flows was greatly reduced. The reduced interaction of these two flows of opposite vorticity is believed to have contributed to the reduction in losses.

The circulation of the tip vortex was found to increase with clearance. At 15% clearance the tip vortex circulation was found to equal the bound circulation. This result confirms that there was little interaction between the tip-leakage and endwall flows at 15% clearance.

Measurements downstream of the blade row indicated that the flow in the blade-end region was substantially underturned at the larger clearances. At 10% clearance, the gap flow was turned only about half as much as the main flow, while at 15% clearance the turning was further reduced to about one fifth. Well away from the endwall region, the main flow turning remained essentially unchanged at the zero clearance value of approximately 50°. A simple model, based on the assumption that the gap flow experiences no tangential force, was found to provide reasonable estimates of the mass averaged outlet flow angle with clearance.

The underturning of the leakage flow led to a redistribution of the mass flow across the passage span as the axial velocity of the gap flow increased in response to the low static pressure established at the cascade outlet. This redistribution of the mass flow was found to be quite significant, particularly at 15% clearance, where the gap flow axial velocity was found to be about 30% larger than the mass-averaged value while the midspan axial velocity was reduced by about 20% compared to the mean value. The reduced mass flow rate at midspan resulted in a progressive unloading of the blade with increasing clearance.

In terms of the computational investigation, the Dawes code was found to be a powerful tool for investigating the aerodynamics of damaged turbine blades. The code predicted many of the measured results: the reduction in the midspan loading, the spanwise redistribution of the mass flow, and the attenuation of the driving pressure differences at the endwall were all duplicated to some extent by the Navier-Stokes solver. The most notable discrepancy occurred between the measured and predicted losses. Although the solver does predict a reduction of the endloss at enlarged clearances, this reduction was found to be considerably less than measured.

7.2 Recommendations for Further Study

In the present study, tip damage was taken to consist simply of a clearance gap opened to unusually large clearances. The effects of other forms of tip damage (i.e., rounding of the tip in both the tangential and chordwise directions) still need to be examined. In order to minimize the research time required, this might best be accomplished using a combination of experimental measurements and computational calculations.

The blade pressure differences were found to no longer be representative of the driving pressure differences across the gap at very large clearances; however, it was shown in Section 6.1.5 that the existing tip-leakage loss models are capable of predicting the decrease in loss at extended clearances if the endwall driving pressure differences are used. Further investigations are required, particularly in the gap region, in order to develop a correlation which could be used to predict the attenuation of the driving pressure differences near the endwall with clearance. Such a correlation could be used in conjunction with the existing tip-leakage loss models to give reasonable predictions of the tip-leakage loss for damaged blades.

Further experiments are required to investigate the effects of other parameters (e.g., blade loading, blade geometry, and Mach number) which would influence the loss and flow turning characteristics of damaged blades. Again, the Dawes code could be used to expand and extrapolate from a limited experimental data set.

References

Abbott, M., 1993, "The Aerodynamic Effect of Roughness on the Performance of a Turbine Cascade," M.Eng. Thesis, Department of Mechanical and Aerospace Engineering, Carleton University, Ottawa, Canada.

Ainley, D. G., and Mathieson, G. C. R., 1951, "A Method of Performance Estimation for Axial-Flow Turbines," ARC R&M 2974.

Amrud, K. K., 1985, "Tip Leakage in a Planar Cascade of Turbine Blades," M.Eng. Thesis, Department of Mechanical and Aerospace Engineering, Carleton University, Ottawa, Canada.

Baldwin, B., and Lomax, H., 1978, "Thin Layer Approximation and Algebraic Model for Separated Turbulent Flows," AIAA Paper 78-257.

Benedict, R. P., 1960, "The Response of a Pressure-Sensing System," ASME *Journal of Basic Engineering*, Vol. 82, pp. 482-488.

Benner, M. W., 1994, "Losses in Axial-Flow Turbines at Off-Design Incidence," PhD Thesis in progress, Department of Mechanical and Aerospace Engineering, Carleton University, Ottawa, Canada.

Bindon, J. P., 1987a, "Pressure Distributions in the Tip Clearance Region of an Unshrouded Axial Turbine as Affecting the Problem of Tip Burnout," ASME Paper 87-GT-230.

Bindon, J. P., 1987b, "Visualisation of Tip Clearance Flow in a Linear Turbine Cascade," Proceedings, 8th International Symposium on Air Breathing Engines, ISABE 87-7032, pp. 436-444.

Bindon, J. P., 1989, "The Measurement and Formation of Tip Clearance Loss," ASME *Journal of Turbomachinery*, Vol. 111, No. 3, pp. 257-263.

Booth, T. C., Dodge, P. R., and Hepworth, H. K., 1982, "Rotor-Tip Leakage: Part I - Basic Methodology," ASME *Journal of Engineering for Power*, Vol. 104, pp. 154-161.

Cao, D., 1993, "Flow in an Idealized Turbine Tip Gap," M.Eng. Thesis, Department of Mechanical and Aerospace Engineering, Carleton University, Ottawa, Canada.

Carter, A. D. S., 1948, "Three-Dimensional Flow Theories for Axial Compressors and Turbines," *Proc. Inst. Mech. Engrs.*, Vol. 159, pp. 255-268.

Chan, J. K. K., Yaras, M. I., and Sjolander, S. A., 1994, "Interaction Between Inlet Boundary Layer, Tip-Leakage and Secondary Flows in a Low-Speed Turbine Cascade," ASME Paper 94-GT-250.

Chung, H. T., and Baek, J. H., 1992, "Influence of Trailing-Edge Grid Structure on Navier-Stokes Computation of Turbomachinery Cascade Flow," *International Journal for Numerical Methods in Fluids*, Vol. 15, pp. 883-894.

Cleak, J. G. E., and Gregory-Smith, D. G., 1992, "Turbulence Modelling for Secondary Flow Prediction in a Turbine Cascade," ASME *Journal of Turbomachinery*, Vol. 114, pp. 590-598.

Cue, R. W., and Muir, D. E., 1991, "Engine Performance Monitoring and Troubleshooting Techniques for the CF-18 Aircraft," ASME *Journal of Engineering for Gas Turbines and Power*, Vol. 113, pp. 11-19.

Danias, G., 1987, "Contributions to the Study of Tip Leakage Flow in a Planar Cascade of Turbine Blades," M.Eng. Thesis, Department of Mechanical and Aerospace Engineering, Carleton University, Ottawa, Canada.

Dawes, W. N., 1986a, "Application of Full Navier-Stokes Solvers to Turbomachinery Flow Problems," *Numerical Techniques for Viscous Flow Calculation in Turbomachinery Blading*, V. K. I. Lecture Series 2.

Dawes, W. N., 1986b, "A Computer Program for the Analysis of Three Dimensional Viscous Compressible Flow in Turbomachinery Blade Rows," Whittle Laboratory, Cambridge University, United Kingdom.

Dawes, W. N., 1987, "A Numerical Analysis of the Three-Dimensional Viscous Flow in a Transonic Compressor Rotor and Comparison With Experiment," ASME *Journal of Turbomachinery*, Vol. 109, pp. 83-90.

Dawes, W. N., 1988, "Development of a 3D Navier Stokes Solver for Application to all Types of Turbomachinery," ASME Paper 88-GT-70.

Dawes, W. N., 1990, "A Comparison of Zero and One Equation Turbulence Modelling for Turbomachinery Calculations," ASME Paper 90-GT-303.

Dawes, W. N., 1992a, "Toward Improved Throughflow Capability: The Use of Three-Dimensional Viscous Flow Solvers in a Multistage Environment," ASME *Journal of Turbomachinery*, Vol. 114, pp. 8-17.

Dawes, W. N., 1992b, "The Simulation of Three-Dimensional Viscous Flow in Turbomachinery Geometries Using a Solution-Adaptive Unstructured Mesh Methodology," ASME *Journal of Turbomachinery*, Vol. 114, pp. 528-537.

Dawes, W. N., 1993, "The Extension of a Solution-Adaptive Three-Dimensional Navier-Stokes Solver Toward Geometries of Arbitrary Complexity," ASME *Journal of Turbomachinery*, Vol. 115, pp. 283-295.

Dawes, W. N., 1994a, "A Simulation of the Unsteady Interaction of a Centrifugal Impeller With Its Vaned Diffuser: Flow Analysis," ASME Paper 94-GT-105.

Dawes, W. N., 1994b, "A Numerical Study of the Interaction of a Transonic Compressor Rotor Overtip Leakage Vortex With the Following Stator Blade Row," ASME Paper 94-GT-156.

Denton, J. D., 1993, "Loss Mechanisms in Turbomachines," ASME Paper 93-GT-435.

Dishart, P. T., and Moore, J., 1990, "Tip Leakage Losses in a Linear Turbine Cascade," ASME *Journal of Turbomachinery*, Vol. 112, No. 3, pp. 599-608.

Dominy, R. G., and Hodson, H. P., 1993, "An Investigation of Factors Influencing the Calibration of Five-Hole Probes for Three-Dimensional Flow Measurements," ASME *Journal of Turbomachinery*, Vol. 115, pp. 513-519.

Dunham, J., and Came, P. M., 1970, "Improvements to the Ainley & Mathieson Method of Turbine Performance Prediction," ASME *Journal of Engineering for Power*, Vol. 92, No. 3, pp. 252-256.

Everett, K. N., Gerner, A. A., and Durston, D. A., 1983, "Seven-Hole Probes for High Angle Flow Measurement: Theory and Calibration," AIAA Journal, Vol. 21, pp. 992-998.

Gerner, A. A., and Maurer, C. L., 1981, "Calibration of Seven-Hole Probes Suitable for High Angles in Subsonic Compressible Flows," USAFA-TR-81-4.

Goobie, S. M., 1989, "A Test Section for Investigating the Off-Design Performance of Planar Cascades," M.Eng. Thesis, Department of Mechanical and Aerospace Engineering, Carleton University, Ottawa, Canada.

Gregory-Smith, D. G., Graves, C.P., and Walsh, J. A., 1988, "Growth of Secondary Losses and Vorticity in an Axial Turbine Cascade," ASME *Journal of Turbomachinery*, Vol. 110, pp. 1-8.

Harrison, S., 1989, "Secondary Loss Generation in a Linear Cascade of High-Turning Turbine Blades," ASME Paper 89-GT-47.

Hétu, N., 1993, "Behaviour of Separation Bubbles in Sharp-Edged Gaps of Finite Dimensions," M.Eng. Thesis, Department of Mechanical and Aerospace Engineering, Carleton University, Ottawa, Canada.

Heyes, F. J. G., Hodson, H. P., and Dailey, G. M., 1992, "The Effect of Blade Tip Geometry on the Tip Leakage Flow in Axial Turbine Cascades," ASME *Journal of Turbomachinery*, Vol. 114, pp. 643-651.

Heyes, F. J. G., and Hodson, H. P., 1993, "Measurement and Prediction of Tip Clearance Flow in Linear Turbine Cascades," ASME *Journal of Turbomachinery*, Vol. 115, pp. 376-382.

Inoue, M., Kuroumaru, M., and Fukuhara, M., 1986, "Behaviour of Tip Leakage Flow Behind an Axial Compressor Rotor," ASME *Journal of Engineering for Gas Turbines and Power*, Vol. 108, pp. 7-14.

Inoue, M., and Kuroumaru, M., 1989, "Structure of Tip Clearance Flow in an Isolated Axial Compressor Rotor," ASME *Journal of Turbomachinery*, Vol. 111, pp. 250-256.

Isaacs, D. P., 1994, "The Aerodynamics of Turbine Blades with Trailing Edge Damage," M.Eng. Thesis, Department of Mechanical and Aerospace Engineering, Carleton University, Ottawa, Canada.

Jameson, A., and Baker, T. J., 1984, "Multigrid Solution of the Euler Equations for Aircraft Configurations," AIAA Paper 84-93.

Kacker, S. C., and Okapuu, U., 1982, "A Mean Line Prediction Method for Axial Flow Turbine Efficiency," ASME *Journal of Engineering for Power*, Vol. 104, No. 1, pp. 111-119.

Kang, S., and Hirsch, C., 1993a, "Experimental Study on the Three-Dimensional Flow Within a Compressor Cascade With Tip Clearance: Part I - Velocity and Pressure Fields," ASME *Journal of Turbomachinery*, Vol. 115. pp. 435-443.

Kang, S., and Hirsch, C., 1993b, "Experimental Study on the Three-Dimensional Flow Within a Compressor Cascade With Tip Clearance: Part II - The Tip Leakage Vortex," ASME *Journal of Turbomachinery*, Vol. 115, pp. 444-452.

Kind, R. J., Sjolander, S. A., and Yaras, M. I., 1944, "Retained Lift: Theoretical Difficulties With the Concept and an Alternative Explanation of Observations," Technical Review, accepted for publication by ASME Transactions.

Lakshminarayana, B., and Horlock, J. H., 1962, "Tip-Clearance Flow and Losses for an Isolated Compressor Blade," ARC R&M 3316.

Lewis, W. E., 1966, "Fixed-Direction Probes for Aerodynamic Measurements," *Proc. Inst. Mech. Engrs.*, Vol. 180, pp. 141-152.

Lewis, R. I., and Yeung, E. H. C., 1977, "Vortex Shedding Mechanisms In Relation to Tip Clearance Flows and Losses in Axial Fans," ARC R&M 3829.

Moore, J., 1983, "Flow Trajectories, Mixing and Entropy Fluxes in a Turbine Cascade," AGARD-CP-351.

Moore, J., and Adhye, R. Y., 1985, "Secondary Flows and Losses Downstream of a Turbine Cascade," ASME *Journal of Engineering for Gas Turbines and Power*, Vol. 107, pp. 961-968.

Moore, J., and Moore, J. G., 1985, "Performance Evaluation of Linear Turbine Cascades Using Three-Dimensional Viscous Flow Calculations," ASME *Journal of Engineering for Gas Turbines and Power*, Vol. 107, pp. 969-975.

Moore, J., and Tilton, J. S., 1988, "Tip Leakage Flow in a Linear Turbine Cascade," ASME *Journal of Turbomachinery*, Vol. 110, pp. 18-26.

Moore, J., Moore, J. G., Heckel, S. P., and Ballesteros, R., 1994, "Reynolds Stresses and Dissipation Mechanisms in a Turbine Tip Leakage Vortex," ASME Paper 94-GT-267.

Rains, D. A., 1954, "Tip Clearance Flows in Axial Flow Compressors and Pumps," California Institute of Technology, Hydrodynamics and Mechanical Engineering Laboratories, Report No. 5, June.

Roache, P. J., 1994, "Perspective: A Method for Uniform Reporting of Grid Refinement Studies," ASME *Journal of Fluids Engineering*, Vol. 116, pp. 405-413.

Rodger, P., 1992, "Establishing Two-Dimensional Flow in a Large-Scale Planar Turbine Cascade," M.Eng. Thesis, Department of Mechanical and Aerospace Engineering, Carleton University, Ottawa, Canada.

Rodger, P., Sjolander, S. A., and Moustapha, S. H., 1992, "Establishing Two-Dimensional Flow in a Large-Scale Planar Turbine Cascade," AIAA Paper 92-3066.

Sharma, O. P., and Butler, T. L., 1987, "Predictions of Endwall Losses and Secondary Flows in Axial Flow Turbine Cascades," ASME *Journal of Turbomachinery*, Vol. 109, pp. 229-236.

Sieverding, C. H., 19c5, "Secondary Flows in Straight and Annular Turbine Cascades," Thermodynamics and Fluid Mechanics of Turbomachinery, Vol. II, Proceedings of NATO Advanced Study Institute.

Sieverding, C. H., and Van den Bosch, P., 1983, "The Use of Coloured Smoke to Visualize Secondary Flows in a Turbine-Blade Cascade," Journal of Fluid Mechanics, Vol. 134, pp. 85-89.

Sitaram, N., Lakshminarayana, B., and Ravindranath, A., 1981, "Conventional Probes for the Relative Flow Measurement in a Turbomachinery Rotor Blade Passage," ASME *Journal of Engineering for Power*, Vol. 103, pp. 406-414.

Sjolander, S. A., 1994, Private Communication, Carleton University, Ottawa, Canada.

Sjolander, S. A., and Amrud, K. K., 1987, "Effects of Tip Clearance on Blade Loading in a Planar Cascade of Turbine Blades," ASME *Journal of Turbomachinery*, Vol. 109, No. 2, pp. 237-245.

Sjolander, S. A., and Cao, D., 1994, "Measurements of the Flow in an Idealized Turbine Tip Gap," ASME Paper 94-GT-74.

Sjolander, S. A., Isaacs, D., and Klein, W. A., 1993, "Aerodynamics of Turbine Blades with Trailing-Edge Damage: Measurements and Computations," Proceedings, XI International Symposium on Air Breathing Engines, Vol. II, pp. 1327-1334.

Storer, J. A., and Barton, J. P., 1991, "An Investigation of the Flow Within the Clearance Space of a Compressor Blade Tip," Proceedings, 10th International Symposium on Air Breathing Engines, pp. 143-151.

Storer, J. A., and Cumpsty, N. A., 1991, "Tip Leakage Flow in Axial Compressors," ASME *Journal of Turbomachinery*, Vol. 113, pp. 252-259.

Storer, J. A., and Cumpsty, N. A., 1993, "An Approximate Analysis and Prediction Method for Tip Clearance Loss in Axial Compressors," ASME Paper 93-GT-140.

Tremblay, B., 1989, "Measurement and Correlation of Off-Design Performance of Axial-Flow Turbines," M.Eng. Thesis, Department of Mechanical and Aerospace Engineering, Carleton University, Ottawa, Canada.

Turner, M. G., Liang, T., Beauchamp, P. P., and Jennions, I. K., 1993, "The Use of Orthogonal Grids in Turbine CFD Computations," ASME Paper 93-GT-38.

Vavra, M. H., 1960, *Aero-Thermodynamics and Flow in Turbomachines*, John Wiley and Sons, Inc., New York.

Verhiel, J. R., 1994, "Prediction of the Effects of Spanwise Mixing for Turbines with Damaged Blades," M.Eng. Thesis, Department of Mechanical and Aerospace Engineering, Carleton University, Ottawa, Canada.

Walker, P. J., and Dawes, W. N., 1990, "The Extension and Application of Three-Dimensional Time-Marching Analyses to Incompressible Turbomachinery Flows," ASME *Journal of Turbomachinery*, Vol. 112, pp. 385-390.

Walsh, J. A., and Gregory-Smith, D. G., 1990, "Inlet Skew and the Growth of Secondary Losses and Vorticity in a Turbine Cascade," ASME *Journal of Turbomachinery*, Vol. 112, pp. 633-642.

Whitehouse, D. R., 1992, "The Effect of Axial Velocity Ratio, Turbulence Intensity, Incidence and Leading Edge Geometry on the Off-Design Performance of a Turbine Blade Cascade," M.Eng. Thesis, Department of Mechanical and Aerospace Engineering, Carleton University, Ottawa, Canada.

Yamamoto, A., 1988, "Interaction Mechanisms Between Tip Leakage Flow and the Passage Vortex in a Linear Turbine Rotor Cascade," ASME *Journal of Turbomachinery*, Vol. 110, No. 3, pp. 329-338.

Yamamoto, A., 1989, "Endwall Flow/Loss Mechanisms in a Linear Turbine Cascade With Blade Tip Clearance," ASME *Journal of Turbomachinery*, Vol. 111, No. 3, pp. 264-275.

Yaras, M. I., 1987, "Flow in the Tip Gap of a Rectangular Turbine Cascade," M.Eng. Thesis, Department of Mechanical and Aerospace Engineering, Carleton University, Ottawa, Canada.

Yaras, M. I., 1990, "Measurements and Prediction of Tip-Clearance Effects in a Linear Turbine Cascade," PhD Thesis, Department of Mechanical and Aerospace Engineering, Carleton University, Ottawa, Canada.

Yaras, M. I., and Sjolander, S. A., 1989, "Losses in the Tip-Leakage Flow of a Planar Cascade of Turbine Blades," AGARD-CP-469, "Secondary Flows in Turbomachines," Paper 20.

Yaras, M. I., Zhu, Y., and Sjolander, S. A., 1989, "Flow Field in the Tip Gap of a Planar Cascade of Turbine Blades," ASME *Journal of Turbomachinery*, Vol. 111, No. 3, pp. 276-283.

Yaras, M. I., and Sjolander, S. A., 1990, "Development of the Tip-Leakage Flow Downstream of a Planar Cascade of Turbine Blades: Vorticity Field," ASME *Journal of Turbomachinery*, Vol. 112, pp. 609-617.

Yaras, M. I., and Sjolander, S. A., 1991, "Review of Studies on Tip Clearance Effects in Axial Turbomachinery," Report No. M&AE 91-3, Department of Mechanical and Aerospace Engineering, Carleton University, Ottawa, Canada, April.

Yaras, M. I., and Sjolander, S. A., 1992a, "Prediction of Tip-Leakage Losses in Axial Turbines," ASME *Journal of Turbomachinery*, Vol. 114, pp. 204-210.

Yaras, M. I., and Sjolander, S. A., 1992b, "Effects of Simulated Rotation on Tip Leakage in a Planar Cascade of Turbine Blades: Part I - Tip Gap Flow," ASME *Journal of Turbomachinery*, Vol. 114, pp. 652-659.

Yaras, M. I., Sjolander, S. A., and Kind, R. J., 1992, "Effects of Simulated Rotation on Tip Leakage in a Planar Cascade of Turbine Blades: Part II - Downstream Flow Field and Blade Loading," ASME *Journal of Turbomachinery*, Vol. 114, pp. 660-667.

Appendices

Appendix A
Blade and Cascade Geometry

This appendix summarizes the geometric and aerodynamic parameters of the current cascade and CC1 blade:

Inlet flow angle, α_1	0.0°
Inlet metal angle, β_1	11.1°
Exit metal angle, β_2	49.6°
Metal turning, $\Delta\beta$	60.7°
Design incidence, i_{des}	-11.1°
Stagger, γ	37.2°
Leading-edge wedge angle, We	54.0°
Chord length, c	250 mm
Axial chord length, c_x	199 mm
Blade spacing, S	150 mm
Blade span, h	203 mm
Pitch-to-chord ratio, S/c	0.600
Aspect ratio, h/c	0.812
Leading-edge diameter-to-chord ratio, d/S	0.00677
Maximum thickness-to-chord ratio, t_{max}/c	0.0984
Zweifel Coefficient, ψ_T	0.74

Appendix B
Control Surface Settings at Various Clearances

This appendix tabulates the control surface settings used to establish a uniform inlet flow and a reasonably periodic outlet flow at each clearance studied. These settings are included:

1) to fully document each test case for repeatability purposes; and
2) in the hopes that one day such a matrix will be useful to future experimental studies involving the cascade.

A schematic diagram of the test section control surfaces is given in Figure B.1. As illustrated in the figure, all angles are positive measured clockwise from the horizontal.

Clearance Size τ/c	Control Surface Settings				
	Upper Tailboard [deg]	Lower Tailboard [deg]	Upper Sideflap [deg]	Lower Sideflap [deg]	Boundary Layer Bleed Holes
0.00	48.5	46.5	-11	-30	Not used
0.10	52.0	47.5	5	-30	Not used
0.15	53.0	48.5	6	-30	Not used

Table B.1 Control surface settings.

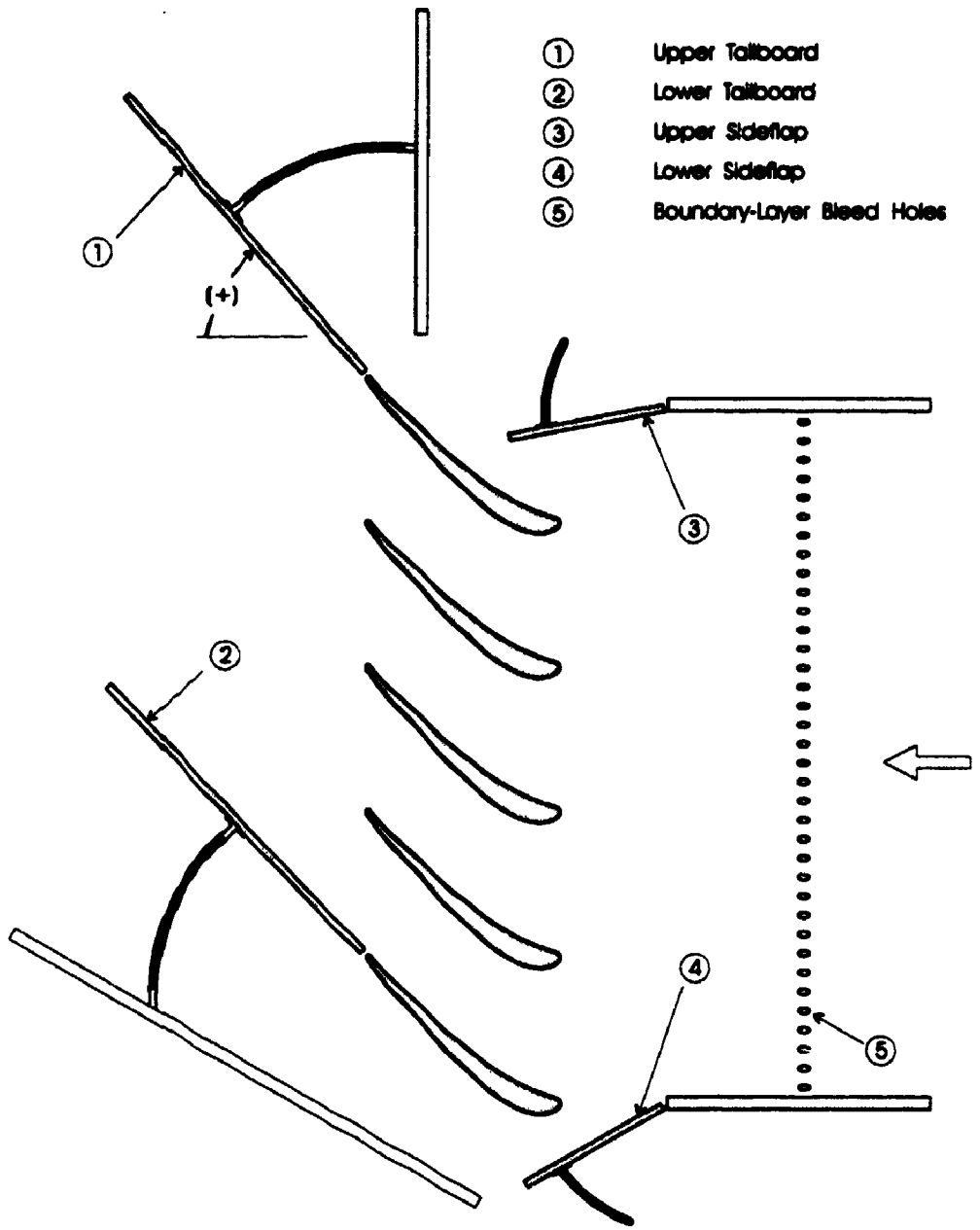

Figure B.1 Schematic of the test section control surfaces.

Appendix C
Blade Surface Static Tap Locations

This appendix lists the blade surface static tap locations relative to the co-ordinate system shown in Figure C.1. The position of each pressure tap row, relative to the blade tip, is also tabulated.

Suction surface static tap locations					
Tap No.	x [inches]	y [inches]	Tap No.	x [inches]	y [inches]
1	-3.2052	2.8267	21	0.5801	0.0701
2	-2.9803	3.0725	22	0.7399	-0.1905
3	-2.7554	3.1290	23	0.8984	-0.4560
4	-2.5317	3.1364	24	1.0582	-0.7276
5	-2.2872	3.0971	25	1.2179	-1.0053
6	-2.0844	3.0283	26	1.3765	-1.2892
7	-1.8472	2.9140	27	1.5363	-1.5768
8	-1.6112	2.7689	28	1.6948	-1.8718
9	-1.4220	2.6276	29	1.8533	-2.1704
10	-1.2155	2.4543	30	2.0131	-2.4752
11	-1.0400	2.2884	31	2.1716	-2.7825
12	-0.8677	2.1053	32	2.3290	-3.0946
13	-0.6932	1.9049	33	2.4875	-3.4105
14	-0.5334	1.7083	34	2.6448	-3.7288
15	-0.3748	1.4982	35	2.8033	-4.0496
16	-0.2175	1.2794	36	2.9275	-4.3089
17	-0.0578	1.0483	37	3.0541	-4.5682
18	0.1020	0.8136			
19	0.2618	0.5715			
20	0.4203	0.3232			

Pressure surface static tap locations					
Tap No.	x [inches]	y [inches]	Tap No.	x [inches]	y [inches]
38	-3.0664	2.6104	58	0.2913	-0.6268
39	-2.8980	2.5145	59	0.4510	-0.8480
40	-2.7394	2.4187	60	0.6108	-1.0741
41	-2.5809	2.3167	61	0.7706	-1.3015
42	-2.3830	2.1827	62	0.9304	-1.5338
43	-2.1999	2.0512	63	1.0889	-1.7673
44	-2.0070	1.9025	64	1.2474	-2.0033
45	-1.8312	1.7599	65	1.4072	-2.2429
46	-1.6555	1.6100	66	1.5670	-2.4850
47	-1.4809	1.4502	67	1.7648	-2.7947
48	-1.3052	1.2818	68	2.0426	-3.2360
49	-1.1454	1.1208	69	2.2331	-3.5506
50	-0.9857	0.9537	70	2.4064	-3.8455
51	-0.8271	0.7780	71	2.5784	-4.1442
52	-0.6673	0.5961	72	2.7272	-4.4109
53	-0.5063	0.4068	73	2.8734	-4.6825
54	-0.3466	0.2114			
55	-0.1880	0.0098			
56	-0.0283	-0.1966			
57	0.1315	-0.4093			

Blade-surface-pressure-tap row locations relative to the blade tip			
Row No.	Δz/h	Row No.	Δz/h
1	0.0212	8	0.1943
2	0.0460	9	0.2190
3	0.0707	10	0.2684
4	0.0954	11	0.3178
5	0.1201	12	0.3673
6	0.1448	13	0.4167
7	0.1695	14	0.4661

Table C.1 Blade surface static tap locations.

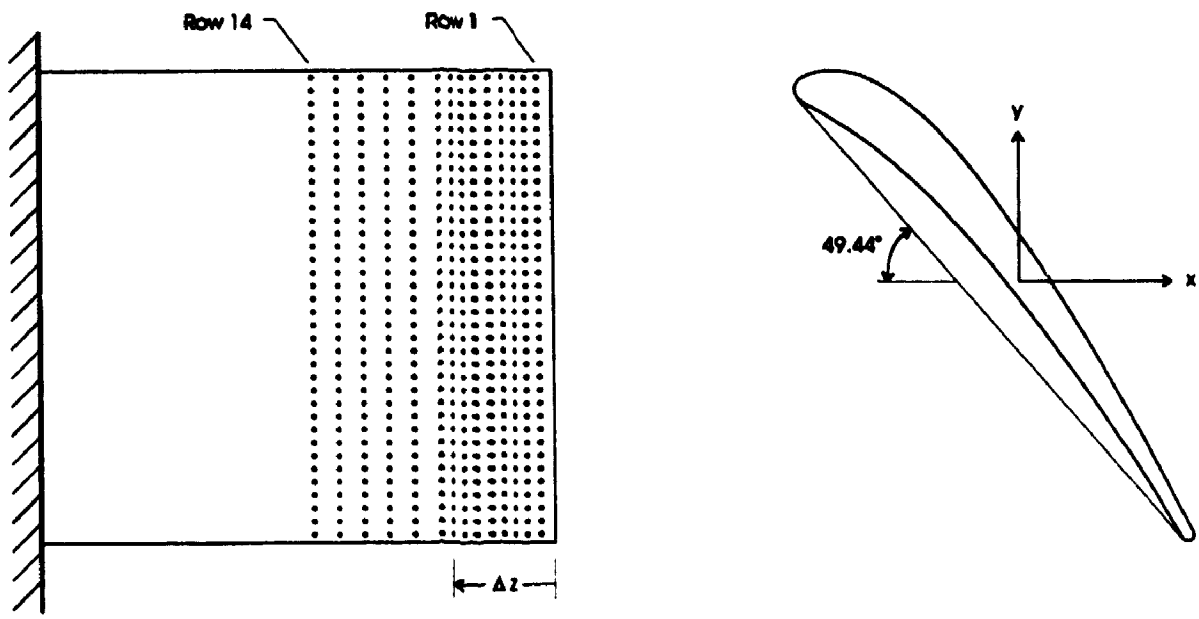

Figure C.1 Co-ordinate system for blade static tap locations.

Appendix D
Three-Hole Probe Calibration Procedure

This appendix describes the procedure used to calibrate the three-hole probe. The probe was previously calibrated by Yaras (1990) over a wide range of flow angles varying from -70° to +70° at a one degree increment. However, it was observed from preliminary outlet flow periodicity measurements that the flow angles at midspan were typically less than ±5°. For this reason, the probe was recalibrated over a range of ±10° using a smaller 0.5° interval for increased accuracy.

The calibration data is reduced to form the following non-dimensional coefficients according to the method of Lewis (1966):

$$
\begin{aligned}
K_1 &= \frac{P_1 - P_s}{q} \\
K_{12} &= \frac{P_1 - P_2}{q} \\
K_{13} &= \frac{P_1 - P_3}{q} \\
K_{\phi 2} &= \frac{P_1 - P_2}{P_1 - P_3} \\
K_{\phi 3} &= \frac{P_1 - P_3}{P_1 - P_2}
\end{aligned}
\tag{D.1}
$$

where the pressure indices correspond to the port numbering shown in Figure D.1.

During the data reduction, the sign of the flow angle relative to the probe axis is determined by comparing probe pressures P_2 and P_3. The magnitude of the flow misalignment angle is obtained from either the $K_{\phi 2}$ or the $K_{\phi 3}$ coefficients, depending on whether the misalignment angle is positive or negative. It can be observed from Figures D.2 and D.3 that $K_{\phi 2}$ is more sensitive to flow misalignment changes at positive yaw angles while $K_{\phi 3}$ is most sensitive at negative yaw angles. Once the flow angle is determined, the local dynamic pressure can be extracted using either the K_{12} or the K_{13} coefficients. Again, it can be observed from Figures D.4 and D.5 that K_{12} appears better suited for negative yaw angles where less scatter is encountered, while K_{13} is most suitable for positive yaw angles. Lastly, the static pressure can be calculated using the K_1 coefficient and the known values of flow angle and dynamic pressure.

Yaras (1987) studied in some detail the effects of Reynolds number changes on the three-hole probe calibration curves. The results showed that the probe became sensitive to Reynolds number effects only at large flow misalignments, typically in excess of ±50°, and that these effects were in fact negligible within ±10°. For further information on the probe sensitivity to Reynolds number effects or the effects of pitch misalignment the reader is referred to Yaras (1987).

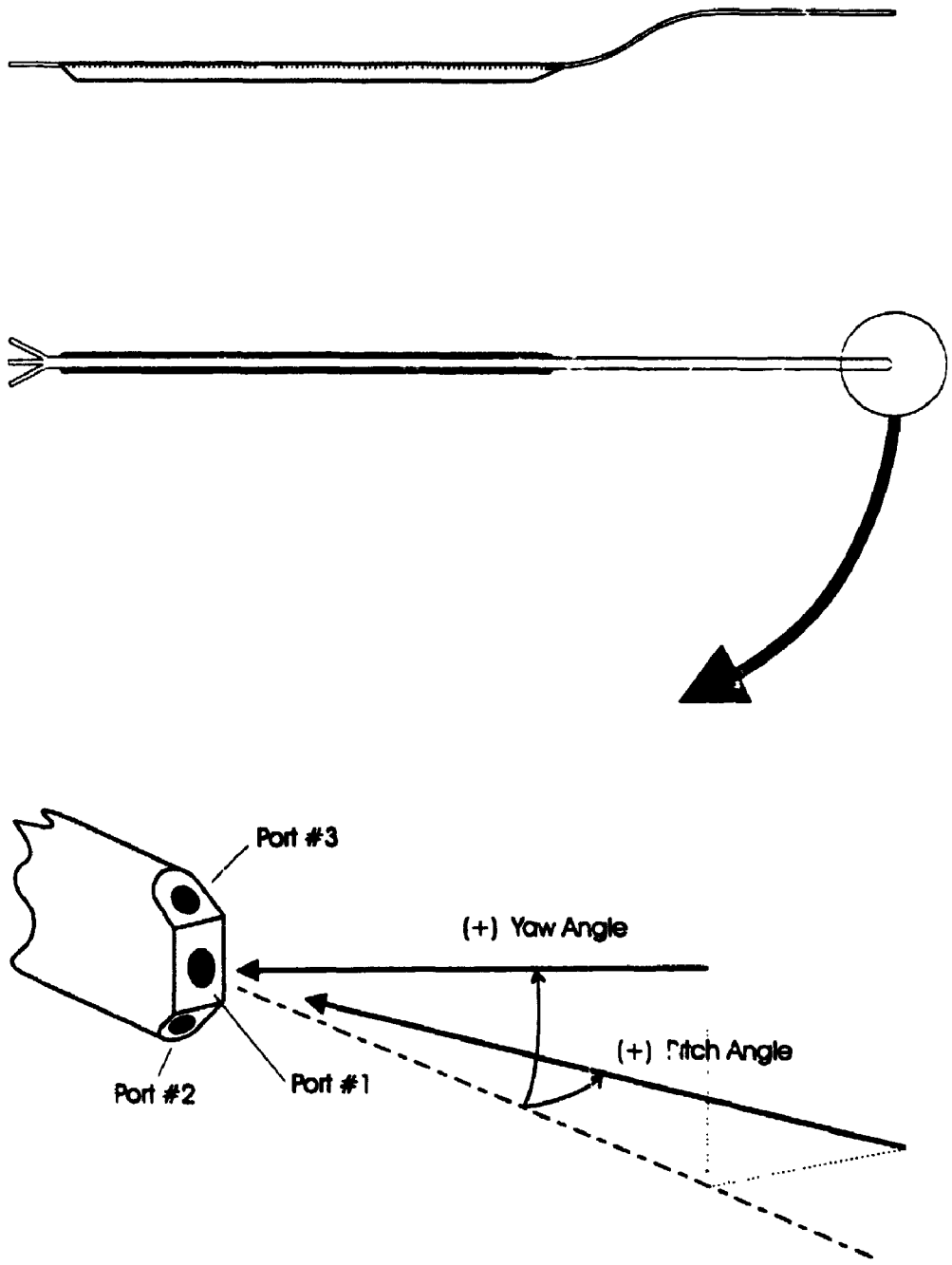

Figure D.1 Three-hole probe port numbering.

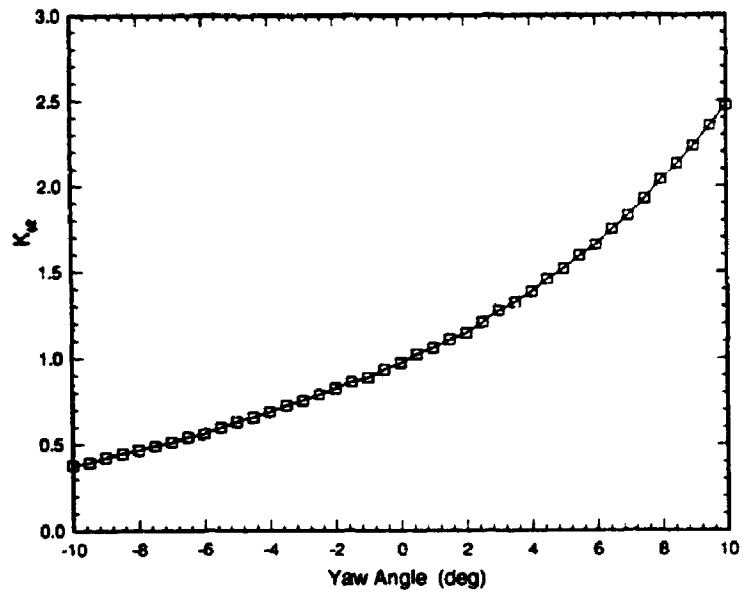

Figure D.2 Variation of $K_{\phi 2}$ with yaw angle.

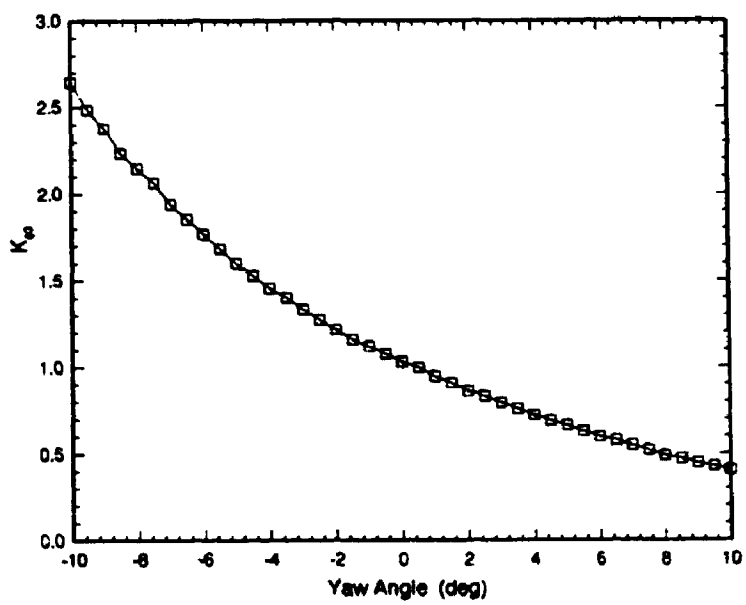

Figure D.3 Variation of $K_{\phi 3}$ with yaw angle.

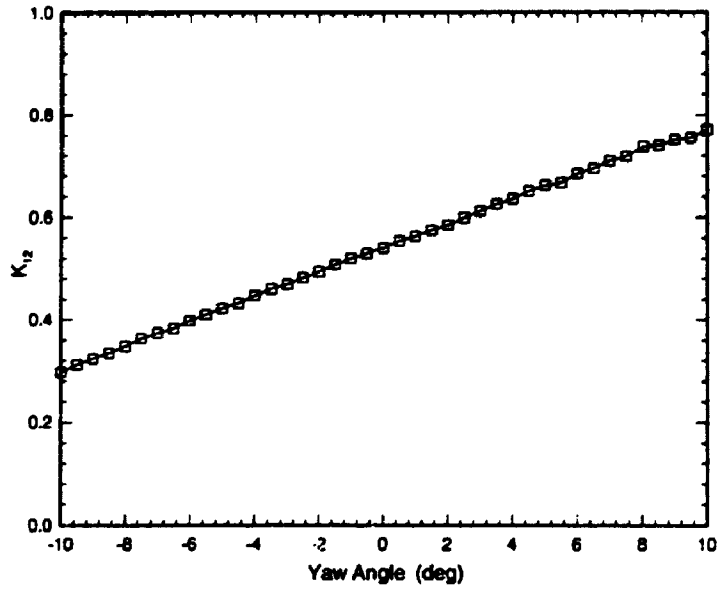

Figure D.4 Variation of K_{12} with yaw angle.

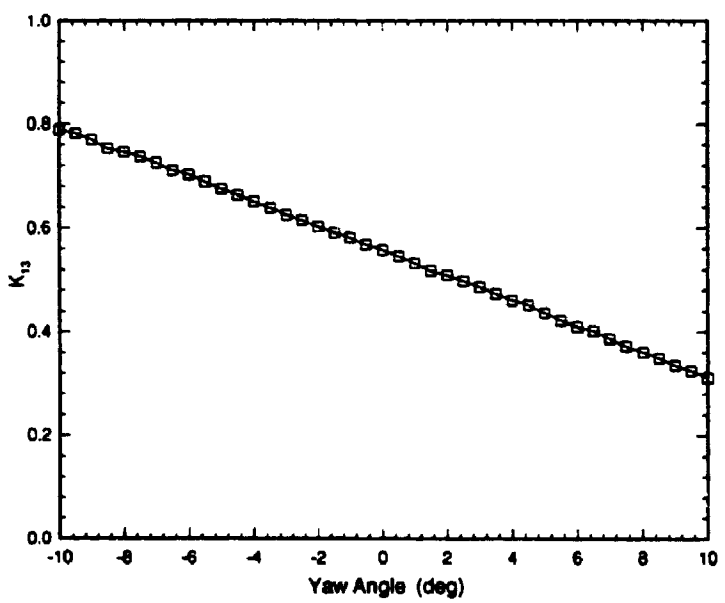

Figure D.5 Variation of K_{13} with yaw angle.

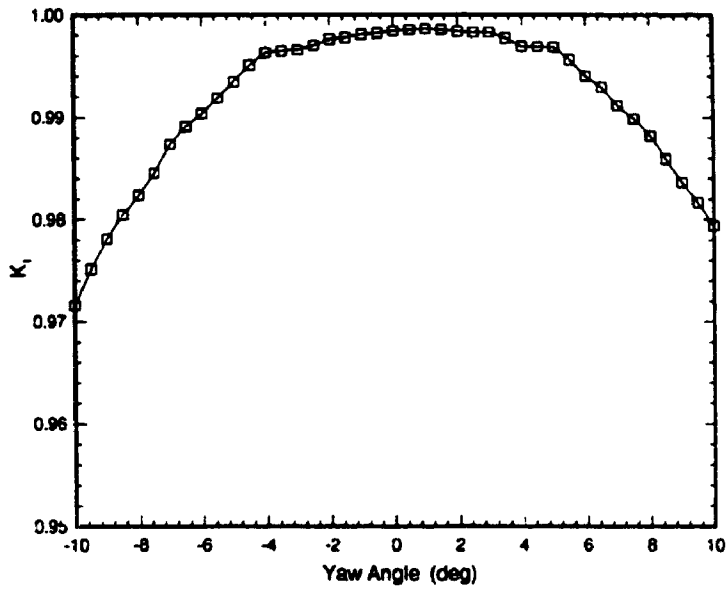

Figure D.6 Variation of K_1 with yaw angle.

Appendix E
Seven-Hole Probe Calibration Procedure

This appendix describes the procedure used in the calibration of the seven-hole probe for use in the non-nulling mode. The basic theory described herein was first proposed by Gerner & Maurer (1981). The present calibration method is only valid for incompressible flows; extension to compressible flows (e.g., Gerner & Maurer (1981), Everett *et al.* (1983)) requires the inclusion of an additional independent pressure coefficient in order to account for compressibility effects.

Low Angle Regime:

At small misalignment angles, the flow over the probe is expected to remain attached and all seven pressure port readings (see Figure E.1) are used to define the following non-dimensional parameters:

$$C_{\alpha_1} = \frac{P_4 - P_1}{P_7 - \overline{P_{1\to 6}}}$$

$$C_{\alpha_2} = \frac{P_3 - P_6}{P_7 - \overline{P_{1\to 6}}} \qquad \text{(E.1)}$$

$$C_{\alpha_3} = \frac{P_2 - P_5}{P_7 - \overline{P_{1\to 6}}}$$

where $\overline{P_{1\to 6}}$ is the average of the six surrounding peripheral port pressures. The numerator in each non-dimensional parameter is based on the difference between diametrically opposed pressure port readings. This implies that the coefficients are sensitive to flow angularity in three separate planes, each 60° apart, passing through the probe axis. The denominator in the above expressions, referred to as the *pseudo-dynamic*

pressure, measures the difference between the central port pressure, P_7, which approximates the total pressure at small flow misalignments, and the average of the surrounding port pressures, $\overline{P_{1\to 6}}$, which approximates the local static pressure.

Of the three coefficients, only two are required to uniquely define the flow direction. By equally weighing each coefficient of Equation E.1 along the two tangential coordinate axes shown in Figure E.2, the following angle coefficients are defined:

$$C_\alpha = \frac{2C_{\alpha_1} + C_{\alpha_2} - C_{\alpha_3}}{3}$$
$$C_\beta = \frac{C_{\alpha_2} + C_{\alpha_3}}{\sqrt{3}} \tag{E.2}$$

By calibrating the probe in a known flow, the local pitch angle, α, yaw angle, β, total-pressure coefficient, C_{P_t}, and dynamic pressure coefficient, C_q, can all be related to the two non-dimensional coefficients of Equation E.2:

$$\alpha = f_1(C_\alpha, C_\beta)$$
$$\beta = f_2(C_\alpha, C_\beta)$$
$$C_{P_t} = f_3(C_\alpha, C_\beta) \tag{E.3}$$
$$C_q = f_4(C_\alpha, C_\beta)$$

where the total- and dynamic-pressure coefficients are defined as follows:

$$C_{P_t} = \frac{P_7 - P_o}{P_7 - \overline{P_{1\to 6}}}$$
$$C_q = \frac{P_7 - \overline{P_{1\to 6}}}{P_o - P} \tag{E.4}$$

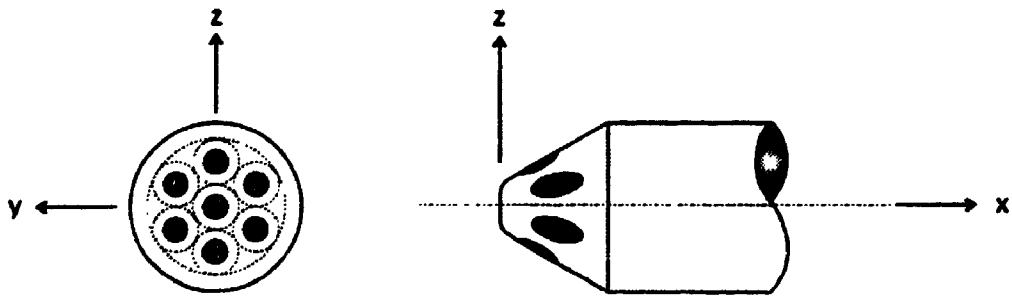

Figure E.1 Seven-hole probe port numbering scheme.

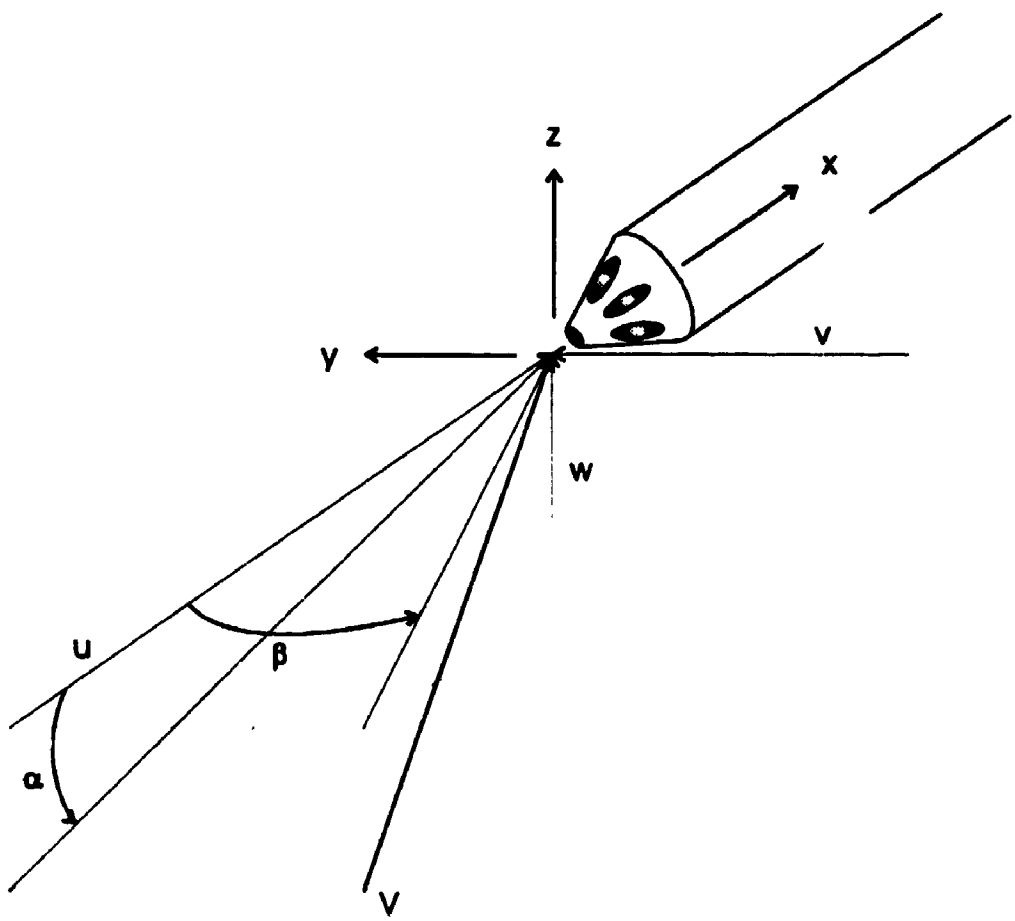

Figure E.2 Tangential coordinate system used for low angle regime.

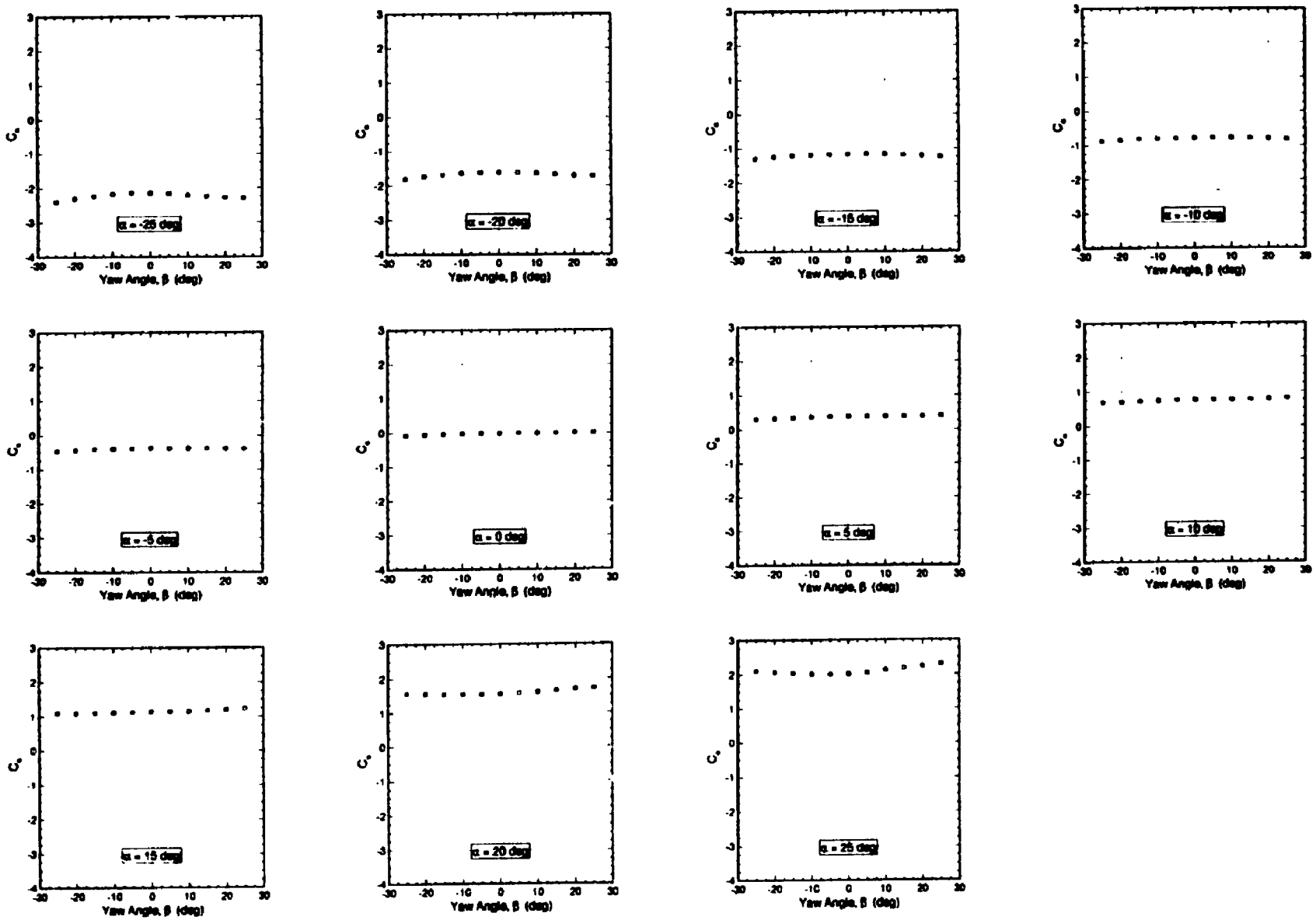

Figure E.3 C_α calibration data for Sector 7.

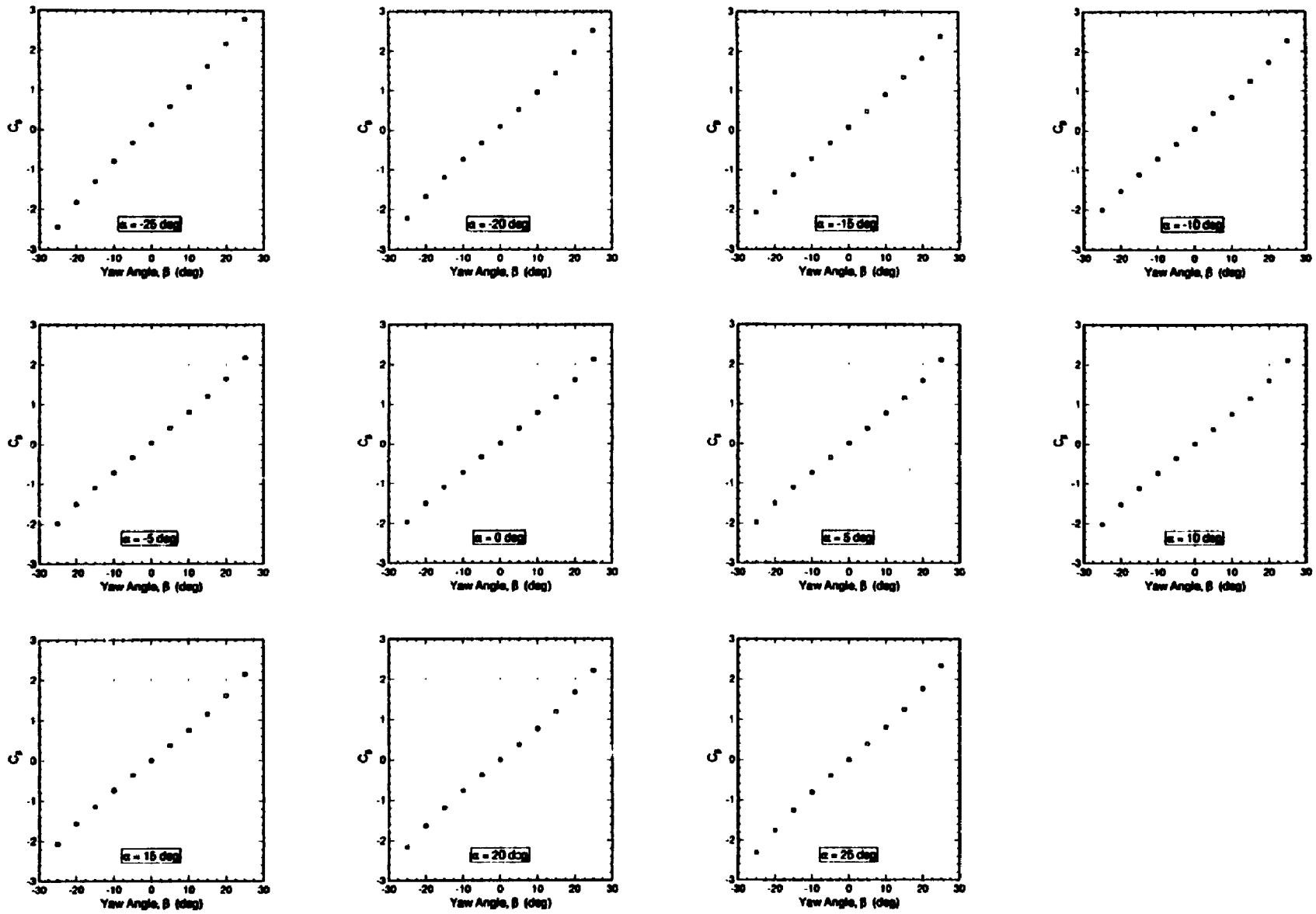

Figure E.4 C_β calibration data for Sector 7.

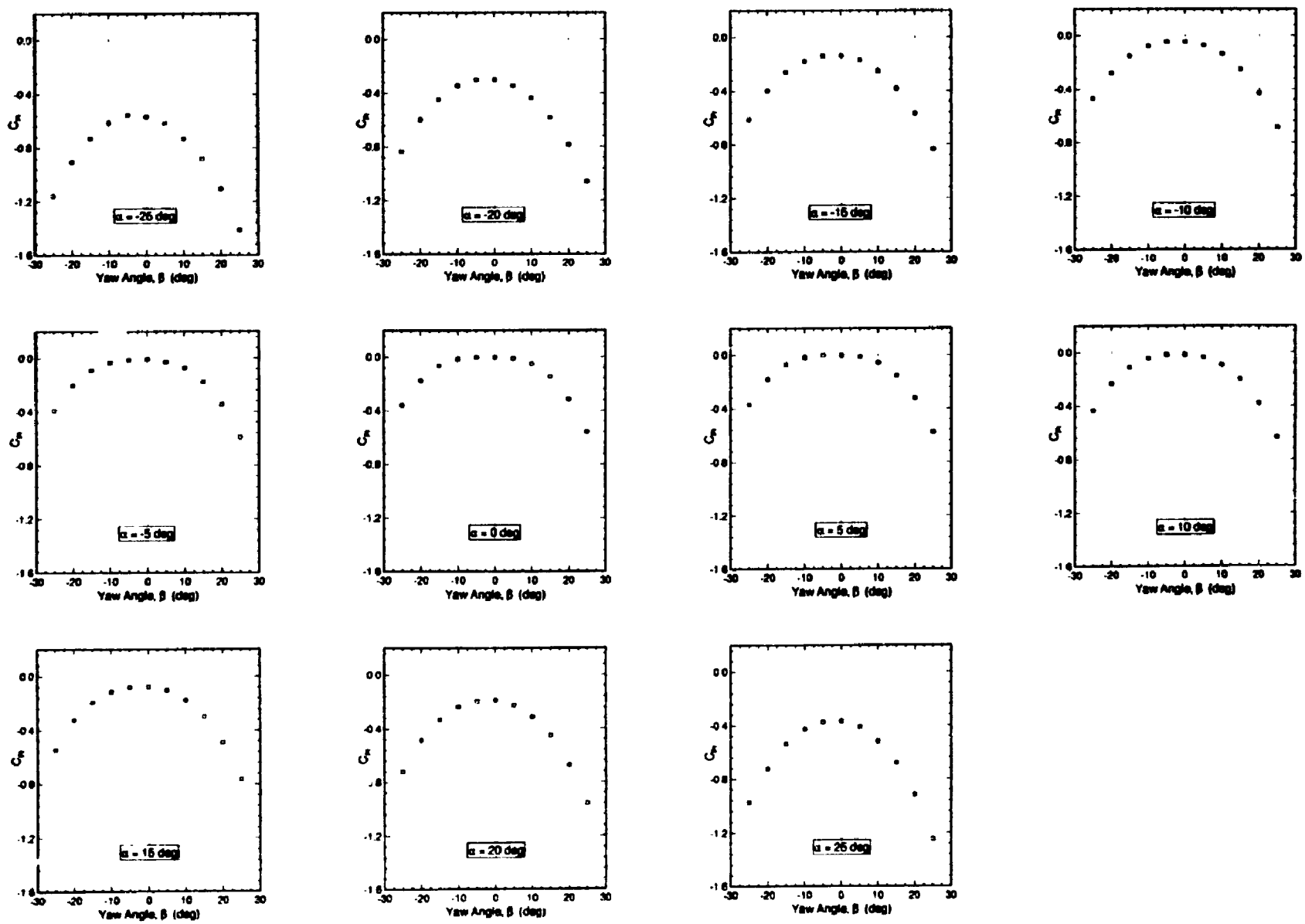

Figure E.5 C_{P_t} calibration data for Sector 7.

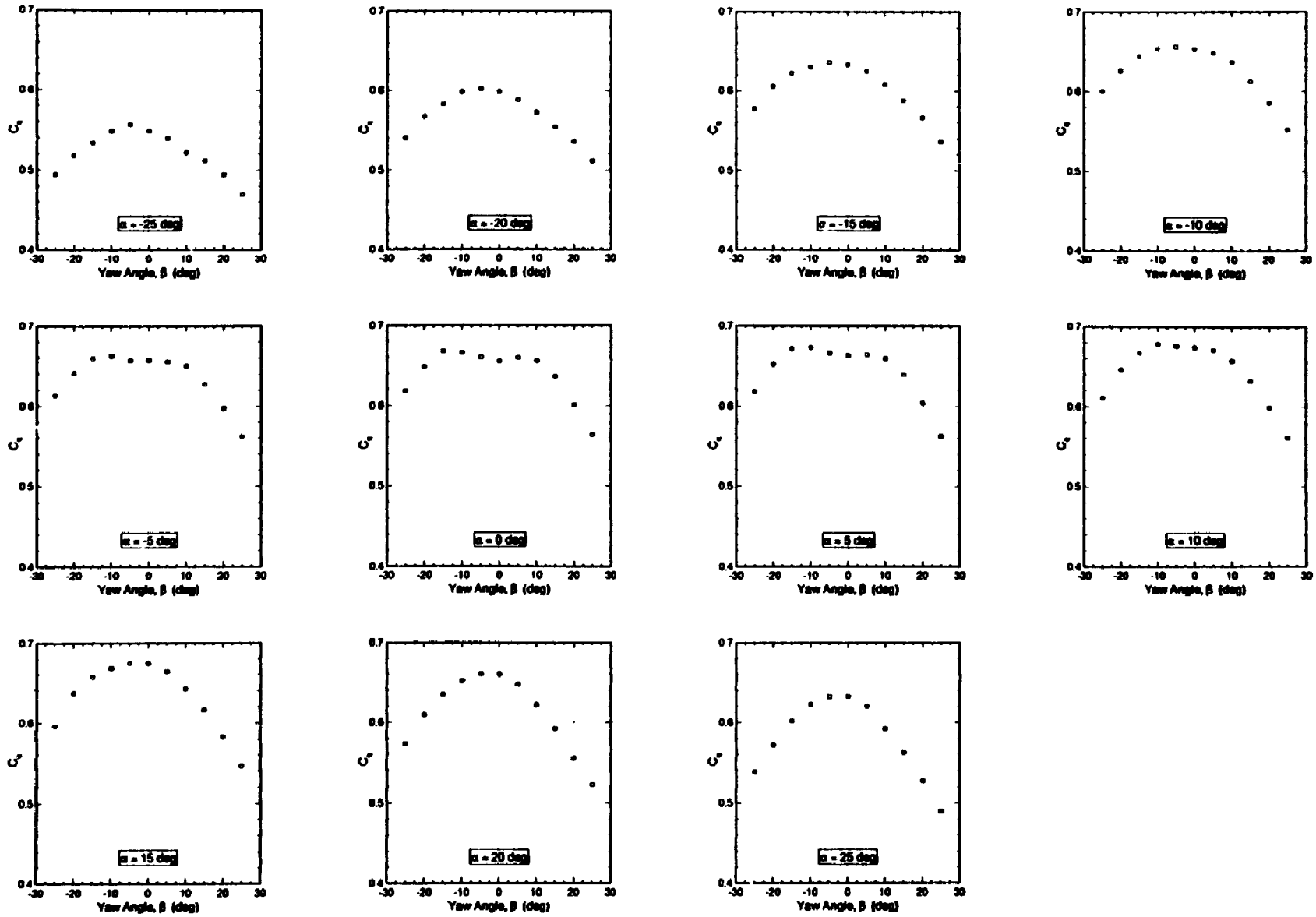

Figure E.6 C_q calibration data for Sector 7.

The low-angle-regime procedure outlined above is used as long as the central port reads the highest pressure, which is typical of flow misalignment angles of less than 25°. Figures E.3 to E.6 present the low-angle-regime calibration data obtained at a reference velocity of approximately 30 m/sec.

High Angle Regime:

At large flow misalignment angles the flow will tend to separate over the leeward side of the probe. It is therefore necessary to redefine the pressure coefficients so that they contain only the port pressures in the attached flow region. This is done by grouping the pressure ports into six 60° wedge-shaped sectors each containing the central port and three adjacent peripheral ports; Figure E.7 shows the resultant spacial division.

At large misalignment angles, Gerner & Maurer (1981) found that it was more appropriate to use a polar coordinate system, shown in Figure E.8, to define the non-dimensional calibration coefficients:

$$C_{\theta_n} = \frac{P_n - P_7}{P_n - \frac{P_{n-} + P_{n+}}{2}}$$

$$C_{\phi_n} = \frac{P_{n-} - P_{n+}}{P_n - \frac{P_{n-} + P_{n+}}{2}} \qquad \text{(E.5)}$$

where the subscripts n, $n+$, and $n-$ represent the peripheral-pressure-port number, and the adjacent ports clockwise and counterclockwise to port n, respectively. These non-dimensional coefficients can be related to the pitch angle, θ, roll angle, ϕ, total pressure coefficient, C_{P_t}, and dynamic pressure coefficient, C_q, as follows:

$$
\begin{aligned}
\theta_n &= f_1(C_{\theta_n}, C_{\phi_n}) \\
\phi_n &= f_2(C_{\theta_n}, C_{\phi_n}) \\
C_{P_{t_n}} &= f_3(C_{\theta_n}, C_{\phi_n}) \\
C_{q_n} &= f_4(C_{\theta_n}, C_{\phi_n})
\end{aligned}
\tag{E.6}
$$

where the total- and dynamic-pressure coefficients are given by:

$$
\begin{aligned}
C_{P_{t_n}} &= \frac{P_n - P_o}{P_n - \dfrac{P_{n-} + P_{n+}}{2}} \\
C_{q_n} &= \frac{P_n - \dfrac{P_{n-} + P_{n+}}{2}}{P_o - P}
\end{aligned}
\tag{E.7}
$$

Similar to the low angle regime, the functions in Equation E.6 can be determined by calibrating the probe in a known flow. Figures E.9 to E.12 present the high-angle-regime calibration data for Sector 1 obtained at a reference velocity of 30 m/sec.

<u>Data Reduction Software:</u>

A data reduction program for the seven-hole probe was developed by Benner (1994). The program, written in Turbo Pascal, expects an input file of the following format:

$$
\begin{array}{lllllll}
N & & & & & & \\
C_{P_1} & C_{P_2} & C_{P_3} & C_{P_4} & C_{P_5} & C_{P_6} & C_{P_7} \qquad : \textit{first data point} \\
 & & & \vdots & & & \\
C_{P_1} & C_{P_2} & C_{P_3} & C_{P_4} & C_{P_5} & C_{P_6} & C_{P_7} \qquad : \textit{Nth data point}
\end{array}
$$

The static pressure coefficients, listed above, are based on the measured port pressures and are defined as follows:

$$C_{P_n} = \frac{P_n - P_{ref}}{q_{ref}}, \quad n = 1 \ldots 7 \tag{E.8}$$

where P_{ref} is the reference static pressure and q_{ref} is the reference dynamic pressure. The program identifies the sector to which the data belongs and then uses a bilinear interpolation scheme to extract the following flow parameters:

$$\alpha, \beta, C_{P_o}, C_{P_q}, \frac{u}{V}, \frac{v}{V}, \frac{w}{V}$$

where the flow angles (α, β) and the non-dimensional velocities $\left(\frac{u}{V}, \frac{v}{V}, \frac{w}{V}\right)$ are referenced to the probe axis (see Figure E.2). A coordinate transformation is then used to obtain the flow angles and non-dimensional velocities for the cascade frame-of-reference. C_{P_o} and C_{P_q} are non-dimensional forms of the total and dynamic pressures and are defined as

$$C_{P_o} = \frac{P_o - P_{ref}}{q_{ref}}$$
$$C_{P_q} = \frac{q}{q_{ref}} \tag{E.9}$$

where P_o and q are the local total pressure and dynamic pressure, respectively.

3 of/de 3

PM-1 3½"x4" PHOTOGRAPHIC MICROCOPY TARGET
NBS 1010a ANSI/ISO #2 EQUIVALENT

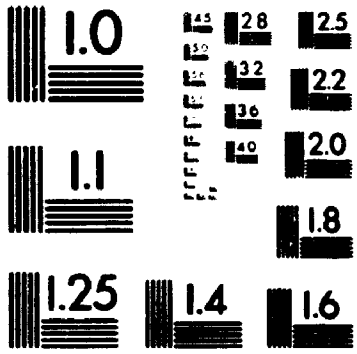

PRECISION℠ RESOLUTION TARGETS

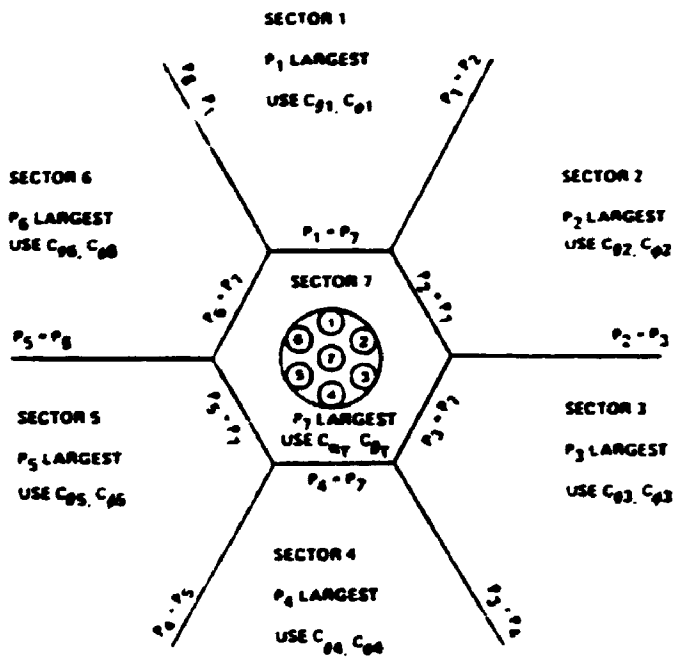

Figure E.7 Division of angular space by Gerner *et al.* (1984); reproduced from Danias (1987).

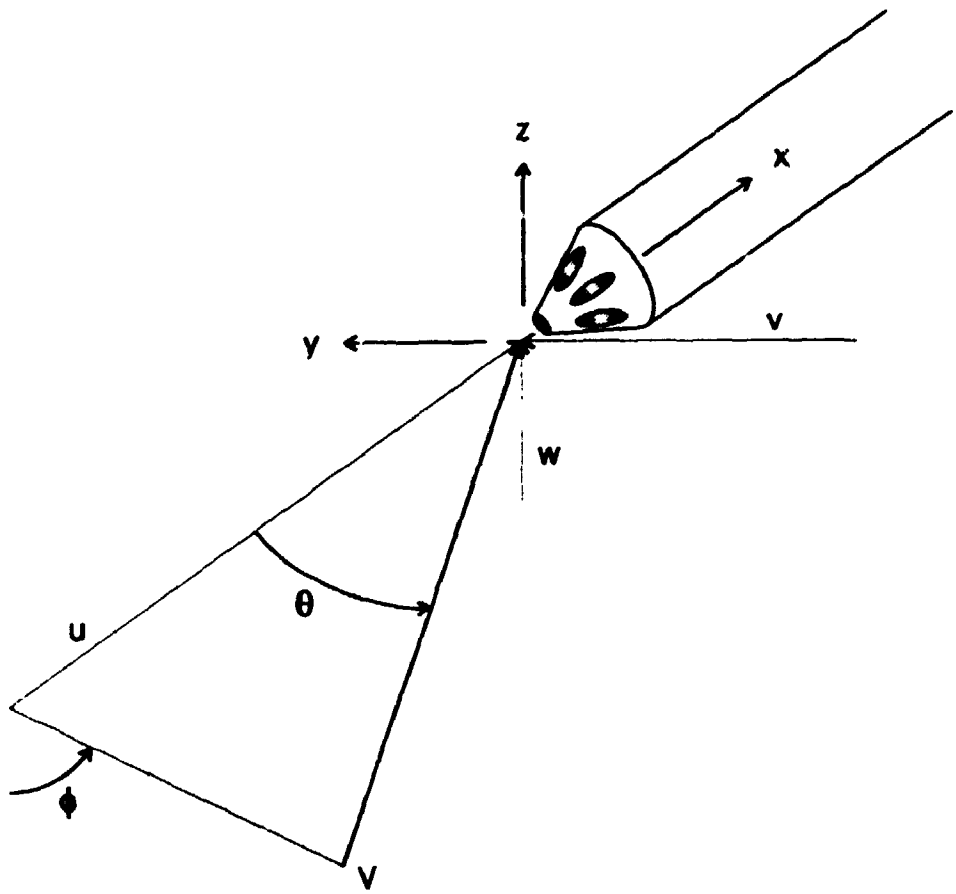

Figure E.8 Polar coordinate system used for high angle regime.

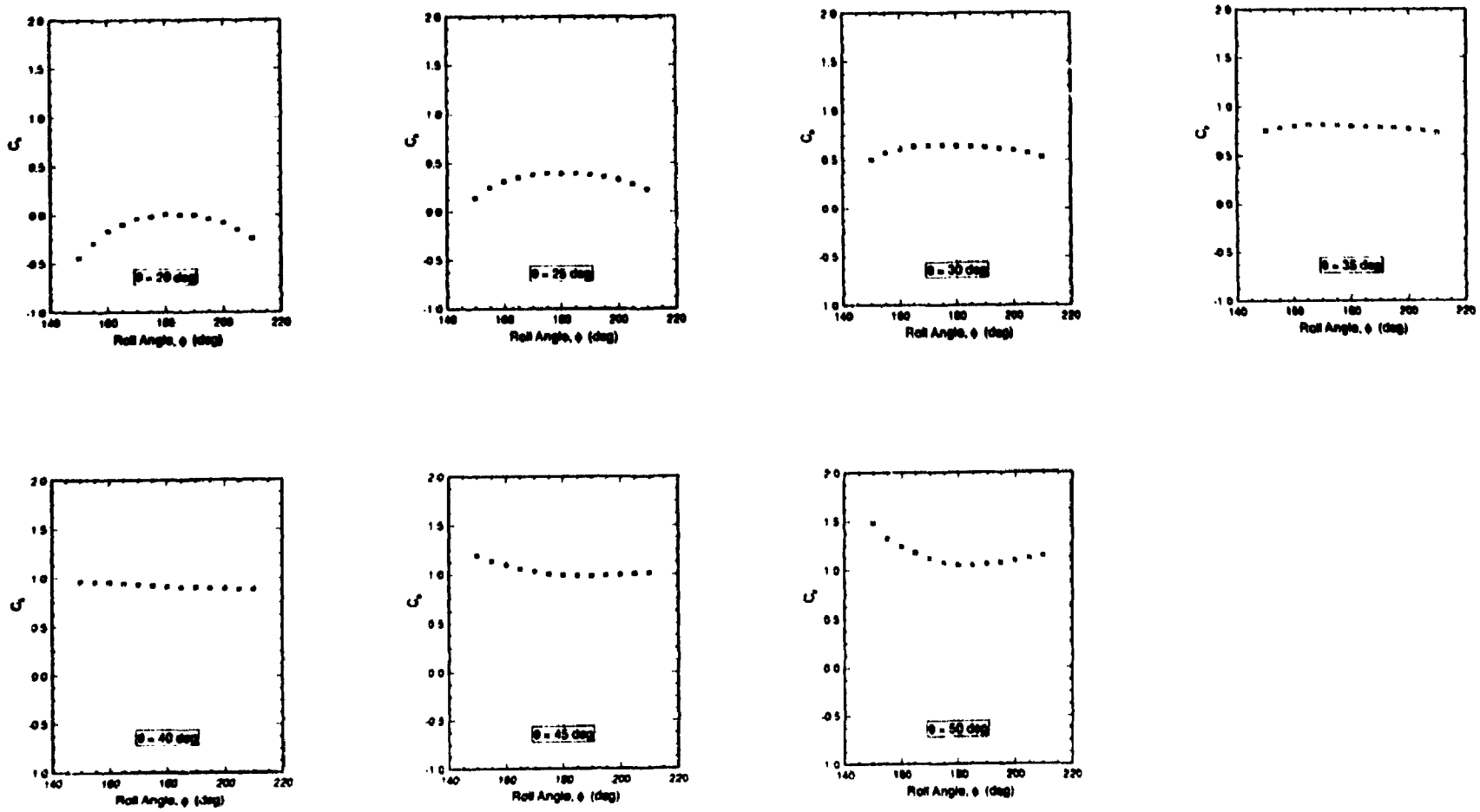

Figure E.9 C_θ calibration data for Sector 1.

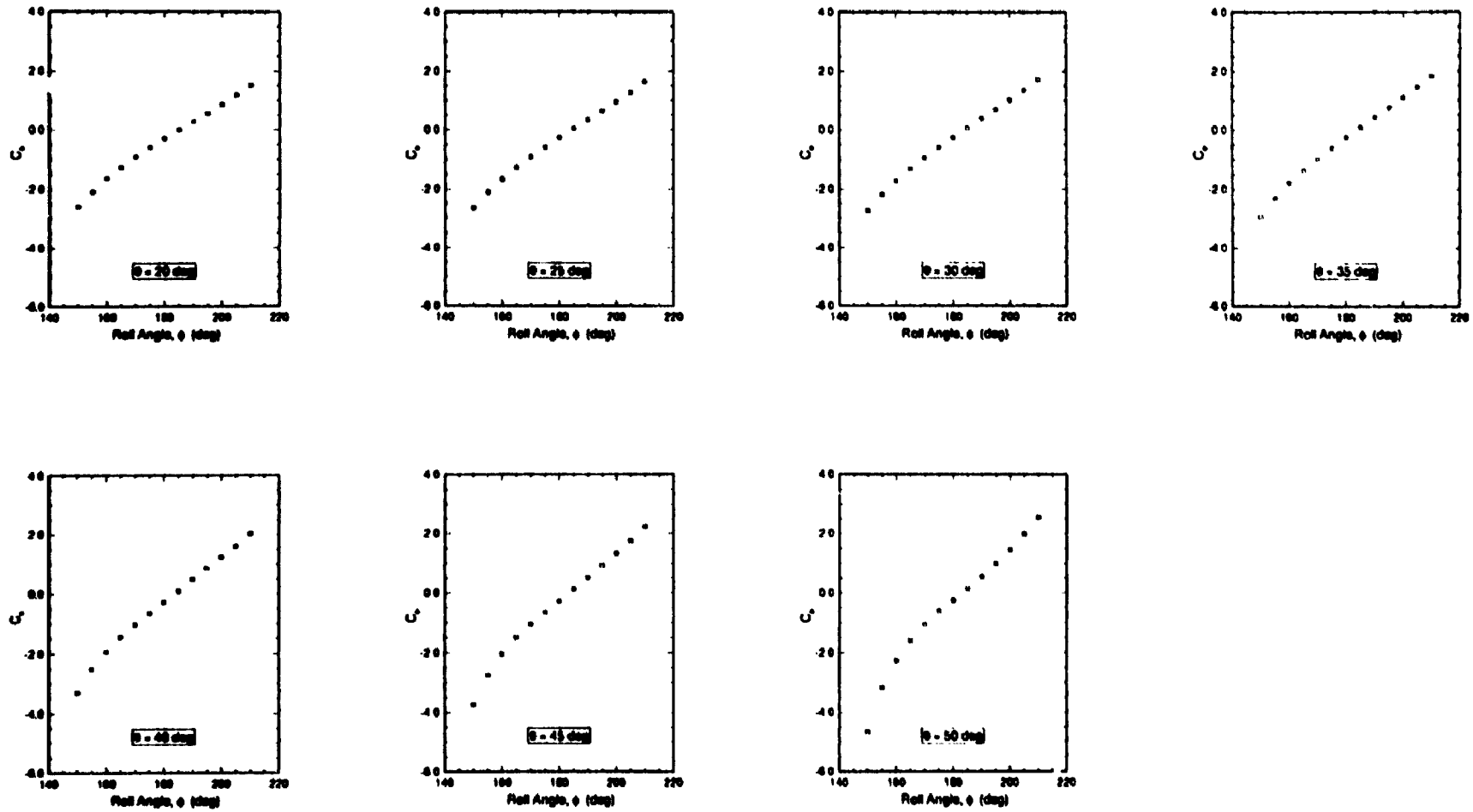

Figure E.10 C_ϕ calibration data for Sector 1.

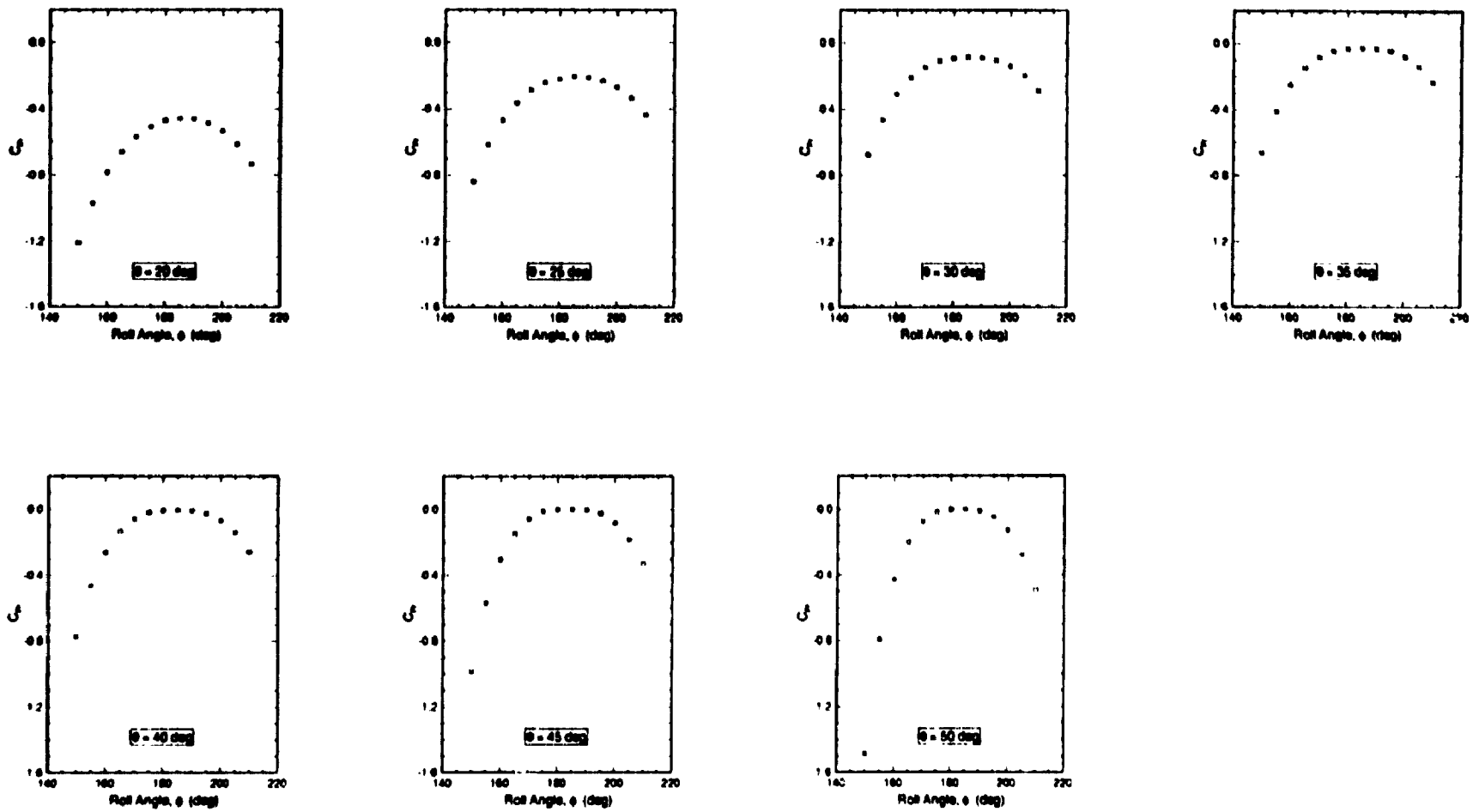

Figure E.11 C_{P_i} calibration data for Sector 1.

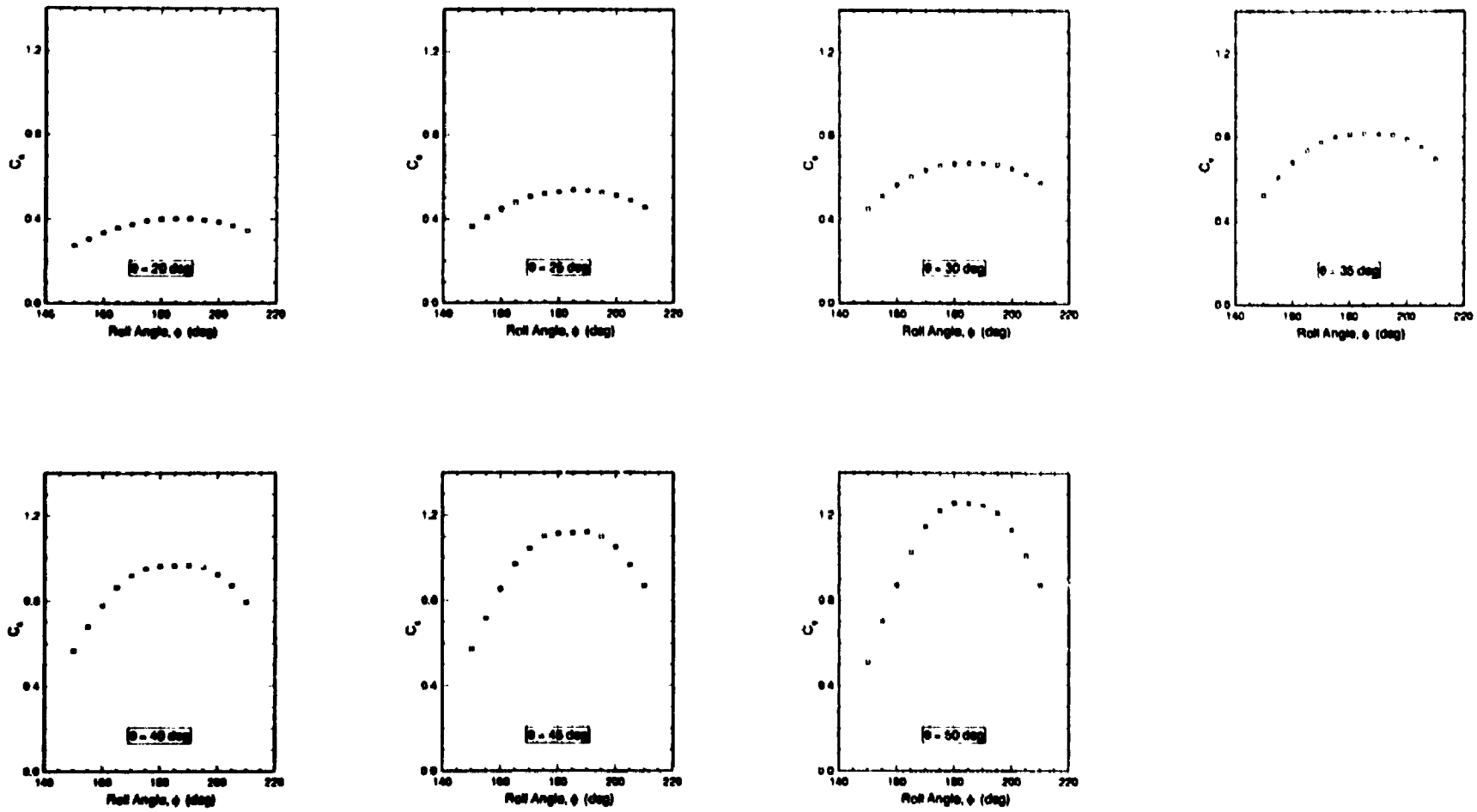

Figure E.12 C_q calibration data for Sector 1.

Appendix F
Transducer Calibration Curves

This appendix presents the calibration curves for both of the pressure transducers used in the experiments. Each of the Baratron pressure transducers (Model No. 220CD) was calibrated using a micro-manometer. During calibration the pressure was applied in a random manner and varied in both directions in order to minimize the effects of hysteresis. The data presented below was obtained prior to beginning the measurements; the calibration curves were checked twice thereafter and found to be very stable.

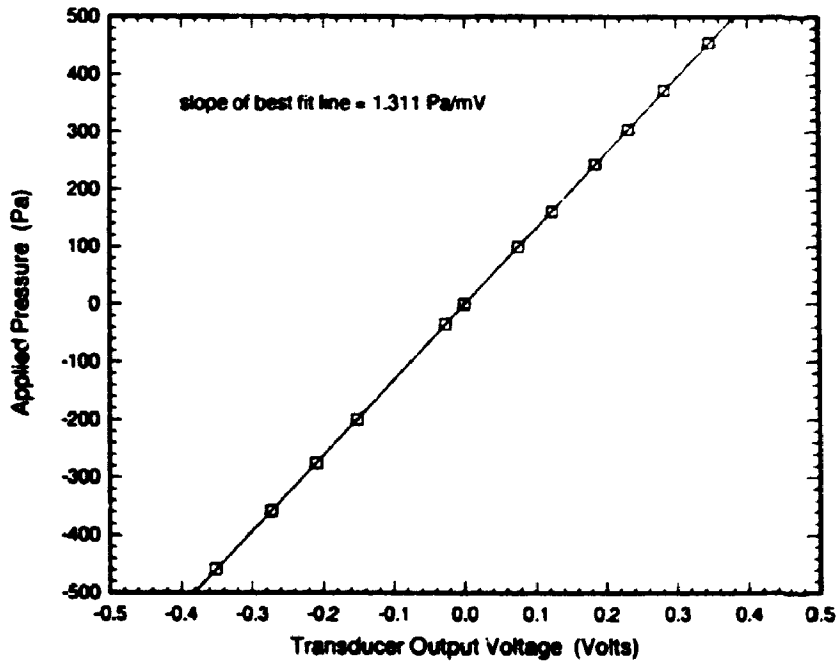

Figure F.1 Pressure transducer calibration curve for Baratron Serial No. 92225203A.

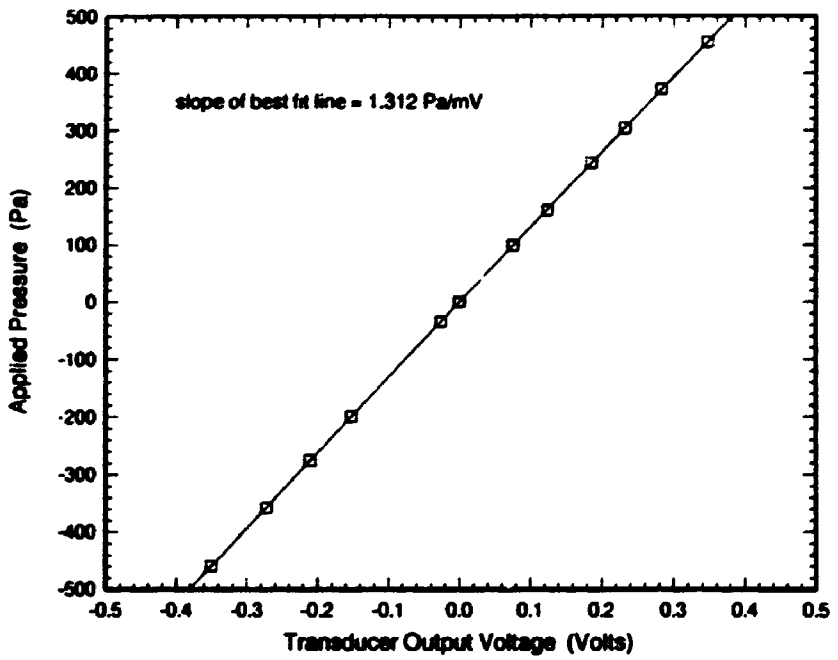

Figure F.2 Pressure transducer calibration curve for Baratron Serial No. 92225204A.

Appendix G
Experimental Designs

This appendix describes several parts which have been designed in the course of this research. As described in Chapter 3, the present cascade has been used previously to study the tip-clearance flow at smaller clearances. In order to accommodate the large tip clearances used in the current study, several parts of the cascade had to be redesigned. These parts, which included wedge-shaped spacing blocks and extensions for the side walls, were designed by Verhiel (1994).

As the clearance size was increased, the angle between the tipwall window (Figure G.2) and the hubwall became significantly larger. Base plates (Figures G.3 and G.4) were designed to mount on to the tipwall window allowing the traverse gear to be positioned in a plane normal to the hubwall for each clearance.

As described in Chapter 4, a large amount testing was done to determine the *wait* and *sampling* times required for the cascade measurements. In order to improve the response time of the experimental set-up, the effective volume of the system had to be reduced (see Section 4.2.1). In addition to shortening the length of tubing used in the pressure lines, brass inserts (Figure G.1) were designed to be fitted to the Baratron transducers to minimize their effective volume.

ITEM	QTY.	MATL.	DESCRIPTION
1/8" TUBING	1	BRASS	4.5" LENGTH TUBE

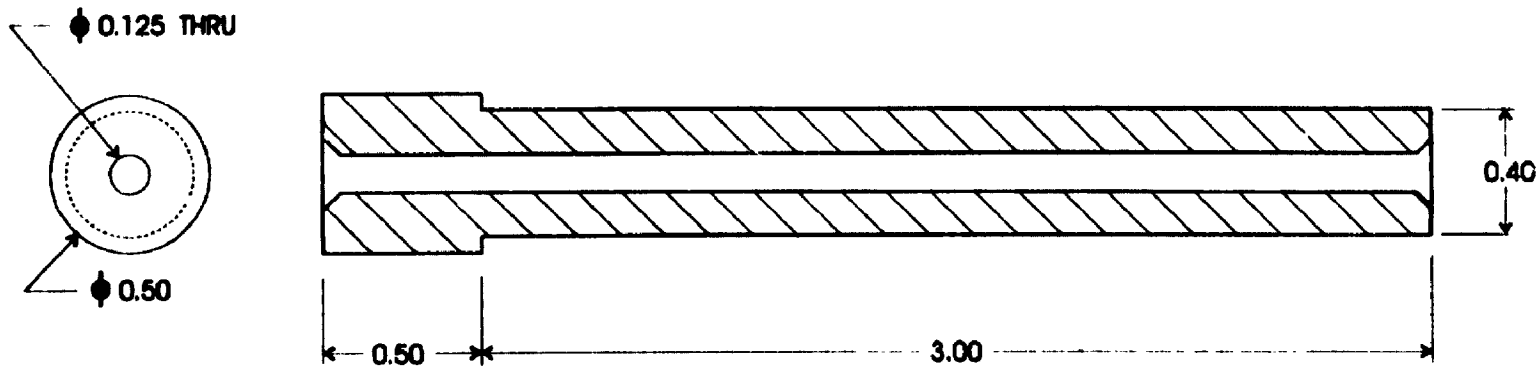

NOTES: USE 45 DEG. MILLING TOOL FOR CHAMFERS

1/8" TUBING SHOULD BE FITTED THROUGH THE ENTIRE LENGTH OF THE PIECE AND SOLDERED TO THE INSERT AT BOTH ENDS

EXCESS TUBING SHOULD BE LEFT TO PROTRUDE FROM THE LEFT FACE OF THE INSERT (i.e. THE LARGER DIAMETER FACE)

TITLE BARATRON INSERT		BY STEFANO DE CECCO	
SCALE 2:1	UNITS INCHES	CHKD.	APPD.
DWG. NO. LEFT-INS-002		MATERIAL BRASS	
DATE JULY 19, 1993			

Figure G.1 Transducer insert.

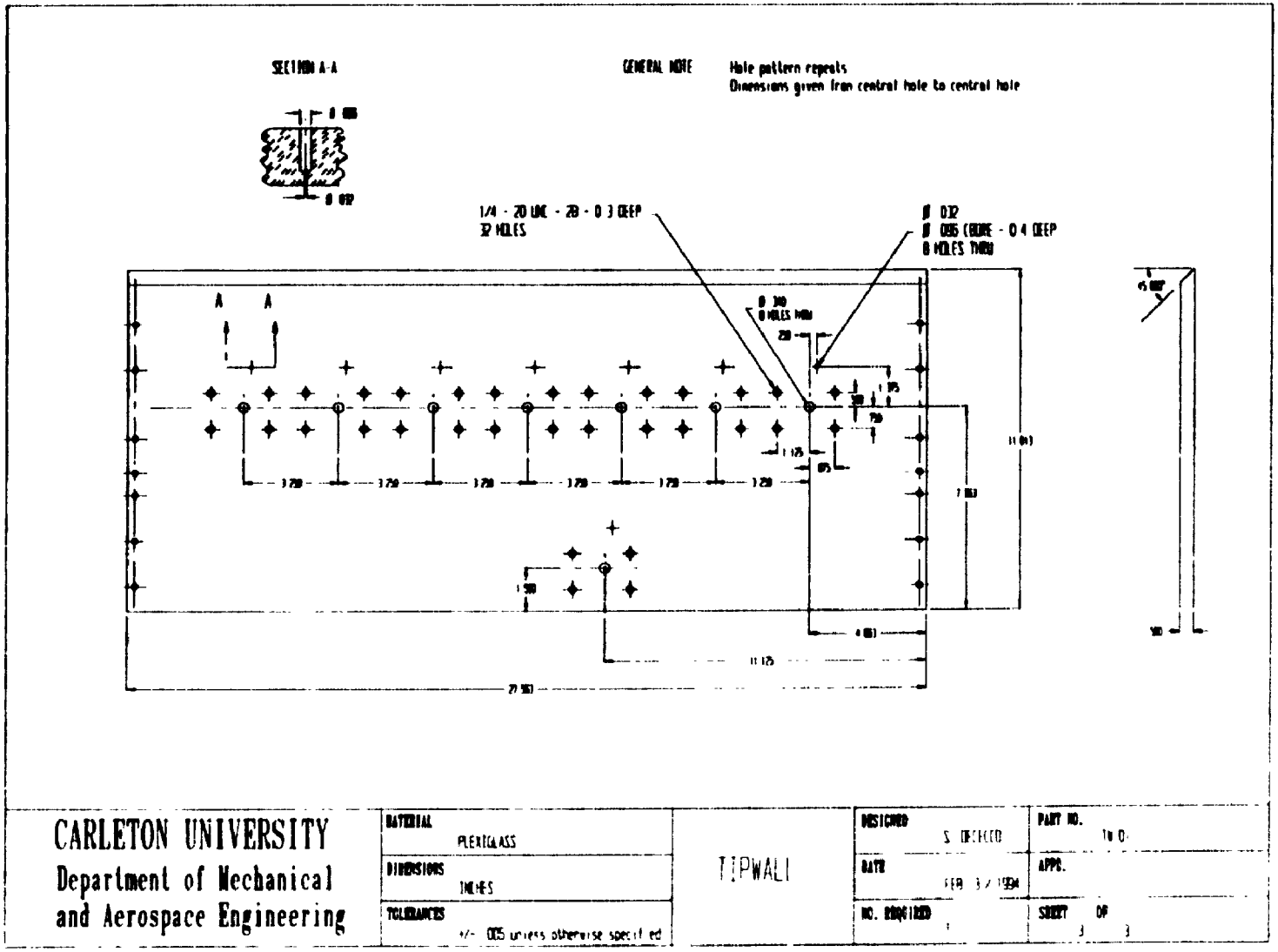

Figure G.2 Plexiglass tipwall window.

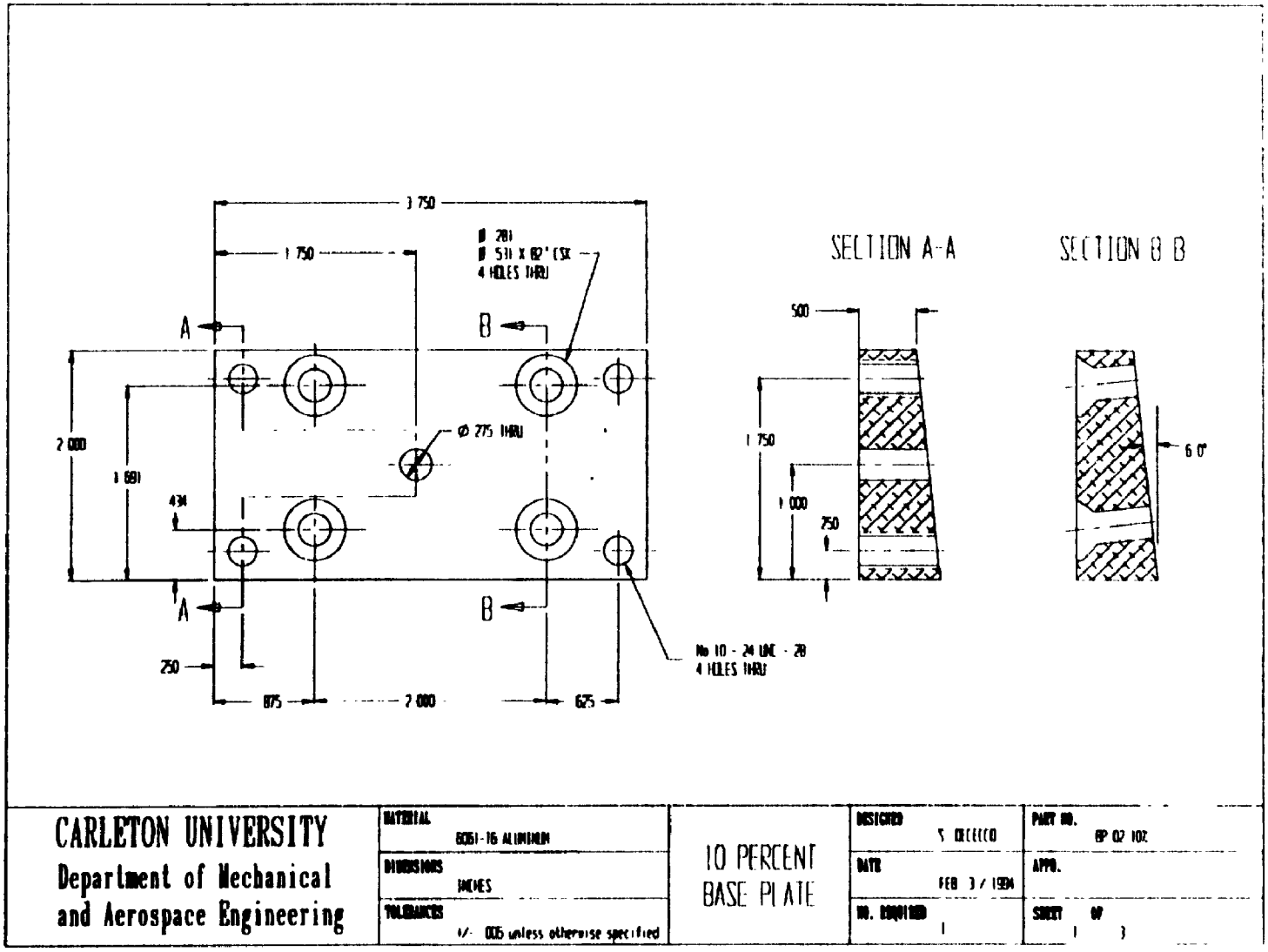

Figure G.3 Traverse gear baseplate for measurements at 10% clearance.

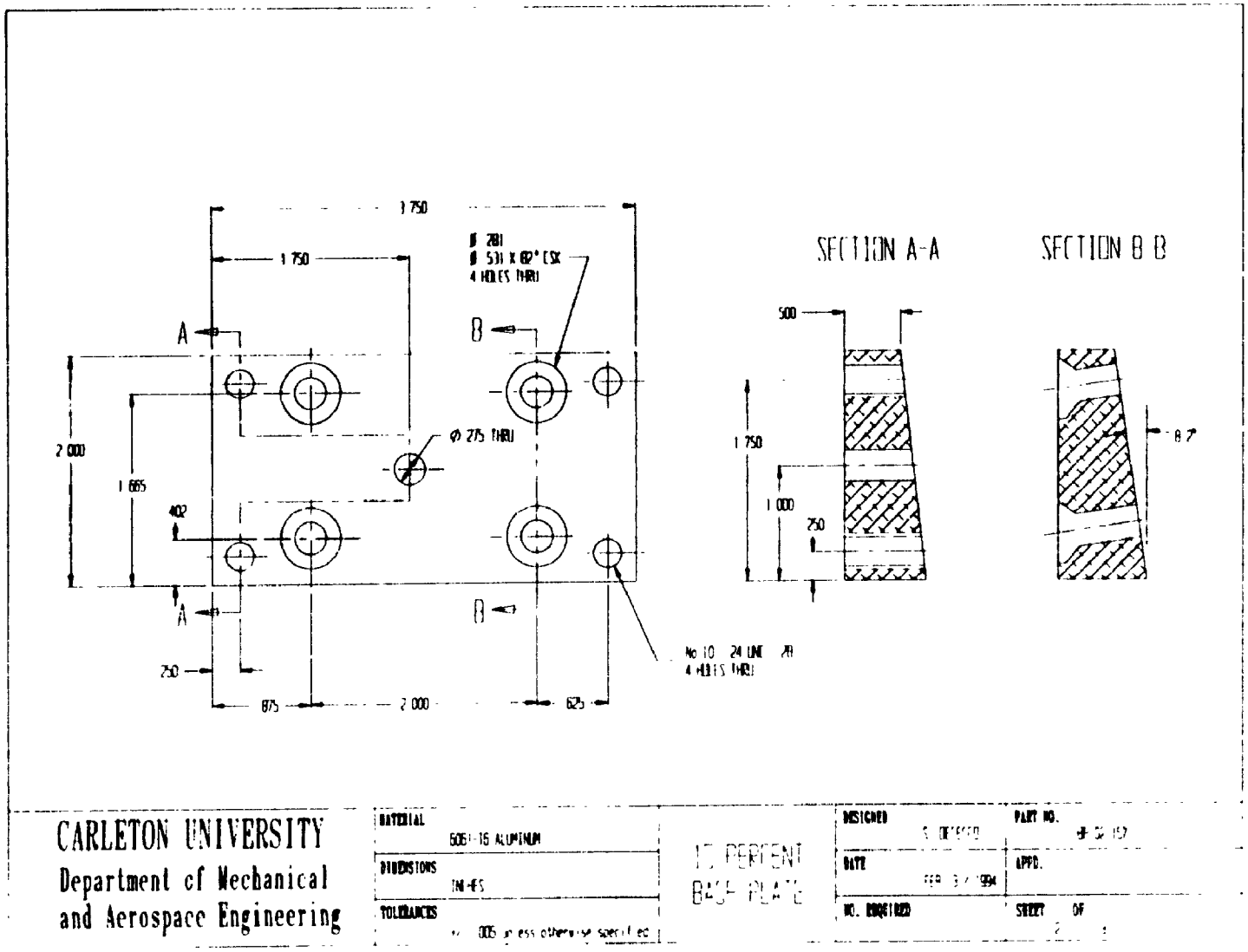

Figure G.4 Traverse gear baseplate for measurements at 15% clearance.

Appendix H
Sample Dawes Code Input File

This appendix gives a sample listing of a typical Dawes code input file for a blade with $\tau/c = 0.10$. The grid dimensions are 35×107×35 and the inlet and outlet Mach numbers are 0.26 and 0.42, respectively. The solution is marched for 3000 timesteps using a fine grid local timestep multiplier of 0.5. The artificial viscosity coefficients used in the solution ($K^{(2)} = 1$, $K^{(4)} = 0.01$, $\alpha = 2$) are identical to those suggested by Dawes (1986a).

```
  10%clr.in
  35  107   35 4193 3000   24   80    2    2    0
   0    0    0    0    0    0    0
   1    0
  2.00000
  0.00000
  0.00100
-144.38277-116.23786 -93.54036 -75.23592 -60.47428 -48.56973 -38.96929 -31.22700
 -24.98322 -19.94791 -15.88717 -12.61239  -9.97143  -7.84163  -6.12405  -4.73890
  -3.62184  -2.72099  -1.99450  -1.40862  -0.93614  -0.55510  -0.24781   0.00000
   0.24781   0.55006   0.91838   1.36658   1.91092   2.57034   3.36668   4.32489
   5.47302   6.84223   8.46649  10.38218  12.62737  15.24087  18.26093  21.72373
  25.66151  30.10060  35.05927  40.54563  46.55569  53.07174  60.06125  67.47646
  75.25466  83.31952  91.58302  99.94846 108.31391 116.57742 124.64227 132.42047
 139.83568 146.82520 153.34123 159.35129 164.83766 169.79633 174.23541 178.17319
 181.63597 184.65604 187.26953 189.51472 191.43042 193.05467 194.42387 195.57201
 196.53021 197.32655 197.98598 198.53030 198.97852 199.34683 199.64908 199.89688
 200.14468 200.44304 200.80226 201.23476 201.75549 202.38245 203.13730 204.04614
 205.14040 206.45787 208.04411 209.95395 212.25340 215.02194 218.35526 222.36858
 227.20061 233.01837 240.02296 248.45650 258.61047 270.83585 285.55521 303.27731
 324.61472 350.30496 381.23602
  0.00100
 -28.32677 -22.80496 -18.35189 -14.76070 -11.86458  -9.52900  -7.64547  -6.12649
  -4.90151  -3.91362  -3.11694  -2.47445  -1.95632  -1.53847  -1.20149  -0.92973
  -0.71058  -0.53384  -0.39131  -0.27636  -0.18366  -0.10891  -0.04862   0.00000
   1.31297   2.12321   2.77193   3.37720   3.95736   4.51911   5.13273   5.78670
   6.50571   7.25753   8.01947   8.80712   9.48541  10.03584  10.37352  10.39703
  10.02848   9.23641   7.90899   5.96500   3.29564  -0.12417  -4.44919  -9.66799
 -15.79587 -22.71875 -30.19229 -38.06784 -46.19894 -54.50549 -62.86451 -71.14409
 -79.19541 -87.00333 -94.38660-101.30160-107.68100-113.55939-118.84127-123.55875
-127.73108-131.37369-134.54716-137.30324-139.66255-141.65405-143.30518-144.71121
-145.89969-146.89780-147.65039-148.32373-148.93652-149.44531-149.92969-152.00000
-152.29117-152.64174-153.06381-153.57199-154.18385-154.92053-155.80748-156.87537
-158.16110-159.70914-161 57297-163.81702-166.51886-169.77188-173.68852-178.40416
-184.08177-190.91762-199.14798-209.05734-220.98822-235.35298-252.64816-273.47156
-298.54294-328.72888-365.07275
  0.00100
  0.00000   0.00000   0.00000   0.00000   0.00000   0.00000   0.00000   0.00000
  0.00000   0.00000   0.00000   0.00000   0.00000   0.00000   0.00000   0.00000
  0.00000   0.00000   0.00000   0.00000   0.00000   0.00000   0.00000   0.00000
  3.22298   4.79273   6.13307   7.42670   8.60338   9.65799  10.67298  11.72052
 12.77169  13.92746  15.17908  16.55520  17.94785  19.37706  20.78886  22.10756
```

```
  23.27623    24.34668    25.25338    25.95119    26.41094    26.68469    26.60779    26.24583
  25.57981    24.63845    23.65687    22.61489    21.60775    20.53784    19.35833    18.18237
  16.97063    15.70561    14.58989    13.52248    12.54259    11.68364    10.99494    10.39745
   9.89944     9.50575     9.18803     8.91797     8.70723     8.59924     8.47632     8.24875
   7.62033     6.75650     5.90723     5.02002     4.09863     3.23047     2.28906     0.00000
   0.00000     0.00000     0.00000     0.00000     0.00000     0.00000     0.00000     0.00000
   0.00000     0.00000     0.00000     0.00000     0.00000     0.00000     0.00000     0.00000
   0.00000     0.00000     0.00000     0.00000     0.00000     0.00000     0.00000     0.00000
   0.00000     0.00000     0.00000
   0.00100
100000.00 100000.00 100000.00 100000.00 100000.00 100000.00 100000.00 100000.00
100000.00 100000.00 100000.00 100000.00 100000.00 100000.00 100000.00 100000.00
100000.00 100000.00 100000.00 100000.00 100000.00 100000.00 100000.00 100000.00
100000.00 100000.00 100000.00 100000.00 100000.00 100000.00 100000.00 100000.00
100000.00 100000.00 100000.00 100000.00 100000.00 100000.00 100000.00 100000.00
100000.00 100000.00 100000.00 100000.00 100000.00 100000.00 100000.00 100000.00
100000.00 100000.00 100000.00 100000.00 100000.00 100000.00 100000.00 100000.00
100000.00 100000.00 100000.00 100000.00 100000.00 100000.00 100000.00 100000.00
100000.00 100000.00 100000.00 100000.00 100000.00 100000.00 100000.00 100000.00
100000.00 100000.00 100000.00 100000.00 100000.00 100000.00 100000.00 100000.00
100000.00 100000.00 100000.00 100000.00 100000.00 100000.00 100000.00 100000.00
100000.00 100000.00 100000.00 100000.00 100000.00 100000.00 100000.00 100000.00
100000.00 100000.00 100000.00 100000.00 100000.00 100000.00 100000.00 100000.00
100000.00 100000.00 100000.00
   0.00100
-144.38277-116.23786 -93.54036 -75.23592 -60.47428 -48.56973 -38.96929 -31.22700
 -24.98322 -19.94791 -15.88717 -12.61239  -9.97143  -7.84163  -6.12405  -4.73890
  -3.62184  -2.72099  -1.99450  -1.40862  -0.93614  -0.55510  -0.24781   0.00000
   0.24781   0.55006   0.91838   1.36658   1.91092   2.57034   3.36668   4.32489
   5.47302   6.84223   8.46649  10.38218  12.62737  15.24087  18.26093  21.72373
  25.66151  30.10060  35.05927  40.54563  46.55569  53.07174  60.06125  67.47646
  75.25466  83.31952  91.58302  99.94846 108.31391 116.57742 124.64227 132.42047
 139.83568 146.82520 153.34123 159.35129 164.83766 169.79633 174.23541 178.17319
 181.63597 184.65604 187.26953 189.51472 191.43042 193.05467 194.42387 195.57201
 196.53021 197.32655 197.98598 198.53030 198.97852 199.34683 199.64908 199.89688
 200.14468 200.44304 200.80226 201.23476 201.75549 202.38245 203.13730 204.04614
 205.14040 206.45787 208.04411 209.95395 212.25340 215.02194 218.35526 222.36858
 227.20061 233.01837 240.02296 248.45650 258.61047 270.83585 285.55521 303.27731
 324.61472 350.30496 381.23602
   0.00100
 -28.32677 -22.80496 -18.35189 -14.76070 -11.86458  -9.52900  -7.64547  -6.12649
  -4.90151  -3.91362  -3.11694  -2.47445  -1.95632  -1.53847  -1.20149  -0.92973
  -0.71058  -0.53384  -0.39131  -0.27636  -0.18366  -0.10891  -0.04862   0.00000
   1.31297   2.12321   2.77193   3.37720   3.95736   4.51911   5.13273   5.78670
   6.50571   7.25753   8.01947   8.80712   9.48541  10.03584  10.37352  10.39703
  10.02848   9.23641   7.90899   5.96500   3.29564  -0.12411  -4.44919  -9.66799
 -15.79587 -22.71875 -30.19229 -38.06784 -46.19894 -54.50549 -62.86451 -71.14409
 -79.19541 -87.00333 -94.38660-101.30160-107.68100-113.55939-118.84127-123.55875
-127.73108-131.37369-134.54716-137.30324-139.66255-141.65405-143.30518-144.71121
-145.89969-146.89780-147.65039-148.32373-148.93652-149.44531-149.92969-152.00000
-152.29117-152.64174-153.06381-153.57199-154.18385-154.92053-155.80748-156.87537
-158.16110-159.70914-161.57297-163.81702-166.51886-169.77188-173.68852-178.40416
-184.08177-190.91762-199.14798-209.05734-220.98822-235.35298-252.64816-273.47156
-298.54294-328.72888-365.07275
   0.00100
   0.00000     0.00000     0.00000     0.00000     0.00000     0.00000     0.00000     0.00000
   0.00000     0.00000     0.00000     0.00000     0.00000     0.00000     0.00000     0.00000
   0.00000     0.00000     0.00000     0.00000     0.00000     0.00000     0.00000     0.00000
   3.22298     4.79273     6.13307     7.42670     8.60338     9.65799    10.67298    11.72052
  12.77169    13.92746    15.17908    16.55520    17.94785    19.37706    20.78886    22.10756
  23.27623    24.34668    25.25338    25.95119    26.41094    26.68469    26.60779    26.24583
  25.57981    24.63845    23.65687    22.61489    21.60775    20.53784    19.35833    18.18237
  16.97063    15.70561    14.58989    13.52248    12.54259    11.68364    10.99494    10.39745
   9.89944     9.50575     9.18803     8.91797     8.70723     8.59924     8.47632     8.24875
   7.62033     6.75650     5.90723     5.02002     4.09863     3.23047     2.28906     0.00000
   0.00000     0.00000     0.00000     0.00000     0.00000     0.00000     0.00000     0.00000
   0.00000     0.00000     0.00000     0.00000     0.00000     0.00000     0.00000     0.00000
   0.00000     0.00000     0.00000     0.00000     0.00000     0.00000     0.00000     0.00000
   0.00000     0.00000     0.00000
```

```
   0.00100
 100228.00 100228.00 100228.00 100228.00 100228.00 100228.00 100228.00 100228.00
 100228.00 100228.00 100228.00 100228.00 100228.00 100228.00 100228.00 100228.00
 100228.00 100228.00 100228.00 100228.00 100228.00 100228.00 100228.00 100228.00
 100228.00 100228.00 100228.00 100228.00 100228.00 100228.00 100228.00 100228.00
 100228.00 100228.00 100228.00 100228.00 100228.00 100228.00 100228.00 100228.00
 100228.00 100228.00 100228.00 100228.00 100228.00 100228.00 100228.00 100228.00
 100228.00 100228.00 100228.00 100228.00 100228.00 100228.00 100228.00 100228.00
 100228.00 100228.00 100228.00 100228.00 100228.00 100228.00 100228.00 100228.00
 100228.00 100228.00 100228.00 100228.00 100228.00 100228.00 100228.00 100228.00
 100228.00 100228.00 100228.00 100228.00 100228.00 100228.00 100228.00 100228.00
 100228.00 100228.00 100228.00 100228.00 100228.00 100228.00 100228.00 100228.00
 100228.00 100228.00 100228.00 100228.00 100228.00 100228.00 100228.00 100228.00
 100228.00 100228.00 100228.00 100228.00 100228.00 100228.00 100228.00 100228.00
 100228.00 100228.00 100228.00
   1005.40      1.40      0.50 300000.00     10.00      0.00
  23125.00  23125.00  21675.00  21675.00
  24614.00  24574.34  24574.34  24574.34  24574.34  24574.34  24574.34  24563.62
  24573.61  24574.34  24574.34  24574.34  24574.34  24574.34  24574.03  24542.27
  24508.50  24479.87  24454.61  24425.37  24386.24  24317.05  24225.68  24114.80
  24002.20  23891.38  23793.28  23702.62  23647.28  23584.05  23530.91  23485.44
  23427.70  23313.51  23125.00
    300.00    300.00    300.00    300.00    300.00    300.00    300.00    300.00
    300.00    300.00    300.00    300.00    300.00    300.00    300.00    300.00
    300.00    300.00    300.00    300.00    300.00    300.00    300.00    300.00
    300.00    300.00    300.00    300.00    300.00    300.00    300.00    300.00
    300.00    300.00    300.00
      0.00      0.00      0.00      0.00      0.00      0.00      0.00      0.00
      0.00      0.00      0.00      0.00      0.00      0.00      0.00      0.00
      0.00      0.00      0.00      0.00      0.00      0.00      0.00      0.00
      0.00      0.00      0.00      0.00      0.00      0.00      0.00      0.00
      0.00      0.00      0.00
    103.00    103.00    103.00    103.00    103.00    103.00    103.00    102.60
    102.97    103.00    103.00    103.00    103.00    103.00    102.99    101.80
    100.53     99.44     98.47     97.33     95.80     93.03     89.27     84.51
     79.42     74.11     69.10     64.15     60.95     57.09     53.64     50.51
     46.25     36.43      0.00
      0.00      0.00      0.00      0.00      0.00      0.00      0.00      0.00
      0.00      0.00      0.00      0.00      0.00      0.00      0.00      0.00
      0.00      0.00      0.00      0.00      0.00      0.00      0.00      0.00
      0.00      0.00      0.00      0.00      0.00      0.00      0.00      0.00
      0.00      0.00      0.00
      0.00      0.00      0.00      0.00      0.00      0.00      0.00      0.00
      0.00      0.00      0.00      0.00      0.00      0.00      0.00      0.00
      0.00      0.00      0.00      0.00      0.00      0.00      0.00      0.00
      0.00      0.00      0.00      0.00      0.00      0.00      0.00      0.00
      0.00      0.00      0.00
   1.00000   0.99206   0.97519   0.95186   0.92159   0.88486   0.84367   0.79752
   0.74938   0.69826   0.64615   0.59454   0.54293   0.49280   0.44467   0.39851
   0.35583   0.31563   0.27841   0.24417   0.21390   0.18610   0.16179   0.13945
   0.12010   0.10323   0.08834   0.07543   0.06452   0.05459   0.04665   0.03921
   0.03375   0.02829
   1.00000   1.24893   1.55585   1.92997   2.37987   2.91247   3.53153   4.23608
   5.01871   5.86398   6.74744   7.63545   8.48631   9.25271   9.88574  10.33987
  10.57838  10.57837  10.33987   9.88574   9.25271   8.48630   7.63545   6.74744
   5.86397   5.01872   4.23608   3.53154   2.91247   2.37987   1.92997   1.55584
   1.24893   1.00001
 3000 4000 5000 6000 7000
 1 2 3 4 5 6 7 8 9101112
 1 2 3 4 5 6 7 8 91011121314151617181920
    1    2    3    4    5
   1.00000   1.00000   1.00000   1.00000   0.01000   2.00000
   20
   1.00000   1.00000   1.00000   1.00000   1.00000   1.00000   1.00000   1.00000
   1.00000   1.00000   1.00000   1.00000   1.00000   1.00000   1.00000   1.00000
   1.00000   0.90000   0.60000   0.00000   0.00000   0.00000   0.00000   0.00000
   0.00000   0.00000   0.00000   0.00000   0.00000   0.00000   0.00000   0.00000
   0.00000   0.00000   0.00000
```

Appendix I
Modifications to CASTLE and CENTREPOINT: Pre- and Post-Processors for the Dawes Code

This appendix describes some of the modifications made to the CASTLE Preprocessor and CENTREPOINT Postprocessor developed by Isaacs (1994). It is assumed that the reader is familiar with the earlier documentation presented in Isaacs (1994).

CASTLE Pre-Processor:

The following commands expand on the previous glossary of CASTLE geometric parameters presented by Isaacs (1994):

[set bl *{none}{thompson}{user <filename>}*] Set the inlet boundary layer type. (Note that it is necessary that the grid be plotted prior to defining the inlet boundary layer type since the spanwise nodal distribution is required for the boundary-layer calculations). If *none* is specified (default), the inlet total pressure distribution remains uniform at the centreline value. If *thompson* is specified, the user will be prompted for the inlet boundary layer thickness, δ [mm], and the skin friction coefficient, c_f, and a Thompson velocity profile will be set. If *user* is specified, CASTLE reads the boundary-layer data from the specified file. This data must consist of two columns: the first containing the distance from the wall normalized by the passage span, z/H, and the second containing the local dynamic pressure at that station normalized by the inlet centreline value, q/q_{ref}. Using this data as a look-up-table, the inlet total-pressure distribution for the computations is scaled on the inlet centreline value to give a geometrically similar boundary-layer.

[show spanwise nodes] Once the grid has been plotted, this command will give a listing of the respective radii for the spanwise nodes. This facilitates the choice of K_{tip} and the assignment of the thickness factors, $K_{thickness}$, and gives the user a quick impression of the number of nodes in the tip gap.

CENTREPOINT Post-Processor:

The variable extraction listing for the CENTREPOINT post-processor was expanded in the course of the present research. The following is meant only as an addendum to the previous description of CENTREPOINT by Isaacs (1994).

Currently the list of possible extraction variables includes:

```
(1)   Axial Velocity
(2)   Tangential Velocity
(3)   Radial Velocity
(4)   Mach Number
(5)   Static Pressure
(6)   Static Density
(7)   Phi
(8)   Dynamic Viscosity
(9)   Total Pressure Loss Coefficient, Cpo
(10)  Total Pressure Loss Coefficient, Y
(11)  Projected Flow Velocity Vectors
(12)  Horizontally Projected Flow Angle
      INLET CENTRELINE QUANTITIES
(13)  Total Pressure Loss Coefficient, Cpo_CL
(14)  Static Pressure Coefficient, Cps_CL
```

Items (13) and (14) were included during the present research. Extraction variable (13) differs from the previous total-pressure loss coefficient in that it is referenced to the inlet centreline value as opposed to the mass-averaged total pressure at the inlet. Likewise, extraction variable (14) is a static-pressure coefficient referenced to the inlet centreline static pressure.

The equations for the total-pressure coefficient and the static-pressure coefficient are:

$$C_{Po_{CL}} = \frac{P_o - P_{o_{CL}}}{P_{o_{CL}} - P_{CL}} \tag{I.1}$$

$$C_{P_{CL}} = \frac{P - P_{CL}}{P_{o_{CL}} - P_{CL}} \tag{I.2}$$

The centreline values, $P_{o_{CL}}$ and P_{CL}, are evaluated at the (I,J,K) index of (IMP,2,KMP), where IMP and KMP correspond to the mid-pitch and mid-span, respectively.

Appendix J
Simple Model for Predicting Underturning at Large Clearances

This appendix details the derivation of a simple model which can be used to predict the flow underturning of a blade with large clearance.

It is found that the gap flow experiences very little turning at large clearances. As a result, the spanwise axial velocity distribution is readjusted by the flow field in order to match the gap flow static pressure to that of the main flow at the outlet of the blade row. Since turbine blade rows tend to accelerate the flow, an increase in the gap flow axial velocity is generally required. This redistribution of the mass flow in the annulus must be taken into account when predicting the average blade outlet angle.

The ensuing analysis accounts for this redistributed mass flow by using a step function, as shown in Figure J.1. The outlet axial velocity distribution is assumed constant across the blade span up to the blade tip, where the value jumps from Ca_2 for the main flow to Ca_{2_g} for the gap flow. The inlet velocity, C_1, inlet flow angle, α_1, and the nominal (zero clearance) outlet flow angle, α_2, are all assumed known. In addition, the following assumptions are made:

- the effective gap height, τ, is constant over entire chord length;
- all fluid passing through the gap experiences no tangential force;
- flow turning is unchanged past the blade;
- total pressure losses are assumed negligible compared to the dynamic pressures;
- compressibility effects can be neglected.

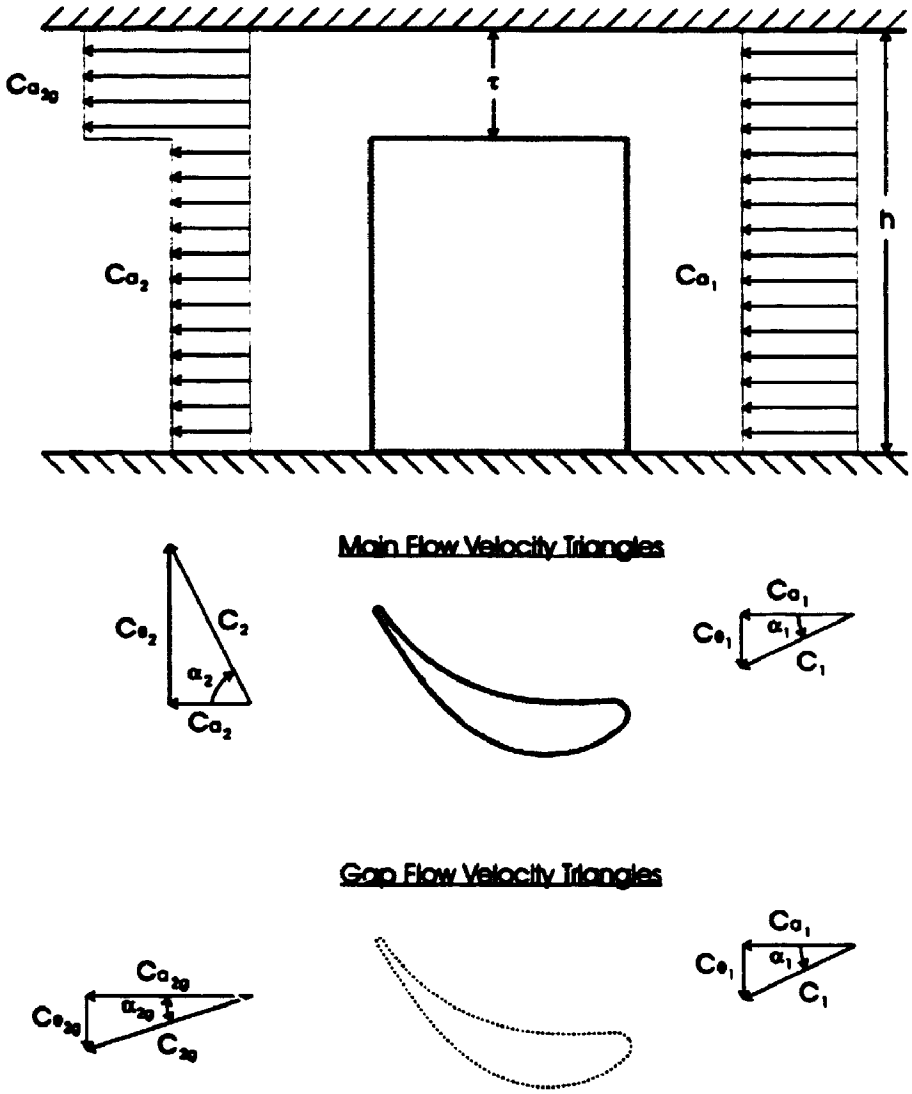

Figure J.1 Idealized flow in a turbine with large clearance.

Applying Bernoulli's equation to the main flow gives:

$$P_{s_2} + \frac{1}{2}\rho C_2^2 = P_{s_1} + \frac{1}{2}\rho C_1^2$$

The main flow velocity triangles, given at the bottom of Figure J.1, show that the inlet and outlet total velocities can be expressed in terms of their respective axial velocity and flow angle

$$Ca_1 = C_1 \cos\alpha_1$$
$$Ca_2 = C_2 \cos\alpha_2$$

allowing the main flow static pressure drop across the blade row to be expressed as:

$$P_{s_1} - P_{s_2} = \frac{1}{2}\rho\left[\left(\frac{Ca_2}{\cos\alpha_2}\right)^2 - \left(\frac{Ca_1}{\cos\alpha_1}\right)^2\right] \tag{J.1}$$

The gap flow velocity triangles are also shown in Figure J.1. Since it is assumed that the gap flow experiences no tangential force as it passes the blade row (i.e., $Ce_{2g} = Ce_1$), the static pressure drop experienced by the gap flow can be expressed in terms of the axial velocities:

$$P_{s_1} - P_{s_2} = \frac{1}{2}\rho\left[Ca_{2g}{}^2 - Ca_1{}^2\right] \tag{J.2}$$

To ensure a uniform static pressure downstream, both the main flow and the gap flow must experience the same static pressure drop. By equating Equations (J.1) and (J.2),

$$\frac{1}{2}\rho\left[\left(\frac{Ca_2}{\cos\alpha_2}\right)^2 - \left(\frac{Ca_1}{\cos\alpha_1}\right)^2\right] = \frac{1}{2}\rho\left[Ca_{2g}{}^2 - Ca_1{}^2\right]$$

and simplifying, the gap flow axial velocity ratio can be expressed as:

$$\left(\frac{Ca_{2g}}{Ca_1}\right)^2 = 1 + \frac{1}{\cos^2\alpha_2}\left(\frac{Ca_2}{Ca_1}\right)^2 - \frac{1}{\cos^2\alpha_1} \tag{J.3}$$

The axial velocities in the blade passage are also constrained by the continuity equation. For incompressible flows this gives:

$$\rho Ca_1 h = \rho Ca_2(h - \tau) + \rho Ca_{2g}\tau$$

which can be reduced to obtain:

$$\frac{Ca_2}{Ca_1} = \left(\frac{h}{h-\tau}\right)\left[1 - \frac{Ca_{2g}}{Ca_1}\left(\frac{\tau}{h}\right)\right]$$

Letting $\kappa = \tau/h$ allows the previous equation to be rewritten as:

$$\frac{Ca_2}{Ca_1} = \left(\frac{1}{1-\kappa}\right)\left[1 - \frac{Ca_{2g}}{Ca_1}\kappa\right] \tag{J.4}$$

Substituting Equation (J.4) into (J.3) gives

$$\left(\frac{Ca_{2g}}{Ca_1}\right)^2 = 1 + \frac{1}{\cos^2\alpha_2}\left(\frac{1}{1-\kappa}\right)^2\left[1 - \frac{Ca_{2g}}{Ca_1}\kappa\right]^2 - \frac{1}{\cos^2\alpha_1}$$

which can be rearranged to obtain

$$\left[1 - \frac{\kappa^2}{\cos^2\alpha_2}\left(\frac{1}{1-\kappa}\right)^2\right]\left(\frac{Ca_{2g}}{Ca_1}\right)^2 + \left[\frac{2\kappa}{\cos^2\alpha_2}\left(\frac{1}{1-\kappa}\right)^2\right]\left(\frac{Ca_{2g}}{Ca_1}\right) + \left[\frac{1}{\cos^2\alpha_1} - 1 - \frac{1}{\cos^2\alpha_2}\left(\frac{1}{1-\kappa}\right)^2\right] = 0$$

The previous equation is quadratic in $\left(\frac{Ca_{2g}}{Ca_1}\right)$ with the solution taking the following form

$$\frac{Ca_{2g}}{Ca_1} = \frac{-b \pm \sqrt{b^2 - 4ac}}{2a}$$

where

$$a = 1 - \frac{\kappa^2}{\cos^2\alpha_2}\left(\frac{1}{1-\kappa}\right)^2$$
$$b = \frac{2\kappa}{\cos^2\alpha_2}\left(\frac{1}{1-\kappa}\right)^2 \tag{J.5}$$
$$c = \frac{1}{\cos^2\alpha_1} - 1 - \frac{1}{\cos^2\alpha_2}\left(\frac{1}{1-\kappa}\right)^2$$

Having solved for the gap flow axial velocity, the main flow axial velocity can be determined using Equation J.4. With the outlet axial velocity distribution now known, the mass-averaged outlet flow angle can be determined. Continuity states that the mass-averaged outlet axial velocity is given by:

$$Ca_2'' = Ca_1$$

Likewise, the mass-averaged tangential velocity, Ce_2'', can be determined from:

$$\dot{m}\, Ce_2'' = \dot{m}_g\, Ce_{2g} + (\dot{m} - \dot{m}_g)\, Ce_2 \tag{J.6}$$

The outlet tangential velocities can be expressed in terms of their axial components

$$Ce_{2g} = -C_1 \sin\alpha_1 = -Ca_1 \tan\alpha_1$$
$$Ce_2 = C_2 \sin\alpha_2 = Ca_2 \tan\alpha_2$$

thus allowing Equation (J.6) to be rewritten as

$$\frac{Ce_2''}{Ca_2''} = \left(\frac{1}{1-\kappa}\right)\left[1 - \kappa\left(\frac{Ca_{2g}}{Ca_1}\right)\right]^2 \tan\alpha_2 - \kappa\left(\frac{Ca_{2g}}{Ca_1}\right)\tan\alpha_1 \tag{J.7}$$

The mass-averaged flow angle is then obtained using:

$$\alpha_2'' = \tan^{-1}\left(\frac{Ce_2''}{Ca_2''}\right) \tag{J.8}$$

It is evident from Equations (J.7) and (J.5) that the mass-averaged outlet flow angle is a function of the gap/span ratio, κ, inlet flow angle, α_1, and the nominal (zero clearance) outlet flow angle, α_2. However, the nature of the equations makes it somewhat cumbersome to solve for α_2'' directly, even if these values are all known. Instead, using a method similar to the profile loss calculation proposed by Ainley & Mathieson (1951),

the mass-averaged flow angle can be calculated by interpolating between two extremes cases: nozzle blades and impulse blades. Figure J.2 plots the variation of the mass-averaged outlet flow angle at different nominal exit flow angles for nozzle blades with $\alpha_1 = 0\,deg$. Similarly, Figure J.3 plots the variation for impulse blades with $\alpha_1 = \alpha_2$. The expression for the mass-averaged exit flow then becomes:

$$\alpha_2'' = \alpha_{2\,[\alpha_1 = 0]}'' + \left(\frac{\alpha_1}{\alpha_2}\right)\left\{\alpha_{2\,[\alpha_1 = \alpha_2]}'' - \alpha_{2\,[\alpha_1 = 0]}''\right\} \tag{J.9}$$

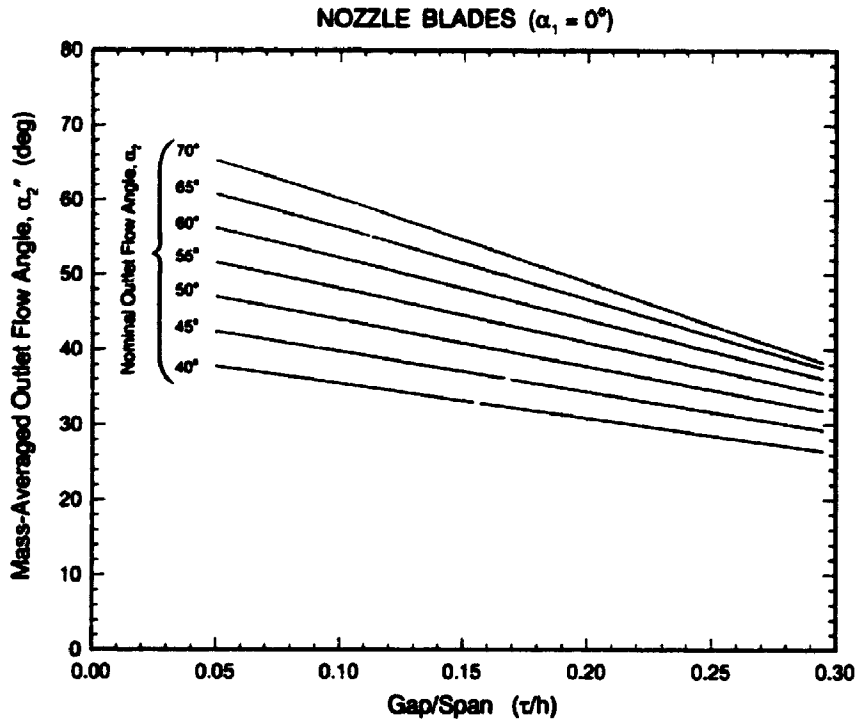

Figure J.2 Predicted mass-averaged outlet flow angle for blades with α_1 = *0 deg*.

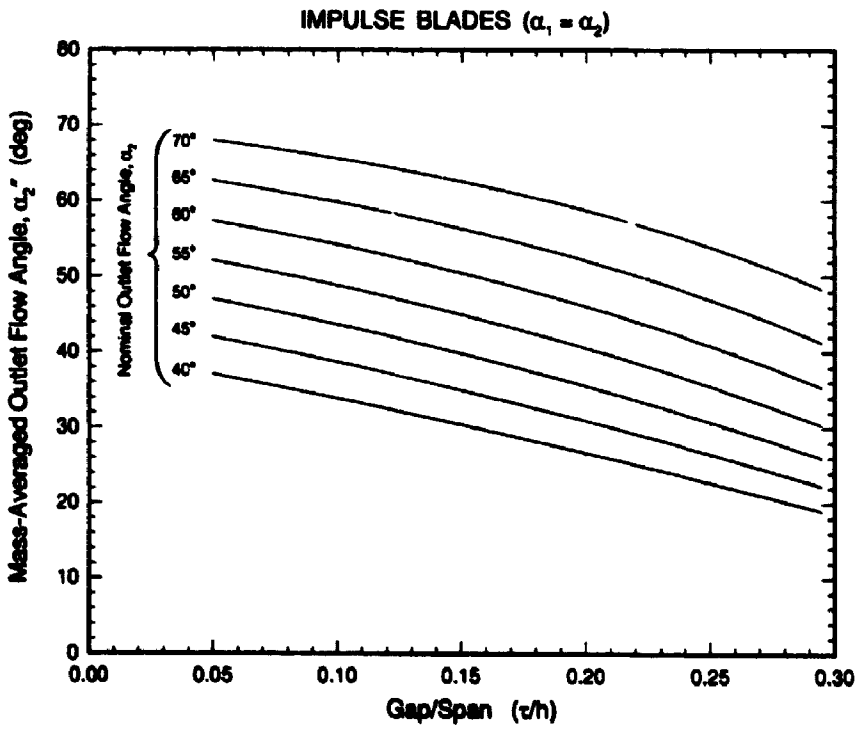

Figure J.3 Predicted mass-averaged outlet flow angle for blades with $\alpha_1 = \alpha_2$.

END

17-11-95

FIN